Technical Description of version 4.0 of the Community Land Model (CLM)

Keith W. Oleson, David M. Lawrence, Gordon B. Bonan, Mark G. Flanner, Erik Kluzek, Peter J. Lawrence, Samuel Levis, Sean C. Swenson, Peter E. Thornton

Aiguo Dai, Mark Decker, Robert Dickinson, Johannes Feddema, Colette L. Heald, Forrest Hoffman, Jean-Francois Lamarque, Natalie Mahowald, Guo-Yue Niu, Taotao Qian, James Randerson, Steve Running, Koichi Sakaguchi, Andrew Slater, Reto Stöckli, Aihui Wang, Zong-Liang Yang, Xiaodong Zeng, Xubin Zeng

Technical Description of version 4.0 of the Community Land Model (CLM)

Keith W. Oleson, David M. Lawrence, Gordon B. Bonan, Mark G. Flanner, Erik Kluzek, Peter J. Lawrence, Samuel Levis, Sean C. Swenson, Peter E. Thornton

Aiguo Dai, Mark Decker, Robert Dickinson, Johannes Feddema, Colette L. Heald, Forrest Hoffman, Jean-Francois Lamarque, Natalie Mahowald, Guo-Yue Niu, Taotao Qian, James Randerson, Steve Running, Koichi Sakaguchi, Andrew Slater, Reto Stöckli, Aihui Wang, Zong-Liang Yang, Xiaodong Zeng, Xubin Zeng

TABLE OF CONTENTS

LIST OF FIGURES

LIST OF TABLES

ACKNOWLEDGEMENTS

1. Introduction

The purpose of this technical note is to describe the physical parameterizations and numerical implementation of version 4.0 of the Community Land Model (CLM4.0) which is the land surface parameterization used with the Community Atmosphere Model (CAM4.0) and the Community Climate System Model (CCSM4.0). Scientific justification and evaluation of these parameterizations can be found in the referenced scientific papers (section 18). Chapters 1-16 constitute the description of CLM when coupled to CAM or CCSM, while Chapter 17 describes processes that pertain specifically to the operation of CLM in offline mode (uncoupled to an atmospheric model). Chapters 13 and 14 provide brief overviews only of the urban and carbon-nitrogen submodels. Full technical descriptions of these submodels can be found in Oleson et al. (2010) and Thornton et al. (2010, in preparation), respectively. These technical notes and the CLM4 User's Guide together provide the user with the scientific description and operating instructions for CLM.

1.1 Model History and Overview

1.1.1 History

The early development of the Community Land Model can be described as the merging of a community-developed land model focusing on biogeophysics and a concurrent effort at NCAR to expand the NCAR Land Surface Model (NCAR LSM, Bonan 1996) to include the carbon cycle, vegetation dynamics, and river routing. The concept of a community-developed land component of the Community Climate System Model (CCSM) was initially proposed at the CCSM Land Model Working Group (LMWG) meeting in February 1996. Initial software specifications and development

focused on evaluating the best features of three existing land models: the NCAR LSM (Bonan 1996, 1998) used in the Community Climate Model (CCM3) and the initial version of CCSM; the Institute of Atmospheric Physics, Chinese Academy of Sciences land model (IAP94) (Dai and Zeng 1997); and the Biosphere-Atmosphere Transfer Scheme (BATS) (Dickinson et al. 1993) used with CCM2. A scientific steering committee was formed to review the initial specifications of the design provided by Robert Dickinson, Gordon Bonan, Xubin Zeng, and Yongjiu Dai and to facilitate further development. Steering committee members were selected so as to provide guidance and expertise in disciplines not generally well-represented in land surface models (e.g., carbon cycling, ecological modeling, hydrology, and river routing) and included scientists from NCAR, the university community, and government laboratories (R. Dickinson, G. Bonan, X. Zeng, Paul Dirmeyer, Jay Famiglietti, Jon Foley, and Paul Houser).

The specifications for the new model, designated the Common Land Model, were discussed and agreed upon at the June 1998 CCSM Workshop LMWG meeting. An initial code was developed by Y. Dai and was examined in March 1999 by Mike Bosilovich, P. Dirmeyer, and P. Houser. At this point an extensive period of code testing was initiated. Keith Oleson, Y. Dai, Adam Schlosser, and P. Houser presented preliminary results of offline 1-dimensional testing at the June 1999 CCSM Workshop LMWG meeting. Results from more extensive offline testing at plot, catchment, and large scale (up to global) were presented by Y. Dai, A. Schlosser, K. Oleson, M. Bosilovich, Zong-Liang Yang, Ian Baker, P. Houser, and P. Dirmeyer at the LMWG meeting hosted by COLA (Center for Ocean-Land-Atmosphere Studies) in November

1999. Field data used for validation included sites adopted by the Project for Intercomparison of Land-surface Parameterization Schemes (Henderson-Sellers et al. 1993) (Cabauw, Valdai, Red-Arkansas river basin) and others [FIFE (Sellers et al. 1988), BOREAS (Sellers et al. 1995), HAPEX-MOBILHY (André et al. 1986), ABRACOS (Gash et al. 1996), Sonoran Desert (Unland et al. 1996), GSWP (Dirmeyer et al. 1999)]. Y. Dai also presented results from a preliminary coupling of the Common Land Model to CCM3, indicating that the land model could be successfully coupled to a climate model.

Results of coupled simulations using CCM3 and the Common Land Model were presented by X. Zeng at the June 2000 CCSM Workshop LMWG meeting. Comparisons with the NCAR LSM and observations indicated major improvements to the seasonality of runoff, substantial reduction of a summer cold bias, and snow depth. Some deficiencies related to runoff and albedo were noted, however, that were subsequently addressed. Z.-L. Yang and I. Baker demonstrated improvements in the simulation of snow and soil temperatures. Sam Levis reported on efforts to incorporate a river routing model to deliver runoff to the ocean model in CCSM. Soon after the workshop, the code was delivered to NCAR for implementation into the CCSM framework. Documentation for the Common Land Model is provided by Dai et al. (2001) while the coupling with CCM3 is described in Zeng et al. (2002). The model was introduced to the modeling community in Dai et al. (2003).

Concurrent with the development of the Common Land Model, the NCAR LSM was undergoing further development at NCAR in the areas of carbon cycling, vegetation dynamics, and river routing. The preservation of these advancements necessitated several modifications to the Common Land Model. The biome-type land cover

classification scheme was replaced with a plant functional type (PFT) representation with the specification of PFTs and leaf area index from satellite data (Oleson and Bonan 2000, Bonan et al. 2002a, b). This also required modifications to parameterizations for vegetation albedo and vertical burying of vegetation by snow. Changes were made to canopy scaling, leaf physiology, and soil water limitations on photosynthesis to resolve deficiencies indicated by the coupling to a dynamic vegetation model. Vertical heterogeneity in soil texture was implemented to improve coupling with a dust emission model. A river routing model was incorporated to improve the fresh water balance over oceans. Numerous modest changes were made to the parameterizations to conform to the strict energy and water balance requirements of CCSM. Further substantial software development was also required to meet coding standards. The resulting model was adopted in May 2002 as the Community Land Model (CLM2.0) for use with the Community Atmosphere Model (CAM2.0, the successor to CCM3) and version 2 of the Community Climate System Model (CCSM2.0).

K. Oleson reported on initial results from a coupling of CCM3 with CLM2 at the June 2001 CCSM Workshop LMWG meeting. Generally, the CLM2 preserved most of the improvements seen in the Common Land Model, particularly with respect to surface air temperature, runoff, and snow. These simulations are documented in Bonan et al. (2002a). Further small improvements to the biogeophysical parameterizations, ongoing software development, and extensive analysis and validation within CAM2.0 and CCSM2.0 culminated in the release of CLM2.0 to the community in May 2002.

Following this release, Peter Thornton implemented changes to the model structure required to represent carbon and nitrogen cycling in the model. This involved changing

data structures from a single vector of spatially independent sub-grid patches to one that recognizes three hierarchical scales within a model grid cell: land unit, snow/soil column, and PFT. Furthermore, as an option, the model can be configured so that PFTs can share a single soil column and thus "compete" for water. This version of the model (CLM2.1) was released to the community in February 2003. CLM2.1, without the compete option turned on, produced only round off level changes when compared to CLM2.0.

CLM3.0 implemented further software improvements related to performance and model output, a re-writing of the code to support vector-based computational platforms, and improvements in biogeophysical parameterizations to correct deficiencies in the coupled model climate. Of these parameterization improvements, two were shown to have a noticeable impact on simulated climate. A variable aerodynamic resistance for heat/moisture transfer from ground to canopy air that depends on canopy density was implemented. This reduced unrealistically high surface temperatures in semi-arid regions. The second improvement added stability corrections to the diagnostic 2-m air temperature calculation which reduced biases in this temperature. Competition between PFTs for water, in which PFTs share a single soil column, is the default mode of operation in this model version. CLM3.0 was released to the community in June 2004. Dickinson et al. (2006) describe the climate statistics of CLM3.0 when coupled to CCSM3.0. Hack et al. (2006) provide an analysis of selected features of the land hydrological cycle. Lawrence et al. (2007) examine the impact of changes in CLM3.0 hydrological parameterizations on partitioning of evapotranspiration (ET) and its effect on the timescales of ET response to precipitation events, interseasonal soil moisture storage, soil moisture memory, and land-atmosphere coupling. Qian et al. (2006)

evaluate CLM3.0's performance in simulating soil moisture content, runoff, and river discharge when forced by observed precipitation, temperature and other atmospheric data.

Although the simulation of land surface climate by CLM3.0 is in many ways adequate, most of the unsatisfactory aspects of the simulated climate noted by the above studies can be traced directly to deficiencies in simulation of the hydrological cycle. In 2004, a project was initiated to improve the hydrology in CLM3.0 as part of the development of CLM version 3.5. A selected set of promising approaches to alleviating the hydrologic biases in CLM3.0 were tested and implemented. These included new surface datasets based on Moderate Resolution Imaging Spectroradiometer (MODIS) products, new parameterizations for canopy integration, canopy interception, frozen soil, soil water availability, and soil evaporation, a TOPMODEL-based model for surface and subsurface runoff, a groundwater model for determining water table depth, and the introduction of a factor to simulate nitrogen limitation on plant productivity. Oleson et al. (2008a) show that CLM3.5 exhibits significant improvements over CLM3.0 in its partitioning of global ET which result in wetter soils, less plant water stress, increased transpiration and photosynthesis, and an improved annual cycle of total water storage. Phase and amplitude of the runoff annual cycle is generally improved. Dramatic improvements in vegetation biogeography result when CLM3.5 is coupled to a dynamic global vegetation model. Stöckli et al. (2008) examine the performance of CLM3.5 at local scales by making use of a network of long-term ground-based ecosystem observations [FLUXNET (Baldocchi et al. 2001)]. Data from 15 FLUXNET sites were

used to demonstrate significantly improved soil hydrology and energy partitioning in CLM3.5. CLM3.5 was released to the community in May, 2007.

The motivation for the next version of the model documented here, CLM4.0 (denoted hereafter as CLM), was to (1) incorporate several recent scientific advances in the understanding and representation of land surface processes, (2) expand model capabilities, and (3) improve surface and atmospheric forcing datasets. Included in the first category are more sophisticated representations of soil hydrology and snow processes. In particular, new treatments of soil column-groundwater interactions, soil evaporation, aerodynamic parameters for sparse/dense canopies, vertical burial of vegetation by snow, snow cover fraction, and aging, black carbon and dust deposition, and vertical distribution of solar energy for snow were implemented. Major new capabilities in the model include a representation of the carbon-nitrogen cycle, the ability to model land cover change in a transient mode, inclusion of organic soil and deep soil into the existing mineral soil treatment to enable more realistic modeling of permafrost, an urban canyon model to contrast rural and urban energy balance and climate (CLMU), and an updated volatile organic compounds (VOC) model. Items of note in the last category include refinement of the global PFT, wetland, and lake distributions, more realistic optical properties for grasslands and croplands, and an improved diurnal cycle and spectral distribution of incoming solar radiation to force the model in offline mode.

1.1.2 Surface Heterogeneity and Data Structure

Spatial land surface heterogeneity in CLM is represented as a nested subgrid hierarchy in which grid cells are composed of multiple landunits, snow/soil columns, and PFTs (Figure 1.1). Each grid cell can have a different number of landunits, each landunit

Figure 1.1. Current default configuration of the CLM subgrid hierarchy emphasizing the

vegetated landunit.
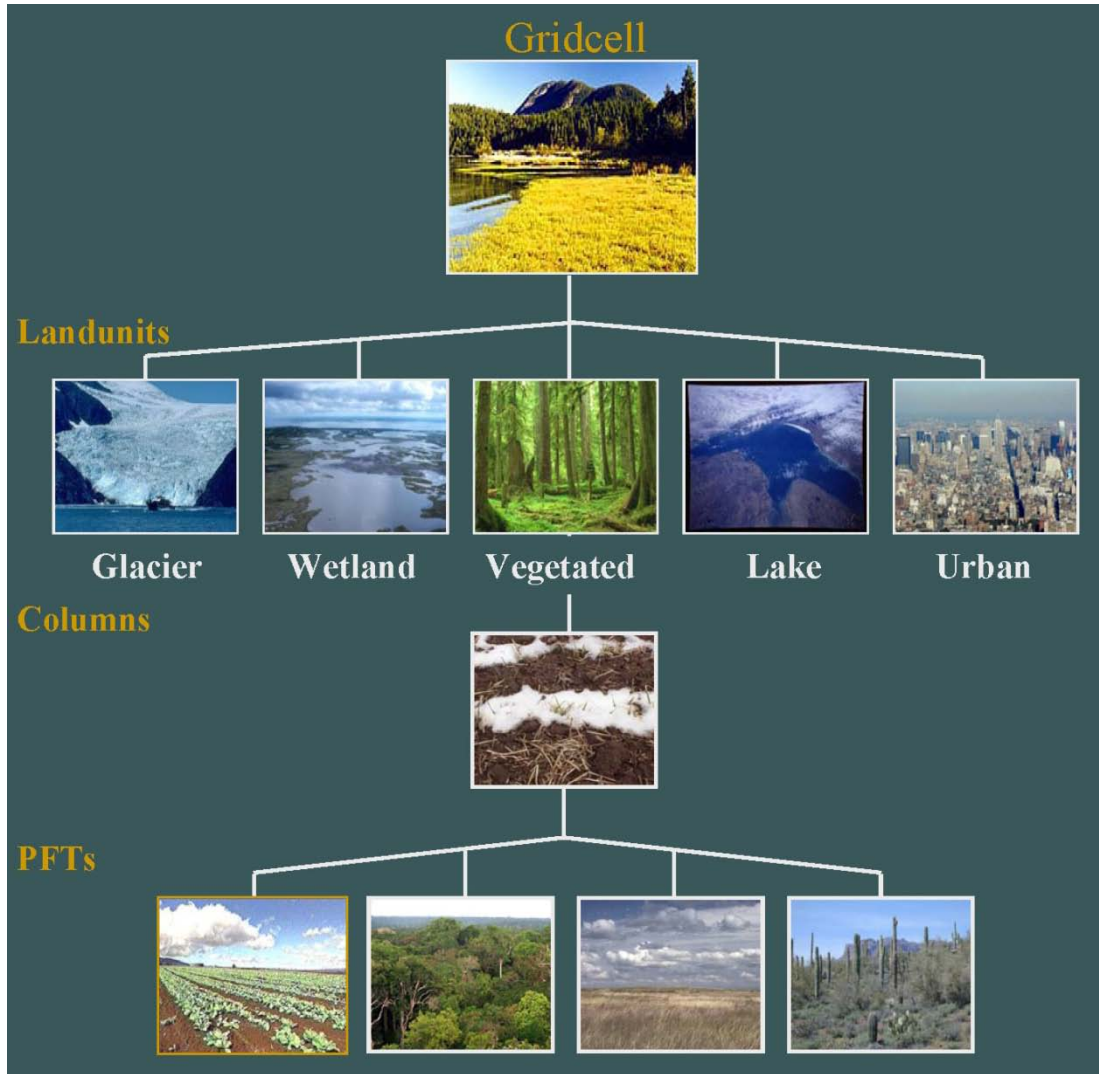
can have a different number of columns, and each column can have multiple PFTs. The first subgrid level, the landunit, is intended to capture the broadest spatial patterns of subgrid heterogeneity. The current landunits are glacier, lake, wetland, urban, and vegetated. The landunit level could be used to further delineate these patterns, for example, the vegetated landunit could be split into natural and managed (e.g., crops) landunits. Or the urban landunit could be divided into density classes such as, for example, city core, industrial/commercial, and suburban.

The second subgrid level, the column, is intended to capture potential variability in the soil and snow state variables within a single landunit. For example, the vegetated landunit could contain several columns with independently evolving vertical profiles of soil water and temperature. Following the example used earlier, the managed vegetation landunit could be divided into two columns, irrigated and non-irrigated. The snow/soil column is represented by fifteen layers for soil and up to five layers for snow, depending on snow depth. The central characteristic of the column subgrid level is that this is where the state variables for water and energy in the soil and snow are defined, as well as the fluxes of these components within the soil and snow. Regardless of the number and type of PFTs occupying space on the column, the column physics operates with a single set of upper boundary fluxes, as well as a single set of transpiration fluxes from multiple soil levels. These boundary fluxes are weighted averages over all PFTs. Currently, for glacier, lake, wetland, and vegetated landunits, a single column is assigned to each landunit. The urban landunit has five columns (roof, sunlit and shaded wall, and pervious and impervious canyon floor) (Oleson et al. 2010).

The third subgrid level is referred to as the PFT level, but it also includes the treatment for bare ground. It is intended to capture the biogeophysical and biogeochemical differences between broad categories of plants in terms of their functional characteristics. Up to 16 possible PFTs that differ in physiology and structure may coexist on a single column. All fluxes to and from the surface are defined at the PFT level, as are the vegetation state variables (e.g. vegetation temperature and canopy water storage).

In addition to state and flux variable data structures for conserved components at each subgrid level (e.g., energy, water, carbon), each subgrid level also has a physical state data structure for handling quantities that are not involved in conservation checks (diagnostic variables). For example, the urban canopy air temperature and humidity are defined through physical state variables at the landunit level, the number of snow layers and the soil roughness lengths are defined as physical state variables at the column level, and the leaf area index and the fraction of canopy that is wet are defined as physical state variables at the PFT level.

The current default configuration of the model subgrid hierarchy is illustrated in Figure 1.1. Here, only four PFTs are shown associated with the single column beneath the vegetated landunit but up to sixteen are possible.

Note that the biogeophysical processes related to soil and snow requires PFT level properties to be aggregated to the column level. For example, the net heat flux into the ground is required as a boundary condition for the solution of snow/soil temperatures (section 6). This column level property must be determined by aggregating the net heat flux from all PFTs sharing the column. This is generally accomplished in the model by

computing a weighted sum of the desired quantity over all PFTs whose weighting depends on the PFT area relative to all PFTs, unless otherwise noted in the text.

1.1.3 Biogeophysical Processes

Biogeophysical processes are simulated for each subgrid landunit, column, and PFT independently and each subgrid unit maintains its own prognostic variables. The same atmospheric forcing is used to force all subgrid units within a grid cell. The surface variables and fluxes required by the atmosphere are obtained by averaging the subgrid quantities weighted by their fractional areas. The processes simulated include (Figure 1.2):

- Vegetation composition, structure, and phenology (section 2)

- Absorption, reflection, and transmittance of solar radiation (section 3, 4)

- Absorption and emission of longwave radiation (section 4)

- Momentum, sensible heat (ground and canopy), and latent heat (ground evaporation, canopy evaporation, transpiration) fluxes (section 5)

- Heat transfer in soil and snow including phase change (section 6)

- Canopy hydrology (interception, throughfall, and drip) (section 7)

- Snow hydrology (snow accumulation and melt, compaction, water transfer between snow layers) (section 7)

- Soil hydrology (surface runoff, infiltration, redistribution of water within the column, sub-surface drainage, groundwater) (section 7)

- Stomatal physiology and photosynthesis (section 8)

- Lake temperatures and fluxes (section 9)

- Dust deposition and fluxes (section 10)

- Routing of runoff from rivers to ocean (section 11)

- Volatile organic compounds (section 12)

- Urban energy balance and climate (section 13)

- Carbon-nitrogen cycling (section 14)

- Dynamic landcover change (section 15)

- Dynamic global vegetation (section 16)

Figure 1.2. Land biogeophysical and hydrologic processes simulated by CLM.

Water table depth is z_∇ and aquifer recharge rate is $q_{recharge}$. Adapted from Bonan (2002).
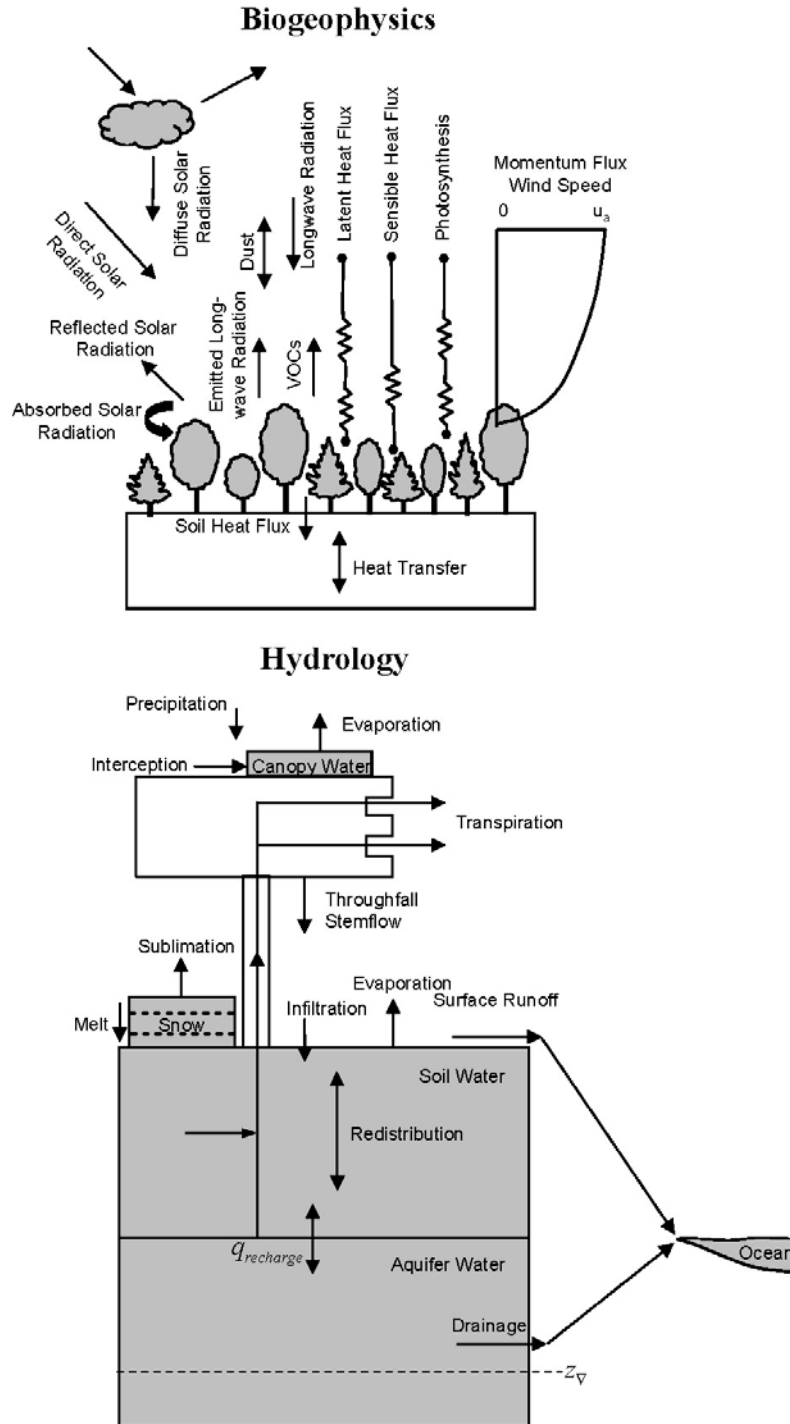
1.2 Model Requirements

1.2.1 Atmospheric Coupling

The current state of the atmosphere (Table 1.1) at a given time step is used to force the land model. This atmospheric state is provided by an atmospheric model in coupled mode. The land model then initiates a full set of calculations for surface energy, constituent, momentum, and radiative fluxes. The land model calculations are implemented in two steps. The land model proceeds with the calculation of surface energy, constituent, momentum, and radiative fluxes using the snow and soil hydrologic states from the previous time step. The land model then updates the soil and snow hydrology calculations based on these fluxes. These fields are passed to the atmosphere (Table 1.2). The albedos sent to the atmosphere are for the solar zenith angle at the next time step but with surface conditions from the current time step.

Table 1.1. Atmospheric input to land model

[1]Reference height	z'_{atm}	m
Zonal wind at z_{atm}	u_{atm}	m s^{-1}
Meridional wind at z_{atm}	v_{atm}	m s^{-1}
Potential temperature	$\overline{\theta_{atm}}$	K
Specific humidity at z_{atm}	q_{atm}	kg kg^{-1}
Pressure at z_{atm}	P_{atm}	Pa
Temperature at z_{atm}	T_{atm}	K
Incident longwave radiation	$L_{atm}\downarrow$	W m^{-2}
[2]Liquid precipitation	q_{rain}	mm s^{-1}
[2]Solid precipitation	q_{sno}	mm s^{-1}
Incident direct beam visible solar radiation	$S_{atm}\downarrow^{\mu}_{vis}$	W m^{-2}
Incident direct beam near-infrared solar radiation	$S_{atm}\downarrow^{\mu}_{nir}$	W m^{-2}
Incident diffuse visible solar radiation	$S_{atm}\downarrow_{vis}$	W m^{-2}
Incident diffuse near-infrared solar radiation	$S_{atm}\downarrow_{nir}$	W m^{-2}
Carbon dioxide (CO_2) concentration	c_a	ppmv
[3]Aerosol deposition rate	D_{sp}	kg m^{-2} s^{-1}
[4]Nitrogen deposition rate	NF_{ndep_sminn}	g (N) m^{-2} yr^{-1}

[1]The atmospheric reference height received from the atmospheric model z'_{atm} is assumed to be the height above the surface as defined by the roughness length z_0 plus displacement height d. Thus, the reference height used for flux computations (chapter 5) is $z_{atm} = z'_{atm} + z_0 + d$. The reference heights for temperature, wind, and specific humidity ($z_{atm,h}$, $z_{atm,m}$, $z_{atm,w}$) are required. These are set equal to z_{atm}.

[2]The CAM provides convective and large-scale liquid and solid precipitation, which are added to yield total liquid precipitation q_{rain} and solid precipitation q_{sno}.

[3]There are 14 aerosol deposition rates required depending on species and affinity for bonding with water; 8 of these are dust deposition rates (dry and wet rates for 4 dust size bins, $D_{dst,dry1}, D_{dst,dry2}, D_{dst,dry3}, D_{dst,dry4}$, $D_{dst,wet1}, D_{dst,wet2}, D_{dst,wet3}, D_{dst,wet4}$), 3 are black carbon deposition rates (dry and wet hydrophilic and dry hydrophobic rates, $D_{bc,dryhphil}, D_{bc,wethphil}, D_{bc,dryhphob}$), and 3 are organic carbon deposition rates (dry and wet hydrophilic and dry hydrophobic rates, $D_{oc,dryhphil}, D_{oc,wethphil}, D_{oc,dryhphob}$). These fluxes are computed interactively by the atmospheric model (when prognostic aerosol representation is active) or are prescribed from a time-varying (annual cycle or transient), globally-gridded deposition file defined in the namelist (see the CLM4 User's Guide). Aerosol deposition rates were calculated in a transient 1850-2009 CAM simulation (at a resolution of 1.9x2.5x26L) with interactive chemistry (troposphere and stratosphere) driven by CCSM3 20th century sea-surface temperatures and emissions (Lamarque et al. 2010) for short-lived gases and aerosols; observed concentrations were specified for methane, N_2O, the ozone-depleting substances (CFCs) ,and CO_2. The fluxes are used by the snow-related parameterizations (sections 3 and 7).

[4]The nitrogen deposition rate is required by the carbon-nitrogen model when active and represents the total deposition of mineral nitrogen onto the land surface, combining deposition of NO_y and NH_x. The rate is supplied either as a time-invariant spatially-varying annual mean rate or time-varying for a transient simulation. Nitrogen deposition rates were calculated from the same CAM chemistry simulation that generated the aerosol deposition rates.

Density of air (ρ_{atm}) (kg m^{-3}) is also required but is calculated directly from

$$\rho_{atm} = \frac{P_{atm} - 0.378 e_{atm}}{R_{da} T_{atm}}$$ where P_{atm} is atmospheric pressure (Pa), e_{atm} is atmospheric

vapor pressure (Pa), R_{da} is the gas constant for dry air (J kg^{-1} K^{-1}) (Table 1.4), and T_{atm}

is the atmospheric temperature (K). The atmospheric vapor pressure e_{atm} is derived from

atmospheric specific humidity q_{atm} (kg kg^{-1}) as $e_{atm} = \frac{q_{atm} P_{atm}}{0.622 + 0.378 q_{atm}}$.

The O$_2$ partial pressure (Pa) is required but is calculated from molar ratio and the

atmospheric pressure P_{atm} as $o_i = 0.209 P_{atm}$.

Table 1.2. Land model output to atmospheric model

[1]Latent heat flux	$\lambda_{vap} E_v + \lambda E_g$	W m^{-2}
Sensible heat flux	$H_v + H_g$	W m^{-2}
Water vapor flux	$E_v + E_g$	mm s^{-1}
Zonal momentum flux	τ_x	kg m^{-1} s^{-2}
Meridional momentum flux	τ_y	kg m^{-1} s^{-2}
Emitted longwave radiation	$L\uparrow$	W m^{-2}
Direct beam visible albedo	$I\uparrow_{vis}^{\mu}$	-
Direct beam near-infrared albedo	$I\uparrow_{nir}^{\mu}$	-
Diffuse visible albedo	$I\uparrow_{vis}$	-
Diffuse near-infrared albedo	$I\uparrow_{nir}$	-
Absorbed solar radiation	$\vec{S}$	W m^{-2}
Radiative temperature	T_{rad}	K
Temperature at 2 meter height	T_{2m}	K
Specific humidity at 2 meter height	q_{2m}	kg kg^{-1}
Snow water equivalent	W_{sno}	m
Aerodynamic resistance	r_{am}	s m^{-1}
Friction velocity	u_*	m s^{-1}
[2]Dust flux	F_j	kg m^{-2} s^{-1}
Net ecosystem exchange	NEE	kgCO$_2$ m^{-2} s^{-1}

[1] λ_{vap} is the latent heat of vaporization (J kg^{-1}) (Table 1.4) and λ is either the latent heat of vaporization λ_{vap} or latent heat of sublimation λ_{sub} (J kg^{-1}) (Table 1.4) depending on the liquid water and ice content of the top snow/soil layer (section 5.4).

[2]There are $j = 1,\ldots,4$ dust transport bins.

1.2.2 Initialization

Initialization of the land model (i.e., providing the model with initial temperature and moisture states) depends on the type of run (startup or restart) (see the CLM4 User's Guide). An startup run starts the model from either initial conditions that are set internally in the Fortran code (referred to as arbitrary initial conditions) or from an initial conditions dataset that enables the model to start from a spun up state (i.e., where the land is in equilibrium with the simulated climate). In restart runs, the model is continued from a previous simulation and initialized from a restart file that ensures that the output is bit-for-bit the same as if the previous simulation had not stopped. The fields that are required from the restart or initial conditions files can be obtained by examining the code. Arbitrary initial conditions are specified as follows.

Vegetated, wetland, and glacier landunits have fifteen vertical layers, while lakes have ten. For soil points, temperature calculations are done over all layers, $N_{levgrnd} = 15$, while hydrology calculations are done over the top ten layers, $N_{levsoi} = 10$, the bottom five layers being specified as bedrock. Soil points are initialized with surface ground temperature T_g and soil layer temperature T_i, for $i = 1, \ldots, N_{levgrnd}$, of 274 K, vegetation temperature T_v of 283 K, no snow or canopy water ($W_{sno} = 0$, $W_{can} = 0$), and volumetric soil water content $\theta_i = 0.3$ mm^3 mm^{-3} for layers $i = 1, \ldots, N_{levsoi}$ and $\theta_i = 0.0$ mm^3 mm^{-3} for layers $i = N_{levsoi} + 1, \ldots, N_{levgrnd}$. Lake temperatures ($T_g$ and T_i) are initialized at 277 K and $W_{sno} = 0$. Wetland temperatures (T_g and T_i) are initialized at 277 K, $\theta_i = 1.0$ for layers $i = 1, \ldots, N_{levsoi}$ and $\theta_i = 0.0$ for layers $i = N_{levsoi} + 1, \ldots, N_{levgrnd}$, and $W_{sno} = 0$.

Glacier temperatures ($T_g = T_{snl+1}$ and T_i for $i = snl+1, \ldots, N_{levgrnd}$ where snl is the negative of the number of snow layers, i.e., snl ranges from –5 to 0) are initialized to 250 K with a snow water equivalent $W_{sno} = 1000$ mm, snow depth $z_{sno} = \dfrac{W_{sno}}{\rho_{sno}}$ (m) where $\rho_{sno} = 250$ kg m^{-3} is an initial estimate for the bulk density of snow, and $\theta_i = 1.0$ for $i = 1, \ldots, N_{levgrnd}$. The snow layer structure (e.g., number of snow layers snl and layer thickness) is initialized based on the snow depth (section 6.1). The snow liquid water and ice contents (kg m^{-2}) are initialized as $w_{liq,i} = 0$ and $w_{ice,i} = \Delta z_i \rho_{sno}$, respectively, where $i = snl+1, \ldots, 0$ are the snow layers, and Δz_i is the thickness of snow layer i (m). The soil liquid water and ice contents are initialized as $w_{liq,i} = 0$ and $w_{ice,i} = \Delta z_i \rho_{ice} \theta_i$ for $T_i \leq T_f$, and $w_{liq,i} = \Delta z_i \rho_{liq} \theta_i$ and $w_{ice,i} = 0$ for $T_i > T_f$, where ρ_{ice} and ρ_{liq} are the densities of ice and liquid water (kg m^{-3}) (Table 1.4), and T_f is the freezing temperature of water (K) (Table 1.4). All vegetated, wetland, and glacier landunits are initialized with water stored in the unconfined aquifer and unsaturated soil $W_a = W_t = 4800$ mm and water table depth $z_\nabla = 4.8$ m.

1.2.3 Surface Data

Required surface data for each land grid cell are listed in Table 1.3 and include the glacier, lake, wetland, and urban portions of the grid cell (vegetation occupies the remainder); the fractional cover of each PFT; monthly leaf and stem area index and canopy top and bottom heights for each PFT; soil color; soil texture, and soil organic matter density. A number of urban parameter fields are also required. Their description

20

can be found in the CLMU technical note (Oleson et al. 2010). The fields are aggregated to the model's grid from high-resolution surface datasets (Table 1.3).

Soil color determines dry and saturated soil albedo (section 3.2). The sand, clay, and organic matter content determine soil thermal and hydrologic properties (section 6.3 and 7.4.1). The maximum fractional saturated area is used in determining surface runoff and infiltration (section 7.3). At the base spatial resolution of 0.5°, the percentage of each PFT is with respect to the vegetated portion of the grid cell and the sum of the PFTs is 100%. The percent lake, wetland, glacier, and urban at their base resolution are specified with respect to the entire grid cell. The surface dataset creation routines re-adjust the PFT percentages to ensure that the sum of all land cover types in the grid cell sum to 100%. A minimum threshold of 1% of the grid cell by area is required of lakes, glaciers, and wetlands. The minimum threshold for urban areas is 0.1%. The number of longitude points per latitude, the latitude and longitude at center of grid cell, the north, south, east, and west edges and the area of each grid cell are also contained on the surface dataset. The number of longitude points should be the same for each latitude for a regular grid. The latitude and longitude (degrees) are used to determine the solar zenith angle (section 3.3).

Soil colors are from Lawrence and Chase (2007) (section 3.2). The International Geosphere-Biosphere Programme (IGBP) soil dataset (Global Soil Data Task 2000) of 4931 soil mapping units and their sand and clay content for each soil layer were used to create a mineral soil texture dataset (Bonan et al. 2002b) and an organic matter density dataset (Lawrence and Slater, 2008) that vary with depth. Percent lake and wetland were derived from Cogley's (1991) 1.0° by 1.0° data for perennial freshwater lakes and

swamps/marshes. Glaciers were obtained from the IGBP Data and Information System Global 1-km Land Cover Data Set (IGBP DISCover) (Loveland et al. 2000). Urban areas are derived from LandScan 2004, a population density dataset derived from census data, nighttime lights satellite observations, road proximity and slope (Dobson et al., 2000) as described by Jackson et al. (2010). PFTs and their abundance are derived from MODIS satellite data as described in Lawrence and Chase (2007) (section 15.3.3). Prescribed PFT leaf area index is derived from the MODIS satellite data of Myneni et al. (2002) using the de-aggregation methods described in Lawrence and Chase (2007) (section 2.3). Prescribed PFT stem area index is derived from PFT leaf area index phenology combined with the methods of Zeng et al. (2002). Prescribed canopy top and bottom heights are from Bonan (1996) as described in Bonan et al. (2002b). If the carbon-nitrogen model is active, it supplies the leaf and stem area index and canopy top and bottom heights dynamically, and the prescribed values are ignored.

Table 1.3. Surface data required for CLM, their base spatial resolution, and method of

aggregation to the model's grid

Surface Field	Resolution	Aggregation Method
Percent glacier	0.5°	Area average
Percent lake	1°	Area average
Percent wetland	1°	Area average
Percent urban	0.5°	Area average
Percent sand, percent clay	5-minute	Soil mapping unit with greatest areal extent in grid cell
Soil organic matter density	1°	Area average
Soil color	0.5°	Soil color class with greatest areal extent in grid cell
Maximum fractional saturated area	0.5°	Area average
PFTs (percent of vegetated land)	0.5°	Area average
Monthly leaf and stem area index	0.5°	Area average
Canopy height (top, bottom)	0.5°	Area average (does not vary within PFT)

1.2.4 Adjustable Parameters and Physical Constants

Values of certain adjustable parameters inherent in the biogeophysical parameterizations have either been obtained from the literature or arrived at based on comparisons with observations. These are described in the text. Physical constants, generally shared by all of the components in the coupled modeling system, are presented in Table 1.4.

Table 1.4. Physical constants			
Pi	π	3.14159265358979323846	-
Acceleration of gravity	g	9.80616	m s^{-2}
Standard pressure	P_{std}	101325	Pa
Stefan-Boltzmann constant	σ	5.67×10^{-8}	W m^{-2} K^{-4}
Boltzmann constant	κ	1.38065×10^{-23}	J K^{-1} molecule^{-1}
Avogadro's number	N_A	6.02214×10^{26}	molecule kmol^{-1}
Universal gas constant	R_{gas}	$N_A\kappa$	J K^{-1} kmol^{-1}
Molecular weight of dry air	MW_{da}	28.966	kg kmol^{-1}
Dry air gas constant	R_{da}	R_{gas}/MW_{da}	J K^{-1} kg^{-1}
Molecular weight of water vapor	MW_{wv}	18.016	kg kmol^{-1}
Water vapor gas constant	R_{wv}	R_{gas}/MW_{wv}	J K^{-1} kg^{-1}
Von Karman constant	k	0.4	-
Freezing temperature of fresh water	T_f	273.15	K
Density of liquid water	ρ_{liq}	1000	kg m^{-3}
Density of ice	ρ_{ice}	917	kg m^{-3}
Specific heat capacity of dry air	C_p	1.00464×10^3	J kg^{-1} K^{-1}
Specific heat capacity of water	C_{liq}	4.188×10^3	J kg^{-1} K^{-1}
Specific heat capacity of ice	C_{ice}	2.11727×10^3	J kg^{-1} K^{-1}
Latent heat of vaporization	λ_{vap}	2.501×10^6	J kg^{-1}
Latent heat of fusion	L_f	3.337×10^5	J kg^{-1}
Latent heat of sublimation	λ_{sub}	$\lambda_{vap}+L_f$	J kg^{-1}
[1]Thermal conductivity of water	λ_{liq}	0.6	W m^{-1} K^{-1}
[1]Thermal conductivity of ice	λ_{ice}	2.29	W m^{-1} K^{-1}
[1]Thermal conductivity of air	λ_{air}	0.023	W m^{-1} K^{-1}
Radius of the earth	R_e	6.37122×10^6	m

[1]Not shared by other components of the coupled modeling system.

2. Ecosystem Composition and Structure

2.1 *Vegetation Composition*

Vegetated surfaces are comprised of up to 15 possible plant functional types (PFTs) plus bare ground (Table 2.1). These plant types differ in leaf and stem optical properties that determine reflection, transmittance, and absorption of solar radiation (Table 3.1), root distribution parameters that control the uptake of water from the soil (Table 8.3), aerodynamic parameters that determine resistance to heat, moisture, and momentum transfer (Table 5.1), and photosynthetic parameters that determine stomatal resistance, photosynthesis, and transpiration (Tables 8.1, 8.2). The composition and abundance of PFTs within a grid cell can either be prescribed as time-invariant fields (e.g., using the present day dataset described in section 15.3.3) or can evolve with time if the model is run in transient landcover mode (section 15).

Table 2.1. Plant functional types

Plant functional type	Acronym
Needleleaf evergreen tree – temperate	NET Temperate
Needleleaf evergreen tree - boreal	NET Boreal
Needleleaf deciduous tree – boreal	NDT Boreal
Broadleaf evergreen tree – tropical	BET Tropical
Broadleaf evergreen tree – temperate	BET Temperate
Broadleaf deciduous tree – tropical	BDT Tropical
Broadleaf deciduous tree – temperate	BDT Temperate
Broadleaf deciduous tree – boreal	BDT Boreal
Broadleaf evergreen shrub - temperate	BES Temperate
Broadleaf deciduous shrub – temperate	BDS Temperate
Broadleaf deciduous shrub – boreal	BDS Boreal
C_3 arctic grass	-
C_3 grass	-
C_4 grass	-
Crop1	-
[1]Crop2	-

[1]Two types of crops are allowed to account for the different physiology of crops, but currently only the first crop type is specified in the surface dataset.

2.2   Vegetation Structure

Vegetation structure is defined by leaf and stem area indices (L, S) (section 2.3) and canopy top and bottom heights (z_{top}, z_{bot}) (Table 2.2). Separate leaf and stem area indices and canopy heights are prescribed for each PFT. Daily leaf and stem area indices are obtained from gridded datasets of monthly values (section 2.3). Canopy top and bottom heights are also obtained from gridded datasets. However, these are currently

invariant in space and time and were obtained from PFT-specific values (Bonan et al. 2002a).

Table 2.2. Plant functional type heights

Plant functional type	z_{top} (m)	z_{bot} (m)
NET Temperate	17	8.5
NET Boreal	17	8.5
NDT Boreal	14	7
BET Tropical	35	1
BET temperate	35	1
BDT tropical	18	10
BDT temperate	20	11.5
BDT boreal	20	11.5
BES temperate	0.5	0.1
BDS temperate	0.5	0.1
BDS boreal	0.5	0.1
C_3 arctic grass	0.5	0.01
C_3 grass	0.5	0.01
C_4 grass	0.5	0.01
Crop1	0.5	0.01
Crop2	0.5	0.01

2.3   Phenology

Leaf and stem area indices (m^2 leaf area m^{-2} ground area) are updated daily by linearly interpolating between monthly values. Monthly PFT leaf area index values are developed from the 1-km MODIS-derived monthly grid cell average leaf area index of Myneni et al. (2002), as described in Lawrence and Chase (2007). Stem area index is calculated from the monthly PFT leaf area index using the methods of Zeng et al. (2002).

27

The leaf and stem area indices are adjusted for vertical burying by snow (Wang and Zeng 2009) as

$$A = A^* \left(1 - f_{veg}^{sno}\right) \qquad (2.1)$$

where A^* is the leaf or stem area before adjustment for snow, A is the remaining exposed leaf or stem area, f_{veg}^{sno} is the vertical fraction of vegetation covered by snow

$$
\begin{aligned}
f_{veg}^{sno} &= \frac{z_{sno} - z_{bot}}{z_{top} - z_{bot}} \qquad &&\text{for tree and shrub} \\
f_{veg}^{sno} &= \frac{\min\left(z_{sno}, z_c\right)}{z_c} \qquad &&\text{for grass and crop}
\end{aligned}
\qquad , \qquad (2.2)
$$

where $z_{sno} - z_{bot} \geq 0$, $0 \leq f_{veg}^{sno} \leq 1$, z_{sno} is the depth of snow (m) (section 7.2), and $z_c = 0.2$ is the snow depth when short vegetation is assumed to be completely buried by snow (m). For numerical reasons, exposed leaf and stem area are set to zero if less than 0.05. If the sum of exposed leaf and stem area is zero, then the surface is treated as snow-covered ground.

3. Surface Albedos

3.1 Canopy Radiative Transfer

Radiative transfer within vegetative canopies is calculated from the two-stream approximation of Dickinson (1983) and Sellers (1985) as described by Bonan (1996)

$$-\bar{\mu}\frac{dI\uparrow}{d(L+S)}+\left[1-(1-\beta)\omega\right]I\uparrow-\omega\beta I\downarrow=\omega\bar{\mu}K\beta_0 e^{-K(L+S)} \tag{3.1}$$

$$\bar{\mu}\frac{dI\downarrow}{d(L+S)}+\left[1-(1-\beta)\omega\right]I\downarrow-\omega\beta I\uparrow=\omega\bar{\mu}K(1-\beta_0)e^{-K(L+S)} \tag{3.2}$$

where $I\uparrow$ and $I\downarrow$ are the upward and downward diffuse radiative fluxes per unit incident flux, $K=G(\mu)/\mu$ is the optical depth of direct beam per unit leaf and stem area, μ is the cosine of the zenith angle of the incident beam, $G(\mu)$ is the relative projected area of leaf and stem elements in the direction $\cos^{-1}\mu$, $\bar{\mu}$ is the average inverse diffuse optical depth per unit leaf and stem area, ω is a scattering coefficient, β and β_0 are upscatter parameters for diffuse and direct beam radiation, respectively, L is the exposed leaf area index (section 2.3), and S is the exposed stem area index (section 2.3). Given the direct beam albedo $\alpha_{g,\Lambda}^\mu$ and diffuse albedo $\alpha_{g,\Lambda}$ of the ground (section 3.2), these equations are solved to calculate the fluxes, per unit incident flux, absorbed by the vegetation, reflected by the vegetation, and transmitted through the vegetation for direct and diffuse radiation and for visible ($<0.7\,\mu\text{m}$) and near-infrared ($\geq 0.7\,\mu\text{m}$) wavebands. The optical parameters $G(\mu)$, $\bar{\mu}$, ω, β, and β_0 are calculated based on work in Sellers (1985) as follows.

The relative projected area of leaves and stems in the direction $\cos^{-1}\mu$ is

$$G(\mu) = \phi_1 + \phi_2 \mu \tag{3.3}$$

where $\phi_1 = 0.5 - 0.633\chi_L - 0.33\chi_L^2$ and $\phi_2 = 0.877(1 - 2\phi_1)$ for $-0.4 \le \chi_L \le 0.6$. χ_L is the departure of leaf angles from a random distribution and equals +1 for horizontal leaves, 0 for random leaves, and –1 for vertical leaves.

The average inverse diffuse optical depth per unit leaf and stem area is

$$\bar{\mu} = \int_0^1 \frac{\mu'}{G(\mu')} d\mu' = \frac{1}{\phi_2} \left[1 - \frac{\phi_1}{\phi_2} \ln\left(\frac{\phi_1 + \phi_2}{\phi_1} \right) \right] \tag{3.4}$$

where μ' is the direction of the scattered flux.

The optical parameters ω, β, and β_0, which vary with wavelength (Λ), are weighted combinations of values for vegetation and snow. The model determines that snow is on the canopy if $T_v \le T_f$, where T_v is the vegetation temperature (K) (section 5) and T_f is the freezing temperature of water (K) (Table 1.4). In this case, the optical parameters are

$$\omega_\Lambda = \omega_\Lambda^{veg}(1 - f_{wet}) + \omega_\Lambda^{sno} f_{wet} \tag{3.5}$$

$$\omega_\Lambda \beta_\Lambda = \omega_\Lambda^{veg} \beta_\Lambda^{veg}(1 - f_{wet}) + \omega_\Lambda^{sno} \beta_\Lambda^{sno} f_{wet} \tag{3.6}$$

$$\omega_\Lambda \beta_{0,\Lambda} = \omega_\Lambda^{veg} \beta_{0,\Lambda}^{veg}(1 - f_{wet}) + \omega_\Lambda^{sno} \beta_{0,\Lambda}^{sno} f_{wet} \tag{3.7}$$

where f_{wet} is the wetted fraction of the canopy (section 7.1). The snow and vegetation weights are applied to the products $\omega_\Lambda \beta_\Lambda$ and $\omega_\Lambda \beta_{0,\Lambda}$ because these products are used in the two-stream equations. If there is no snow on the canopy,

$$\omega_\Lambda = \omega_\Lambda^{veg} \tag{3.8}$$

$$\omega_\Lambda \beta_\Lambda = \omega_\Lambda^{veg} \beta_\Lambda^{veg} \tag{3.9}$$

$$\omega_\Lambda \beta_{0,\Lambda} = \omega_\Lambda^{veg} \beta_{0,\Lambda}^{veg}. \tag{3.10}$$

For vegetation, $\omega_\Lambda^{veg} = \alpha_\Lambda + \tau_\Lambda$. α_Λ is a weighted combination of the leaf and stem reflectances ($\alpha_\Lambda^{leaf}, \alpha_\Lambda^{stem}$)

$$\alpha_\Lambda = \alpha_\Lambda^{leaf} w_{leaf} + \alpha_\Lambda^{stem} w_{stem} \tag{3.11}$$

where $w_{leaf} = L/(L+S)$ and $w_{stem} = S/(L+S)$. τ_Λ is a weighted combination of the leaf and stem transmittances ($\tau_\Lambda^{leaf}, \tau_\Lambda^{stem}$)

$$\tau_\Lambda = \tau_\Lambda^{leaf} w_{leaf} + \tau_\Lambda^{stem} w_{stem}. \tag{3.12}$$

The upscatter for diffuse radiation is

$$\omega_\Lambda^{veg} \beta_\Lambda^{veg} = \frac{1}{2}\left[\alpha_\Lambda + \tau_\Lambda + (\alpha_\Lambda - \tau_\Lambda)\cos^2 \bar\theta \right] \tag{3.13}$$

where $\bar\theta$ is the mean leaf inclination angle relative to the horizontal plane (i.e., the angle between leaf normal and local vertical) (Sellers 1985). Here, $\cos\bar\theta$ is approximated by

$$\cos\bar\theta = \frac{1+\chi_L}{2} \tag{3.14}$$

Using this approximation, for vertical leaves ($\chi_L = -1$, $\bar\theta = 90^\circ$), $\omega_\Lambda^{veg} \beta_\Lambda^{veg} = 0.5(\alpha_\Lambda + \tau_\Lambda)$, and for horizontal leaves ($\chi_L = 1$, $\bar\theta = 0^\circ$), $\omega_\Lambda^{veg} \beta_\Lambda^{veg} = \alpha_\Lambda$, which agree with both Dickinson (1983) and Sellers (1985). For random (spherically distributed) leaves ($\chi_L = 0$, $\bar\theta = 60^\circ$), the approximation yields $\omega_\Lambda^{veg} \beta_\Lambda^{veg} = 5/8\,\alpha_\Lambda + 3/8\,\tau_\Lambda$ whereas the approximate solution of Dickinson (1983) is $\omega_\Lambda^{veg} \beta_\Lambda^{veg} = 2/3\,\alpha_\Lambda + 1/3\,\tau_\Lambda$. This discrepancy arises from the fact that a spherical leaf

31

angle distribution has a true mean leaf inclination $\bar{\theta} \approx 57$ (Campbell and Norman 1998) in equation (3.13), while $\bar{\theta} = 60$ in equation (3.14).

The upscatter for direct beam radiation is

$$\omega_\Lambda^{veg} \beta_{0,\Lambda}^{veg} = \frac{1 + \bar{\mu} K}{\bar{\mu} K} a_s (\mu)_\Lambda \tag{3.15}$$

where the single scattering albedo is

$$
\begin{aligned}
a_s (\mu)_\Lambda &= \frac{\omega_\Lambda^{veg}}{2} \int_0^1 \frac{\mu' G(\mu)}{\mu G(\mu') + \mu' G(\mu)} d\mu' \\
&= \frac{\omega_\Lambda^{veg}}{2} \frac{G(\mu)}{\mu \phi_2 + G(\mu)} \left[1 - \frac{\mu \phi_1}{\mu \phi_2 + G(\mu)} \ln \left(\frac{\mu \phi_1 + \mu \phi_2 + G(\mu)}{\mu \phi_1} \right) \right].
\end{aligned}
\tag{3.16}
$$

The upward diffuse fluxes per unit incident direct beam and diffuse flux (i.e., the surface albedos) are

$$I \uparrow_\Lambda^\mu = \frac{h_1}{\sigma} + h_2 + h_3 \tag{3.17}$$

$$I \uparrow_\Lambda = h_7 + h_8 . \tag{3.18}$$

The downward diffuse fluxes per unit incident direct beam and diffuse radiation, respectively, are

$$I \downarrow_\Lambda^\mu = \frac{h_4}{\sigma} e^{-K(L+S)} + h_5 s_1 + \frac{h_6}{s_1} \tag{3.19}$$

$$I \downarrow_\Lambda = h_9 s_1 + \frac{h_{10}}{s_1} . \tag{3.20}$$

The parameters h_1 to h_{10}, σ, and s_1 are from Sellers (1985) [note the error in h_4 in Sellers (1985)]:

$$b = 1 - \omega_\Lambda + \omega_\Lambda \beta_\Lambda \tag{3.21}$$

$$c = \omega_\Lambda \beta_\Lambda \tag{3.22}$$

$$d = \omega_\Lambda \bar{\mu} K \beta_{0,\Lambda} \tag{3.23}$$

$$f = \omega_\Lambda \bar{\mu} K \left(1 - \beta_{0,\Lambda}\right) \tag{3.24}$$

$$h = \frac{\sqrt{b^2 - c^2}}{\bar{\mu}} \tag{3.25}$$

$$\sigma = \left(\bar{\mu} K\right)^2 + c^2 - b^2 \tag{3.26}$$

$$u_1 = b - c / \alpha_{g,\Lambda}^\mu \quad \text{or} \quad u_1 = b - c / \alpha_{g,\Lambda} \tag{3.27}$$

$$u_2 = b - c \alpha_{g,\Lambda}^\mu \quad \text{or} \quad u_2 = b - c \alpha_{g,\Lambda} \tag{3.28}$$

$$u_3 = f + c \alpha_{g,\Lambda}^\mu \quad \text{or} \quad u_3 = f + c \alpha_{g,\Lambda} \tag{3.29}$$

$$s_1 = \exp\left\{-\min\left[h(L+S), 40\right]\right\} \tag{3.30}$$

$$s_2 = \exp\left\{-\min\left[K(L+S), 40\right]\right\} \tag{3.31}$$

$$p_1 = b + \bar{\mu} h \tag{3.32}$$

$$p_2 = b - \bar{\mu} h \tag{3.33}$$

$$p_3 = b + \bar{\mu} K \tag{3.34}$$

$$p_4 = b - \bar{\mu} K \tag{3.35}$$

$$d_1 = \frac{p_1 \left(u_1 - \bar{\mu} h\right)}{s_1} - p_2 \left(u_1 + \bar{\mu} h\right) s_1 \tag{3.36}$$

$$d_2 = \frac{u_2 + \bar{\mu} h}{s_1} - \left(u_2 - \bar{\mu} h\right) s_1 \tag{3.37}$$

$$h_1 = -d p_4 - c f \tag{3.38}$$

$$h_2 = \frac{1}{d_1}\left[\left(d - \frac{h_1}{\sigma}p_3\right)\frac{(u_1 - \bar{\mu}h)}{s_1} - p_2\left(d - c - \frac{h_1}{\sigma}(u_1 + \bar{\mu}K)\right)s_2\right] \tag{3.39}$$

$$h_3 = \frac{-1}{d_1}\left[\left(d - \frac{h_1}{\sigma}p_3\right)(u_1 + \bar{\mu}h)s_1 - p_1\left(d - c - \frac{h_1}{\sigma}(u_1 + \bar{\mu}K)\right)s_2\right] \tag{3.40}$$

$$h_4 = -fp_3 - cd \tag{3.41}$$

$$h_5 = \frac{-1}{d_2}\left[\left(\frac{h_4(u_2 + \bar{\mu}h)}{\sigma s_1}\right) + \left(u_3 - \frac{h_4}{\sigma}(u_2 - \bar{\mu}K)\right)s_2\right] \tag{3.42}$$

$$h_6 = \frac{1}{d_2}\left[\frac{h_4}{\sigma}(u_2 - \bar{\mu}h)s_1 + \left(u_3 - \frac{h_4}{\sigma}(u_2 - \bar{\mu}K)\right)s_2\right] \tag{3.43}$$

$$h_7 = \frac{c(u_1 - \bar{\mu}h)}{d_1 s_1} \tag{3.44}$$

$$h_8 = \frac{-c(u_1 + \bar{\mu}h)s_1}{d_1} \tag{3.45}$$

$$h_9 = \frac{u_2 + \bar{\mu}h}{d_2 s_1} \tag{3.46}$$

$$h_{10} = \frac{-s_1(u_2 - \bar{\mu}h)}{d_2}. \tag{3.47}$$

Plant functional type optical properties (Table 3.1) for trees and shrubs are from Dorman and Sellers (1989). Leaf and stem optical properties (VIS and NIR reflectance and transmittance) were derived for grasslands and crops from full optical range spectra of measured optical properties (Asner et al. 1998). Optical properties for intercepted snow (Table 3.2) are from Sellers et al. (1986).

Table 3.1. Plant functional type optical properties

Plant Functional Type	χ_L	α_{vis}^{leaf}	α_{nir}^{leaf}	α_{vis}^{stem}	α_{nir}^{stem}	τ_{vis}^{leaf}	τ_{nir}^{leaf}	τ_{vis}^{stem}	τ_{nir}^{stem}
NET Temperate	0.01	0.07	0.35	0.16	0.39	0.05	0.10	0.001	0.001
NET Boreal	0.01	0.07	0.35	0.16	0.39	0.05	0.10	0.001	0.001
NDT Boreal	0.01	0.07	0.35	0.16	0.39	0.05	0.10	0.001	0.001
BET Tropical	0.10	0.10	0.45	0.16	0.39	0.05	0.25	0.001	0.001
BET temperate	0.10	0.10	0.45	0.16	0.39	0.05	0.25	0.001	0.001
BDT tropical	0.01	0.10	0.45	0.16	0.39	0.05	0.25	0.001	0.001
BDT temperate	0.25	0.10	0.45	0.16	0.39	0.05	0.25	0.001	0.001
BDT boreal	0.25	0.10	0.45	0.16	0.39	0.05	0.25	0.001	0.001
BES temperate	0.01	0.07	0.35	0.16	0.39	0.05	0.10	0.001	0.001
BDS temperate	0.25	0.10	0.45	0.16	0.39	0.05	0.25	0.001	0.001
BDS boreal	0.25	0.10	0.45	0.16	0.39	0.05	0.25	0.001	0.001
C_3 arctic grass	-0.30	0.11	0.35	0.31	0.53	0.05	0.34	0.120	0.250
C_3 grass	-0.30	0.11	0.35	0.31	0.53	0.05	0.34	0.120	0.250
C_4 grass	-0.30	0.11	0.35	0.31	0.53	0.05	0.34	0.120	0.250
Crop1	-0.30	0.11	0.35	0.31	0.53	0.05	0.34	0.120	0.250
Crop2	-0.30	0.11	0.35	0.31	0.53	0.05	0.34	0.120	0.250

Table 3.2. Intercepted snow optical properties

Parameter	Waveband (Λ)	
	vis	nir
ω^{sno}	0.8	0.4
β^{sno}	0.5	0.5
β_0^{sno}	0.5	0.5

3.2   Ground Albedos

The overall direct beam $\alpha_{g,\Lambda}^{\mu}$ and diffuse $\alpha_{g,\Lambda}$ ground albedos are weighted combinations of "soil" and snow albedos

$$\alpha_{g,\Lambda}^{\mu} = \alpha_{soi,\Lambda}^{\mu}\left(1 - f_{sno}\right) + \alpha_{sno,\Lambda}^{\mu} f_{sno} \tag{3.48}$$

$$\alpha_{g,\Lambda} = \alpha_{soi,\Lambda}\left(1 - f_{sno}\right) + \alpha_{sno,\Lambda} f_{sno} \tag{3.49}$$

where f_{sno} is the fraction of the ground covered with snow which is calculated as (Niu and Yang 2007)

$$f_{sno} = \tanh\left\{\frac{z_{sno}}{2.5 z_{0m,g}\left[\min\left(\rho_{sno}, 800\right)/\rho_{new}\right]^{m}}\right\} \tag{3.50}$$

where z_{sno} is the depth of snow (m) (section 7.2), $z_{0m,g} = 0.01$ is the momentum roughness length for soil (m) (section 5), $\rho_{new} = 100$ kg m^{-3} is the density of new snow, and $m = 1$ is suggested for global applications. The snow density is calculated from $\rho_{sno} = W_{sno}/z_{sno}$ where W_{sno} is the snow water equivalent (kg m^{-2}) (section 7.2).

$\alpha_{soi,\Lambda}^{\mu}$ and $\alpha_{soi,\Lambda}$ vary with glacier, lake, wetland, and soil surfaces. Glacier albedos are from NCAR LSM (Bonan 1996)

$$\alpha_{soi,vis}^{\mu} = \alpha_{soi,vis} = 0.80$$

$$\alpha_{soi,nir}^{\mu} = \alpha_{soi,nir} = 0.55.$$

Unfrozen lake and wetland albedos depend on the cosine of the solar zenith angle μ

$$\alpha_{soi,\Lambda}^{\mu} = \alpha_{soi,\Lambda} = 0.05\left(\mu + 0.15\right)^{-1}. \tag{3.51}$$

Frozen lake and wetland albedos are from NCAR LSM (Bonan 1996)

$$\alpha_{soi,vis}^{\mu} = \alpha_{soi,vis} = 0.60$$

$$\alpha_{soi,nir}^{\mu} = \alpha_{soi,nir} = 0.40.$$

As in NCAR LSM (Bonan 1996), soil albedos vary with color class

$$\alpha_{soi,\Lambda}^{\mu} = \alpha_{soi,\Lambda} = \left(\alpha_{sat,\Lambda} + \Delta \right) \leq \alpha_{dry,\Lambda} \qquad (3.52)$$

where Δ depends on the volumetric water content of the first soil layer θ_1 (section 7.4)

as $\Delta = 0.11 - 0.40\theta_1 > 0$, and $\alpha_{sat,\Lambda}$ and $\alpha_{dry,\Lambda}$ are albedos for saturated and dry soil

color classes (Table 3.3).

CLM soil colors are prescribed so that they best reproduce observed MODIS local

solar noon surface albedo values at the CLM grid cell following the methods of Lawrence

and Chase (2007). The soil colors are fitted over the range of 20 soil classes shown in

Table 3.3 and compared to the MODIS monthly local solar noon all-sky surface albedo as

described in Strahler et al. (1999) and Schaaf et al. (2002). The CLM two-stream

radiation model was used to calculate the model equivalent surface albedo using

climatological monthly soil moisture along with the vegetation parameters of PFT

fraction, LAI, and SAI. The soil color that produced the closest all-sky albedo in the

two-stream radiation model was selected as the best fit for the month. The fitted monthly

soil colors were averaged over all snow-free months to specify a representative soil color

for the grid cell. In cases where there was no snow-free surface albedo for the year, the

soil color derived from snow-affected albedo was used to give a representative soil color

that included the effects of the minimum permanent snow cover.

Table 3.3. Dry and saturated soil albedos

Color Class	Dry vis	Dry nir	Saturated vis	Saturated nir	Color Class	Dry vis	Dry nir	Saturated vis	Saturated nir
1	0.36	0.61	0.25	0.50	11	0.24	0.37	0.13	0.26
2	0.34	0.57	0.23	0.46	12	0.23	0.35	0.12	0.24
3	0.32	0.53	0.21	0.42	13	0.22	0.33	0.11	0.22
4	0.31	0.51	0.20	0.40	14	0.20	0.31	0.10	0.20
5	0.30	0.49	0.19	0.38	15	0.18	0.29	0.09	0.18
6	0.29	0.48	0.18	0.36	16	0.16	0.27	0.08	0.16
7	0.28	0.45	0.17	0.34	17	0.14	0.25	0.07	0.14
8	0.27	0.43	0.16	0.32	18	0.12	0.23	0.06	0.12
9	0.26	0.41	0.15	0.30	19	0.10	0.21	0.05	0.10
10	0.25	0.39	0.14	0.28	20	0.08	0.16	0.04	0.08

3.2.1 *Snow Albedo*

Snow albedo and solar absorption within each snow layer are simulated with the Snow, Ice, and Aerosol Radiative Model (SNICAR), which incorporates a two-stream radiative transfer solution from Toon et al. (1989). Albedo and the vertical absorption profile depend on solar zenith angle, albedo of the substrate underlying snow, mass concentrations of atmospheric-deposited aerosols (black carbon, mineral dust, and organic carbon), and ice effective grain size (r_e), which is simulated with a snow aging routine described in section 3.2.3. Representation of impurity mass concentrations within the snowpack is described in section 7.2.3. Implementation of SNICAR in CLM is also described somewhat by Flanner and Zender (2005) and Flanner et al. (2007).

The two-stream solution requires the following bulk optical properties for each snow layer and spectral band: extinction optical depth (τ), single-scatter albedo (ω), and

scattering asymmetry parameter (g). The snow layers used for radiative calculations are identical to snow layers applied elsewhere in CLM, except for the case when snow mass is greater than zero but no snow layers exist. When this occurs, a single radiative layer is specified to have the column snow mass and an effective grain size of freshly-fallen snow (section 3.2.3). The bulk optical properties are weighted functions of each constituent k, computed for each snow layer and spectral band as

$$\tau = \sum_{1}^{k} \tau_k \tag{3.53}$$

$$\omega = \frac{\sum_{1}^{k} \omega_k \tau_k}{\sum_{1}^{k} \tau_k} \tag{3.54}$$

$$g = \frac{\sum_{1}^{k} g_k \omega_k \tau_k}{\sum_{1}^{k} \omega_k \tau_k} \tag{3.55}$$

For each constituent (ice, two black carbon species, two organic carbon species, and four dust species), ω, g, and the mass extinction cross-section ψ (m^2 kg^{-1}) are computed offline with Mie Theory, e.g., applying the computational technique from Bohren and Huffman (1983). The extinction optical depth for each constituent depends on its mass extinction cross-section and layer mass, w_k (kg m^{-2}) as

$$\tau_k = \psi_k w_k \tag{3.56}$$

The two-stream solution (Toon et al. 1989) applies a tri-diagonal matrix solution to produce upward and downward radiative fluxes at each layer interface, from which net radiation, layer absorption, and surface albedo are easily derived. Solar fluxes are computed in five spectral bands, listed in Table 3.4. Because snow albedo varies strongly

across the solar spectrum, it was determined that four bands were needed to accurately represent the near-infrared (NIR) characteristics of snow, whereas only one band was needed for the visible spectrum. Boundaries of the NIR bands were selected to capture broad radiative features and maximize accuracy and computational efficiency. We partition NIR (0.7-5.0μm) surface downwelling flux from CLM according to the weights listed in Table 3.4, which are unique for diffuse and direct incident flux. These fixed weights were determined with offline hyperspectral radiative transfer calculations for an atmosphere typical of mid-latitude winter (Flanner et al. 2007). The tri-diagonal solution includes intermediate terms that allow for easy interchange of two-stream techniques. We apply the Eddington solution for the visible band (following Wiscombe and Warren 1980) and the hemispheric mean solution (Toon et al. 1989) for NIR bands. These choices were made because the Eddington scheme works well for highly scattering media, but can produce negative albedo for absorptive NIR bands with diffuse incident flux. Delta scalings are applied to τ, ω, and g (Wiscombe and Warren 1980) in all spectral bands, producing effective values (denoted with *) that are applied in the two-stream solution

$$\tau^* = (1 - \omega g^2)\tau \tag{3.57}$$

$$\omega^* = \frac{(1 - g^2)\omega}{1 - g^2\omega} \tag{3.58}$$

$$g^* = \frac{g}{1 + g} \tag{3.59}$$

Table 3.4. Spectral bands and weights used for snow radiative transfer

Spectral band	Direct-beam weight	Diffuse weight
Band 1: 0.3-0.7μm (visible)	(1.0)	(1.0)
Band 2: 0.7-1.0μm (near-IR)	0.494	0.586
Band 3: 1.0-1.2μm (near-IR)	0.181	0.202
Band 4: 1.2-1.5μm (near-IR)	0.121	0.109
Band 5: 1.5-5.0μm (near-IR)	0.204	0.103

Under direct-beam conditions, singularities in the radiative approximation are occasionally approached in spectral bands 4 and 5 that produce unrealistic conditions (negative energy absorption in a layer, negative albedo, or total absorbed flux greater than incident flux). When any of these three conditions occur, the Eddington approximation is attempted instead, and if both approximations fail, the cosine of the solar zenith angle is adjusted by 0.02 (conserving incident flux) and a warning message is produced. This situation occurs in only about 1 in 10^6 computations of snow albedo. After looping over the five spectral bands, absorption fluxes and albedo are averaged back into the bulk NIR band used by the rest of CLM.

Soil albedo (or underlying substrate albedo), which is defined for visible and NIR bands, is a required boundary condition for the snow radiative transfer calculation. Currently, the bulk NIR soil albedo is applied to all four NIR snow bands. With ground albedo as a lower boundary condition, SNICAR simulates solar absorption in all snow layers as well as the underlying soil or ground. With a thin snowpack, penetrating solar radiation to the underlying soil can be quite large and heat cannot be released from the

soil to the atmosphere in this situation. Thus, solar radiation penetration is limited to snowpacks with total snow depth greater than or equal to 0.1 m ($z_{sno} \geq 0.1$) to prevent unrealistic soil warming within a single timestep.

The radiative transfer calculation is performed twice for each column containing a mass of snow greater than 1×10^{-30} kg m^{-2} (excluding lake and urban columns); once each for direct-beam and diffuse incident flux. Absorption in each layer i of pure snow is initially recorded as absorbed flux per unit incident flux on the ground ($S_{sno,i}$), as albedos must be calculated for the next timestep with unknown incident flux. Because a single snow plus soil column is used for the vertical temperature calculation over the entire grid cell, even though some fraction of the grid cell is snow-free, the absorbed solar flux by the ground per unit incident flux, or absorptivity (S_g), depends on bulk snow absorptivity S_{sno} as

$$S_g = 1 - \left[\alpha_{soi} \left(1 - f_{sno} \right) + \left(1 - S_{sno} \right) f_{sno} \right] \tag{3.60}$$

which can be expressed as

$$S_g = S_{sno} f_{sno} + \left(1 - f_{sno} \right) \left(1 - \alpha_{soi} \right). \tag{3.61}$$

To extend equation (3.61) to the multi-snow-layer absorption case, and conserve energy, the weighted snow plus snow-free ground absorption fluxes that are used for column temperature calculations are

$$S_{g,i} = S_{sno,i} f_{sno} + (1 - f_{sno})(1 - \alpha_{soi}) \frac{S_{sno,i}}{1 - \alpha_{sno}}. \tag{3.62}$$

This weighting is performed for direct-beam and diffuse, visible and NIR fluxes. After the ground-incident fluxes (transmitted through the vegetation canopy) have been calculated for the current time step (sections 3.1 and 4.1), the layer absorption factors

$(S_{g,i})$ are multiplied by the ground-incident fluxes to produce solar absorption (W m^{-2}) in each snow layer and the underlying ground.

3.2.2 *Snowpack Optical Properties*

Ice optical properties for the five spectral bands are derived offline and stored in a namelist-defined lookup table for online retrieval (see CLM4 User's Guide). Mie properties are first computed at fine spectral resolution (470 bands), and are then weighted into the five bands applied by CLM according to incident solar flux, $I^{\downarrow}(\lambda)$. For example, the broadband mass-extinction cross section ($\overline{\psi}$) over wavelength interval λ_1 to λ_2 is

$$\overline{\psi} = \frac{\displaystyle\int_{\lambda_1}^{\lambda_2} \psi(\lambda) I^{\downarrow}(\lambda) \mathrm{d}\lambda}{\displaystyle\int_{\lambda_1}^{\lambda_2} I^{\downarrow}(\lambda) \mathrm{d}\lambda} \tag{3.63}$$

Broadband single-scatter albedo ($\overline{\omega}$) is additionally weighted by the diffuse albedo for a semi-infinite snowpack (α_{sno})

$$\overline{\omega} = \frac{\displaystyle\int_{\lambda_1}^{\lambda_2} \omega(\lambda) I^{\downarrow}(\lambda) \alpha_{sno}(\lambda) \mathrm{d}\lambda}{\displaystyle\int_{\lambda_1}^{\lambda_2} I^{\downarrow}(\lambda) \alpha_{sno}(\lambda) \mathrm{d}\lambda} \tag{3.64}$$

Inclusion of this additional albedo weight was found to improve accuracy of the five-band albedo solutions (relative to 470-band solutions) because of the strong dependence of optically-thick snowpack albedo on ice grain single-scatter albedo (Flanner et al. 2007). The lookup tables contain optical properties for lognormal distributions of ice

particles over the range of effective radii: 30μm $<$ r_e $<$ 1500μm, at 1μm resolution. Single-scatter albedos for the end-members of this size range are listed in Table 3.5.

Optical properties for black carbon are described in Flanner et al. (2007). Single-scatter albedo, mass extinction cross-section, and asymmetry parameter values for all snowpack species, in the five spectral bands used, are listed in Tables 3.5, 3.6, and 3.7. These properties were also derived with Mie Theory, using various published sources of indices of refraction and assumptions about particle size distribution. Weighting into the five CLM spectral bands was determined only with incident solar flux, as in equation (3.62).

Table 3.5. Single-scatter albedo values used for snowpack impurities and ice

Species	Band 1	Band 2	Band 3	Band 4	Band 5
Hydrophilic black carbon	0.516	0.434	0.346	0.276	0.139
Hydrophobic black carbon	0.288	0.187	0.123	0.089	0.040
Hydrophilic organic carbon	0.997	0.994	0.990	0.987	0.951
Hydrophobic organic carbon	0.963	0.921	0.860	0.814	0.744
Dust 1	0.979	0.994	0.993	0.993	0.953
Dust 2	0.944	0.984	0.989	0.992	0.983
Dust 3	0.904	0.965	0.969	0.973	0.978
Dust 4	0.850	0.940	0.948	0.953	0.955
Ice (r_e = 30μm)	0.9999	0.9999	0.9992	0.9938	0.9413
Ice (r_e = 1500μm)	0.9998	0.9960	0.9680	0.8730	0.5500

Table 3.6. Mass extinction values (m^2 kg^{-1}) used for snowpack impurities and ice.

Species	Band 1	Band 2	Band 3	Band 4	Band 5
Hydrophilic black carbon	25369	12520	7739	5744	3527
Hydrophobic black carbon	11398	5923	4040	3262	2224
Hydrophilic organic carbon	37774	22112	14719	10940	5441
Hydrophobic organic carbon	3289	1486	872	606	248
Dust 1	2687	2420	1628	1138	466
Dust 2	841	987	1184	1267	993
Dust 3	388	419	400	397	503
Dust 4	197	203	208	205	229
Ice ($r_e = 30\mu m$)	55.7	56.1	56.3	56.6	57.3
Ice ($r_e = 1500\mu m$)	1.09	1.09	1.09	1.09	1.1

Table 3.7. Asymmetry scattering parameters used for snowpack impurities and ice.

Species	Band 1	Band 2	Band 3	Band 4	Band 5
Hydrophilic black carbon	0.52	0.34	0.24	0.19	0.10
Hydrophobic black carbon	0.35	0.21	0.15	0.11	0.06
Hydrophilic organic carbon	0.77	0.75	0.72	0.70	0.64
Hydrophobic organic carbon	0.62	0.57	0.54	0.51	0.44
Dust 1	0.69	0.72	0.67	0.61	0.44
Dust 2	0.70	0.65	0.70	0.72	0.70
Dust 3	0.79	0.75	0.68	0.63	0.67
Dust 4	0.83	0.79	0.77	0.76	0.73
Ice ($r_e = 30\mu m$)	0.88	0.88	0.88	0.88	0.90
Ice ($r_e = 1500\mu m$)	0.89	0.90	0.90	0.92	0.97

3.2.3 *Snow Aging*

Snow aging is represented as evolution of the ice effective grain size (r_e). Previous studies have shown that use of spheres which conserve the surface area-to-volume ratio (or specific surface area) of ice media composed of more complex shapes produces relatively small errors in simulated hemispheric fluxes (e.g., Grenfell and Warren 1999). Effective radius is the surface area-weighted mean radius of an ensemble of spherical particles and is directly related to specific surface area (*SSA*) as $r_e = 3/(\rho_{ice}SSA)$, where ρ_{ice} is the density of ice. Hence, r_e is a simple and practical metric for relating the snowpack microphysical state to dry snow radiative characteristics.

Wet snow processes can also drive rapid changes in albedo. The presence of liquid water induces rapid coarsening of the surrounding ice grains (e.g., Brun 1989), and liquid water tends to refreeze into large ice clumps that darken the bulk snowpack. The presence of small liquid drops, by itself, does not significantly darken snowpack, as ice and water have very similar indices of refraction throughout the solar spectrum. Pooled or ponded water, however, can significantly darken snowpack by greatly reducing the number of refraction events per unit mass. This influence is not currently accounted for.

The net change in effective grain size occurring each time step is represented in each snow layer as a summation of changes caused by dry snow metamorphism ($dr_{e,dry}$), liquid water-induced metamorphism ($dr_{e,wet}$), refreezing of liquid water, and addition of freshly-fallen snow. The mass of each snow layer is partitioned into fractions of snow carrying over from the previous time step (f_{old}), freshly-fallen snow (f_{new}), and refrozen liquid water (f_{rfz}), such that snow r_e is updated each time step t as

$$r_e(t) = \left[r_e(t-1) + dr_{e,dry} + dr_{e,wet} \right] f_{old} + r_{e,0} f_{new} + r_{e,rfz} f_{rfrz} \tag{3.65}$$

Here, the effective radius of freshly-fallen snow ($r_{e,0}$) is fixed globally at 54.5μm (corresponding to a specific surface area of 60 m² kg⁻¹), and the effective radius of refrozen liquid water ($r_{e,rfz}$) is set to 1000μm.

Dry snow aging is based on a microphysical model described by Flanner and Zender (2006). This model simulates diffusive vapor flux amongst collections of ice crystals with various size and inter-particle spacing. Specific surface area and effective radius are prognosed for any combination of snow temperature, temperature gradient, density, and initial size distribution. The combination of warm snow, large temperature gradient, and low density produces the most rapid snow aging, whereas aging proceeds

slowly in cold snow, regardless of temperature gradient and density. Because this model is currently too computationally expensive for inclusion in climate models, we fit parametric curves to model output over a wide range of snow conditions and apply these parameters in CLM. The functional form of the parametric equation is

$$\frac{dr_{e,dry}}{dt} = \left(\frac{dr_e}{dt}\right)_0 \left(\frac{\eta}{(r_e - r_{e,0}) + \eta}\right)^{1/\kappa}$$

(3.66)

The parameters $(dr_e/dt)_0$, η, and κ are retrieved interactively from a lookup table with dimensions corresponding to snow temperature, temperature gradient, and density. The domain covered by this lookup table includes temperature ranging from 223 to 273 K, temperature gradient ranging from 0 to 300 K m^{-1}, and density ranging from 50 to 400 kg m^{-3}. Temperature gradient is calculated at the midpoint of each snow layer n, using mid-layer temperatures (T_n) and snow layer thicknesses (dz_n), as

$$\left(\frac{dT}{dz}\right)_n = \frac{1}{dz_n} \text{abs}\left[\frac{T_{n-1}dz_n + T_n dz_{n-1}}{dz_n + dz_{n-1}} + \frac{T_{n+1}dz_n + T_n dz_{n+1}}{dz_n + dz_{n+1}}\right]$$

(3.67)

For the bottom snow layer ($n = 0$), T_{n+1} is taken as the temperature of the top soil layer, and for the top snow layer it is assumed that $T_{n-1} = T_n$.

The contribution of liquid water to enhanced metamorphism is based on parametric equations published by Brun (1989), who measured grain growth rates under different liquid water contents. This relationship, expressed in terms of r_e (μm) and subtracting an offset due to dry aging, depends on the mass liquid water fraction f_{liq} as

$$\frac{dr_e}{dt} = \frac{10^{18} C_1 f_{liq}^3}{4\pi r_e^2}$$

(3.68)

The constant C_1 is 4.22×10^{-13}, and: $f_{liq} = w_{liq}/(w_{liq} + w_{ice})$ (section 7.2).

In cases where snow mass is greater than zero, but a snow layer has not yet been defined, r_e is set to $r_{e,0}$. When snow layers are combined or divided, r_e is calculated as a mass-weighted mean of the two layers, following computations of other state variables (section 7.2.6). Finally, the allowable range of r_e, corresponding to the range over which Mie optical properties have been defined, is 30-1500μm.

3.3 Solar Zenith Angle

The CLM uses the same formulation for solar zenith angle as the Community Atmosphere Model. The cosine of the solar zenith angle μ is

$$\mu = \sin\phi \sin\delta - \cos\phi \cos\delta \cos h \qquad (3.69)$$

where h is the solar hour angle (radians) (24 hour periodicity), δ is the solar declination angle (radians), and ϕ is latitude (radians) (positive in Northern Hemisphere). The solar hour angle h (radians) is

$$h = 2\pi d + \theta \qquad (3.70)$$

where d is calendar day ($d = 0.0$ at 0Z on January 1), and θ is longitude (radians) (positive east of the Greenwich meridian).

The solar declination angle δ is calculated as in Berger (1978a,b) and is valid for one million years past or hence, relative to 1950 A.D. The orbital parameters may be specified directly or the orbital parameters are calculated for the desired year. The required orbital parameters to be input by the user are the obliquity of the Earth ε (degrees, $-90° < \varepsilon < 90°$), Earth's eccentricity e ($0.0 < e < 0.1$), and the longitude of the perihelion relative to the moving vernal equinox $\tilde{\omega}$ ($0° < \tilde{\omega} < 360°$) (unadjusted for the apparent orbit of the Sun around the Earth (Berger et al. 1993)). The solar declination δ (radians) is

$$\delta = \sin^{-1}\left[\sin(\varepsilon)\sin(\lambda)\right] \tag{3.71}$$

where ε is Earth's obliquity and λ is the true longitude of the Earth.

The obliquity of the Earth ε (degrees) is

$$\varepsilon = \varepsilon * + \sum_{i=1}^{i=47} A_i \cos\left(f_i t + \delta_i\right) \tag{3.72}$$

where $\varepsilon *$ is a constant of integration (Table 3.8), A_i, f_i, and δ_i are amplitude, mean

rate, and phase terms in the cosine series expansion (Berger 1978a,b), and $t = t_0 - 1950$

where t_0 is the year. The series expansion terms are not shown here but can be found in

the source code file shr_orb_mod.F90.

The true longitude of the Earth λ (radians) is counted counterclockwise from the

vernal equinox ($\lambda = 0$ at the vernal equinox)

$$\lambda = \lambda_m + \left(2e - \frac{1}{4}e^3\right)\sin\left(\lambda_m - \tilde{\omega}\right) + \frac{5}{4}e^2 \sin 2\left(\lambda_m - \tilde{\omega}\right) + \frac{13}{12}e^3 \sin 3\left(\lambda_m - \tilde{\omega}\right) \tag{3.73}$$

where λ_m is the mean longitude of the Earth at the vernal equinox, e is Earth's

eccentricity, and $\tilde{\omega}$ is the longitude of the perihelion relative to the moving vernal

equinox. The mean longitude λ_m is

$$\lambda_m = \lambda_{m0} + \frac{2\pi\left(d - d_{ve}\right)}{365} \tag{3.74}$$

where $d_{ve} = 80.5$ is the calendar day at vernal equinox (March 21 at noon), and

$$\lambda_{m0} = 2\left[\left(\frac{1}{2}e + \frac{1}{8}e^3\right)(1+\beta)\sin\tilde{\omega} - \frac{1}{4}e^2\left(\frac{1}{2}+\beta\right)\sin 2\tilde{\omega} + \frac{1}{8}e^3\left(\frac{1}{3}+\beta\right)\sin 3\tilde{\omega}\right] \tag{3.75}$$

where $\beta = \sqrt{1-e^2}$. Earth's eccentricity e is

$$e = \sqrt{\left(e^{\cos}\right)^2 + \left(e^{\sin}\right)^2} \qquad (3.76)$$

where

$$e^{\cos} = \sum_{j=1}^{19} M_j \cos\left(g_j t + B_j\right),$$

$$e^{\sin} = \sum_{j=1}^{19} M_j \sin\left(g_j t + B_j\right) \qquad (3.77)$$

are the cosine and sine series expansions for e, and M_j, g_j, and B_j are amplitude, mean rate, and phase terms in the series expansions (Berger 1978a,b). The longitude of the perihelion relative to the moving vernal equinox $\tilde{\omega}$ (degrees) is

$$\tilde{\omega} = \Pi \frac{180}{\pi} + \psi \qquad (3.78)$$

where Π is the longitude of the perihelion measured from the reference vernal equinox (i.e., the vernal equinox at 1950 A.D.) and describes the absolute motion of the perihelion relative to the fixed stars, and ψ is the annual general precession in longitude and describes the absolute motion of the vernal equinox along Earth's orbit relative to the fixed stars. The general precession ψ (degrees) is

$$\psi = \frac{\tilde{\psi} t}{3600} + \zeta + \sum_{i=1}^{78} F_i \sin\left(f_i' t + \delta_i'\right) \qquad (3.79)$$

where $\tilde{\psi}$ (arcseconds) and ζ (degrees) are constants (Table 3.8), and F_i, f_i', and δ_i' are amplitude, mean rate, and phase terms in the sine series expansion (Berger 1978a,b). The longitude of the perihelion Π (radians) depends on the sine and cosine series expansions for the eccentricity e as follows:

51

$$
\Pi = \begin{cases}
0 & \text{for } -1\times10^{-8} \leq e^{\cos} \leq 1\times10^{-8} \text{ and } e^{\sin} = 0 \\
1.5\pi & \text{for } -1\times10^{-8} \leq e^{\cos} \leq 1\times10^{-8} \text{ and } e^{\sin} < 0 \\
0.5\pi & \text{for } -1\times10^{-8} \leq e^{\cos} \leq 1\times10^{-8} \text{ and } e^{\sin} > 0 \\
\tan^{-1}\left[\dfrac{e^{\sin}}{e^{\cos}}\right] + \pi & \text{for } e^{\cos} < -1\times10^{-8} \\
\tan^{-1}\left[\dfrac{e^{\sin}}{e^{\cos}}\right] + 2\pi & \text{for } e^{\cos} > 1\times10^{-8} \text{ and } e^{\sin} < 0 \\
\tan^{-1}\left[\dfrac{e^{\sin}}{e^{\cos}}\right] & \text{for } e^{\cos} > 1\times10^{-8} \text{ and } e^{\sin} \geq 0
\end{cases}. \qquad (3.80)
$$

The numerical solution for the longitude of the perihelion $\tilde{\omega}$ is constrained to be between 0 and 360 degrees (measured from the autumn equinox). A constant 180 degrees is then added to $\tilde{\omega}$ because the Sun is considered as revolving around the Earth (geocentric coordinate system) (Berger et al. 1993).

Table 3.8. Orbital parameters

Parameter	
$\varepsilon *$	23.320556
$\tilde{\psi}$ (arcseconds)	50.439273
ζ (degrees)	3.392506

4. Radiative Fluxes

The net radiation at the surface is $\left(\vec{S}_v + \vec{S}_g\right) - \left(\vec{L}_v + \vec{L}_g\right)$, where $\vec{S}$ is the net solar flux absorbed by the vegetation ("v") and the ground ("g") and $\vec{L}$ is the net longwave flux (positive toward the atmosphere) (W m^{-2}).

4.1 Solar Fluxes

With reference to Figure 4.1, the direct beam flux transmitted through the canopy, per unit incident flux, is $e^{-K(L+S)}$, and the direct beam and diffuse fluxes absorbed by the vegetation, per unit incident flux, are

$$\vec{I}_\Lambda^\mu = 1 - I\uparrow_\Lambda^\mu - \left(1 - \alpha_{g,\Lambda}\right)I\downarrow_\Lambda^\mu - \left(1 - \alpha_{g,\Lambda}^\mu\right)e^{-K(L+S)} \tag{4.1}$$

$$\vec{I}_\Lambda = 1 - I\uparrow_\Lambda - \left(1 - \alpha_{g,\Lambda}\right)I\downarrow_\Lambda . \tag{4.2}$$

$I\uparrow_\Lambda^\mu$ and $I\uparrow_\Lambda$ are the upward diffuse fluxes, per unit incident direct beam and diffuse flux (section 3.1). $I\downarrow_\Lambda^\mu$ and $I\downarrow_\Lambda$ are the downward diffuse fluxes below the vegetation per unit incident direct beam and diffuse radiation (section 3.1). $\alpha_{g,\Lambda}^\mu$ and $\alpha_{g,\Lambda}$ are the direct beam and diffuse ground albedos (section 3.2). L and S are the exposed leaf area index and stem area index (section 2.3). K is the optical depth of direct beam per unit leaf and stem area (section 3.1).

Figure 4.1. Schematic diagram of (a) direct beam radiation, (b) diffuse solar radiation, and (c) longwave radiation absorbed, transmitted, and reflected by vegetation and ground. For clarity, terms involving $T^{n+1} - T^n$ are not shown in (c).

$$(a)$$

$$1$$

$$I\uparrow_\Lambda^\mu$$

$$\vec{I}_\Lambda^\mu$$

$$I\downarrow_\Lambda^\mu \qquad e^{-K(L+S)}$$

$$\alpha_{g,\Lambda} \qquad \alpha_{g,\Lambda}^\mu$$

$$(b)$$

$$1$$

$$I\uparrow_\Lambda$$

$$\vec{I}_\Lambda$$

$$I\downarrow_\Lambda$$

$$\alpha_{g,\Lambda}$$

$$(c)$$

$$L_{atm}\downarrow$$

$$L_{vg}\uparrow = (1-\varepsilon_v)L_g\uparrow + \varepsilon_v\sigma T_v^4$$

$$\vec{L}_v$$

$$L_v\downarrow = (1-\varepsilon_v)L_{atm}\downarrow + \varepsilon_v\sigma T_v^4$$

$$L_g\uparrow = (1-\varepsilon_g)L_v\downarrow + \varepsilon_g\sigma T_g^4$$

$$\vec{L}_g$$
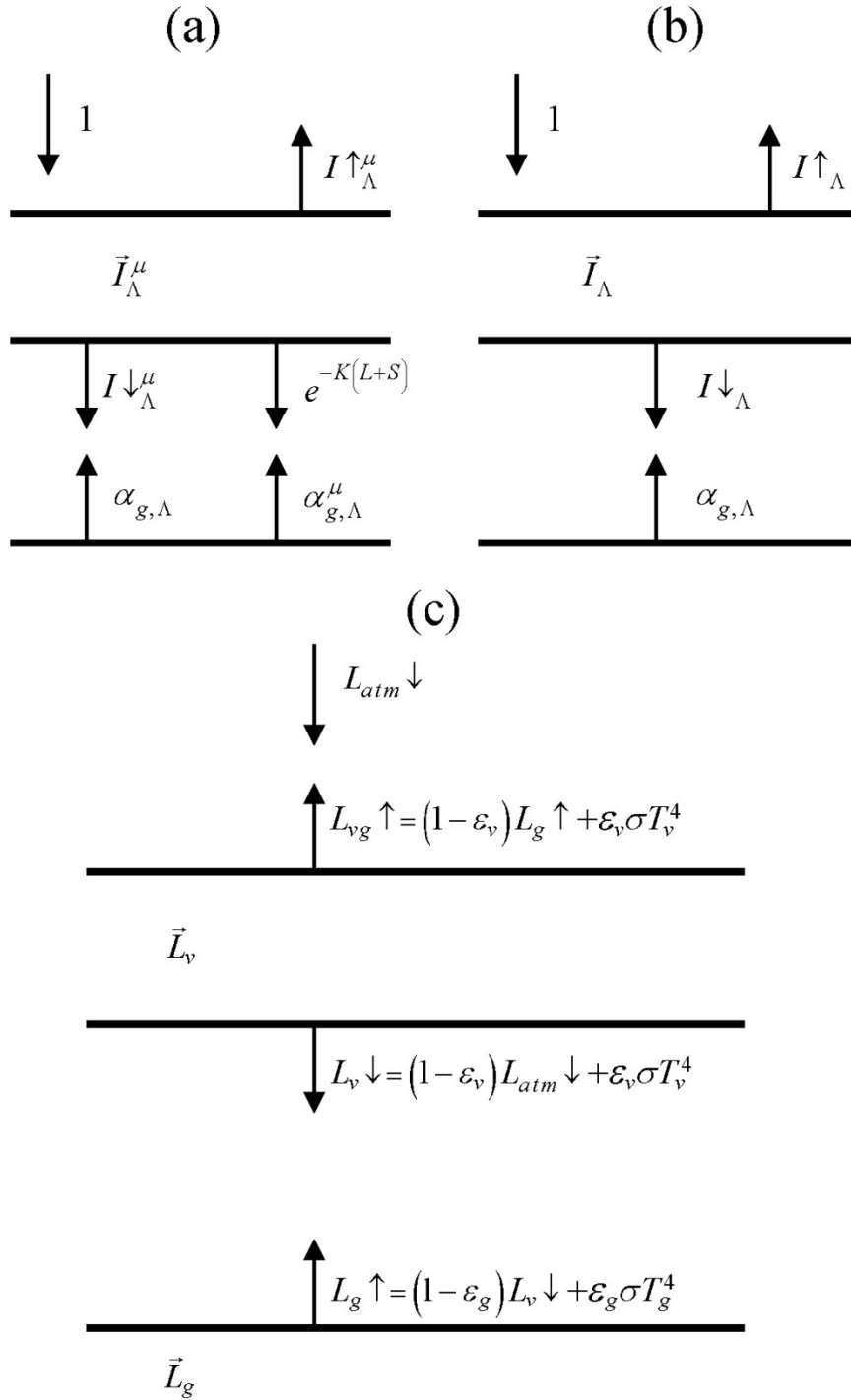
The total solar radiation absorbed by the vegetation and ground is

$$\vec{S}_v = \sum_\Lambda S_{atm} \downarrow_\Lambda^\mu \vec{I}_\Lambda^\mu + S_{atm} \downarrow_\Lambda \vec{I}_\Lambda \tag{4.3}$$

$$\begin{aligned}\vec{S}_g = \sum_\Lambda S_{atm} \downarrow_\Lambda^\mu e^{-K(L+S)} \left(1 - \alpha_{g,\Lambda}^\mu\right) + \\ \left(S_{atm} \downarrow_\Lambda^\mu I \downarrow_\Lambda^\mu + S_{atm} \downarrow_\Lambda I \downarrow_\Lambda\right)\left(1 - \alpha_{g,\Lambda}\right)\end{aligned} \tag{4.4}$$

where $S_{atm} \downarrow_\Lambda^\mu$ and $S_{atm} \downarrow_\Lambda$ are the incident direct beam and diffuse solar fluxes (W m^{-2}).

For non-vegetated surfaces, $e^{-K(L+S)} = 1$, $\vec{I}_\Lambda^\mu = \vec{I}_\Lambda = 0$, $I \downarrow_\Lambda^\mu = 0$, and $I \downarrow_\Lambda = 1$, so that

$$\begin{aligned}\vec{S}_g = \sum_\Lambda S_{atm} \downarrow_\Lambda^\mu \left(1 - \alpha_{g,\Lambda}^\mu\right) + S_{atm} \downarrow_\Lambda \left(1 - \alpha_{g,\Lambda}\right) \\ \vec{S}_v = 0\end{aligned} \tag{4.5}$$

Solar radiation is conserved as

$$\sum_\Lambda \left(S_{atm} \downarrow_\Lambda^\mu + S_{atm} \downarrow_\Lambda\right) = \left(\vec{S}_v + \vec{S}_g\right) + \sum_\Lambda \left(S_{atm} \downarrow_\Lambda^\mu I \uparrow_\Lambda^\mu + S_{atm} \downarrow_\Lambda I \uparrow_\Lambda\right) \tag{4.6}$$

where the latter term in parentheses is reflected solar radiation.

Photosynthesis and transpiration depend non-linearly on solar radiation, via the light response of stomata. The canopy is treated as two leaves (sunlit and shaded) and the solar radiation in the visible waveband (< 0.7 µm) absorbed by the vegetation is apportioned to the sunlit and shaded leaves as described by Thornton and Zimmermann (2007).

The sunlit fraction of the canopy is

$$f_{sun} = \frac{1 - e^{-KL}}{KL} \tag{4.7}$$

where e^{-KL} is the fractional area of sunflecks on a horizontal plane below the leaf area index L. Here, $KL \le 40$. The shaded fraction is $f_{sha} = 1 - f_{sun}$, and the sunlit and shaded leaf area indices are $L^{sun} = f_{sun}L$ and $L^{sha} = f_{sha}L$. In calculating f_{sun},

$$K = \frac{G(\mu)}{\mu} \tag{4.8}$$

where $G(\mu)$ and μ are parameters in the two-stream approximation (section 3.1). To prevent numerical instabilities, $f_{sun} = 1$, $f_{sha} = 0$, $L^{sun} = L$, and $L^{sha} = 0$ when $L \le 0.01$. When the sun is below the horizon ($\mu \le 0$), $f_{sun} = 0$, $f_{sha} = 1$, $L^{sun} = 0$, and $L^{sha} = L$.

Solar radiation in the visible waveband (< 0.7 µm) is partitioned to the sunlit and shaded leaves, excluding that which is absorbed by stems. Sunlit leaves receive the absorbed direct beam radiation and additionally the absorbed diffuse radiation (originating from scattered direct beam radiation or from atmospheric diffuse radiation) apportioned by f_{sun}. Shaded leaves receive the absorbed diffuse radiation apportioned by f_{sha}.

The total visible waveband direct beam radiation absorbed by the canopy is $S_{atm} \downarrow_{vis}^{\mu} \vec{I}_{vis}^{\mu}$. This radiation is partitioned into unscattered direct beam absorbed by the canopy (ϕ_{dir}^{μ}) and scattered direct beam absorbed as diffuse radiation (ϕ_{dif}^{μ}). These two fluxes are

$$\phi_{dir}^{\mu} = S_{atm} \downarrow_{vis}^{\mu} \left[1 - e^{-K(L+S)}\right] (1 - \omega_{vis}) \tag{4.9}$$

$$\phi_{dif}^{\mu} = S_{atm} \downarrow_{vis}^{\mu} \vec{I}_{vis}^{\mu} - \phi_{dir}^{\mu} \ge 0 \tag{4.10}$$

With reference to Figure 4.1, ϕ_{dir}^{μ} is the portion of the incoming visible waveband direct beam radiation ($S_{atm}\downarrow_{vis}^{\mu}$) that is not transmitted through the canopy as direct beam radiation ($1-e^{-K(L+S)}$) that is absorbed ($1-\omega_{vis}$), where ω_{vis} is the scattering coefficient (section 3.1). The remainder of the absorbed visible waveband direct beam radiation is assumed to be scattered direct beam absorbed as diffuse radiation (ϕ_{dif}^{μ}).

The incoming visible waveband diffuse radiation absorbed by the canopy is

$$\phi_{dif} = S_{atm}\downarrow_{vis}\vec{I}_{vis} \tag{4.11}$$

The absorbed photosynthetically active (visible waveband) radiation averaged for the sunlit leaf area is

$$\phi^{sun} = \left(\phi_{dir}^{\mu} + \phi_{dif}^{\mu}f_{sun} + \phi_{dif}f_{sun}\right)\left(\frac{L}{L+S}\right)\bigg/L^{sun} \quad \text{for } L^{sun} > 0 \tag{4.12}$$

and the similar absorbed radiation for the average shaded leaf is

$$\phi^{sha} = \left(\phi_{dif}^{\mu}f_{sha} + \phi_{dif}f_{sha}\right)\left(\frac{L}{L+S}\right)\bigg/L^{sha} \qquad \text{for } L^{sha} > 0 \tag{4.13}$$

These equations assume the leaves absorb $L/(L+S)$ of the solar radiation absorbed by the vegetation.

4.2   Longwave Fluxes

The net longwave radiation (W m^{-2}) (positive toward the atmosphere) at the surface is

$$\vec{L} = L\uparrow - L_{atm}\downarrow \tag{4.14}$$

where $L\uparrow$ is the upward longwave radiation from the surface and $L_{atm}\downarrow$ is the downward atmospheric longwave radiation (W m^{-2}). The radiative temperature T_{rad} (K) is defined from the upward longwave radiation as

$$T_{rad} = \left(\frac{L\uparrow}{\sigma}\right)^{1/4} \tag{4.15}$$

where σ is the Stefan-Boltzmann constant (W m^{-2} K^{-4}) (Table 1.4). With reference to Figure 4.1, the upward longwave radiation from the surface to the atmosphere is

$$L\uparrow = \delta_{veg} L_{vg}\uparrow + \left(1 - \delta_{veg}\right)\left(1 - \varepsilon_g\right)L_{atm}\downarrow + \\ \left(1 - \delta_{veg}\right)\varepsilon_g\sigma\left(T_g^n\right)^4 + 4\varepsilon_g\sigma\left(T_g^n\right)^3\left(T_g^{n+1} - T_g^n\right) \tag{4.16}$$

where $L_{vg}\uparrow$ is the upward longwave radiation from the vegetation/soil system for exposed leaf and stem area $L + S \geq 0.05$, δ_{veg} is a step function and is zero for $L + S < 0.05$ and one otherwise, ε_g is the ground emissivity, and T_g^{n+1} and T_g^n are the snow/soil surface temperatures at the current and previous time steps, respectively (section 6).

For non-vegetated surfaces, the above equation reduces to

$$L\uparrow = \left(1 - \varepsilon_g\right)L_{atm}\downarrow + \varepsilon_g\sigma\left(T_g^n\right)^4 + 4\varepsilon_g\sigma\left(T_g^n\right)^3\left(T_g^{n+1} - T_g^n\right) \tag{4.17}$$

where the first term is the atmospheric longwave radiation reflected by the ground, the second term is the longwave radiation emitted by the ground, and the last term is the increase (decrease) in longwave radiation emitted by the ground due to an increase (decrease) in ground temperature.

For vegetated surfaces, the upward longwave radiation from the surface reduces to

$$L\uparrow = L_{vg}\uparrow + 4\varepsilon_g\sigma\left(T_g^n\right)^3\left(T_g^{n+1} - T_g^n\right) \tag{4.18}$$

where

$$
\begin{aligned}
L_{vg} \uparrow = {} & \left(1 - \varepsilon_g\right)\left(1 - \varepsilon_v\right)\left(1 - \varepsilon_v\right) L_{atm} \downarrow \\
& + \varepsilon_v \left[1 + \left(1 - \varepsilon_g\right)\left(1 - \varepsilon_v\right)\right] \sigma \left(T_v^n\right)^3 \left[T_v^n + 4\left(T_v^{n+1} - T_v^n\right)\right] \\
& + \varepsilon_g \left(1 - \varepsilon_v\right) \sigma \left(T_g^n\right)^4 \\
= {} & \left(1 - \varepsilon_g\right)\left(1 - \varepsilon_v\right)\left(1 - \varepsilon_v\right) L_{atm} \downarrow \\
& + \varepsilon_v \sigma \left(T_v^n\right)^4 \\
& + \varepsilon_v \left(1 - \varepsilon_g\right)\left(1 - \varepsilon_v\right) \sigma \left(T_v^n\right)^4 \\
& + 4 \varepsilon_v \sigma \left(T_v^n\right)^3 \left(T_v^{n+1} - T_v^n\right) \\
& + 4 \varepsilon_v \left(1 - \varepsilon_g\right)\left(1 - \varepsilon_v\right) \sigma \left(T_v^n\right)^3 \left(T_v^{n+1} - T_v^n\right) \\
& + \varepsilon_g \left(1 - \varepsilon_v\right) \sigma \left(T_g^n\right)^4
\end{aligned}
\tag{4.19}
$$

where ε_v is the vegetation emissivity and T_v^{n+1} and T_v^n are the vegetation temperatures at the current and previous time steps, respectively (section 5). The first term in the equation above is the atmospheric longwave radiation that is transmitted through the canopy, reflected by the ground, and transmitted through the canopy to the atmosphere. The second term is the longwave radiation emitted by the canopy directly to the atmosphere. The third term is the longwave radiation emitted downward from the canopy, reflected by the ground, and transmitted through the canopy to the atmosphere. The fourth term is the increase (decrease) in longwave radiation due to an increase (decrease) in canopy temperature that is emitted by the canopy directly to the atmosphere. The fifth term is the increase (decrease) in longwave radiation due to an increase (decrease) in canopy temperature that is emitted downward from the canopy, reflected from the ground, and transmitted through the canopy to the atmosphere. The last term is the longwave radiation emitted by the ground and transmitted through the canopy to the atmosphere.

The upward longwave radiation from the ground is

$$L_g \uparrow = \left(1 - \varepsilon_g\right) L_v \downarrow + \varepsilon_g \sigma \left(T_g^n\right)^4 \qquad (4.20)$$

where $L_v \downarrow$ is the downward longwave radiation below the vegetation

$$L_v \downarrow = \left(1 - \varepsilon_v\right) L_{atm} \downarrow + \varepsilon_v \sigma \left(T_v^n\right)^4 + 4\varepsilon_v \sigma \left(T_v^n\right)^3 \left(T_v^{n+1} - T_v^n\right). \qquad (4.21)$$

The net longwave radiation flux for the ground is (positive toward the atmosphere)

$$\vec{L}_g = \varepsilon_g \sigma \left(T_g^n\right)^4 - \delta_{veg} \varepsilon_g L_v \downarrow - \left(1 - \delta_{veg}\right) \varepsilon_g L_{atm} \downarrow . \qquad (4.22)$$

The above expression for $\vec{L}_g$ is the net longwave radiation forcing that is used in the soil

temperature calculation (section 6). Once updated soil temperatures have been obtained,

the term $4\varepsilon_g \sigma \left(T_g^n\right)^3 \left(T_g^{n+1} - T_g^n\right)$ is added to $\vec{L}_g$ to calculate the ground heat flux (section

5.4)

The net longwave radiation flux for vegetation is (positive toward the atmosphere)

$$\vec{L}_v = \left[2 - \varepsilon_v \left(1 - \varepsilon_g\right)\right] \varepsilon_v \sigma \left(T_v\right)^4 - \varepsilon_v \varepsilon_g \sigma \left(T_g^n\right)^4 - \varepsilon_v \left[1 + \left(1 - \varepsilon_g\right)\left(1 - \varepsilon_v\right)\right] L_{atm} \downarrow . \quad (4.23)$$

These equations assume that absorptivity equals emissivity. The emissivity of the

ground is

$$\varepsilon_g = \varepsilon_{soi} \left(1 - f_{sno}\right) + \varepsilon_{sno} f_{sno} \qquad (4.24)$$

where $\varepsilon_{soi} = 0.96$ for soil, 0.97 for glacier, and 0.96 for wetland, $\varepsilon_{sno} = 0.97$, and f_{sno} is

the fraction of ground covered by snow (section 3.2). The vegetation emissivity is

$$\varepsilon_v = 1 - e^{-(L+S)/\bar{\mu}} \qquad (4.25)$$

where L and S are the leaf and stem area indices (section 2.3) and $\bar{\mu} = 1$ is the average

inverse optical depth for longwave radiation.

5.   Momentum, Sensible Heat, and Latent Heat Fluxes

The zonal τ_x and meridional τ_y momentum fluxes (kg m^{-1} s^{-2}), sensible heat flux H (W m^{-2}), and water vapor flux E (kg m^{-2} s^{-1}) between the atmosphere at reference height $z_{atm,x}$ (m) [where x is height for wind (momentum) (m), temperature (sensible heat) (h), and humidity (water vapor) (w); with zonal and meridional winds u_{atm} and v_{atm} (m s^{-1}), potential temperature θ_{atm} (K), and specific humidity q_{atm} (kg kg^{-1})] and the surface [with u_s, v_s, θ_s, and q_s] are

$$\tau_x = -\rho_{atm} \frac{\left(u_{atm} - u_s\right)}{r_{am}} \tag{5.1}$$

$$\tau_y = -\rho_{atm} \frac{\left(v_{atm} - v_s\right)}{r_{am}} \tag{5.2}$$

$$H = -\rho_{atm} C_p \frac{\left(\theta_{atm} - \theta_s\right)}{r_{ah}} \tag{5.3}$$

$$E = -\rho_{atm} \frac{\left(q_{atm} - q_s\right)}{r_{aw}}. \tag{5.4}$$

These fluxes are derived in the next section from Monin-Obukhov similarity theory developed for the surface layer (i.e., the nearly constant flux layer above the surface sublayer). In this derivation, u_s and v_s are defined to equal zero at height $z_{0m} + d$ (the apparent sink for momentum) so that r_{am} is the aerodynamic resistance (s m^{-1}) for momentum between the atmosphere at height $z_{atm,m}$ and the surface at height $z_{0m} + d$. Thus, the momentum fluxes become

$$\tau_x = -\rho_{atm} \frac{u_{atm}}{r_{am}} \tag{5.5}$$

61

$$\tau_y = -\rho_{atm} \frac{v_{atm}}{r_{am}}.$$ (5.6)

Likewise, θ_s and q_s are defined at heights $z_{0h} + d$ and $z_{0w} + d$ (the apparent sinks for heat and water vapor, respectively). Consequently, r_{ah} and r_{aw} are the aerodynamic resistances (s m^{-1}) to sensible heat and water vapor transfer between the atmosphere at heights $z_{atm,h}$ and $z_{atm,w}$ and the surface at heights $z_{0h} + d$ and $z_{0w} + d$, respectively. The specific heat capacity of air C_p (J kg^{-1} K^{-1}) is a constant (Table 1.4). The atmospheric potential temperature used here is

$$\theta_{atm} = T_{atm} + \Gamma_d z_{atm,h}$$ (5.7)

where T_{atm} is the air temperature (K) at height $z_{atm,h}$ and $\Gamma_d = 0.0098$ K m^{-1} is the negative of the dry adiabatic lapse rate [this expression is first-order equivalent to $\theta_{atm} = T_{atm} \left(P_{srf} / P_{atm} \right)^{R_{da}/C_p}$ (Stull 1988), where P_{srf} is the surface pressure (Pa), P_{atm} is the atmospheric pressure (Pa), and R_{da} is the gas constant for dry air (J kg^{-1} K^{-1}) (Table 1.4)]. By definition, $\theta_s = T_s$. The density of moist air (kg m^{-3}) is

$$\rho_{atm} = \frac{P_{atm} - 0.378 e_{atm}}{R_{da} T_{atm}}$$ (5.8)

where the atmospheric vapor pressure e_{atm} (Pa) is derived from the atmospheric specific humidity q_{atm}

$$e_{atm} = \frac{q_{atm} P_{atm}}{0.622 + 0.378 q_{atm}}.$$ (5.9)

5.1 Monin-Obukhov Similarity Theory

The surface vertical kinematic fluxes of momentum $\overline{u'w'}$ and $\overline{v'w'}$ (m^2 s^{-2}), sensible heat $\overline{\theta'w'}$ (K m s^{-1}), and latent heat $\overline{q'w'}$ (kg kg^{-1} m s^{-1}), where u', v', w', θ', and q' are zonal horizontal wind, meridional horizontal wind, vertical velocity, potential temperature, and specific humidity turbulent fluctuations about the mean, are defined from Monin-Obukhov similarity applied to the surface layer. This theory states that when scaled appropriately, the dimensionless mean horizontal wind speed, mean potential temperature, and mean specific humidity profile gradients depend on unique functions of $\zeta = \dfrac{z-d}{L}$ (Zeng et al. 1998) as

$$\frac{k(z-d)}{u_*}\frac{\partial |\boldsymbol{u}|}{\partial z} = \phi_m(\zeta) \tag{5.10}$$

$$\frac{k(z-d)}{\theta_*}\frac{\partial \theta}{\partial z} = \phi_h(\zeta) \tag{5.11}$$

$$\frac{k(z-d)}{q_*}\frac{\partial q}{\partial z} = \phi_w(\zeta) \tag{5.12}$$

where z is height in the surface layer (m), d is the displacement height (m), L is the Monin-Obukhov length scale (m) that accounts for buoyancy effects resulting from vertical density gradients (i.e., the atmospheric stability), k is the von Karman constant (Table 1.4), and $|\boldsymbol{u}|$ is the atmospheric wind speed (m s^{-1}). ϕ_m, ϕ_h, and ϕ_w are universal (over any surface) similarity functions of ζ that relate the constant fluxes of momentum, sensible heat, and latent heat to the mean profile gradients of $|\boldsymbol{u}|$, θ, and q in the surface

layer. In neutral conditions, $\phi_m = \phi_h = \phi_w = 1$. The velocity (i.e., friction velocity) u_* (m s^{-1}), temperature θ_* (K), and moisture q_* (kg kg^{-1}) scales are

$$u_*^2 = \sqrt{\left(\overline{u'w'}\right)^2 + \left(\overline{v'w'}\right)^2} = \frac{|\tau|}{\rho_{atm}} \tag{5.13}$$

$$\theta_* u_* = -\overline{\theta'w'} = -\frac{H}{\rho_{atm}C_p} \tag{5.14}$$

$$q_* u_* = -\overline{q'w'} = -\frac{E}{\rho_{atm}} \tag{5.15}$$

where $|\tau|$ is the shearing stress (kg m^{-1} s^{-2}), with zonal and meridional components

$\overline{u'w'} = -\dfrac{\tau_x}{\rho_{atm}}$ and $\overline{v'w'} = -\dfrac{\tau_y}{\rho_{atm}}$, respectively, H is the sensible heat flux (W m^{-2}) and

E is the water vapor flux (kg m^{-2} s^{-1}).

The dimensionless length scale L is the Monin-Obukhov length defined as

$$L = -\frac{u_*^3}{k\left(\dfrac{g}{\overline{\theta_{v,atm}}}\right)\overline{\theta_v'w'}} = \frac{u_*^2 \overline{\theta_{v,atm}}}{kg\theta_{v*}} \tag{5.16}$$

where g is the acceleration of gravity (m s^{-2}) (Table 1.4), and $\overline{\theta_{v,atm}} = \overline{\theta_{atm}}\left(1 + 0.61q_{atm}\right)$

is the reference virtual potential temperature. $L > 0$ indicates stable conditions. $L < 0$ indicates unstable conditions. $L = \infty$ for neutral conditions. The temperature scale θ_{v*} is defined as

$$\theta_{v*} u_* = \left[\theta_*\left(1 + 0.61q_{atm}\right) + 0.61\overline{\theta_{atm}}q_*\right]u_* \tag{5.17}$$

where $\overline{\theta_{atm}}$ is the atmospheric potential temperature.

Following Panofsky and Dutton (1984), the differential equations for $\phi_m(\zeta)$, $\phi_h(\zeta)$, and $\phi_w(\zeta)$ can be integrated formally without commitment to their exact forms. Integration between two arbitrary heights in the surface layer z_2 and z_1 ($z_2 > z_1$) with horizontal winds $|u|_1$ and $|u|_2$, potential temperatures θ_1 and θ_2, and specific humidities q_1 and q_2 results in

$$|u|_2 - |u|_1 = \frac{u_*}{k}\left[\ln\left(\frac{z_2 - d}{z_1 - d}\right) - \psi_m\left(\frac{z_2 - d}{L}\right) + \psi_m\left(\frac{z_1 - d}{L}\right)\right] \tag{5.18}$$

$$\theta_2 - \theta_1 = \frac{\theta_*}{k}\left[\ln\left(\frac{z_2 - d}{z_1 - d}\right) - \psi_h\left(\frac{z_2 - d}{L}\right) + \psi_h\left(\frac{z_1 - d}{L}\right)\right] \tag{5.19}$$

$$q_2 - q_1 = \frac{q_*}{k}\left[\ln\left(\frac{z_2 - d}{z_1 - d}\right) - \psi_w\left(\frac{z_2 - d}{L}\right) + \psi_w\left(\frac{z_1 - d}{L}\right)\right]. \tag{5.20}$$

The functions $\psi_m(\zeta)$, $\psi_h(\zeta)$, and $\psi_w(\zeta)$ are defined as

$$\psi_m(\zeta) = \int_{z_{0m}/L}^{\zeta} \frac{\left[1 - \phi_m(x)\right]}{x}\,dx \tag{5.21}$$

$$\psi_h(\zeta) = \int_{z_{0h}/L}^{\zeta} \frac{\left[1 - \phi_h(x)\right]}{x}\,dx \tag{5.22}$$

$$\psi_w(\zeta) = \int_{z_{0w}/L}^{\zeta} \frac{\left[1 - \phi_w(x)\right]}{x}\,dx \tag{5.23}$$

where z_{0m}, z_{0h}, and z_{0w} are the roughness lengths (m) for momentum, sensible heat, and water vapor, respectively.

Defining the surface values

$$|u|_1 = 0 \text{ at } z_1 = z_{0m} + d,$$

$$\theta_1 = \theta_s \text{ at } z_1 = z_{0h} + d, \text{ and}$$

$$q_1 = q_s \text{ at } z_1 = z_{0w} + d,$$

and the atmospheric values at $z_2 = z_{atm,x}$

$$|\boldsymbol{u}|_2 = V_a = \sqrt{u_{atm}^2 + v_{atm}^2 + U_c^2} \geq 1, \qquad (5.24)$$

$$\theta_2 = \theta_{atm}, \text{ and}$$

$$q_2 = q_{atm},$$

the integral forms of the flux-gradient relations are

$$V_a = \frac{u_*}{k}\left[\ln\left(\frac{z_{atm,m} - d}{z_{0m}}\right) - \psi_m\left(\frac{z_{atm,m} - d}{L}\right) + \psi_m\left(\frac{z_{0m}}{L}\right)\right] \qquad (5.25)$$

$$\theta_{atm} - \theta_s = \frac{\theta_*}{k}\left[\ln\left(\frac{z_{atm,h} - d}{z_{0h}}\right) - \psi_h\left(\frac{z_{atm,h} - d}{L}\right) + \psi_h\left(\frac{z_{0h}}{L}\right)\right] \qquad (5.26)$$

$$q_{atm} - q_s = \frac{q_*}{k}\left[\ln\left(\frac{z_{atm,w} - d}{z_{0w}}\right) - \psi_w\left(\frac{z_{atm,w} - d}{L}\right) + \psi_w\left(\frac{z_{0w}}{L}\right)\right]. \qquad (5.27)$$

The constraint $V_a \geq 1$ is required simply for numerical reasons to prevent H and E from becoming small with small wind speeds. The convective velocity U_c accounts for the contribution of large eddies in the convective boundary layer to surface fluxes as follows

$$\begin{array}{llll} U_c = 0 & \zeta \geq 0 & \text{(stable)} \\ U_c = \beta w_* & \zeta < 0 & \text{(unstable)} \end{array} \qquad (5.28)$$

where w_* is the convective velocity scale

$$w_* = \left(\frac{-gu_*\theta_{v*}z_i}{\theta_{v,atm}}\right)^{1/3}, \qquad (5.29)$$

$z_i = 1000$ is the convective boundary layer height (m), and $\beta = 1$.

The momentum flux gradient relations are (Zeng et al. 1998)

$$\phi_m(\zeta) = 0.7k^{2/3}(-\zeta)^{1/3} \quad \text{for } \zeta < -1.574 \text{ (very unstable)}$$
$$\phi_m(\zeta) = (1-16\zeta)^{-1/4} \quad \text{for } -1.574 \leq \zeta < 0 \text{ (unstable)}$$
$$\phi_m(\zeta) = 1 + 5\zeta \quad \text{for } 0 \leq \zeta \leq 1 \text{ (stable)}$$
$$\phi_m(\zeta) = 5 + \zeta \quad \text{for } \zeta > 1 \text{ (very stable).}$$

(5.30)

The sensible and latent heat flux gradient relations are (Zeng et al. 1998)

$$\phi_h(\zeta) = \phi_w(\zeta) = 0.9k^{4/3}(-\zeta)^{-1/3} \quad \text{for } \zeta < -0.465 \text{ (very unstable)}$$
$$\phi_h(\zeta) = \phi_w(\zeta) = (1-16\zeta)^{-1/2} \quad \text{for } -0.465 \leq \zeta < 0 \text{ (unstable)}$$
$$\phi_h(\zeta) = \phi_w(\zeta) = 1 + 5\zeta \quad \text{for } 0 \leq \zeta \leq 1 \text{ (stable)}$$
$$\phi_h(\zeta) = \phi_w(\zeta) = 5 + \zeta \quad \text{for } \zeta > 1 \text{ (very stable).}$$

(5.31)

To ensure continuous functions of $\phi_m(\zeta)$, $\phi_h(\zeta)$, and $\phi_w(\zeta)$, the simplest approach (i.e., without considering any transition regimes) is to match the relations for very unstable and unstable conditions at $\zeta_m = -1.574$ for $\phi_m(\zeta)$ and $\zeta_h = \zeta_w = -0.465$ for $\phi_h(\zeta) = \phi_w(\zeta)$ (Zeng et al. 1998). The flux gradient relations can be integrated to yield wind profiles for the following conditions:

Very unstable $(\zeta < -1.574)$

$$V_a = \frac{u_*}{k}\left\{\left[\ln\frac{\zeta_m L}{z_{0m}} - \psi_m(\zeta_m)\right] + 1.14\left[(-\zeta)^{1/3} - (-\zeta_m)^{1/3}\right] + \psi_m\left(\frac{z_{0m}}{L}\right)\right\}$$

(5.32)

Unstable $(-1.574 \leq \zeta < 0)$

$$V_a = \frac{u_*}{k}\left\{\left[\ln\frac{z_{atm,m} - d}{z_{0m}} - \psi_m(\zeta)\right] + \psi_m\left(\frac{z_{0m}}{L}\right)\right\}$$

(5.33)

Stable $(0 \leq \zeta \leq 1)$

$$V_a = \frac{u_*}{k} \left\{ \left[\ln \frac{z_{atm,m} - d}{z_{0m}} + 5\zeta \right] - 5\frac{z_{0m}}{L} \right\}$$ (5.34)

Very stable $(\zeta > 1)$

$$V_a = \frac{u_*}{k} \left\{ \left[\ln \frac{L}{z_{0m}} + 5 \right] + \left[5\ln \zeta + \zeta - 1 \right] - 5\frac{z_{0m}}{L} \right\}$$ (5.35)

where

$$\psi_m(\zeta) = 2\ln\left(\frac{1+x}{2} \right) + \ln\left(\frac{1+x^2}{2} \right) - 2\tan^{-1} x + \frac{\pi}{2}$$ (5.36)

and $x = (1 - 16\zeta)^{1/4}$.

The potential temperature profiles are:

Very unstable $(\zeta < -0.465)$

$$\theta_{atm} - \theta_s = \frac{\theta_*}{k} \left\{ \left[\ln \frac{\zeta_h L}{z_{0h}} - \psi_h(\zeta_h) \right] + 0.8 \left[(-\zeta_h)^{-1/3} - (-\zeta)^{-1/3} \right] + \psi_h\left(\frac{z_{0h}}{L} \right) \right\}$$ (5.37)

Unstable $(-0.465 \leq \zeta < 0)$

$$\theta_{atm} - \theta_s = \frac{\theta_*}{k} \left\{ \left[\ln \frac{z_{atm,h} - d}{z_{0h}} - \psi_h(\zeta) \right] + \psi_h\left(\frac{z_{0h}}{L} \right) \right\}$$ (5.38)

Stable $(0 \leq \zeta \leq 1)$

$$\theta_{atm} - \theta_s = \frac{\theta_*}{k} \left\{ \left[\ln \frac{z_{atm,h} - d}{z_{0h}} + 5\zeta \right] - 5\frac{z_{0h}}{L} \right\}$$ (5.39)

Very stable $(\zeta > 1)$

$$\theta_{atm} - \theta_s = \frac{\theta_*}{k} \left\{ \left[\ln \frac{L}{z_{0h}} + 5 \right] + \left[5\ln \zeta + \zeta - 1 \right] - 5\frac{z_{0h}}{L} \right\}.$$ (5.40)

68

The specific humidity profiles are:

Very unstable $(\zeta < -0.465)$

$$q_{atm} - q_s = \frac{q_*}{k}\left\{\left[\ln\frac{\zeta_w L}{z_{0w}} - \psi_w(\zeta_w)\right] + 0.8\left[(-\zeta_w)^{-1/3} - (-\zeta)^{-1/3}\right] + \psi_w\left(\frac{z_{0w}}{L}\right)\right\} \quad (5.41)$$

Unstable $(-0.465 \le \zeta < 0)$

$$q_{atm} - q_s = \frac{q_*}{k}\left\{\left[\ln\frac{z_{atm,w} - d}{z_{0w}} - \psi_w(\zeta)\right] + \psi_w\left(\frac{z_{0w}}{L}\right)\right\} \quad (5.42)$$

Stable $(0 \le \zeta \le 1)$

$$q_{atm} - q_s = \frac{q_*}{k}\left\{\left[\ln\frac{z_{atm,w} - d}{z_{0w}} + 5\zeta\right] - 5\frac{z_{0w}}{L}\right\} \quad (5.43)$$

Very stable $(\zeta > 1)$

$$q_{atm} - q_s = \frac{q_*}{k}\left\{\left[\ln\frac{L}{z_{0w}} + 5\right] + \left[5\ln\zeta + \zeta - 1\right] - 5\frac{z_{0w}}{L}\right\} \quad (5.44)$$

where

$$\psi_h(\zeta) = \psi_w(\zeta) = 2\ln\left(\frac{1 + x^2}{2}\right). \quad (5.45)$$

Using the definitions of u_*, θ_*, and q_*, an iterative solution of these equations can be used to calculate the surface momentum, sensible heat, and water vapor flux using atmospheric and surface values for $|u|$, θ, and q except that L depends on u_*, θ_*, and q_*. However, the bulk Richardson number

$$R_{iB} = \frac{\theta_{v,atm} - \theta_{v,s}}{\overline{\theta_{v,atm}}} \frac{g(z_{atm,m} - d)}{V_a^2} \quad (5.46)$$

69

is related to ζ (Arya 2001) as

$$R_{iB} = \zeta \left[\ln\left(\frac{z_{atm,h} - d}{z_{0h}} \right) - \psi_h(\zeta) \right] \left[\ln\left(\frac{z_{atm,m} - d}{z_{0m}} \right) - \psi_m(\zeta) \right]^{-2}. \tag{5.47}$$

Using $\phi_h = \phi_m^2 = (1 - 16\zeta)^{-1/2}$ for unstable conditions and $\phi_h = \phi_m = 1 + 5\zeta$ for stable conditions to determine $\psi_m(\zeta)$ and $\psi_h(\zeta)$, the inverse relationship $\zeta = f(R_{iB})$ can be solved to obtain a first guess for ζ and thus L from

$$\zeta = \frac{R_{iB} \ln\left(\dfrac{z_{atm,m} - d}{z_{0m}} \right)}{1 - 5\min(R_{iB}, 0.19)} \qquad 0.01 \le \zeta \le 2 \qquad \text{for } R_{iB} \ge 0 \text{ (neutral or stable)}$$

$$\zeta = R_{iB} \ln\left(\frac{z_{atm,m} - d}{z_{0m}} \right) \qquad -100 \le \zeta \le -0.01 \quad \text{for } R_{iB} < 0 \text{ (unstable)} \tag{5.48}$$

Upon iteration (section 5.3.2), the following is used to determine ζ and thus L

$$\zeta = \frac{(z_{atm,m} - d)kg\theta_{v*}}{u_*^2 \overline{\theta_{v,atm}}} \tag{5.49}$$

where

$$0.01 \le \zeta \le 2 \qquad \text{for } \zeta \ge 0 \text{ (neutral or stable)}$$
$$-100 \le \zeta \le -0.01 \quad \text{for } \zeta < 0 \text{ (unstable)} \qquad .$$

The difference in virtual potential air temperature between the reference height and the surface is

$$\theta_{v,atm} - \theta_{v,s} = (\theta_{atm} - \theta_s)(1 + 0.61 q_{atm}) + 0.61\overline{\theta_{atm}}(q_{atm} - q_s). \tag{5.50}$$

The momentum, sensible heat, and water vapor fluxes between the surface and the atmosphere can also be written in the form

$$\tau_x = -\rho_{atm} \frac{(u_{atm} - u_s)}{r_{am}} \tag{5.51}$$

$$\tau_y = -\rho_{atm} \frac{(v_{atm} - v_s)}{r_{am}} \qquad (5.52)$$

$$H = -\rho_{atm} C_p \frac{(\theta_{atm} - \theta_s)}{r_{ah}} \qquad (5.53)$$

$$E = -\rho_{atm} \frac{(q_{atm} - q_s)}{r_{aw}} \qquad (5.54)$$

where the aerodynamic resistances (s m^{-1}) are

$$r_{am} = \frac{V_a}{u_*^2} = \frac{1}{k^2 V_a} \left[\ln\left(\frac{z_{atm,m} - d}{z_{0m}} \right) - \psi_m \left(\frac{z_{atm,m} - d}{L} \right) + \psi_m \left(\frac{z_{0m}}{L} \right) \right]^2 \qquad (5.55)$$

$$r_{ah} = \frac{\theta_{atm} - \theta_s}{\theta_* u_*} = \frac{1}{k^2 V_a} \left[\ln\left(\frac{z_{atm,m} - d}{z_{0m}} \right) - \psi_m \left(\frac{z_{atm,m} - d}{L} \right) + \psi_m \left(\frac{z_{0m}}{L} \right) \right]$$
$$\left[\ln\left(\frac{z_{atm,h} - d}{z_{0h}} \right) - \psi_h \left(\frac{z_{atm,h} - d}{L} \right) + \psi_h \left(\frac{z_{0h}}{L} \right) \right] \qquad (5.56)$$

$$r_{aw} = \frac{q_{atm} - q_s}{q_* u_*} = \frac{1}{k^2 V_a} \left[\ln\left(\frac{z_{atm,m} - d}{z_{0m}} \right) - \psi_m \left(\frac{z_{atm,m} - d}{L} \right) + \psi_m \left(\frac{z_{0m}}{L} \right) \right]$$
$$\left[\ln\left(\frac{z_{atm,w} - d}{z_{0w}} \right) - \psi_w \left(\frac{z_{atm,w} - d}{L} \right) + \psi_w \left(\frac{z_{0w}}{L} \right) \right]. \qquad (5.57)$$

A 2-m height "screen" temperature is useful for comparison with observations

$$T_{2m} = \theta_s + \frac{\theta_*}{k} \left[\ln\left(\frac{2 + z_{0h}}{z_{0h}} \right) - \psi_h \left(\frac{2 + z_{0h}}{L} \right) + \psi_h \left(\frac{z_{0h}}{L} \right) \right] \qquad (5.58)$$

where for convenience, "2-m" is defined as 2 m above the apparent sink for sensible heat ($z_{0h} + d$). Similarly, a 2-m height specific humidity is defined as

$$q_{2m} = q_s + \frac{q_*}{k} \left[\ln\left(\frac{2 + z_{0w}}{z_{0w}} \right) - \psi_w \left(\frac{2 + z_{0w}}{L} \right) + \psi_w \left(\frac{z_{0w}}{L} \right) \right]. \qquad (5.59)$$

Relative humidity is

$$RH_{2m} = \min\left(100, \frac{q_{2m}}{q_{sat}^{T_{2m}}} \times 100\right) \qquad (5.60)$$

where $q_{sat}^{T_{2m}}$ is the saturated specific humidity at the 2-m temperature T_{2m} (section 5.5).

5.2 Sensible and Latent Heat Fluxes for Non-Vegetated Surfaces

Surfaces are considered non-vegetated for the surface flux calculations if leaf plus stem area index $L + S < 0.05$ (section 2.3). By definition, this includes bare soil, wetlands, and glaciers. The solution for lakes is described in section 9. For these surfaces, the surface temperature $\theta_s = T_s$ is also the ground surface temperature T_g (this can be either the soil or snow surface) so that the sensible heat flux H_g (W m^{-2}) is, with reference to Figure 5.1,

$$H_g = -\rho_{atm} C_p \frac{\left(\theta_{atm} - T_g\right)}{r_{ah}} \qquad (5.61)$$

where ρ_{atm} is the density of atmospheric air (kg m^{-3}), C_p is the specific heat capacity of air (J kg^{-1} K^{-1}) (Table 1.4), θ_{atm} is the atmospheric potential temperature (K), and r_{ah} is the aerodynamic resistance to sensible heat transfer (s m^{-1}).

The water vapor flux E_g (kg m^{-2} s^{-1}) is, with reference to Figure 5.2,

$$E_g = -\frac{\beta_{soi} \rho_{atm} \left(q_{atm} - q_g\right)}{r_{aw}} \qquad (5.62)$$

where β_{soi} is an empirical function of soil water (Sakaguchi and Zeng 2009), q_{atm} is the atmospheric specific humidity (kg kg^{-1}), q_g is the specific humidity of the soil surface (kg kg^{-1}), and r_{aw} is the aerodynamic resistance to water vapor transfer (s m^{-1}). The

specific humidity of the soil surface q_g is assumed to be proportional to the saturation specific humidity

$$q_g = \alpha q_{sat}^{T_g} \tag{5.63}$$

where $q_{sat}^{T_g}$ is the saturated specific humidity at the ground surface temperature T_g (section 5.5). The factor α is a weighted combination of values for soil and snow

$$\alpha = \alpha_{soi,1}\left(1 - f_{sno}\right) + \alpha_{sno}f_{sno} \tag{5.64}$$

where f_{sno} is the fraction of ground covered by snow (section 3.2), and $\alpha_{sno} = 1.0$. $\alpha = 1.0$ for wetlands and glaciers. $\alpha_{soi,1}$ refers to the surface soil layer and is a function of the surface soil water matric potential ψ as in Philip (1957)

$$\alpha_{soi,1} = \exp\left(\frac{\psi_1 g}{1 \times 10^3 R_{wv} T_g}\right) \tag{5.65}$$

where R_{wv} is the gas constant for water vapor (J kg^{-1} K^{-1}) (Table 1.4), g is the gravitational acceleration (m s^{-2}) (Table 1.4), and ψ_1 is the soil water matric potential of the top soil layer (mm). The soil water matric potential ψ_1 is

$$\psi_1 = \psi_{sat,1}s_1^{-B_1} \geq -1 \times 10^8 \tag{5.66}$$

where $\psi_{sat,1}$ is the saturated matric potential (mm) (section 7.4.1), B_1 is the Clapp and Hornberger (1978) parameter (section 7.4.1), and s_1 is the wetness of the top soil layer with respect to saturation. The surface wetness s_1 is a function of the liquid water and ice content

$$s_1 = \frac{1}{\Delta z_1 \theta_{sat,1}}\left[\frac{w_{liq,1}}{\rho_{liq}} + \frac{w_{ice,1}}{\rho_{ice}}\right] \qquad 0.01 \leq s_1 \leq 1.0 \tag{5.67}$$

73

where Δz_1 is the thickness of the top soil layer (m), ρ_{liq} and ρ_{ice} are the density of liquid water and ice (kg m^{-3}) (Table 1.4), $w_{liq,1}$ and $w_{ice,1}$ are the mass of liquid water and ice of the top soil layer (kg m^{-2}) (section 7), and $\theta_{sat,1}$ is the saturated volumetric water content (i.e., porosity) of the top soil layer (mm^3 mm^{-3}) (section 7.4.1). If $q_{sat}^{T_g} > q_{atm}$ and $q_{atm} > q_g$, then $q_g = q_{atm}$ and $\dfrac{d q_g}{d T_g} = 0$. This prevents large increases (decreases) in q_g for small increases (decreases) in soil moisture in very dry soils.

The function β_{soi} ranges from 0 to 1 and is intended to represent the molecular diffusion process from the soil pore to the surface within the dry part of the soil (Sakaguchi and Zeng 2009) as

$$\beta_{soi} = \begin{cases} 1 & \theta_1 \geq \theta_{fc,1} \text{ or } q_{atm} - q_g > 0 \\ 0.25\left(1 - f_{sno}\right)\left[1 - \cos\left(\pi\dfrac{\theta_1}{\theta_{fc,1}}\right)\right]^2 + f_{sno} & \theta_1 < \theta_{fc,1} \end{cases}. \tag{5.68}$$

where $\theta_{fc,1}$ is the field capacity of the top soil layer and $0.01 \leq \theta_1/\theta_{fc,1} \leq 1$. The volumetric water content of the top soil layer (mm^3 mm^{-3}) is

$$\theta_1 = \frac{1}{\Delta z_1}\left[\frac{w_{liq,1}}{\rho_{liq}} + \frac{w_{ice,1}}{\rho_{ice}}\right]. \tag{5.69}$$

The volumetric water content at field capacity is derived by assuming a hydraulic conductivity of 0.1 mm day^{-1} and inverting the hydraulic conductivity function (section 7.4.1) as

$$\theta_{fc,1} = \theta_{sat,1}\left[\frac{0.1}{86400 k_{sat,1}}\right]^{\frac{1}{2B_i+3}} \tag{5.70}$$

where $k_{sat,1}$ is the saturated hydraulic conductivity of the top soil layer (mm s^{-1}) (section 7.4.1) and the exponent B_1 is a function of soil texture (section 7.4.1).

The roughness lengths used to calculate r_{am}, r_{ah}, and r_{aw} are $z_{0m} = z_{0m,g}$, $z_{0h} = z_{0h,g}$, and $z_{0w} = z_{0w,g}$. The displacement height $d = 0$. The momentum roughness length is $z_{0m,g} = 0.01$ for soil, glaciers, and wetland, and $z_{0m,g} = 0.0024$ for snow-covered surfaces ($f_{sno} > 0$). In general, z_{0m} is different from z_{0h} because the transfer of momentum is affected by pressure fluctuations in the turbulent waves behind the roughness elements, while for heat and water vapor transfer no such dynamical mechanism exists. Rather, heat and water vapor must be transferred by molecular diffusion across the interfacial sublayer. The following relation from Zilitinkevich (1970) is adopted by Zeng and Dickinson (1998)

$$z_{0h,g} = z_{0w,g} = z_{0m,g} e^{-a\left(u_* z_{0m,g}/\upsilon\right)^{0.45}} \tag{5.71}$$

where the quantity $u_* z_{0m,g}/\upsilon$ is the roughness Reynolds number (and may be interpreted as the Reynolds number of the smallest turbulent eddy in the flow) with the kinematic viscosity of air $\upsilon = 1.5 \times 10^{-5}$ m^2 s^{-1} and $a = 0.13$.

The numerical solution for the fluxes of momentum, sensible heat, and water vapor flux from non-vegetated surfaces proceeds as follows:

1. An initial guess for the wind speed V_a is obtained from eq. (5.24) assuming an initial convective velocity $U_c = 0$ m s^{-1} for stable conditions ($\theta_{v,atm} - \theta_{v,s} \geq 0$ as evaluated from eq. (5.50)) and $U_c = 0.5$ for unstable conditions ($\theta_{v,atm} - \theta_{v,s} < 0$).

2.   An initial guess for the Monin-Obukhov length L is obtained from the bulk Richardson number using eqs. (5.46) and (5.48).

3.   The following system of equations is iterated three times:

- Friction velocity u_* (eqs. (5.32), (5.33), (5.34), (5.35))

- Potential temperature scale θ_* (eqs. (5.37), (5.38), (5.39), (5.40))

- Humidity scale q_* (eqs. (5.41), (5.42), (5.43), (5.44))

- Roughness lengths for sensible $z_{0h,g}$ and latent heat $z_{0w,g}$ (eq. (5.71))

- Virtual potential temperature scale θ_{v*} (eq. (5.17))

- Wind speed including the convective velocity, V_a (eq. (5.24))

- Monin-Obukhov length L (eq. (5.49))

4.   Aerodynamic resistances r_{am}, r_{ah}, and r_{aw} (eqs. (5.55), (5.56), (5.57))

5.   Momentum fluxes τ_x, τ_y (eqs. (5.5), (5.6))

6.   Sensible heat flux H_g (eq. (5.61))

7.   Water vapor flux E_g (eq. (5.62))

8.   2-m height air temperature T_{2m} and specific humidity q_{2m} (eqs. (5.58), (5.59))

The partial derivatives of the soil surface fluxes with respect to ground temperature, which are needed for the soil temperature calculations (section 6.1) and to update the soil surface fluxes (section 5.4), are

$$\frac{\partial H_g}{\partial T_g} = \frac{\rho_{atm} C_p}{r_{ah}} \tag{5.72}$$

$$\frac{\partial E_g}{\partial T_g} = \frac{\beta_{soi} \rho_{atm}}{r_{aw}} \frac{dq_g}{dT_g} \tag{5.73}$$

where

$$\frac{dq_g}{dT_g} = \alpha \frac{dq_{sat}^{T_g}}{dT_g}.$$ (5.74)

The partial derivatives $\frac{\partial r_{ah}}{\partial T_g}$ and $\frac{\partial r_{aw}}{\partial T_g}$, which cannot be determined analytically, are

ignored for $\frac{\partial H_g}{\partial T_g}$ and $\frac{\partial E_g}{\partial T_g}$.

5.3 Sensible and Latent Heat Fluxes and Temperature for Vegetated Surfaces

In the case of a vegetated surface, the sensible heat H and water vapor flux E are

partitioned into vegetation and ground fluxes that depend on vegetation T_v and ground

T_g temperatures in addition to surface temperature T_s and specific humidity q_s. Because

of the coupling between vegetation temperature and fluxes, Newton-Raphson iteration is

used to solve for the vegetation temperature and the sensible heat and water vapor fluxes

from vegetation simultaneously using the ground temperature from the previous time

step. In section 5.3.1, the equations used in the iteration scheme are derived. Details on

the numerical scheme are provided in section 5.3.2.

5.3.1 Theory

The air within the canopy is assumed to have negligible capacity to store heat so

that the sensible heat flux H between the surface at height $z_{0h} + d$ and the atmosphere at

height $z_{atm,h}$ must be balanced by the sum of the sensible heat from the vegetation H_v

and the ground H_g

$$H = H_v + H_g$$ (5.75)

where, with reference to Figure 5.1,

$$H = -\rho_{atm}C_p \frac{\left(\theta_{atm} - T_s\right)}{r_{ah}}$$
(5.76)

$$H_v = -\rho_{atm}C_p \left(T_s - T_v\right)\frac{\left(L + S\right)}{r_b}$$
(5.77)

$$H_g = -\rho_{atm}C_p \frac{\left(T_s - T_g\right)}{r_{ah}{}'}$$
(5.78)

where ρ_{atm} is the density of atmospheric air (kg m^{-3}), C_p is the specific heat capacity of air (J kg^{-1} K^{-1}) (Table 1.4), θ_{atm} is the atmospheric potential temperature (K), and r_{ah} is the aerodynamic resistance to sensible heat transfer (s m^{-1}).

Here, T_s is the surface temperature at height $z_{0h} + d$, also referred to as the canopy air temperature. L and S are the exposed leaf and stem area indices (section 2.3), r_b is the leaf boundary layer resistance (s m^{-1}), and $r_{ah}{}'$ is the aerodynamic resistance (s m^{-1}) to heat transfer between the ground at height $z_{0h}{}'$ and the canopy air at height $z_{0h} + d$.

Figure 5.1. Schematic diagram of sensible heat fluxes for (a) non-vegetated surfaces and (b) vegetated surfaces.

(a)

$z_{atm,h}$ ---- θ_{atm}

r_{ah}

z_{0h} ---- $T_s = T_g$

(b)

$z_{atm,h}$ ---- θ_{atm}

r_{ah}

$z_{0h}+d$ ---- T_s — T_v

$r_b/L+S$

r_{ah}'

z_{0h}' ---- T_g
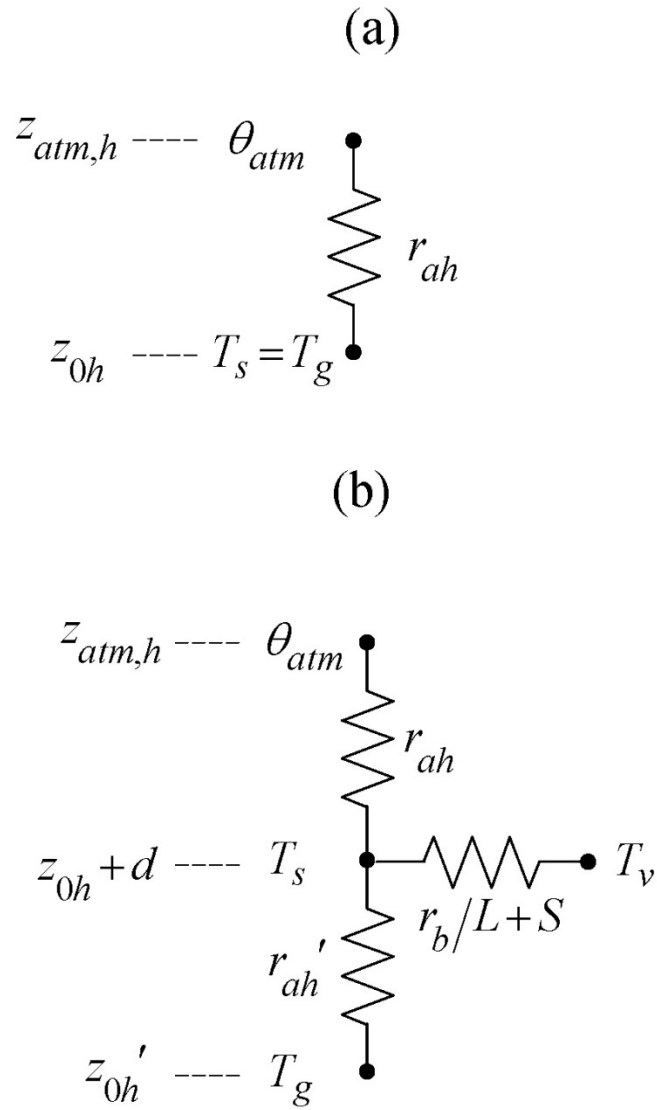
Figure 5.2. Schematic diagram of water vapor fluxes for (a) non-vegetated surfaces and (b) vegetated surfaces.
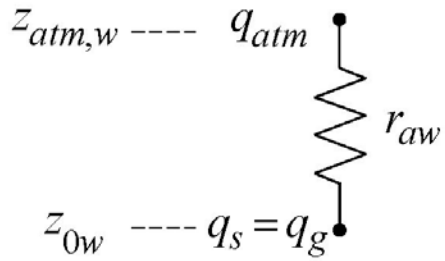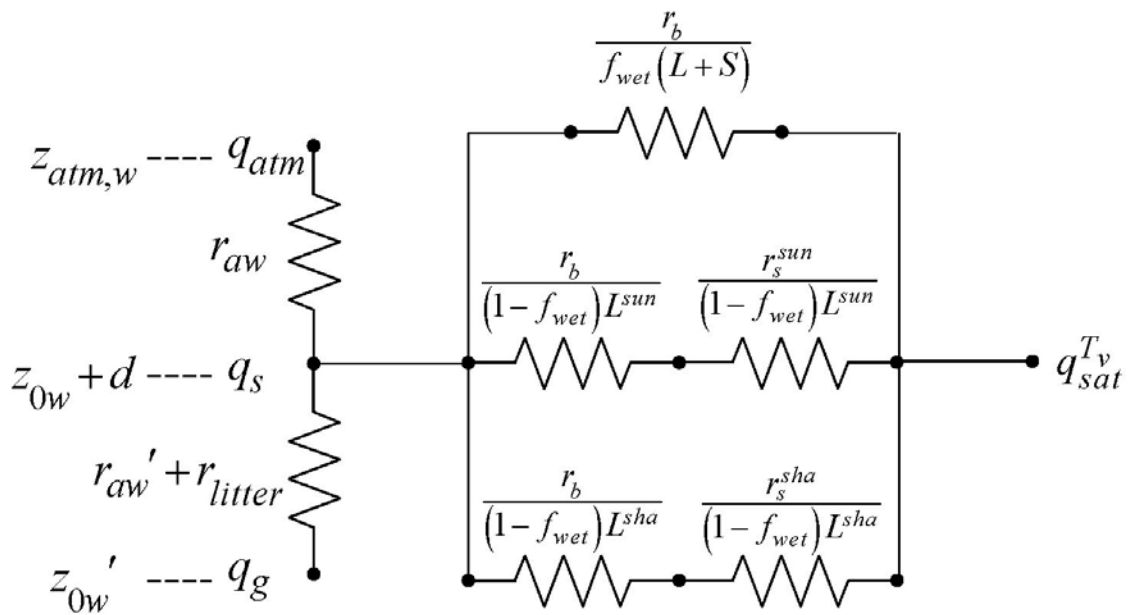
Equations (5.75)-(5.78) can be solved for the canopy air temperature T_s

$$T_s = \frac{c_a^h \theta_{atm} + c_g^h T_g + c_v^h T_v}{c_a^h + c_g^h + c_v^h}$$

(5.79)

where

$$c_a^h = \frac{1}{r_{ah}}$$

(5.80)

$$c_g^h = \frac{1}{r_{ah}'}$$

(5.81)

$$c_v^h = \frac{(L+S)}{r_b}$$

(5.82)

are the sensible heat conductances from the canopy air to the atmosphere, the ground to canopy air, and leaf surface to canopy air, respectively (m s^{-1}).

When the expression for T_s is substituted into equation (5.77), the sensible heat flux from vegetation H_v is a function of θ_{atm}, T_g, and T_v

$$H_v = -\rho_{atm} C_p \left[c_a^h \theta_{atm} + c_g^h T_g - \left(c_a^h + c_g^h \right) T_v \right] \frac{c_v^h}{c_a^h + c_v^h + c_g^h}.$$

(5.83)

Similarly, the expression for T_s can be substituted into equation (5.78) to obtain the sensible heat flux from ground H_g

$$H_g = -\rho_{atm} C_p \left[c_a^h \theta_{atm} + c_v^h T_v - \left(c_a^h + c_v^h \right) T_g \right] \frac{c_g^h}{c_a^h + c_v^h + c_g^h}.$$

(5.84)

The air within the canopy is assumed to have negligible capacity to store water vapor so that the water vapor flux E between the surface at height $z_{0w} + d$ and the

atmosphere at height $z_{atm,w}$ must be balanced by the sum of the water vapor flux from the vegetation E_v and the ground E_g

$$E = E_v + E_g \qquad (5.85)$$

where, with reference to Figure 5.2,

$$E = -\rho_{atm} \frac{\left(q_{atm} - q_s\right)}{r_{aw}} \qquad (5.86)$$

$$E_v = -\rho_{atm} \frac{\left(q_s - q_{sat}^{T_v}\right)}{r_{total}} \qquad (5.87)$$

$$E_g = -\rho_{atm} \frac{\beta_{soi}\left(q_s - q_g\right)}{r_{aw}{}' + r_{litter}} \qquad (5.88)$$

where q_{atm} is the atmospheric specific humidity (kg kg^{-1}), r_{aw} is the aerodynamic resistance to water vapor transfer (s m^{-1}), $q_{sat}^{T_v}$ (kg kg^{-1}) is the saturation water vapor specific humidity at the vegetation temperature (section 5.5), q_g is the specific humidity at the ground surface (section 5.2), $r_{aw}{}'$ is the aerodynamic resistance (s m^{-1}) to water vapor transfer between the ground at height $z_{0w}{}'$ and the canopy air at height $z_{0w} + d$, β_{soi} is an empirical function of soil water (section 5.2), and r_{litter} is a resistance for the plant litter layer (s m^{-1}). r_{total} is the total resistance to water vapor transfer from the canopy to the canopy air and includes contributions from leaf boundary layer and sunlit and shaded stomatal resistances r_b, r_s^{sun}, and r_s^{sha} (Figure 5.2). The water vapor flux from vegetation is the sum of water vapor flux from wetted leaf and stem area E_v^w

(evaporation of water intercepted by the canopy) and transpiration from dry leaf surfaces
E_v^t

$$E_v = E_v^w + E_v^t.$$ (5.89)

Equations (5.85)-(5.88) can be solved for the canopy specific humidity q_s

$$q_s = \frac{c_a^w q_{atm} + c_g^w q_g + c_v^w q_{sat}^{T_v}}{c_a^w + c_v^w + c_g^w}$$ (5.90)

where

$$c_a^w = \frac{1}{r_{aw}}$$ (5.91)

$$c_v^w = \frac{(L+S)}{r_b} r''$$ (5.92)

$$c_g^w = \frac{\beta_{soi}}{r_{aw}{}' + r_{litter}}$$ (5.93)

are the water vapor conductances from the canopy air to the atmosphere, the leaf to canopy air, and ground to canopy air, respectively. The term r'' is determined from contributions by wet leaves and transpiration and limited by available water and potential evaporation as

83

$$r'' = \begin{cases} \min\left(f_{wet} + r_{dry}'', \dfrac{E_v^{w,pot} r_{dry}'' + \dfrac{W_{can}}{\Delta t}}{E_v^{w,pot}} \right) & E_v^{w,pot} > 0, \beta_t > 0 \\[4ex] \min\left(f_{wet}, \dfrac{E_v^{w,pot} r_{dry}'' + \dfrac{W_{can}}{\Delta t}}{E_v^{w,pot}} \right) & E_v^{w,pot} > 0, \beta_t \leq 0 \\[4ex] 1 & E_v^{w,pot} \leq 0 \end{cases} \qquad (5.94)$$

where f_{wet} is the fraction of leaves and stems that are wet (section 7.1), W_{can} is canopy

water (kg m^{-2}) (section 7.1), Δt is the time step (s), and β_t is a soil moisture function

limiting transpiration (section 8). The potential evaporation from wet foliage per unit

wetted area is

$$E_v^{w,pot} = -\frac{\rho_{atm}\left(q_s - q_{sat}^{T_v}\right)}{r_b}. \qquad (5.95)$$

The term r_{dry}'' is

$$r_{dry}'' = \frac{f_{dry} r_b}{L}\left(\frac{L^{sun}}{r_b + r_s^{sun}} + \frac{L^{sha}}{r_b + r_s^{sha}} \right) \qquad (5.96)$$

where f_{dry} is the fraction of leaves that are dry (section 7.1), L^{sun} and L^{sha} are the sunlit

and shaded leaf area indices (section 4.1), and r_s^{sun} and r_s^{sha} are the sunlit and shaded

stomatal resistances (s m^{-1}) (section 8).

When the expression for q_s is substituted into equation (5.87), the water vapor flux

from vegetation E_v is a function of q_{atm}, q_g, and $q_{sat}^{T_v}$

$$E_v = -\rho_{atm} \left[c_a^w q_{atm} + c_g^w q_g - \left(c_a^w + c_g^w \right) q_{sat}^{T_v} \right] \frac{c_v^w}{c_a^w + c_v^w + c_g^w}. \tag{5.97}$$

Similarly, the expression for q_s can be substituted into equation (5.88) to obtain the water vapor flux from the ground beneath the canopy E_g

$$E_g = -\rho_{atm} \left[c_a^w q_{atm} + c_v^w q_{sat}^{T_v} - \left(c_a^w + c_v^w \right) q_g \right] \frac{c_g^w}{c_a^w + c_v^w + c_g^w}. \tag{5.98}$$

The aerodynamic resistances to heat (moisture) transfer between the ground at height $z_{0h}{}'$ ($z_{0w}{}'$) and the canopy air at height $z_{0h} + d$ ($z_{0w} + d$) are

$$r_{ah}{}' = r_{aw}{}' = \frac{1}{C_s U_{av}} \tag{5.99}$$

where

$$U_{av} = V_a \sqrt{\frac{1}{r_{am} V_a}} = u_* \tag{5.100}$$

is the magnitude of the wind velocity incident on the leaves (equivalent here to friction velocity) (m s^{-1}) and C_s is the turbulent transfer coefficient between the underlying soil and the canopy air. C_s is obtained by interpolation between values for dense canopy and bare soil (Zeng et al. 2005)

$$C_s = C_{s,bare} W + C_{s,dense} (1 - W) \tag{5.101}$$

where the weight W is

$$W = e^{-(L+S)}. \tag{5.102}$$

The dense canopy turbulent transfer coefficient in Zeng et al. (2005) is modified from its original value of 0.004 (Dickinson et al. 1993) by Sakaguchi and Zeng (2009) to account for stability as

$$C_{s,dense} = \begin{cases} 0.004 & T_s - T_g \leq 0 \\ \dfrac{0.004}{1 + \gamma \min(S, 10)} & T_s - T_g > 0 \end{cases} \qquad (5.103)$$

where $\gamma = 0.5$ and S is a stability parameter determined from

$$S = \frac{g z_{top} (T_s - T_g)}{T_s u_*^2} \qquad (5.104)$$

where g is the gravitational acceleration (m s^{-2}) (Table 1.4), and z_{top} is canopy top height (m) (Table 2.2). The bare soil turbulent transfer coefficient is

$$C_{s,bare} = \frac{k}{a} \left(\frac{z_{0m,g} U_{av}}{\upsilon} \right)^{-0.45} \qquad (5.105)$$

where the kinematic viscosity of air $\upsilon = 1.5 \times 10^{-5}$ m^2 s^{-1} and $a = 0.13$.

The litter resistance r_{litter} (Sakaguchi and Zeng 2009) (s m^{-1}) is

$$r_{litter} = \frac{1}{0.004 u_*} \left(1 - e^{-L_{litter}^{eff}} \right) \qquad (5.106)$$

where the effective litter area index L_{litter}^{eff} (m^2 m^{-2}) is the fraction of plant litter area index L_{litter} (currently set to 0.5 m^2 m^{-2}) that is not covered by snow

$$L_{litter}^{eff} = L_{litter} \left[1 - \min\left(f_{litter}^{snow}, 1 \right) \right]. \qquad (5.107)$$

The effective snow cover of the litter layer is

$$f_{litter}^{snow} = \frac{z_{sno}}{\Delta z_{litter}} \qquad (5.108)$$

where $\Delta z_{litter} = 0.05$ m is assumed as a typical depth for the litter layer, and z_{sno} is the depth of snow (section 7.2) (m).

The leaf boundary layer resistance r_b is

$$r_b = \frac{1}{C_v}\left(U_{av}/d_{leaf}\right)^{-1/2} \tag{5.109}$$

where $C_v = 0.01$ m s$^{-1/2}$ is the turbulent transfer coefficient between the canopy surface and canopy air, and d_{leaf} is the characteristic dimension of the leaves in the direction of wind flow (Table 5.1).

The partial derivatives of the fluxes from the soil beneath the canopy with respect to ground temperature, which are needed for the soil temperature calculations (section 6.1) and to update the soil surface fluxes (section 5.4), are

$$\frac{\partial H_g}{\partial T_g} = \frac{\rho_{atm} C_p}{r'_{ah}} \frac{c_a^h + c_v^h}{c_a^h + c_v^h + c_g^h} \tag{5.110}$$

$$\frac{\partial E_g}{\partial T_g} = \frac{\beta_{soi} \rho_{atm}}{r'_{aw} + r_{litter}} \frac{c_a^w + c_v^w}{c_a^w + c_v^w + c_g^w} \frac{dq_g}{dT_g}. \tag{5.111}$$

The partial derivatives $\dfrac{\partial r'_{ah}}{\partial T_g}$ and $\dfrac{\partial r'_{aw}}{\partial T_g}$, which cannot be determined analytically, are

ignored for $\dfrac{\partial H_g}{\partial T_g}$ and $\dfrac{\partial E_g}{\partial T_g}$.

The roughness lengths used to calculate r_{am}, r_{ah}, and r_{aw} from equations (5.55), (5.56), and (5.57) are $z_{0m} = z_{0m,v}$, $z_{0h} = z_{0h,v}$, and $z_{0w} = z_{0w,v}$. The vegetation displacement height d and the roughness lengths are a function of plant height and adjusted for canopy density following Zeng and Wang (2007)

$$z_{0m,v} = z_{0h,v} = z_{0w,v} = \exp\left[V \ln\left(z_{top} R_{z0m}\right) + \left(1 - V\right)\ln\left(z_{0m,g}\right)\right] \tag{5.112}$$

$$d = z_{top} R_d V \tag{5.113}$$

where z_{top} is canopy top height (m) (Table 2.2), R_{z0m} and R_d are the ratio of momentum roughness length and displacement height to canopy top height, respectively (Table 5.1), and $z_{0m,g}$ is the ground momentum roughness length (m) (section 5.2). The fractional weight V is determined from

$$V = \frac{1 - \exp\left\{-\beta \min\left[L + S, (L+S)_{cr}\right]\right\}}{1 - \exp\left[-\beta (L+S)_{cr}\right]} \tag{5.114}$$

where $\beta = 1$ and $(L+S)_{cr} = 2$ (m^2 m^{-2}) is a critical value of exposed leaf plus stem area for which z_{0m} reaches its maximum.

Table 5.1. Plant functional type aerodynamic parameters

Plant functional type	R_{z0m}	R_d	d_{leaf} (m)
NET Temperate	0.055	0.67	0.04
NET Boreal	0.055	0.67	0.04
NDT Boreal	0.055	0.67	0.04
BET Tropical	0.075	0.67	0.04
BET temperate	0.075	0.67	0.04
BDT tropical	0.055	0.67	0.04
BDT temperate	0.055	0.67	0.04
BDT boreal	0.055	0.67	0.04
BES temperate	0.120	0.68	0.04
BDS temperate	0.120	0.68	0.04
BDS boreal	0.120	0.68	0.04
C_3 arctic grass	0.120	0.68	0.04
C_3 grass	0.120	0.68	0.04
C_4 grass	0.120	0.68	0.04
Crop1	0.120	0.68	0.04
Crop2	0.120	0.68	0.04

5.3.2 Numerical Implementation

Canopy energy conservation gives

$$-\vec{S}_v + \vec{L}_v\left(T_v\right) + H_v\left(T_v\right) + \lambda E_v\left(T_v\right) = 0 \qquad (5.115)$$

where $\vec{S}_v$ is the solar radiation absorbed by the vegetation (section 4.1), $\vec{L}_v$ is the net longwave radiation absorbed by vegetation (section 4.2), and H_v and λE_v are the sensible and latent heat fluxes from vegetation, respectively. The term λ is taken to be the latent heat of vaporization λ_{vap} (Table 1.4).

$\bar{L}_v$, H_v, and λE_v depend on the vegetation temperature T_v. The Newton-Raphson method for finding roots of non-linear systems of equations can be applied to iteratively solve for T_v as

$$\Delta T_v = \frac{\vec{S}_v - \bar{L}_v - H_v - \lambda E_v}{\dfrac{\partial \bar{L}_v}{\partial T_v} + \dfrac{\partial H_v}{\partial T_v} + \dfrac{\partial \lambda E_v}{\partial T_v}} \tag{5.116}$$

where $\Delta T_v = T_v^{n+1} - T_v^{n}$ and the subscript "n" indicates the iteration.

The partial derivatives are

$$\frac{\partial \bar{L}_v}{\partial T_v} = 4\varepsilon_v \sigma \left[2 - \varepsilon_v \left(1 - \varepsilon_g \right) \right] T_v^3 \tag{5.117}$$

$$\frac{\partial H_v}{\partial T_v} = \rho_{atm} C_p \left(c_a^h + c_g^h \right) \frac{c_v^h}{c_a^h + c_v^h + c_g^h} \tag{5.118}$$

$$\frac{\partial \lambda E_v}{\partial T_v} = \lambda \rho_{atm} \left(c_a^w + c_g^w \right) \frac{c_v^w}{c_a^w + c_v^w + c_g^w} \frac{dq_{sat}^{T_v}}{dT_v}. \tag{5.119}$$

The partial derivatives $\dfrac{\partial r_{ah}}{\partial T_v}$ and $\dfrac{\partial r_{aw}}{\partial T_v}$, which cannot be determined analytically, are

ignored for $\dfrac{\partial H_v}{\partial T_v}$ and $\dfrac{\partial \lambda E_v}{\partial T_v}$. However, if ζ changes sign more than four times during

the temperature iteration, $\zeta = -0.01$. This helps prevent "flip-flopping" between stable

and unstable conditions. The total water vapor flux E_v, transpiration flux E_v^t, and

sensible heat flux H_v are updated for changes in leaf temperature as

$$E_v = -\rho_{atm} \left[c_a^w q_{atm} + c_g^w q_g - \left(c_a^w + c_g^w \right) \left(q_{sat}^{T_v} + \frac{dq_{sat}^{T_v}}{dT_v} \Delta T_v \right) \right] \frac{c_v^w}{c_a^w + c_v^w + c_g^w} \tag{5.120}$$

$$E_v^t = -r_{dry}''\,\rho_{atm}\left[c_a^w q_{atm} + c_g^w q_g - \left(c_a^w + c_g^w\right)\left(q_{sat}^{T_v} + \frac{dq_{sat}^{T_v}}{dT_v}\Delta T_v\right)\right]\frac{c_v^h}{c_a^w + c_v^w + c_g^w} \qquad (5.121)$$

$$H_v = -\rho_{atm}C_p\left[c_a^h\theta_{atm} + c_g^h T_g - \left(c_a^h + c_g^h\right)\left(T_v + \Delta T_v\right)\right]\frac{c_v^h}{c_a^h + c_v^h + c_g^h}. \qquad (5.122)$$

The numerical solution for vegetation temperature and the fluxes of momentum, sensible heat, and water vapor flux from vegetated surfaces proceeds as follows:

1. Initial values for canopy air temperature and specific humidity are obtained from

$$T_s = \frac{T_g + \theta_{atm}}{2} \qquad (5.123)$$

$$q_s = \frac{q_g + q_{atm}}{2}. \qquad (5.124)$$

2. An initial guess for the wind speed V_a is obtained from eq. (5.24) assuming an initial convective velocity $U_c = 0$ m s^{-1} for stable conditions ($\theta_{v,atm} - \theta_{v,s} \geq 0$ as evaluated from eq. (5.50)) and $U_c = 0.5$ for unstable conditions ($\theta_{v,atm} - \theta_{v,s} < 0$).

3. An initial guess for the Monin-Obukhov length L is obtained from the bulk Richardson number using equation (5.46) and (5.48).

4. Iteration proceeds on the following system of equations:

   - Friction velocity u_* (eqs. (5.32), (5.33), (5.34), (5.35))

   - Ratio $\dfrac{\theta_*}{\theta_{atm} - \theta_s}$ (eqs. (5.37), (5.38), (5.39), (5.40))

   - Ratio $\dfrac{q_*}{q_{atm} - q_s}$ (eqs. (5.41), (5.42), (5.43), (5.44))

   - Aerodynamic resistances r_{am}, r_{ah}, and r_{aw} (eqs. (5.55), (5.56), (5.57))

   - Magnitude of the wind velocity incident on the leaves U_{av} (eq. (5.100))

- Leaf boundary layer resistance r_b (eq. (5.109))

- Aerodynamic resistances $r_{ah}{}'$ and $r_{aw}{}'$ (eq. (5.99))

- Sunlit and shaded stomatal resistances r_s^{sun} and r_s^{sha} (section 8)

- Sensible heat conductances c_a^h, c_g^h, and c_v^h (eqs. (5.80), (5.81), (5.82))

- Latent heat conductances c_a^w, c_v^w, and c_g^w (eqs. (5.91), (5.92), (5.93))

- Sensible heat flux from vegetation H_v (eq. (5.83))

- Latent heat flux from vegetation λE_v (eq. (5.97))

- If the latent heat flux has changed sign from the latent heat flux computed at the previous iteration ($\lambda E_v^{n+1} \times \lambda E_v^{n} < 0$), the latent heat flux is constrained to be 10% of the computed value. The difference between the constrained and computed value ($\Delta_1 = 0.1\lambda E_v^{n+1} - \lambda E_v^{n+1}$) is added to the sensible heat flux later.

- Change in vegetation temperature ΔT_v (eq. (5.116)) and update the vegetation temperature as $T_v^{n+1} = T_v^n + \Delta T_v$. T_v is constrained to change by no more than 1°K in one iteration. If this limit is exceeded, the energy error is

$$\Delta_2 = \vec{S}_v - \vec{L}_v - \frac{\partial \vec{L}_v}{\partial T_v} \Delta T_v - H_v - \frac{\partial H_v}{\partial T_v} \Delta T_v - \lambda E_v - \frac{\partial \lambda E_v}{\partial T_v} \Delta T_v \qquad (5.125)$$

where $\Delta T_v = 1$ or -1. The error Δ_2 is added to the sensible heat flux later.

- Water vapor flux E_v (eq. (5.120))

- Transpiration E_v^t (eq. (5.121) if $\beta_t > 0$, otherwise $E_v^t = 0$)

- The water vapor flux E_v is constrained to be less than or equal to the sum of transpiration E_v^t and the water available from wetted leaves and stems $W_{can}/\Delta t$. The energy error due to this constraint is

$$\Delta_3 = \max\left(0, E_v - E_v^t - \frac{W_{can}}{\Delta t}\right). \tag{5.126}$$

The error $\lambda\Delta_3$ is added to the sensible heat flux later.

- Sensible heat flux H_v (eq. (5.122)). The three energy error terms, Δ_1, Δ_2, and $\lambda\Delta_3$ are also added to the sensible heat flux.

- The saturated vapor pressure e_i (section 8), saturated specific humidity $q_{sat}^{T_v}$ and its derivative $\dfrac{dq_{sat}^{T_v}}{dT_v}$ at the leaf surface (section 5.5), are re-evaluated based on the new T_v.

- Canopy air temperature T_s (eq. (5.79))

- Canopy air specific humidity q_s (eq. (5.90))

- Temperature difference $\theta_{atm} - \theta_s$

- Specific humidity difference $q_{atm} - q_s$

- Potential temperature scale $\theta_* = \dfrac{\theta_*}{\theta_{atm} - \theta_s}(\theta_{atm} - \theta_s)$ where $\dfrac{\theta_*}{\theta_{atm} - \theta_s}$ was calculated earlier in the iteration

- Humidity scale $q_* = \dfrac{q_*}{q_{atm} - q_s}(q_{atm} - q_s)$ where $\dfrac{q_*}{q_{atm} - q_s}$ was calculated earlier in the iteration

93

- Virtual potential temperature scale θ_{v*} (eq. (5.17))

- Wind speed including the convective velocity, V_a (eq. (5.24))

- Monin-Obukhov length L (eq. (5.49))

- The iteration is stopped after two or more steps if $\tilde{\Delta} T_v < 0.01$ and $\left| \lambda E_v^{n+1} - \lambda E_v^n \right| < 0.1$ where $\tilde{\Delta} T_v = \max \left(\left| T_v^{n+1} - T_v^n \right|, \left| T_v^n - T_v^{n-1} \right| \right)$, or after forty iterations have been carried out.

5. Momentum fluxes τ_x, τ_y (eqs. (5.5), (5.6))

6. Sensible heat flux from ground H_g (eq. (5.84))

7. Water vapor flux from ground E_g (eq. (5.98))

8. 2-m height air temperature T_{2m}, specific humidity q_{2m}, relative humidity RH_{2m} (eqs. (5.58), (5.59), (5.60))

5.4   Update of Ground Sensible and Latent Heat Fluxes

The sensible and water vapor heat fluxes derived above for bare soil and soil beneath canopy are based on the ground surface temperature from the previous time step T_g^n and are used as the surface forcing for the solution of the soil temperature equations (section 6.1). This solution yields a new ground surface temperature T_g^{n+1}. The ground sensible and water vapor fluxes are then updated for T_g^{n+1} as

$$H_g' = H_g + \left(T_g^{n+1} - T_g^n \right) \frac{\partial H_g}{\partial T_g}$$

(5.127)

$$E_g' = E_g + \left(T_g^{n+1} - T_g^n \right) \frac{\partial E_g}{\partial T_g}$$

(5.128)

where H_g and E_g are the sensible heat and water vapor fluxes derived from equations (5.72) and (5.73) for non-vegetated surfaces and equations (5.110) and (5.111) for vegetated surfaces using T_g^n. One further adjustment is made to H_g' and E_g'. If the soil moisture in the top snow/soil layer is not sufficient to support the updated ground evaporation, i.e., if $E_g' > 0$ and $f_{evap} < 1$ where

$$f_{evap} = \frac{\left(w_{ice,snl+1} + w_{liq,snl+1}\right)/\Delta t}{\sum_{j=1}^{npft}\left(E_g'\right)_j (wt)_j} \leq 1, \tag{5.129}$$

an adjustment is made to reduce the ground evaporation accordingly as

$$E_g'' = f_{evap} E_g'. \tag{5.130}$$

The term $\sum_{j=1}^{npft}\left(E_g'\right)_j (wt)_j$ is the sum of E_g' over all evaporating PFTs where $\left(E_g'\right)_j$ is the ground evaporation from the jth PFT on the column, $(wt)_j$ is the relative area of the jth PFT with respect to the column, and $npft$ is the number of PFTs on the column. $w_{ice,snl+1}$ and $w_{liq,snl+1}$ are the ice and liquid water contents (kg m^{-2}) of the top snow/soil layer (section 7). Any resulting energy deficit is assigned to sensible heat as

$$H_g'' = H_g + \lambda\left(E_g' - E_g''\right). \tag{5.131}$$

The ground water vapor flux E_g'' is partitioned into evaporation of liquid water from snow/soil q_{seva} (kg m^{-2} s^{-1}), sublimation from snow/soil ice q_{subl} (kg m^{-2} s^{-1}), liquid dew on snow/soil q_{sdew} (kg m^{-2} s^{-1}), or frost on snow/soil q_{frost} (kg m^{-2} s^{-1}) as

$$q_{seva} = \max\left(E_g'' \frac{w_{liq,snl+1}}{w_{ice,snl+1} + w_{liq,snl+1}}, 0\right) \qquad E_g'' \geq 0, w_{ice,snl+1} + w_{liq,snl+1} > 0 \tag{5.132}$$

$$q_{subl} = E_g'' - q_{seva} \qquad E_g'' \geq 0 \tag{5.133}$$

$$q_{sdew} = \left| E_g'' \right| \qquad E_g'' < 0 \text{ and } T_g \geq T_f \tag{5.134}$$

$$q_{frost} = \left| E_g'' \right| \qquad E_g'' < 0 \text{ and } T_g < T_f. \tag{5.135}$$

The loss or gain in snow mass due to q_{seva}, q_{subl}, q_{sdew}, and q_{frost} on a snow surface are accounted for during the snow hydrology calculations (section 7.2). The loss of soil surface water due to q_{seva} is accounted for in the calculation of infiltration (section 7.3), while losses or gains due to q_{subl}, q_{sdew}, and q_{frost} on a soil surface are accounted for following the sub-surface drainage calculations (section 7.5).

The ground heat flux G is calculated as

$$G = \vec{S}_g - \vec{L}_g - H_g - \lambda E_g \tag{5.136}$$

where $\vec{S}_g$ is the solar radiation absorbed by the ground (section 4.1), $\vec{L}_g$ is the net longwave radiation absorbed by the ground (section 4.2)

$$\vec{L}_g = \varepsilon_g \sigma \left(T_g^n \right)^4 - \delta_{veg} \varepsilon_g L_v \downarrow - \left(1 - \delta_{veg} \right) \varepsilon_g L_{atm} \downarrow + 4 \varepsilon_g \sigma \left(T_g^n \right)^3 \left(T_g^{n+1} - T_g^n \right), \tag{5.137}$$

and H_g and λE_g are the sensible and latent heat fluxes after the adjustments described above.

When converting ground water vapor flux to an energy flux, the term λ is arbitrarily assumed to be

$$\lambda = \begin{cases} \lambda_{sub} & \text{if } w_{liq,snl+1} = 0 \text{ and } w_{ice,snl+1} > 0 \\ \lambda_{vap} & \text{otherwise} \end{cases} \tag{5.138}$$

where λ_{sub} and λ_{vap} are the latent heat of sublimation and vaporization, respectively (J kg^{-1}) (Table 1.4). When converting vegetation water vapor flux to an energy flux, λ_{vap} is used.

The system balances energy as

$$\vec{S}_g + \vec{S}_v + L_{atm}\downarrow - L\uparrow - H_v - H_g - \lambda_{vap}E_v - \lambda E_g - G = 0. \tag{5.139}$$

5.5 Saturation Vapor Pressure

Saturation vapor pressure e_{sat}^T (Pa) and its derivative $\dfrac{de_{sat}^T}{dT}$, as a function of temperature T (ºC), are calculated from the eighth-order polynomial fits of Flatau et al. (1992)

$$e_{sat}^T = 100\left[a_0 + a_1 T + \cdots + a_n T^n\right] \tag{5.140}$$

$$\frac{de_{sat}^T}{dT} = 100\left[b_0 + b_1 T + \cdots + b_n T^n\right] \tag{5.141}$$

where the coefficients for ice are valid for $-75\,°\mathrm{C} \le T < 0\,°\mathrm{C}$ and the coefficients for water are valid for $0\,°\mathrm{C} \le T \le 100\,°\mathrm{C}$ (Table 5.2 and 5.3). The saturated water vapor specific humidity q_{sat}^T and its derivative $\dfrac{dq_{sat}^T}{dT}$ are

$$q_{sat}^T = \frac{0.622 e_{sat}^T}{P_{atm} - 0.378 e_{sat}^T} \tag{5.142}$$

$$\frac{dq_{sat}^T}{dT} = \frac{0.622 P_{atm}}{\left(P_{atm} - 0.378 e_{sat}^T\right)^2}\frac{de_{sat}^T}{dT}. \tag{5.143}$$

Table 5.2. Coefficients for e_{sat}^T

	water	ice
a_0	6.11213476	6.11123516
a_1	$4.44007856 \times 10^{-1}$	$5.03109514 \times 10^{-1}$
a_2	$1.43064234 \times 10^{-2}$	$1.88369801 \times 10^{-2}$
a_3	$2.64461437 \times 10^{-4}$	$4.20547422 \times 10^{-4}$
a_4	$3.05903558 \times 10^{-6}$	$6.14396778 \times 10^{-6}$
a_5	$1.96237241 \times 10^{-8}$	$6.02780717 \times 10^{-8}$
a_6	$8.92344772 \times 10^{-11}$	$3.87940929 \times 10^{-10}$
a_7	$-3.73208410 \times 10^{-13}$	$1.49436277 \times 10^{-12}$
a_8	$2.09339997 \times 10^{-16}$	$2.62655803 \times 10^{-15}$

Table 5.3. Coefficients for $\dfrac{de_{sat}^T}{dT}$

	water	ice
b_0	$4.44017302 \times 10^{-1}$	$5.03277922 \times 10^{-1}$
b_1	$2.86064092 \times 10^{-2}$	$3.77289173 \times 10^{-2}$
b_2	$7.94683137 \times 10^{-4}$	$1.26801703 \times 10^{-3}$
b_3	$1.21211669 \times 10^{-5}$	$2.49468427 \times 10^{-5}$
b_4	$1.03354611 \times 10^{-7}$	$3.13703411 \times 10^{-7}$
b_5	$4.04125005 \times 10^{-10}$	$2.57180651 \times 10^{-9}$
b_6	$-7.88037859 \times 10^{-13}$	$1.33268878 \times 10^{-11}$
b_7	$-1.14596802 \times 10^{-14}$	$3.94116744 \times 10^{-14}$
b_8	$3.81294516 \times 10^{-17}$	$4.98070196 \times 10^{-17}$

6. Soil and Snow Temperatures

The first law of heat conduction is

$$F = -\lambda \nabla T \qquad (6.1)$$

where F is the amount of heat conducted across a unit cross-sectional area in unit time (W m^{-2}), λ is thermal conductivity (W m^{-1} K^{-1}), and ∇T is the spatial gradient of temperature (K m^{-1}). In one-dimensional form

$$F_z = -\lambda \frac{\partial T}{\partial z} \qquad (6.2)$$

where z is in the vertical direction (m) and is positive downward and F_z is positive upward. To account for non-steady or transient conditions, the principle of energy conservation in the form of the continuity equation is invoked as

$$c \frac{\partial T}{\partial t} = -\frac{\partial F_z}{\partial z} \qquad (6.3)$$

where c is the volumetric snow/soil heat capacity (J m^{-3} K^{-1}) and t is time (s). Combining equations (6.2) and (6.3) yields the second law of heat conduction in one-dimensional form

$$c \frac{\partial T}{\partial t} = \frac{\partial}{\partial z} \left[\lambda \frac{\partial T}{\partial z} \right]. \qquad (6.4)$$

This equation is solved numerically to calculate the soil and snow temperatures for a fifteen-layer soil column with up to five overlying layers of snow with the boundary conditions of h as the heat flux into the surface snow/soil layer from the overlying atmosphere and zero heat flux at the bottom of the soil column. The temperature profile is calculated first without phase change and then readjusted for phase change (section 6.2).

6.1 Numerical Solution

The soil column is discretized into fifteen layers where the depth of soil layer i, or node depth, z_i (m), is

$$z_i = f_s \left\{ \exp\left[0.5(i - 0.5) \right] - 1 \right\} \tag{6.5}$$

where $f_s = 0.025$ is a scaling factor. The thickness of each layer Δz_i (m) is

$$\Delta z_i = \begin{cases} 0.5(z_1 + z_2) & i = 1 \\ 0.5(z_{i+1} - z_{i-1}) & i = 2, 3, \ldots, N_{levgrnd} - 1 \\ z_N - z_{N-1} & i = N_{levgrnd} \end{cases} \tag{6.6}$$

where $N_{levgrnd} = 15$ is the number of soil layers. The depths at the layer interfaces $z_{h,i}$ (m) are

$$z_{h,i} = \begin{cases} 0.5(z_i + z_{i+1}) & i = 1, 2, \ldots, N_{levgrnd} - 1 \\ z_{N_{levgrnd}} + 0.5\Delta z_{N_{levgrnd}} & i = N_{levgrnd} \end{cases}. \tag{6.7}$$

The exponential form of equation (6.5) is to obtain more soil layers near the soil surface where the soil water gradient is generally strong (section 7.4).

The overlying snow pack is modeled with up to five layers depending on the total snow depth. The layers from top to bottom are indexed in the Fortran code as $i = -4, -3, -2, -1, 0$, which permits the accumulation or ablation of snow at the top of the snow pack without renumbering the layers. Layer $i = 0$ is the snow layer next to the soil surface and layer $i = snl + 1$ is the top layer, where the variable snl is the negative of the number of snow layers. The number of snow layers and the thickness of each layer is a function of snow depth z_{sno} (m) as follows.

100

$$
\left.\begin{cases} snl = -1 \\ \Delta z_0 = z_{sno} \end{cases} \qquad \text{for } 0.01 \le z_{sno} \le 0.03 \right\},
$$

$$
\left.\begin{cases} snl = -2 \\ \Delta z_{-1} = z_{sno}/2 \qquad \text{for } 0.03 < z_{sno} \le 0.04 \\ \Delta z_0 = \Delta z_{-1} \end{cases} \right\},
$$

$$
\left.\begin{cases} snl = -2 \\ \Delta z_{-1} = 0.02 \qquad \text{for } 0.04 < z_{sno} \le 0.07 \\ \Delta z_0 = z_{sno} - \Delta z_{-1} \end{cases} \right\},
$$

$$
\left.\begin{cases} snl = -3 \\ \Delta z_{-2} = 0.02 \\ \Delta z_{-1} = \left(z_{sno} - 0.02 \right)/2 \qquad \text{for } 0.07 < z_{sno} \le 0.12 \\ \Delta z_0 = \Delta z_{-1} \end{cases} \right\},
$$

$$
\left.\begin{cases} snl = -3 \\ \Delta z_{-2} = 0.02 \\ \Delta z_{-1} = 0.05 \qquad \text{for } 0.12 < z_{sno} \le 0.18 \\ \Delta z_0 = z_{sno} - \Delta z_{-2} - \Delta z_{-1} \end{cases} \right\},
$$

$$
\left.\begin{cases} snl = -4 \\ \Delta z_{-3} = 0.02 \\ \Delta z_{-2} = 0.05 \qquad \text{for } 0.18 < z_{sno} \le 0.29 \\ \Delta z_{-1} = \left(z_{sno} - \Delta z_{-3} - \Delta z_{-2} \right)/2 \\ \Delta z_0 = \Delta z_{-1} \end{cases} \right\},
$$

$$
\left.\begin{cases} snl = -4 \\ \Delta z_{-3} = 0.02 \\ \Delta z_{-2} = 0.05 \qquad \text{for } 0.29 < z_{sno} \le 0.41 \\ \Delta z_{-1} = 0.11 \\ \Delta z_0 = z_{sno} - \Delta z_{-3} - \Delta z_{-2} - \Delta z_{-1} \end{cases} \right\},
$$

$$\begin{cases} snl = -5 \\ \Delta z_{-4} = 0.02 \\ \Delta z_{-3} = 0.05 \\ \Delta z_{-2} = 0.11 \\ \Delta z_{-1} = \left(z_{sno} - \Delta z_{-4} - \Delta z_{-3} - \Delta z_{-2} \right)/2 \\ \Delta z_0 = \Delta z_{-1} \end{cases} \quad \text{for } 0.41 < z_{sno} \leq 0.64 \Bigg\},$$

$$\begin{cases} snl = -5 \\ \Delta z_{-4} = 0.02 \\ \Delta z_{-3} = 0.05 \\ \Delta z_{-2} = 0.11 \\ \Delta z_{-1} = 0.23 \\ \Delta z_0 = z_{sno} - \Delta z_{-4} - \Delta z_{-3} - \Delta z_{-2} - \Delta z_{-1} \end{cases} \quad \text{for } 0.64 < z_{sno} \Bigg\}.$$

The node depths, which are located at the midpoint of the snow layers, and the layer interfaces are both referenced from the soil surface and are defined as negative values

$$z_i = z_{h,i} - 0.5\Delta z_i \qquad i = snl + 1, \ldots, 0 \tag{6.8}$$

$$z_{h,i} = z_{h,i+1} - \Delta z_{i+1} \qquad i = snl, \ldots, -1. \tag{6.9}$$

Note that $z_{h,0}$, the interface between the bottom snow layer and the top soil layer, is zero.

Thermal properties (i.e., temperature T_i [K]; thermal conductivity λ_i [W m^{-1} K^{-1}]; volumetric heat capacity c_i [J m^{-3} K^{-1}]) are defined for soil layers at the node depths (Figure 6.1) and for snow layers at the layer midpoints.

The heat flux F_i (W m^{-2}) from layer i to layer $i+1$ is

$$F_i = -\lambda \left[z_{h,i} \right] \left(\frac{T_i - T_{i+1}}{z_{i+1} - z_i} \right) \tag{6.10}$$

where the thermal conductivity at the interface $\lambda \left[z_{h,i} \right]$ is

$$\lambda\left[z_{h,i}\right] = \begin{cases} \dfrac{\lambda_i \lambda_{i+1}\left(z_{i+1}-z_i\right)}{\lambda_i\left(z_{i+1}-z_{h,i}\right)+\lambda_{i+1}\left(z_{h,i}-z_i\right)} & i = snl+1,\ldots,N_{levgrnd}-1 \\[2ex] 0 & i = N_{levgrnd} \end{cases}. \quad (6.11)$$

These equations are derived, with reference to Figure 6.1, assuming that the heat flux from i (depth z_i) to the interface between i and $i+1$ (depth $z_{h,i}$) equals the heat flux from the interface to $i+1$ (depth z_{i+1}), i.e.,

$$-\lambda_i\frac{T_i-T_m}{z_{h,i}-z_i} = -\lambda_{i+1}\frac{T_m-T_{i+1}}{z_{i+1}-z_{h,i}} \quad (6.12)$$

where T_m is the temperature at the interface of layers i and $i+1$. Solving equation (6.12) for T_m and substituting T_m back into the left side of equation (6.12) yields equations (6.10) and (6.11).

Figure 6.1. Schematic diagram of numerical scheme used to solve for soil temperature. Shown are three soil layers, $i-1$, i, and $i+1$. The thermal conductivity λ, specific heat capacity c, and temperature T are defined at the layer node depth z. T_m is the interface temperature. The thermal conductivity $\lambda[z_h]$ is defined at the interface of two layers z_h. The layer thickness is Δz. The heat fluxes F_{i-1} and F_i are defined as positive upwards.
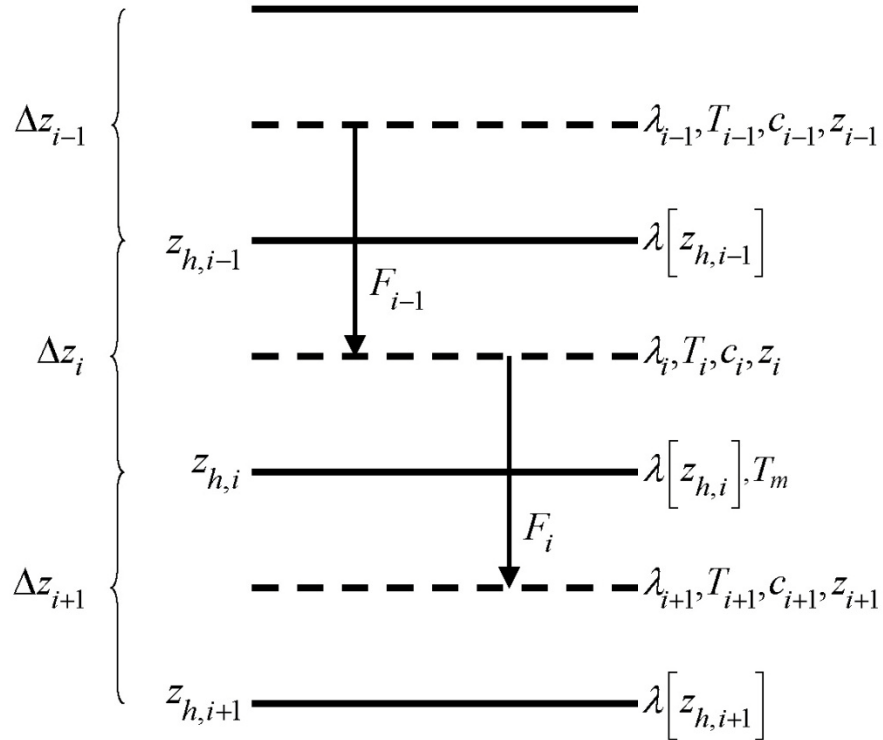
The energy balance for the ith layer is

$$\frac{c_i \Delta z_i}{\Delta t}\left(T_i^{n+1} - T_i^n\right) = -F_{i-1} + F_i \qquad (6.13)$$

where the superscripts n and $n+1$ indicate values at the beginning and end of the time step, respectively, and Δt is the time step (s). This equation is solved using the Crank-Nicholson method, which combines the explicit method with fluxes evaluated at n (F_{i-1}^{n}, F_{i}^{n}) and the implicit method with fluxes evaluated at $n+1$ ($F_{i-1}^{n+1}, F_{i}^{n+1}$)

$$\frac{c_i \Delta z_i}{\Delta t}\left(T_i^{n+1} - T_i^n\right) = \alpha\left(-F_{i-1}^n + F_i^n\right) + \left(1-\alpha\right)\left(-F_{i-1}^{n+1} + F_i^{n+1}\right) \tag{6.14}$$

where $\alpha = 0.5$, resulting in a tridiagonal system of equations

$$r_i = a_i T_{i-1}^{n+1} + b_i T_i^{n+1} + c_i T_{i+1}^{n+1} \tag{6.15}$$

where a_i, b_i, and c_i are the subdiagonal, diagonal, and superdiagonal elements in the tridiagonal matrix and r_i is a column vector of constants.

For the top snow/soil layer $i = snl + 1$, the heat flux from the overlying atmosphere into the surface snow/soil layer h (W m^{-2}, defined as positive into the soil) is

$$h^{n+1} = -\alpha F_{i-1}^n - \left(1-\alpha\right) F_{i-1}^{n+1}. \tag{6.16}$$

The energy balance for layer $i = snl + 1$ is then

$$\frac{c_i \Delta z_i}{\Delta t}\left(T_i^{n+1} - T_i^n\right) = h^{n+1} + \alpha F_i^n + \left(1-\alpha\right) F_i^{n+1}. \tag{6.17}$$

The heat flux h at $n+1$ may be approximated as follows

$$h^{n+1} = h^n + \frac{\partial h}{\partial T_i}\left(T_i^{n+1} - T_i^n\right). \tag{6.18}$$

The resulting equations are then

$$\begin{aligned}
\frac{c_i \Delta z_i}{\Delta t}\left(T_i^{n+1} - T_i^n\right) &= h^n + \frac{\partial h}{\partial T_i}\left(T_i^{n+1} - T_i\right) \\
&- \alpha \frac{\lambda\left[z_{h,i}\right]\left(T_i^n - T_{i+1}^n\right)}{z_{i+1} - z_i} - \left(1-\alpha\right)\frac{\lambda\left[z_{h,i}\right]\left(T_i^{n+1} - T_{i+1}^{n+1}\right)}{z_{i+1} - z_i}
\end{aligned} \tag{6.19}$$

$$a_i = 0 \tag{6.20}$$

$$b_i = 1 + \frac{\Delta t}{c_i \Delta z_i} \left[(1 - \alpha) \frac{\lambda \left[z_{h,i} \right]}{z_{i+1} - z_i} - \frac{\partial h}{\partial T_i} \right] \tag{6.21}$$

$$c_i = -(1 - \alpha) \frac{\Delta t}{c_i \Delta z_i} \frac{\lambda \left[z_{h,i} \right]}{z_{i+1} - z_i} \tag{6.22}$$

$$r_i = T_i^n + \frac{\Delta t}{c_i \Delta z_i} \left[h^n - \frac{\partial h}{\partial T_i} T_i^n + \alpha F_i \right] \tag{6.23}$$

where

$$F_i = -\lambda \left[z_{h,i} \right] \left(\frac{T_i^n - T_{i+1}^n}{z_{i+1} - z_i} \right). \tag{6.24}$$

The heat flux into the snow/soil surface from the overlying atmosphere h is

$$h = \vec{S}_{g,i=snl+1} - \vec{L}_g - H_g - \lambda E_g \tag{6.25}$$

where $\vec{S}_{g,i=snl+1}$ is the solar radiation absorbed by the top layer (section 3.2.1), $\vec{L}_g$ is the longwave radiation absorbed by the ground (positive toward the atmosphere) (section 4.2), H_g is the sensible heat flux from the ground (section 5), and λE_g is the latent heat flux from the ground (section 5). The partial derivative of the heat flux h with respect to ground temperature is

$$\frac{\partial h}{\partial T_g} = -\frac{\partial \vec{L}_g}{\partial T_g} - \frac{\partial H_g}{\partial T_g} - \frac{\partial \lambda E_g}{\partial T_g} \tag{6.26}$$

where the partial derivative of the net longwave radiation is

$$\frac{\partial \vec{L}_g}{\partial T_g} = 4\varepsilon_g \sigma \left(T_g^n \right)^3 \tag{6.27}$$

and the partial derivatives of the sensible and latent heat fluxes are given by equations (5.72) and (5.73) for non-vegetated surfaces, and by equations (5.110) and (5.111) for vegetated surfaces. σ is the Stefan-Boltzmann constant (W m^{-2} K^{-4}) (Table 1.4) and ε_g is the ground emissivity (section 4.2). For purposes of computing h and $\dfrac{\partial h}{\partial T_g}$, the term λ is arbitrarily assumed to be

$$\lambda = \left\{\begin{array}{ll} \lambda_{sub} & \text{if } w_{liq,snl+1} = 0 \text{ and } w_{ice,snl+1} > 0 \\ \lambda_{vap} & \text{otherwise} \end{array}\right\} \qquad (6.28)$$

where λ_{sub} and λ_{vap} are the latent heat of sublimation and vaporization, respectively (J kg^{-1}) (Table 1.4), and $w_{liq,snl+1}$ and $w_{ice,snl+1}$ are the liquid water and ice contents of the top snow/soil layer, respectively (kg m^{-2}) (section 7).

The surface snow/soil layer temperature computed in this way is the layer-averaged temperature and hence has somewhat reduced diurnal amplitude compared with surface temperature. An accurate surface temperature is provided that compensates for this effect and numerical error by tuning the heat capacity of the top layer (through adjustment of the layer thickness) to give an exact match to the analytic solution for diurnal heating. The top layer thickness for $i = snl + 1$ is given by

$$\Delta z_{i*} = 0.5 \left[z_i - z_{h,i-1} + c_a \left(z_{i+1} - z_{h,i-1} \right) \right] \qquad (6.29)$$

where c_a is a tunable parameter, varying from 0 to 1, and is taken as 0.34 by comparing the numerical solution with the analytic solution (Z.-L. Yang 1998, unpublished manuscript). Δz_{i*} is used in place of Δz_i for $i = snl + 1$ in equations (6.19)-(6.24). The

top snow/soil layer temperature computed in this way is the ground surface temperature T_g^{n+1}.

The boundary condition at the bottom of the snow/soil column is zero heat flux, $F_i = 0$, resulting in, for $i = N_{levgrnd}$,

$$\frac{c_i \Delta z_i}{\Delta t}\left(T_i^{n+1} - T_i^n\right) = \alpha \frac{\lambda\left[z_{h,i-1}\right]\left(T_{i-1}^n - T_i^n\right)}{z_i - z_{i-1}} + \left(1-\alpha\right)\frac{\lambda\left[z_{h,i-1}\right]\left(T_{i-1}^{n+1} - T_i^{n+1}\right)}{z_i - z_{i-1}} \tag{6.30}$$

$$a_i = -\left(1-\alpha\right)\frac{\Delta t}{c_i \Delta z_i}\frac{\lambda\left[z_{h,i-1}\right]}{z_i - z_{i-1}} \tag{6.31}$$

$$b_i = 1 + \left(1-\alpha\right)\frac{\Delta t}{c_i \Delta z_i}\frac{\lambda\left[z_{h,i-1}\right]}{z_i - z_{i-1}} \tag{6.32}$$

$$c_i = 0 \tag{6.33}$$

$$r_i = T_i^n - \alpha \frac{\Delta t}{c_i \Delta z_i} F_{i-1} \tag{6.34}$$

where

$$F_{i-1} = -\frac{\lambda\left[z_{h,i-1}\right]}{z_i - z_{i-1}}\left(T_{i-1}^n - T_i^n\right). \tag{6.35}$$

For the interior snow/soil layers, $snl + 1 < i < N_{levgrnd}$,

$$\begin{aligned}\frac{c_i \Delta z_i}{\Delta t}\left(T_i^{n+1} - T_i^n\right) = &-\alpha \frac{\lambda\left[z_{h,i}\right]\left(T_i^n - T_{i+1}^n\right)}{z_{i+1} - z_i} + \alpha \frac{\lambda\left[z_{h,i-1}\right]\left(T_{i-1}^n - T_i^n\right)}{z_i - z_{i-1}}\\ &-\left(1-\alpha\right)\frac{\lambda\left[z_{h,i}\right]\left(T_i^{n+1} - T_{i+1}^{n+1}\right)}{z_{i+1} - z_i} + \left(1-\alpha\right)\frac{\lambda\left[z_{h,i-1}\right]\left(T_{i-1}^{n+1} - T_i^{n+1}\right)}{z_i - z_{i-1}}\end{aligned} \tag{6.36}$$

$$a_i = -\left(1-\alpha\right)\frac{\Delta t}{c_i \Delta z_i}\frac{\lambda\left[z_{h,i-1}\right]}{z_i - z_{i-1}} \tag{6.37}$$

$$b_i = 1 + (1-\alpha)\frac{\Delta t}{c_i \Delta z_i}\left[\frac{\lambda\left[z_{h,i-1}\right]}{z_i - z_{i-1}} + \frac{\lambda\left[z_{h,i}\right]}{z_{i+1} - z_i}\right] \tag{6.38}$$

$$c_i = -(1-\alpha)\frac{\Delta t}{c_i \Delta z_i}\frac{\lambda\left[z_{h,i}\right]}{z_{i+1} - z_i} \tag{6.39}$$

$$r_i = T_i^n + \alpha\frac{\Delta t}{c_i \Delta z_i}\left(F_i - F_{i-1}\right) + \frac{\Delta t}{c_i \Delta z_i}\vec{S}_{g,i}. \tag{6.40}$$

where $\vec{S}_{g,i}$ is the absorbed solar flux in layer i (section 3.2.1).

6.2 Phase Change

Upon solution of the tridiagonal equation set (Press et al. 1992), the snow/soil temperatures are evaluated to determine if phase change will take place as

$$
\begin{array}{llll}
T_i^{n+1} > T_f \text{ and } w_{ice,i} > 0 & i = snl+1,\ldots,N_{levgrnd} & \text{melting} \\
T_i^{n+1} < T_f \text{ and } w_{liq,i} > 0 & i = snl+1,\ldots,0 & \text{freezing} & (6.41) \\
T_i^{n+1} < T_f \text{ and } w_{liq,i} > w_{liq,\max,i} & i = 1,\ldots,N_{levgrnd} & \text{freezing}
\end{array}
$$

where T_i^{n+1} is the soil layer temperature after solution of the tridiagonal equation set, $w_{ice,i}$ and $w_{liq,i}$ are the mass of ice and liquid water (kg m^{-2}) in each snow/soil layer, respectively, and T_f is the freezing temperature of water (K) (Table 1.4). For the freezing process in soil layers, the concept of supercooled soil water from Niu and Yang (2006) is adopted. The supercooled soil water is the liquid water that coexists with ice over a wide range of temperatures below freezing and is implemented through a freezing point depression equation

$$w_{liq,\max,i} = \Delta z_i \theta_{sat,i}\left[\frac{10^3 L_f\left(T_f - T_i\right)}{gT_i\psi_{sat,i}}\right]^{-1/B_i} \quad T_i < T_f \tag{6.42}$$

where $w_{liq,max,i}$ is the maximum liquid water in layer i (kg m^{-2}) when the soil temperature T_i is below the freezing temperature T_f, L_f is the latent heat of fusion (J kg^{-1}) (Table 1.4), g is the gravitational acceleration (m s^{-2}) (Table 1.4), and $\psi_{sat,i}$ and B_i are the soil texture-dependent saturated matric potential (mm) and Clapp and Hornberger (1978) exponent (section 7.4.1).

For the special case when snow is present (snow mass $W_{sno} > 0$) but there are no explicit snow layers ($snl = 0$) (i.e., there is not enough snow present to meet the minimum snow depth requirement of 0.01 m), snow melt will take place for soil layer $i = 1$ if the soil layer temperature is greater than the freezing temperature ($T_1^{n+1} > T_f$).

The rate of phase change is assessed from the energy excess (or deficit) needed to change T_i to freezing temperature, T_f. The excess or deficit of energy H_i (W m^{-2}) is determined as follows

$$
H_i = \begin{cases}
\begin{aligned}
& h + \frac{\partial h}{\partial T}\left(T_f - T_i^n\right) + \alpha F_i^n + \left(1-\alpha\right) F_i^{n+1} \\
& -\frac{c_i \Delta z_i}{\Delta t}\left(T_f - T_i^n\right) & i = snl+1 \\
& \alpha\left(F_i^n - F_{i-1}^n\right) + \left(1-\alpha\right)\left(F_i^{n+1} - F_{i-1}^{n+1}\right) \\
& -\frac{c_i \Delta z_i}{\Delta t}\left(T_f - T_i^n\right) + \vec{S}_{g,i} & i = snl+2,\ldots,N_{levgrnd}
\end{aligned}
\end{cases}
\tag{6.43}
$$

where F_i^{n+1} and F_{i-1}^{n+1} are calculated from equations (6.24) and (6.35) using T_i^{n+1}, and $\vec{S}_{g,i}$ is the solar absorbed flux in layer i. If the melting criteria is met (equation (6.41)) and $H_m = \dfrac{H_i \Delta t}{L_f} > 0$, then the ice mass is readjusted as

$$
w_{ice,i}^{n+1} = w_{ice,i}^n - H_m \geq 0 \qquad i = snl+1,\ldots,N_{levgrnd}.
\tag{6.44}
$$

If the freezing criteria is met (equation (6.41)) and $H_m < 0$, then the ice mass is readjusted for $i = snl + 1, \ldots, 0$ as

$$w_{ice,i}^{n+1} = \min\left(w_{liq,i}^n + w_{ice,i}^n, w_{ice,i}^n - H_m\right) \tag{6.45}$$

and for $i = 1, \ldots, N_{levgrnd}$ as

$$w_{ice,i}^{n+1} = \begin{cases} \min\left(w_{liq,i}^n + w_{ice,i}^n - w_{liq,\max,i}^n, w_{ice,i}^n - H_m\right) & w_{liq,i}^n + w_{ice,i}^n \geq w_{liq,\max,i}^n \\ 0 & w_{liq,i}^n + w_{ice,i}^n < w_{liq,\max,i}^n \end{cases} . \tag{6.46}$$

Liquid water mass is readjusted as

$$w_{liq,i}^{n+1} = w_{liq,i}^n + w_{ice,i}^n - w_{ice,i}^{n+1} \geq 0 . \tag{6.47}$$

Because part of the energy H_i may not be consumed in melting or released in freezing, the energy is recalculated as

$$H_{i*} = H_i - \frac{L_f \left(w_{ice,i}^n - w_{ice,i}^{n+1}\right)}{\Delta t} \tag{6.48}$$

and this energy is used to cool or warm the snow/soil layer (if $\left|H_{i*}\right| > 0$) as

$$T_i^{n+1} = \begin{cases} \left. \left(T_f + \dfrac{\Delta t}{c_i \Delta z_i} H_{i*} \right) \middle/ \left(1 - \dfrac{\Delta t}{c_i \Delta z_i} \dfrac{\partial h}{\partial T} \right) \right. & i = snl + 1 \\ T_f + \dfrac{\Delta t}{c_i \Delta z_i} H_{i*} & i = snl + 2, \ldots N_{levgrnd} \end{cases} . \tag{6.49}$$

For the special case when snow is present ($W_{sno} > 0$), there are no explicit snow layers ($snl = 0$), and $\dfrac{H_1 \Delta t}{L_f} > 0$ (melting), the snow mass W_{sno} (kg m^{-2}) is reduced according to

$$W_{sno}^{n+1} = W_{sno}^n - \frac{H_1 \Delta t}{L_f} \geq 0 . \tag{6.50}$$

111

The snow depth is reduced proportionally

$$z_{sno}^{n+1} = \frac{W_{sno}^{n+1}}{W_{sno}^{n}} z_{sno}^{n}. \tag{6.51}$$

Again, because part of the energy may not be consumed in melting, the energy for the surface soil layer $i = 1$ is recalculated as

$$H_{1*} = H_1 - \frac{L_f \left(W_{sno}^{n} - W_{sno}^{n+1} \right)}{\Delta t}. \tag{6.52}$$

If there is excess energy ($H_{1*} > 0$), this energy becomes available to the top soil layer as

$$H_1 = H_{1*}. \tag{6.53}$$

The ice mass, liquid water content, and temperature of the top soil layer are then determined from equations (6.44), (6.47), and (6.49) using the recalculated energy from equation (6.53). Snow melt M_{1S} (kg m^{-2} s^{-1}) and phase change energy $E_{p,1S}$ (W m^{-2}) for this special case are

$$M_{1S} = \frac{W_{sno}^{n} - W_{sno}^{n+1}}{\Delta t} \geq 0 \tag{6.54}$$

$$E_{p,1S} = L_f M_{1S}. \tag{6.55}$$

The total energy of phase change E_p (W m^{-2}) for the snow/soil column is

$$E_p = E_{p,1S} + \sum_{i=snl+1}^{N_{levgrnd}} E_{p,i} \tag{6.56}$$

where

$$E_{p,i} = L_f \frac{\left(w_{ice,i}^{n} - w_{ice,i}^{n+1} \right)}{\Delta t}. \tag{6.57}$$

The total snow melt M (kg m^{-2} s^{-1}) is

$$M = M_{1S} + \sum_{i=snl+1}^{i=0} M_i \qquad (6.58)$$

where

$$M_i = \frac{\left(w_{ice,i}^n - w_{ice,i}^{n+1}\right)}{\Delta t} \geq 0. \qquad (6.59)$$

The solution for snow/soil temperatures conserves energy as

$$G - E_p - \sum_{i=snl+1}^{i=N_{levgrnd}} \frac{c_i \Delta z_i}{\Delta t}\left(T_i^{n+1} - T_i^n\right) = 0 \qquad (6.60)$$

where G is the ground heat flux (section 5.4).

6.3   Soil and Snow Thermal Properties

The thermal and hydraulic (section 7.4.1) properties of the soil are assumed to be a weighted combination of the mineral and organic properties of the soil (Lawrence and Slater 2008). The soil layer organic matter fraction $f_{om,i}$ is

$$f_{om,i} = \rho_{om,i} / \rho_{om,max} . \qquad (6.61)$$

Soil thermal conductivity λ_i (W m^{-1} K^{-1}) is from Farouki (1981)

$$\lambda_i = \begin{cases} K_{e,i}\lambda_{sat,i} + \left(1 - K_{e,i}\right)\lambda_{dry,i} & S_{r,i} > 1 \times 10^{-7} \\ \lambda_{dry,i} & S_{r,i} \leq 1 \times 10^{-7} \end{cases} \quad i = 1,\dots,N_{levsoi}$$

$$\lambda_i = \lambda_{bedrock} \qquad\qquad\qquad\qquad\qquad i = N_{levsoi} + 1,\dots N_{levgrnd} \qquad (6.62)$$

where $\lambda_{sat,i}$ is the saturated thermal conductivity, $\lambda_{dry,i}$ is the dry thermal conductivity, $K_{e,i}$ is the Kersten number, $S_{r,i}$ is the wetness of the soil with respect to saturation, and $\lambda_{bedrock} = 3$ W m^{-1} K^{-1} is the thermal conductivity assumed for the deep ground layers (typical of saturated granitic rock; Clauser and Huenges, 1995). For glaciers and wetlands,

$$\lambda_i = \begin{cases} \lambda_{liq,i} & T_i \geq T_f \\ \lambda_{ice,i} & T_i < T_f \end{cases} \tag{6.63}$$

where λ_{liq} and λ_{ice} are the thermal conductivities of liquid water and ice, respectively (Table 1.4). The saturated thermal conductivity $\lambda_{sat,i}$ (W m^{-1} K^{-1}) depends on the thermal conductivities of the soil solid, liquid water, and ice constituents

$$\lambda_{sat,i} = \begin{cases} \lambda_{s,i}^{1-\theta_{sat,i}} \lambda_{liq}^{\theta_{sat,i}} & T_i \geq T_f \\ \lambda_{s,i}^{1-\theta_{sat,i}} \lambda_{liq}^{\theta_{sat,i}} \lambda_{ice}^{\theta_{sat,i}-\theta_{liq,i}} & T_i < T_f \end{cases} \tag{6.64}$$

where the thermal conductivity of soil solids $\lambda_{s,i}$ varies with the sand, clay, and organic matter content

$$\lambda_{s,i} = (1 - f_{om,i})\lambda_{s,\min,i} + f_{om,i}\lambda_{s,om} \tag{6.65}$$

where the mineral soil solid thermal conductivity $\lambda_{s,\min,i}$ is

$$\lambda_{s,\min,i} = \frac{8.80\ (\%sand)_i + 2.92\ (\%clay)_i}{(\%sand)_i + (\%clay)_i}, \tag{6.66}$$

and $\lambda_{s,om} = 0.25$ W m^{-1} K^{-1} (Farouki, 1981). $\theta_{sat,i}$ is the volumetric water content at saturation (porosity) (section 7.4.1).

The thermal conductivity of dry soil is

$$\lambda_{dry,i} = (1 - f_{om,i})\lambda_{dry,\min,i} + f_{om,i}\lambda_{dry,om} \tag{6.67}$$

where the thermal conductivity of dry mineral soil $\lambda_{dry,\min,i}$ (W m^{-1} K^{-1}) depends on the bulk density $\rho_{d,i} = 2700(1 - \theta_{sat,i})$ (kg m^{-3}) as

$$\lambda_{dry,\min,i} = \frac{0.135\rho_{d,i} + 64.7}{2700 - 0.947\rho_{d,i}} \tag{6.68}$$

and $\lambda_{dry,om} = 0.05$ W m^{-1} K^{-1} (Farouki, 1981) is the dry thermal conductivity of organic matter. The Kersten number $K_{e,i}$ is a function of the degree of saturation S_r and phase of water

$$K_{e,i} = \begin{cases} \log(S_{r,i}) + 1 \geq 0 \; T_i \geq T_f \\ S_{r,i} \qquad\qquad\quad T_i < T_f \end{cases} \tag{6.69}$$

where

$$S_{r,i} = \left(\frac{w_{liq,i}}{\rho_{liq}\Delta z_i} + \frac{w_{ice,i}}{\rho_{ice}\Delta z_i} \right) \frac{1}{\theta_{sat,i}} = \frac{\theta_{liq,i} + \theta_{ice,i}}{\theta_{sat,i}} \leq 1. \tag{6.70}$$

Thermal conductivity λ_i (W m^{-1} K^{-1}) for snow is from Jordan (1991)

$$\lambda_i = \lambda_{air} + \left(7.75 \times 10^{-5} \rho_{sno,i} + 1.105 \times 10^{-6} \rho_{sno,i}^2 \right) \left(\lambda_{ice} - \lambda_{air} \right) \tag{6.71}$$

where λ_{air} is the thermal conductivity of air (Table 1.4) and $\rho_{sno,i}$ is the bulk density of snow (kg m^{-3})

$$\rho_{sno,i} = \frac{w_{ice,i} + w_{liq,i}}{\Delta z_i}. \tag{6.72}$$

The volumetric heat capacity c_i (J m^{-3} K^{-1}) for soil is from de Vries (1963) and depends on the heat capacities of the soil solid, liquid water, and ice constituents

$$c_i = c_{s,i}\left(1 - \theta_{sat,i} \right) + \frac{w_{ice,i}}{\Delta z_i} C_{ice} + \frac{w_{liq,i}}{\Delta z_i} C_{liq} \tag{6.73}$$

where C_{liq} and C_{ice} are the specific heat capacities (J kg^{-1} K^{-1}) of liquid water and ice, respectively (Table 1.4). The heat capacity of soil solids $c_{s,i}$ (J m^{-3} K^{-1}) is

$$c_{s,i} = (1 - f_{om,i})c_{s,min,i} + f_{om,i}c_{s,om} \tag{6.74}$$

where the heat capacity of mineral soil solids $c_{s,min,i}$ (J m^{-3} K^{-1}) is

$$c_{s,\min,i} = \left(\frac{2.128\ (\%\,sand)_i + 2.385\ (\%\,clay)_i}{(\%\,sand)_i + (\%\,clay)_i} \right) \times 10^6 \quad i = 1, \ldots, N_{levsoi}$$

$$c_{s,\min,i} = c_{s,bedrock} \qquad\qquad\qquad\qquad\qquad i = N_{levsoi} + 1, \ldots, N_{levgrnd}$$

(6.75)

where $c_{s,bedrock} = 2 \times 10^6$ J m^{-3} K^{-1} is the heat capacity of bedrock and $c_{s,om} = 2.5 \times 10^6$ J m^{-3} K^{-1} (Farouki, 1981) is the heat capacity of organic matter. For glaciers, wetlands, and snow

$$c_i = \frac{w_{ice,i}}{\Delta z_i} C_{ice} + \frac{w_{liq,i}}{\Delta z_i} C_{liq}.$$

(6.76)

For the special case when snow is present ($W_{sno} > 0$) but there are no explicit snow layers ($snl = 0$), the heat capacity of the top layer is a blend of ice and soil heat capacity

$$c_1 = c_1^* + \frac{C_{ice} W_{sno}}{\Delta z_1}$$

(6.77)

where c_1^* is calculated from equation (6.73) or (6.76).

7. Hydrology

The model parameterizes interception, throughfall, canopy drip, snow accumulation and melt, water transfer between snow layers, infiltration, evaporation, surface runoff, sub-surface drainage, redistribution within the soil column, and groundwater discharge and recharge to simulate changes in canopy water ΔW_{can}, snow water ΔW_{sno}, soil water $\Delta w_{liq,i}$, and soil ice $\Delta w_{ice,i}$, and water in the unconfined aquifer ΔW_a (all in kg m^{-2} or mm of H$_2$O) (Figure 7.1).

The total water balance of the system is

$$\Delta W_{can} + \Delta W_{sno} + \sum_{i=1}^{N_{levsoi}} \left(\Delta w_{liq,i} + \Delta w_{ice,i} \right) + \Delta W_a = \left(\begin{array}{c} q_{rain} + q_{sno} - E_v - E_g - q_{over} \\ -q_{drai} - q_{rgwl} - q_{snwcp,ice} \end{array} \right) \Delta t \quad (7.1)$$

where q_{rain} is liquid part of precipitation, q_{sno} is solid part of precipitation, E_v is ET from vegetation (section 5), E_g is ground evaporation (section 5), q_{over} is surface runoff (section 7.3), q_{drai} is sub-surface drainage (section 7.5), q_{rgwl} and $q_{snwcp,ice}$ are liquid and solid runoff from glaciers, wetlands, and lakes, and runoff from other surface types due to snow capping (section 7.6) (all in kg m^{-2} s^{-1}), N_{levsoi} is the number of soil layers (note that hydrology calculations are only done over soil layers 1 to N_{levsoi}; ground levels $N_{levsoi} + 1$ to $N_{levgrnd}$ are currently hydrologically inactive; Lawrence et al. 2008) and Δt is the time step (s).

Figure 7.1. Hydrologic processes.

An unconfined aquifer is added to the bottom of the soil column. The depth to the water table is z_∇ (m). Changes in aquifer water content W_a (mm) are controlled by the balance between drainage from the aquifer water q_{drai} and the aquifer recharge rate $q_{recharge}$ (kg m^{-2} s^{-1}) (defined as positive from soil to aquifer).
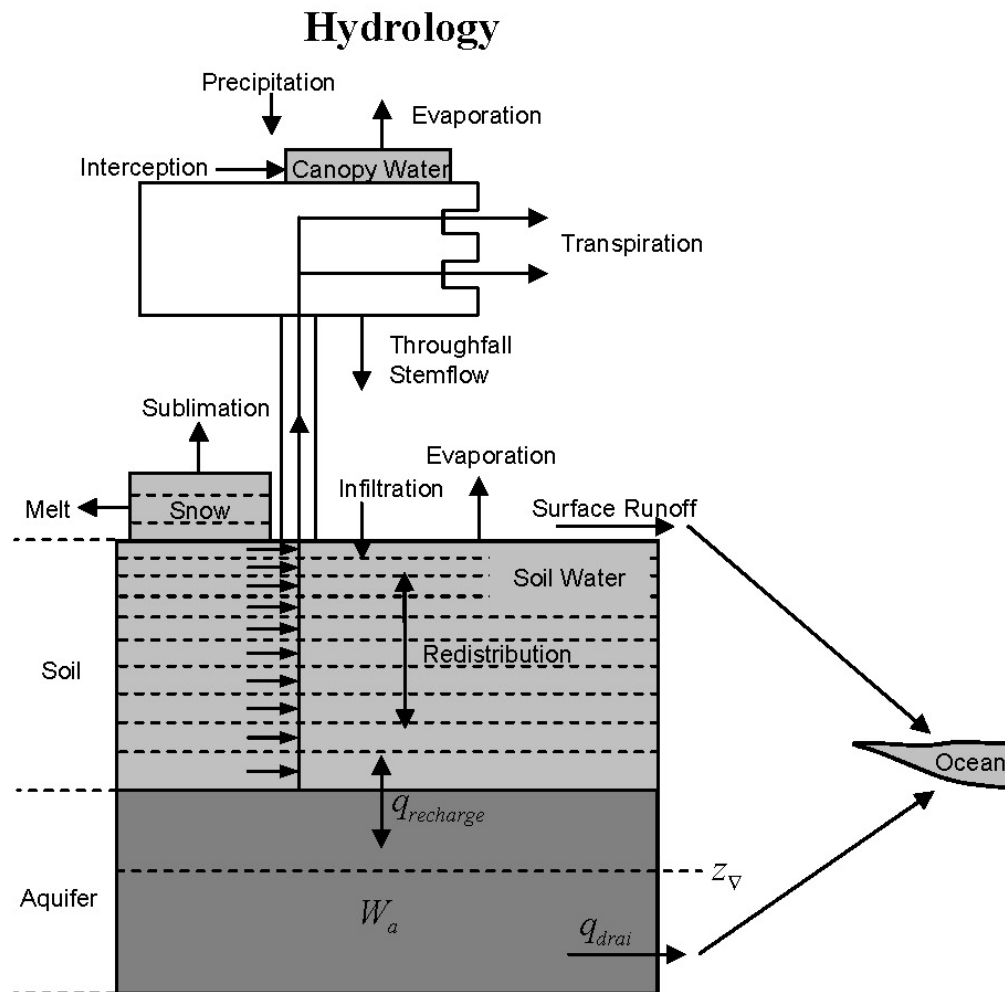
7.1 Canopy Water

Precipitation is either intercepted by the canopy, falls directly through to the snow/soil surface (throughfall), or drips off the vegetation (canopy drip). Interception by vegetation q_{intr} (kg m^{-2} s^{-1}) does not distinguish between liquid and solid phases

$$q_{intr} = \alpha \left(q_{rain} + q_{sno} \right) \left\{ 1 - \exp\left[-0.5 \left(L + S \right) \right] \right\} \tag{7.2}$$

where L and S are the exposed leaf and stem area index, respectively (section 2.3), and $\alpha = 0.25$ scales interception from point to grid cell (Lawrence et al. 2007). Throughfall (kg m^{-2} s^{-1}), however, is divided into liquid and solid phases reaching the ground (soil or snow surface) as

$$q_{thru,liq} = q_{rain} \left[1 - \alpha \left\{ 1 - \exp\left[-0.5 \left(L + S \right) \right] \right\} \right] \tag{7.3}$$

$$q_{thru,ice} = q_{sno} \left[1 - \alpha \left\{ 1 - \exp\left[-0.5 \left(L + S \right) \right] \right\} \right]. \tag{7.4}$$

Similarly, the canopy drip is

$$q_{drip,liq} = \frac{W_{can}^{intr} - W_{can,\max}}{\Delta t} \frac{q_{rain}}{q_{rain} + q_{sno}} \geq 0 \tag{7.5}$$

$$q_{drip,ice} = \frac{W_{can}^{intr} - W_{can,\max}}{\Delta t} \frac{q_{sno}}{q_{rain} + q_{sno}} \geq 0 \tag{7.6}$$

where

$$W_{can}^{intr} = W_{can}^{n} + q_{intr} \Delta t \geq 0 \tag{7.7}$$

is the canopy water after accounting for interception, W_{can}^{n} is the canopy water from the previous time step, and $W_{can,\max}$ (kg m^{-2}) is the maximum amount of water the canopy can hold

$$W_{can,\max} = p \left(L + S \right). \tag{7.8}$$

The maximum storage of solid water is assumed to be the same as that of liquid water, $p = 0.1$ kg m^{-2} (Dickinson et al. 1993). The canopy water is updated as

$$W_{can}^{n+1} = W_{can}^{n} + q_{intr}\Delta t - \left(q_{drip,liq} + q_{drip,ice} \right)\Delta t - E_v^w \Delta t \geq 0.$$ (7.9)

where E_v^w is the flux of water vapor from stem and leaf surfaces (section 5).

The total rate of liquid and solid precipitation reaching the ground is then

$$q_{grnd,liq} = q_{thru,liq} + q_{drip,liq}$$ (7.10)

$$q_{grnd,ice} = q_{thru,ice} + q_{drip,ice}.$$ (7.11)

Solid precipitation reaching the soil or snow surface, $q_{grnd,ice}\Delta t$, is added immediately to the snow pack (section 7.2). The liquid part, $q_{grnd,liq}\Delta t$ is added after surface fluxes (section 5) and snow/soil temperatures (section 6) have been determined.

The wetted fraction of the canopy (stems plus leaves), which is required for the surface albedo (section 3.1) and surface flux (section 5) calculations is (Dickinson et al. 1993)

$$f_{wet} = \begin{cases} \left[\dfrac{W_{can}}{p(L+S)} \right]^{2/3} \leq 1 & L+S > 0 \\ 0 & L+S = 0 \end{cases}$$ (7.12)

while the fraction of the canopy that is dry and transpiring is

$$f_{dry} = \begin{cases} \dfrac{(1-f_{wet})L}{L+S} & L+S > 0 \\ 0 & L+S = 0 \end{cases}.$$ (7.13)

7.2 Snow

The parameterizations for snow are based primarily on Anderson (1976), Jordan (1991), and Dai and Zeng (1997). Snow can have up to five layers. These layers are

indexed in the Fortran code as $i = -4, -3, -2, -1, 0$ where layer $i = 0$ is the snow layer next to the top soil layer and layer $i = -4$ is the top layer of a five-layer snow pack. Since the number of snow layers varies according to the snow depth, we use the notation $snl + 1$ to describe the top layer of snow for the variable layer snow pack, where snl is the negative of the number of snow layers. Refer to Figure 7.2 for an example of the snow layer structure for a three layer snow pack.

Figure 7.2. Example of three layer snow pack ($snl = -3$).

Shown are three snow layers, $i = -2$, $i = -1$, and $i = 0$. The layer node depth is z, the layer interface is z_h, and the layer thickness is Δz.

$z_{h,-3}$ ———————————— Snow/atm interface

Δz_{-2} $\quad z_{-2}$ — — — — — — — — — — $i = snl + 1 = -2$

$z_{h,-2}$ ————————————

Δz_{-1} $\quad z_{-1}$ — — — — — — — — — $i = snl + 2 = -1$

$z_{h,-1}$ ————————————

Δz_0 $\quad z_0$ — — — — — — — — — $i = snl + 3 = 0$

$z_{h,0}$ ———————————— Snow/soil interface
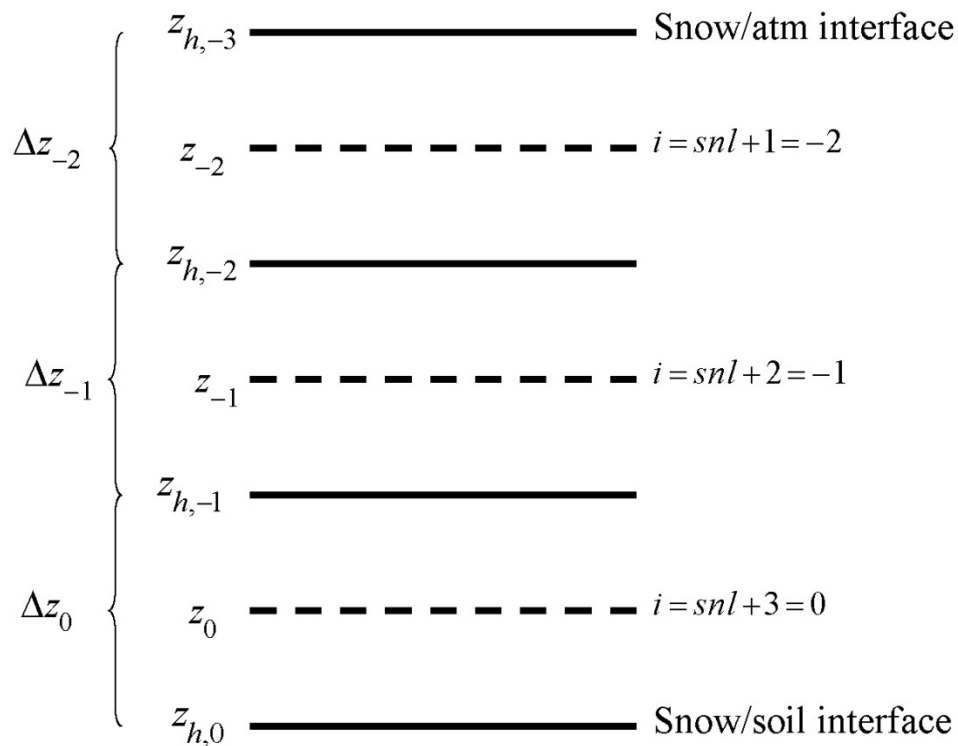
The state variables for snow are the mass of water $w_{liq,i}$ (kg m^{-2}), mass of ice $w_{ice,i}$ (kg m^{-2}), layer thickness Δz_i (m), and temperature T_i (section 6). The water vapor phase is neglected. Snow can also exist in the model without being represented by explicit snow layers. This occurs when the snowpack is less than a specified minimum snow depth ($z_{sno} < 0.01$ m). In this case, the state variable is the mass of snow W_{sno} (kg m^{-2}).

The next two sections (7.2.1 and 7.2.2) describe the ice and water content of the snow pack assuming that at least one snow layer exists. Section 7.2.3 describes how black and organic carbon and mineral dust particles are represented within snow, including meltwater flushing. See section 7.2.4 for a description of how a snow layer is initialized.

7.2.1 Ice Content

The conservation equation for mass of ice in snow layers is

$$\frac{\partial w_{ice,i}}{\partial t} = \begin{cases} q_{ice,i-1} - \dfrac{\left(\Delta w_{ice,i}\right)_p}{\Delta t} & i = snl + 1 \\[4mm] -\dfrac{\left(\Delta w_{ice,i}\right)_p}{\Delta t} & i = snl + 2, \ldots, 0 \end{cases} \tag{7.14}$$

where $q_{ice,i-1}$ is the rate of ice accumulation from precipitation or frost or the rate of ice loss from sublimation (kg m^{-2} s^{-1}) in the top layer and $\left(\Delta w_{ice,i}\right)_p / \Delta t$ is the change in ice due to phase change (melting rate) (section 6.2). The term $q_{ice,i-1}$ is computed in two steps as

$$q_{ice,i-1} = q_{grnd,ice} + \left(q_{frost} - q_{subl}\right) \tag{7.15}$$

where $q_{grnd,ice}$ is the rate of solid precipitation reaching the ground (section 7.1) and q_{frost} and q_{subl} are gains due to frost and losses due to sublimation, respectively (section 5.4). In the first step, immediately after $q_{grnd,ice}$ has been determined after accounting for interception (section 7.1), a new snow depth z_{sno} (m) is calculated from

$$z_{sno}^{n+1} = z_{sno}^{n} + \Delta z_{sno} \tag{7.16}$$

where

$$\Delta z_{sno} = \frac{q_{grnd,ice}\Delta t}{\rho_{sno}} \tag{7.17}$$

and ρ_{sno} is the bulk density of newly fallen snow (kg m^{-3}) (Anderson 1976)

$$\rho_{sno} = \begin{cases} 50 + 1.7(17)^{1.5} & T_{atm} > T_f + 2 \\ 50 + 1.7(T_{atm} - T_f + 15)^{1.5} & T_f - 15 < T_{atm} \le T_f + 2 \\ 50 & T_{atm} \le T_f - 15 \end{cases} \tag{7.18}$$

where T_{atm} is the atmospheric temperature (K), and T_f is the freezing temperature of water (K) (Table 1.4). The mass of snow W_{sno} is

$$W_{sno}^{n+1} = W_{sno}^{n} + q_{grnd,ice}\Delta t . \tag{7.19}$$

The ice content of the top layer and the layer thickness are updated as

$$w_{ice,snl+1}^{n+1} = w_{ice,snl+1}^{n} + q_{grnd,ice}\Delta t \tag{7.20}$$

$$\Delta z_{snl+1}^{n+1} = \Delta z_{snl+1}^{n} + \Delta z_{sno} . \tag{7.21}$$

Since wetlands are modeled as columns of water (no soil), snow is not allowed to accumulate if the surface temperature is above freezing ($T_g > T_f$). In this case, the incoming solid precipitation is assigned to the runoff term q_{rgwl} (section 7.6).

In the second step, after surface fluxes and snow/soil temperatures have been determined (sections 5 and 6), $w_{ice,snl+1}$ is updated for frost or sublimation as

$$w_{ice,snl+1}^{n+1} = w_{ice,snl+1}^{n} + \left(q_{frost} - q_{subl}\right)\Delta t \ . \tag{7.22}$$

If $w_{ice,snl+1}^{n+1} < 0$ upon solution of equation (7.22), the ice content is reset to zero and the liquid water content $w_{liq,snl+1}$ is reduced by the amount required to bring $w_{ice,snl+1}^{n+1}$ up to zero.

The snow water equivalent W_{sno} is capped to not exceed 1000 kg m^{-2}. If the addition of q_{frost} were to result in $W_{sno} > 1000$ kg m^{-2}, the frost term q_{frost} is instead added to the ice runoff term $q_{snwcp,ice}$ (section 7.6).

7.2.2 Water Content

The conservation equation for mass of water in snow layers is

$$\frac{\partial w_{liq,i}}{\partial t} = \left(q_{liq,i-1} - q_{liq,i}\right) + \frac{\left(\Delta w_{liq,i}\right)_p}{\Delta t} \tag{7.23}$$

where $q_{liq,i-1}$ is the flow of liquid water into layer i from the layer above, $q_{liq,i}$ is the flow of water out of layer i to the layer below, $\left(\Delta w_{liq,i}\right)_p / \Delta t$ is the change in liquid water due to phase change (melting rate) (section 6.2). For the top snow layer only,

$$q_{liq,i-1} = q_{grnd,liq} + \left(q_{sdew} - q_{seva}\right) \tag{7.24}$$

where $q_{grnd,liq}$ is the rate of liquid precipitation reaching the snow (section 7.1), q_{seva} is the evaporation of liquid water and q_{sdew} is the liquid dew (section 5.4). After surface fluxes and snow/soil temperatures have been determined (sections 5 and 6), $w_{liq,snl+1}$ is updated for the liquid precipitation reaching the ground and dew or evaporation as

$$w_{liq,snl+1}^{n+1} = w_{liq,snl+1}^{n} + \left(q_{grnd,liq} + q_{sdew} - q_{seva} \right) \Delta t .$$ (7.25)

When the liquid water within a snow layer exceeds the layer's holding capacity, the excess water is added to the underlying layer, limited by the effective porosity $(1-\theta_{ice})$ of the layer. The flow of water is assumed to be zero ($q_{liq,i}=0$) if the effective porosity of either of the two layers ($1-\theta_{ice,i}$ and $1-\theta_{ice,i+1}$) is less than $\theta_{imp}=0.05$, the water impermeable volumetric water content. Thus, water flow between layers, $q_{liq,i}$, for layers $i=snl+1,\ldots,0$, is initially calculated as

$$q_{liq,i} = \frac{\rho_{liq}\left[\theta_{liq,i} - S_r \left(1 - \theta_{ice,i} \right) \right] \Delta z_i}{\Delta t} \geq 0$$ (7.26)

where the volumetric liquid water $\theta_{liq,i}$ and ice $\theta_{ice,i}$ contents are

$$\theta_{ice,i} = \frac{w_{ice,i}}{\Delta z_i \rho_{ice}} \leq 1$$ (7.27)

$$\theta_{liq,i} = \frac{w_{liq,i}}{\Delta z_i \rho_{liq}} \leq 1 - \theta_{ice,i} ,$$ (7.28)

and $S_r = 0.033$ is the irreducible water saturation (snow holds a certain amount of liquid water due to capillary retention after drainage has ceased (Anderson 1976)). The water holding capacity of the underlying layer limits the flow of water $q_{liq,i}$ calculated in equation (7.26), unless the underlying layer is the surface soil layer, as

$$q_{liq,i} \leq \frac{\rho_{liq}\left[1 - \theta_{ice,i+1} - \theta_{liq,i+1} \right] \Delta z_{i+1}}{\Delta t} \quad i = snl+1,\ldots,-1.$$ (7.29)

The volumetric liquid water content $\theta_{liq,i}$ is updated as

$$\theta_{liq,i}^{n+1} = \theta_{liq,i}^{n} + \left(q_{i-1} - q_i \right) \Delta t .$$ (7.30)

Equations (7.26)-(7.30) are solved sequentially from top ($i = snl + 1$) to bottom ($i = 0$) snow layer in each time step. The total flow of liquid water reaching the soil surface is then $q_{liq,0}$ which is used in the calculation of surface runoff and infiltration (section 7.3).

7.2.3 Black and organic carbon and mineral dust within snow

Particles within snow originate from atmospheric aerosol deposition (D_{sp} in Table 1.1 (kg m^{-2} s^{-1}) and influence snow radiative transfer (sections 3.2.1, 3.2.2, and 3.3.3). Particle masses and mixing ratios are represented with a simple mass-conserving scheme. The model maintains masses of the following eight particle species within each snow layer: hydrophilic black carbon, hydrophobic black carbon, hydrophilic organic carbon, hydrophobic organic carbon, and four species of mineral dust with the following particle sizes: 0.1-1.0, 1.0-2.5, 2.5-5.0, and 5.0-10.0 μm. Each of these species has unique optical properties (Table 3.5) and meltwater removal efficiencies (Table 7.1).

The black carbon and organic carbon deposition rates described in Table 1.1 are combined into four categories as follows

$$D_{bc,hphil} = D_{bc,dryhphil} + D_{bc,wethphil} \tag{7.31}$$

$$D_{bc,hphob} = D_{bc,dryhphob} \tag{7.32}$$

$$D_{oc,hphil} = D_{oc,dryhphil} + D_{oc,wethphil} \tag{7.33}$$

$$D_{oc,hphob} = D_{oc,dryhphob} \tag{7.34}$$

Deposited particles are assumed to be instantly mixed (homogeneously) within the surface snow layer and are added after the inter-layer water fluxes are computed (section 7.2.2) so that some aerosol is in the top layer after deposition and is not immediately washed out before radiative calculations are done. Particle masses are then redistributed

each time step based on meltwater drainage through the snow column (section 7.2.2) and snow layer combination and subdivision (section 7.2.6). The change in mass of each of the particle species $\Delta m_{sp,i}$ (kg m^{-2}) is

$$\Delta m_{sp,i} = \left[k_{sp} \left(q_{liq,i-1} c_{sp,i-1} - q_{liq,i} c_i \right) + D_{sp} \right] \Delta t \tag{7.35}$$

where k_{sp} is the meltwater scavenging efficiency that is unique for each species (Table 7.1), $q_{liq,i-1}$ is the flow of liquid water into layer i from the layer above, $q_{liq,i}$ is the flow of water out of layer i into the layer below (kg m^{-2} s^{-1}) (section 7.2.2), $c_{sp,i-1}$ and $c_{sp,i}$ are the particle mass mixing ratios in layers $i-1$ and i (kg kg^{-1}), D_{sp} is the atmospheric deposition rate (zero for all layers except layer $snl+1$), and Δt is the model time step (s). The particle mass mixing ratio is

$$c_i = \frac{m_{sp,i}}{w_{liq,i} + w_{ice,i}}. \tag{7.36}$$

Values of k_{sp} are partially derived from experiments published by Conway et al. (1996). Particles masses are re-distributed proportionately with snow mass when layers are combined or divided, thus conserving particle mass within the snow column. The mass of particles carried out with meltwater through the bottom snow layer is assumed to be permanently lost from the snowpack, and is not maintained within the model.

Table 7.1. Meltwater scavenging efficiency for particles within snow

Species	k_{sp}
Hydrophilic black carbon	0.20
Hydrophobic black carbon	0.03
Hydrophilic organic carbon	0.20
Hydrophobic organic carbon	0.03
Dust species 1 (0.1-1.0 μm)	0.02
Dust species 2 (1.0-2.5 μm)	0.02
Dust species 3 (2.5-5.0 μm)	0.01
Dust species 4 (5.0-10.0 μm)	0.01

7.2.4 Initialization of snow layer

If there are no existing snow layers ($snl + 1 = 1$) but $z_{sno} \geq 0.01$ m after accounting

for solid precipitation q_{sno}, then a snow layer is initialized ($snl = -1$) as follows

$$
\begin{aligned}
\Delta z_0 &= z_{sno} \\
z_o &= -0.5 \Delta z_0 \\
z_{h,-1} &= -\Delta z_0 \\
T_0 &= \min\left(T_f, T_{atm}\right) \\
w_{ice,0} &= W_{sno} \\
w_{liq,0} &= 0
\end{aligned}
\tag{7.37}
$$

7.2.5 Snow Compaction

Snow compaction is initiated after the soil hydrology calculations [surface runoff

(section 7.3), infiltration (section 7.3), soil water (section 7.4), groundwater-soilwater

interactions (section 7.5)] are complete. Compaction of snow includes three types of

processes: destructive metamorphism of new snow (crystal breakdown due to wind or

thermodynamic stress); snow load or overburden (pressure); and melting (changes in

snow structure due to melt-freeze cycles plus changes in crystals due to liquid water).

The total fractional compaction rate for each snow layer $C_{R,i}$ (s^{-1}) is the sum of the three compaction processes

$$C_{R,i} = \frac{1}{\Delta z_i} \frac{\partial \Delta z_i}{\partial t} = C_{R1,i} + C_{R2,i} + C_{R3,i}. \tag{7.38}$$

Compaction is not allowed if the layer is saturated

$$1 - \left(\frac{w_{ice,i}}{\Delta z_i \rho_{ice}} + \frac{w_{liq,i}}{\Delta z_i \rho_{liq}} \right) \leq 0.001 \tag{7.39}$$

or if the ice content is below a minimum value ($w_{ice,i} \leq 0.1$).

Compaction as a result of destructive metamorphism $C_{R1,i}$ (s^{-1}) is temperature dependent (Anderson 1976)

$$C_{R1,i} = \left[\frac{1}{\Delta z_i} \frac{\partial \Delta z_i}{\partial t} \right]_{metamorphism} = -c_3 c_1 c_2 \exp\left[-c_4 \left(T_f - T_i \right) \right] \tag{7.40}$$

where $c_3 = 2.777 \times 10^{-6}$ (s^{-1}) is the fractional compaction rate for $T_i = T_f$, $c_4 = 0.04$ K^{-1}, and

$$
\begin{array}{ll}
c_1 = 1 & \dfrac{w_{ice,i}}{\Delta z_i} \leq 100 \text{ kg m}^{-3} \\[3mm]
c_1 = \exp\left[-0.046\left(\dfrac{w_{ice,i}}{\Delta z_i} - 100 \right) \right] & \dfrac{w_{ice,i}}{\Delta z_i} > 100 \text{ kg m}^{-3} \\[3mm]
c_2 = 2 & \dfrac{w_{liq,i}}{\Delta z_i} > 0.01 \\[3mm]
c_2 = 1 & \dfrac{w_{liq,i}}{\Delta z_i} \leq 0.01
\end{array}
\tag{7.41}
$$

where $w_{ice,i}/\Delta z_i$ and $w_{liq,i}/\Delta z_i$ are the bulk densities of liquid water and ice (kg m^{-3}).

The compaction rate as a result of overburden $C_{R2,i}$ (s^{-1}) is a linear function of the snow load pressure $P_{s,i}$ (kg m^{-2}) (Anderson 1976)

$$C_{R2,i} = \left[\frac{1}{\Delta z_i} \frac{\partial \Delta z_i}{\partial t} \right]_{overburden} = -\frac{P_{s,i}}{\eta} \tag{7.42}$$

where η is a viscosity coefficient (kg s m^{-2}) that varies with density and temperature as

$$\eta = \eta_0 \exp \left[c_5 \left(T_f - T_i \right) + c_6 \frac{w_{ice,i}}{\Delta z_i} \right] \tag{7.43}$$

where $\eta_0 = 9 \times 10^5$ kg s m^{-2}, and $c_5 = 0.08$ K^{-1}, $c_6 = 0.023$ m^3 kg^{-1} are constants. The snow load pressure $P_{s,i}$ is calculated for each layer as the sum of the ice $w_{ice,i}$ and liquid water contents $w_{liq,i}$ of the layers above plus half the ice and liquid water contents of the layer being compacted

$$P_{s,i} = \frac{\left(w_{ice,i} + w_{liq,i} \right)}{2} + \sum_{j=snl+1}^{j=i-1} \left(w_{ice,j} + w_{liq,j} \right). \tag{7.44}$$

The compaction rate due to melting $C_{R3,i}$ (s^{-1}) is taken to be the ratio of the change in snow ice fraction after the melting to the fraction before melting

$$C_{R3,i} = \left[\frac{1}{\Delta z_i} \frac{\partial \Delta z_i}{\partial t} \right]_{melt} = -\frac{1}{\Delta t} \max \left(0, \frac{f_{ice,i}^n - f_{ice,i}^{n+1}}{f_{ice,i}^n} \right) \tag{7.45}$$

where the fraction of ice $f_{ice,i}$ is

$$f_{ice,i} = \frac{w_{ice,i}}{w_{ice,i} + w_{liq,i}} \tag{7.46}$$

and melting is identified during the phase change calculations (section 6.2).

The snow layer thickness after compaction is then

$$\Delta z_i^{n+1} = \Delta z_i^n \left(1 + C_{R,i}\Delta t\right).$$ (7.47)

7.2.6 Snow Layer Combination and Subdivision

After the determination of snow temperature including phase change (section 6), snow hydrology (sections 7.2.1, 7.2.2, and 7.2.3), and the compaction calculations (7.2.5), the number of snow layers is adjusted by either combining or subdividing layers. The combination and subdivision of snow layers is based on Jordan (1991).

7.2.6.1 Combination

If a snow layer has nearly melted or if its thickness Δz_i is less than the prescribed minimum thickness Δz_{min} (Table 7.2), the layer is combined with a neighboring layer. The overlying or underlying layer is selected as the neighboring layer according to the following rules

- If the top layer is being removed, it is combined with the underlying layer

- If the underlying layer is not snow (i.e., it is the top soil layer), the layer is combined with the overlying layer

- If the layer is nearly completely melted, the layer is combined with the underlying layer

- If none of the above rules apply, the layer is combined with the thinnest neighboring layer.

A first pass is made through all snow layers to determine if any layer is nearly melted ($w_{ice,i} \leq 0.1$). If so, the remaining liquid water and ice content of layer i is combined with the underlying neighbor $i+1$ as

$$w_{liq,i+1} = w_{liq,i+1} + w_{liq,i}$$ (7.48)

$$w_{ice,i+1} = w_{ice,i+1} + w_{ice,i} \,. \tag{7.49}$$

This includes the snow layer directly above the top soil layer. In this case, the liquid water and ice content of the melted snow layer is added to the contents of the top soil layer. The layer properties, T_i, $w_{ice,i}$, $w_{liq,i}$, Δz_i, are then re-indexed so that the layers above the eliminated layer are shifted down by one and the number of snow layers is decremented accordingly.

At this point, if there are no explicit snow layers remaining ($snl = 0$), the snow water equivalent W_{sno} and snow depth z_{sno} are set to zero, otherwise, W_{sno} and z_{sno} are re-calculated as

$$W_{sno} = \sum_{i=snl+1}^{i=0} \left(w_{ice,i} + w_{liq,i} \right) \tag{7.50}$$

$$z_{sno} = \sum_{i=snl+1}^{i=0} \Delta z_i \,. \tag{7.51}$$

If the snow depth $0 < z_{sno} < 0.01$ m, the number of snow layers is set to zero, the total ice content of the snowpack $\sum_{i=snl+1}^{i=0} w_{ice,i}$ is assigned to W_{sno}, and the total liquid water $\sum_{i=snl+1}^{i=0} w_{liq,i}$ is assigned to the top soil layer. Otherwise, the layers are combined according to the rules above.

When two snow layers are combined (denoted here as 1 and 2), their thickness combination (c) is

$$\Delta z_c = \Delta z_1 + \Delta z_2 \,, \tag{7.52}$$

their mass combination is

$$w_{liq,c} = w_{liq,1} + w_{liq,2} \qquad (7.53)$$

$$w_{ice,c} = w_{ice,1} + w_{ice,2}, \qquad (7.54)$$

and their temperatures are combined as

$$T_c = T_f + \frac{h_c - L_f w_{liq,c}}{C_{ice} w_{ice,c} + C_{liq} w_{liq,c}} \qquad (7.55)$$

where $h_c = h_1 + h_2$ is the combined enthalpy h_i of the two layers where

$$h_i = \left(C_{ice} w_{ice,i} + C_{liq} w_{liq,i} \right)\left(T_i - T_f \right) + L_f w_{liq,i}. \qquad (7.56)$$

In these equations, L_f is the latent heat of fusion (J kg^{-1}) and C_{liq} and C_{ice} are the specific heat capacities (J kg^{-1} K^{-1}) of liquid water and ice, respectively (Table 1.4). After layer combination, the node depths and layer interfaces (Figure 7.2) are recalculated from

$$z_i = z_{h,i} - 0.5\Delta z_i \qquad i = 0,\ldots, snl + 1 \qquad (7.57)$$

$$z_{h,i-1} = z_{h,i} - \Delta z_i \qquad i = 0,\ldots, snl + 1 \qquad (7.58)$$

where Δz_i is the layer thickness.

Table 7.2. Minimum and maximum thickness of snow layers (m)

Layer	Δz_{min}	N_l	N_u	$(\Delta z_{max})_l$	$(\Delta z_{max})_u$
1 (top)	0.010	1	>1	0.03	0.02
2	0.015	2	>2	0.07	0.05
3	0.025	3	>3	0.18	0.11
4	0.055	4	>4	0.41	0.23
5 (bottom)	0.115	5	-	-	-

The maximum snow layer thickness, Δz_{max}, depends on the number of layers, N_l and N_u

7.2.6.2 Subdivision

The snow layers are subdivided when the layer thickness exceeds the prescribed maximum thickness $\Delta z_{\max}$ with lower and upper bounds that depend on the number of snow layers (Table 7.2). For example, if there is only one layer, then the maximum thickness of that layer is 0.03 m, however, if there is more than one layer, then the maximum thickness of the top layer is 0.02 m. Layers are checked sequentially from top to bottom for this limit. If there is only one snow layer and its thickness is greater than 0.03 m (Table 7.2), the layer is subdivided into two layers of equal thickness, liquid water and ice contents, and temperature. If there is an existing layer below the layer to be subdivided, the thickness Δz_i, liquid water and ice contents, $w_{liq,i}$ and $w_{ice,i}$, and temperature T_i of the excess snow are combined with the underlying layer according to equations (7.52)-(7.55). If there is no underlying layer after adjusting the layer for the excess snow, the layer is subdivided into two layers of equal thickness, liquid water and ice contents. The vertical snow temperature profile is maintained by calculating the slope between the layer above the splitting layer (T_1) and the splitting layer (T_2) and constraining the new temperatures (T_2^{n+1}, T_3^{n+1}) to lie along this slope. The temperature of the lower layer is first evaluated from

$$T_3' = T_2^n - \left(\frac{T_1^n - T_2^n}{\left(\Delta z_1^n + \Delta z_2^n \right)/2} \right)\left(\frac{\Delta z_2^{n+1}}{2} \right),$$
(7.59)

then adjusted as,

$$
\begin{aligned}
T_3^{n+1} &= T_2^n & T_3' &\geq T_f \\
T_2^{n+1} &= T_2^n + \left(\frac{T_1^n - T_2^n}{\left(\Delta z_1 + \Delta z_2^n \right)/2} \right)\left(\frac{\Delta z_2^{n+1}}{2} \right) & T_3' &< T_f
\end{aligned}
$$
(7.60)

where here the subscripts 1, 2, and 3 denote three layers numbered from top to bottom. After layer subdivision, the node depths and layer interfaces are recalculated from equations (7.57) and (7.58).

7.3 Surface Runoff and Infiltration

The simple TOPMODEL-based (Beven and Kirkby 1979) runoff model (SIMTOP) described by Niu et al. (2005) is implemented to parameterize runoff. A key concept underlying this approach is that of fractional saturated/impermeable area f_{sat}, which is determined by the topographic characteristics and soil moisture state of a grid cell. The surface runoff consists of overland flow due to saturation excess (Dunne runoff) and infiltration excess (Hortonian runoff) mechanisms

$$q_{over} = f_{sat} q_{liq,0} + \left(1 - f_{sat}\right) \max \left(0, q_{liq,0} - q_{infl,\max}\right) \tag{7.61}$$

where $q_{liq,0}$ is liquid precipitation reaching the ground plus any melt water from snow (kg m^{-2} s^{-1}) and $q_{infl,\max}$ is a maximum soil infiltration capacity (kg m^{-2} s^{-1}). In Niu et al. (2005), f_{sat} was a function of soil moisture whose potential or maximum value, $f_{\max}$, was solely determined by topographic characteristics. Niu and Yang (2006) modified the expression for f_{sat} to include a dependence on impermeable area fraction in frozen soil, $f_{frz,1}$, of the top $i = 1$ soil layer as

$$f_{sat} = \left(1 - f_{frz,1}\right) f_{\max} \exp\left(-0.5 f_{over} z_{\nabla}\right) + f_{frz,1} \tag{7.62}$$

where $f_{\max}$ is the maximum saturated fraction, f_{over} is a decay factor (m^{-1}), and z_{∇} is the water table depth (m) (section 7.5). The maximum saturated fraction, $f_{\max}$, is defined as the discrete cumulative distribution function (CDF) of the topographic index when the

grid cell mean water table depth is zero. Thus, f_{max} is the percent of pixels in a grid cell whose topographic index is larger than or equal to the grid cell mean topographic index. It should be calculated explicitly from the CDF at each grid cell at the resolution that the model is run. However, because this is a computationally intensive task for global applications, f_{max} is calculated once from the CDF at a spatial resolution of 0.5° by 0.5° following Niu et al. (2005) and then area-averaged to the desired resolution (section 1.2.3). The 0.5° resolution is compatible with the resolution of other CLM input surface datasets (e.g., plant functional types, leaf area index). The decay factor f_{over} for global simulations was determined through sensitivity analysis and comparison with observed runoff to be 0.5 m^{-1}.

The impermeable fraction $f_{frz,i}$ is parameterized as a function of soil ice content (Niu and Yang 2006)

$$f_{frz,i} = \frac{\exp\left[-\alpha\left(1 - \frac{w_{ice,i}}{w_{ice,i} + w_{liq,i}}\right)\right] - \exp(-\alpha)}{1 - \exp(-\alpha)}$$ (7.63)

where $\alpha = 3$ is an adjustable scale-dependent parameter, and $w_{ice,i}$ and $w_{liq,i}$ are the ice and liquid water contents of soil layer i (kg m^{-2}).

The maximum infiltration capacity $q_{infl,max}$ in equation (7.61) is determined from soil texture and soil moisture (Entekhabi and Eagleson 1989) as

$$q_{infl,max} = k_{sat,1}\left[1 + v(s-1)\right].$$ (7.64)

The liquid water content of the top soil layer relative to effective porosity and adjusted for saturated fraction is determined from

$$s = \frac{\dfrac{\theta_{liq,1}}{\max\left(\theta_{imp}, \theta_{sat,1} - \theta_{ice,1}\right)} - f_{sat}}{1 - f_{sat}} \geq 0 \qquad \frac{\theta_{liq,1}}{\max\left(\theta_{imp}, \theta_{sat,1} - \theta_{ice,1}\right)} \geq 0.01 \qquad (7.65)$$

$$1 - f_{sat} \geq 0.01$$

where $\theta_{liq,1}$ and $\theta_{ice,1}$ are the volumetric liquid water and ice contents of the top soil layer, and $\theta_{imp} = 0.05$ is a minimum effective porosity. The variable v is

$$v = -\left(\frac{d\psi}{ds}\right)_{s=1} \frac{1}{0.5\Delta z_1} \qquad (7.66)$$

where Δz_1 is the thickness of the top soil layer (mm) and

$$\left(\frac{d\psi}{ds}\right)_{s=1} = -B_1 \psi_{sat,1} . \qquad (7.67)$$

The saturated hydraulic conductivity $k_{sat,1}$ (kg m^{-2} s^{-1}), volumetric water content at saturation (i.e., porosity) $\theta_{sat,1}$, Clapp and Hornberger (1978) exponent B_1, and saturated soil matric potential $\psi_{sat,1}$ (mm) are determined from soil texture (section 7.4.1).

Infiltration into the surface soil layer is defined as the residual of the surface water balance

$$q_{infl} = q_{liq,0} - q_{over} - q_{seva} \qquad (7.68)$$

when no snow layers exist, and

$$q_{infl} = q_{liq,0} - q_{over} \qquad (7.69)$$

when at least one snow layer is present. q_{seva} is the evaporation of liquid water from the top soil layer (section 5.4). Infiltration q_{infl} and explicit surface runoff q_{over} are not allowed for glaciers and wetlands.

7.4   Soil Water

Soil water is predicted from a multi-layer model, in which the vertical soil moisture transport is governed by infiltration, surface and sub-surface runoff, gradient diffusion, gravity, canopy transpiration through root extraction, and interactions with groundwater (Figure 7.1). The following derivation generally follows that of Z.-L. Yang (1998, unpublished manuscript) with modifications by Zeng and Decker (2009).

For one-dimensional vertical water flow in soils, the conservation of mass is stated as

$$\frac{\partial \theta}{\partial t} = -\frac{\partial q}{\partial z} - Q \tag{7.70}$$

where θ is the volumetric soil water content (mm^3 of water mm^{-3} of soil), t is time (s), z is height above some datum in the soil column (mm) (positive upwards), q is soil water flux ($kg\ m^{-2}\ s^{-1}$ or $mm\ s^{-1}$) (positive upwards), and Q is a soil moisture sink term (mm of water mm^{-1} of soil s^{-1}) (ET loss). This equation is solved numerically by dividing the soil column into multiple layers in the vertical and integrating downward over each layer with an upper boundary condition of the infiltration flux into the top soil layer q_{infl} and a lower boundary condition specified as zero flux.

The soil water flux q in equation (7.70) can be described by Darcy's law

$$q = -k \frac{\partial \psi_h}{\partial z} \tag{7.71}$$

where k is the hydraulic conductivity ($mm\ s^{-1}$), and ψ_h is the hydraulic potential (mm). The hydraulic potential is

$$\psi_h = \psi_m + \psi_z \tag{7.72}$$

138

where ψ_m is the soil matric potential (mm) (which is related to the adsorptive and capillary forces within the soil matrix), and ψ_z is the gravitational potential (mm) (the vertical distance from an arbitrary reference elevation to a point in the soil). If the reference elevation is the soil surface, then $\psi_z = z$. Letting $\psi = \psi_m$, Darcy's law becomes

$$q = -k \left[\frac{\partial(\psi + z)}{\partial z} \right]. \tag{7.73}$$

Darcy's equation can be further manipulated to yield

$$q = -k \left[\frac{\partial(\psi + z)}{\partial z} \right] = -k \left(\frac{\partial \psi}{\partial z} + 1 \right) = -k \left(\frac{\partial \theta}{\partial z} \frac{\partial \psi}{\partial \theta} + 1 \right). \tag{7.74}$$

Substitution of this equation into equation (7.70), with $Q = 0$, yields the Richards equation

$$\frac{\partial \theta}{\partial t} = \frac{\partial}{\partial z} \left[k \left(\frac{\partial \theta}{\partial z} \frac{\partial \psi}{\partial \theta} \right) + 1 \right]. \tag{7.75}$$

Zeng and Decker (2009) note that this θ-based form of the Richards equation cannot maintain the hydrostatic equilibrium soil moisture distribution because of the truncation errors of the finite-difference numerical scheme. They show that this deficiency can be overcome by subtracting the equilibrium state from equation (7.73) as

$$q = -k \left[\frac{\partial(\psi + z - C)}{\partial z} \right] \tag{7.76}$$

where C is a constant hydraulic potential above the water table z_∇

$$C = \psi_E + z = \psi_{sat} \left[\frac{\theta_E(z)}{\theta_{sat}} \right]^{-B} + z = \psi_{sat} + z_\nabla \tag{7.77}$$

so that

$$q = -k \left[\frac{\partial (\psi - \psi_E)}{\partial z} \right]$$ (7.78)

where ψ_E is the equilibrium soil matric potential (mm). Substitution of equations (7.77) and (7.76) into equation (7.75) yields Zeng and Decker's (2009) modified Richards equation

$$\frac{\partial \theta}{\partial t} = \frac{\partial}{\partial z} \left[k \left(\frac{\partial (\psi - \psi_E)}{\partial z} \right) \right] - Q$$ (7.79)

where the soil moisture sink term Q is now included.

7.4.1 Hydraulic Properties

The hydraulic conductivity k_i (mm s^{-1}) and the soil matric potential ψ_i (mm) for layer i vary with volumetric soil water θ_i and soil texture. As with the soil thermal properties (section 6.3) the hydraulic properties of the soil are assumed to be a weighted combination of the mineral properties, which are determined according to sand and clay contents based on work by Clapp and Hornberger (1978) and Cosby et al. (1984), and organic properties of the soil (Lawrence and Slater 2008).

The hydraulic conductivity is defined at the depth of the interface of two adjacent layers $z_{h,i}$ (Figure 7.3) and is a function of the saturated hydraulic conductivity $k_{sat} \left[z_{h,i} \right]$, the total (ice plus liquid) volumetric soil moisture of the two layers θ_i and θ_{i+1} and the impermeable fraction $f_{frz,i}$

$$k\left[z_{h,i}\right] = \begin{cases} \left(1 - \dfrac{f_{frz,i} + f_{frz,i+1}}{2}\right) k_{sat}\left[z_{h,i}\right] \left[\dfrac{0.5\left(\theta_i + \theta_{i+1}\right)}{0.5\left(\theta_{sat,i} + \theta_{sat,i+1}\right)}\right]^{2B_i + 3} & 1 \le i \le N_{levsoi} - 1 \\[2em] \left(1 - f_{frz,i}\right) k_{sat}\left[z_{h,i}\right] \left(\dfrac{\theta_i}{\theta_{sat,i}}\right)^{2B_i + 3} & i = N_{levsoi} \end{cases} \tag{7.80}$$

where $f_{frz,i}$ is defined in equation (7.63).

Because the hydraulic properties of mineral and organic soil may differ significantly, the bulk hydraulic properties of each soil layer are computed as weighted averages of the properties of the mineral and organic components. The water content at saturation (i.e. porosity) is

$$\theta_{sat,i} = (1 - f_{om,i})\theta_{sat,min,i} + f_{om,i}\theta_{sat,om} \tag{7.81}$$

where $f_{om,i}$ is the soil organic matter fraction, $\theta_{sat,om} = 0.9$ (Farouki 1981; Letts et al. 2000) is the porosity of organic matter and the porosity of the mineral soil $\theta_{sat,min,i}$ is

$$\theta_{sai,min,i} = 0.489 - 0.00126(\% \, sand)_i \tag{7.82}$$

The exponent "B" is

$$B_i = (1 - f_{om,i})B_{min,i} + f_{om,i}B_{om} \tag{7.83}$$

where $B_{om} = 2.7$ (Letts et al. 2000) and

$$B_{min,i} = 2.91 + 0.159(\% \, clay)_i . \tag{7.84}$$

The soil matric potential (mm) is defined at the node depth z_i of each layer i (Figure 7.3)

$$\psi_i = \psi_{sat,i} \left(\dfrac{\theta_i}{\theta_{sat,i}}\right)^{-B_i} \ge -1 \times 10^8 \qquad 0.01 \le \dfrac{\theta_i}{\theta_{sat,i}} \le 1 \tag{7.85}$$

where the saturated soil matric potential (mm) is

$$\psi_{sat,i} = (1 - f_{om,i})\psi_{sat,\min,i} + f_{om,i}\psi_{sat,om} \tag{7.86}$$

where $\psi_{sat,om} = -10.3$ mm (Letts et al. 2000) is the saturated organic matter matric potential and the saturated mineral soil matric potential $\psi_{sat,\min,i}$ is

$$\psi_{sat,\min,i} = -10.0 \times 10^{1.88 - 0.0131(\% \, sand)_i}. \tag{7.87}$$

The saturated hydraulic conductivity, $k_{sat}\left[z_{h,i}\right]$ (mm s^{-1}), for organic soils ($k_{sat,om}$) may be two to three orders of magnitude larger than that of mineral soils ($k_{sat,\min}$). Bulk soil layer values of k_{sat} calculated as weighted averages based on f_{om} may therefore be determined primarily by the organic soil properties even for values of f_{om} as low as 1 %. To better represent the influence of organic soil material on the grid cell average saturated hydraulic conductivity, the soil organic matter fraction is further subdivided into "connected" and "unconnected" fractions using a result from percolation theory (Stauffer and Aharony 1994, Berkowitz and Balberg 1992). Assuming that the organic and mineral fractions are randomly distributed throughout a soil layer, percolation theory predicts that above a threshold value $f_{om} = f_{threshold}$, connected flow pathways consisting of organic material only exist and span the soil space. Flow through these pathways interacts only with organic material, and thus can be described by $k_{sat,om}$. This fraction of the grid cell is given by

$$
\begin{aligned}
f_{perc} &= N_{perc}\left(f_{om} - f_{threshold}\right)^{\beta_{perc}} f_{om} & f_{om} &\geq f_{threshold} \\
f_{perc} &= 0 & f_{om} &< f_{threshold}
\end{aligned}
\tag{7.88}
$$

where $\beta^{perc} = 0.139$, $f_{threshold} = 0.5$, and $N_{perc} = \left(1 - f_{threshold}\right)^{-\beta_{perc}}$. In the unconnected portion of the grid cell, $f_{uncon} = \left(1 - f_{perc}\right)$, the saturated hydraulic conductivity is

assumed to correspond to flow pathways that pass through the mineral and organic components in series

$$k_{sat,uncon} = f_{uncon} \left(\frac{(1-f_{om})}{k_{sat,min}} + \frac{(f_{om} - f_{perc})}{k_{sat,om}} \right)^{-1}. \tag{7.89}$$

where saturated hydraulic conductivity for mineral soil depends on soil texture (Cosby et al. 1984) as

$$k_{sat,min} \left[z_{h,i} \right] = 0.0070556 \times 10^{-0.884 + 0.0153(\% \, sand)_i}. \tag{7.90}$$

The bulk soil layer saturated hydraulic conductivity is then computed as

$$k_{sat} \left[z_{h,i} \right] = f_{uncon,i} k_{sat,uncon} \left[z_{h,i} \right] + (1 - f_{uncon,i}) k_{sat,om} \left[z_{h,i} \right]. \tag{7.91}$$

7.4.2 Numerical Solution

With reference to Figure 7.3, the equation for conservation of mass (equation (7.70)) can be integrated over each layer as

$$\int_{-z_{h,i}}^{-z_{h,i-1}} \frac{\partial \theta}{\partial t} dz = -\int_{-z_{h,i}}^{-z_{h,i-1}} \frac{\partial q}{\partial z} dz - \int_{-z_{h,i}}^{-z_{h,i-1}} Q \, dz. \tag{7.92}$$

Note that the integration limits are negative since z is defined as positive upward from the soil surface. This equation can be written as

$$\Delta z_i \frac{\partial \theta_{liq,i}}{\partial t} = -q_{i-1} + q_i - e_i \tag{7.93}$$

where q_i is the flux of water across interface $z_{h,i}$, q_{i-1} is the flux of water across interface $z_{h,i-1}$, and e_i is a layer-averaged soil moisture sink term (ET loss) defined as positive for flow out of the layer (mm s^{-1}). Taking the finite difference with time and evaluating the fluxes implicitly at time $n+1$ yields

$$\frac{\Delta z_i \Delta \theta_{liq,i}}{\Delta t} = -q_{i-1}^{n+1} + q_i^{n+1} - e_i \qquad (7.94)$$

where $\Delta \theta_{liq,i} = \theta_{liq,i}^{n+1} - \theta_{liq,i}^{n}$ is the change in volumetric soil liquid water of layer i in time Δt and Δz_i is the thickness of layer i (mm).

The water removed by transpiration in each layer e_i is a function of the total transpiration E_v^t (section 5) and the effective root fraction $r_{e,i}$

$$e_i = r_{e,i} E_v^t . \qquad (7.95)$$

Figure 7.3. Schematic diagram of numerical scheme used to solve for soil water fluxes. Shown are three soil layers, $i-1$, i, and $i+1$. The soil matric potential ψ and volumetric soil water θ_{liq} are defined at the layer node depth z. The hydraulic conductivity $k[z_h]$ is defined at the interface of two layers z_h. The layer thickness is Δz. The soil water fluxes q_{i-1} and q_i are defined as positive upwards. The soil moisture sink term e (ET loss) is defined as positive for flow out of the layer.
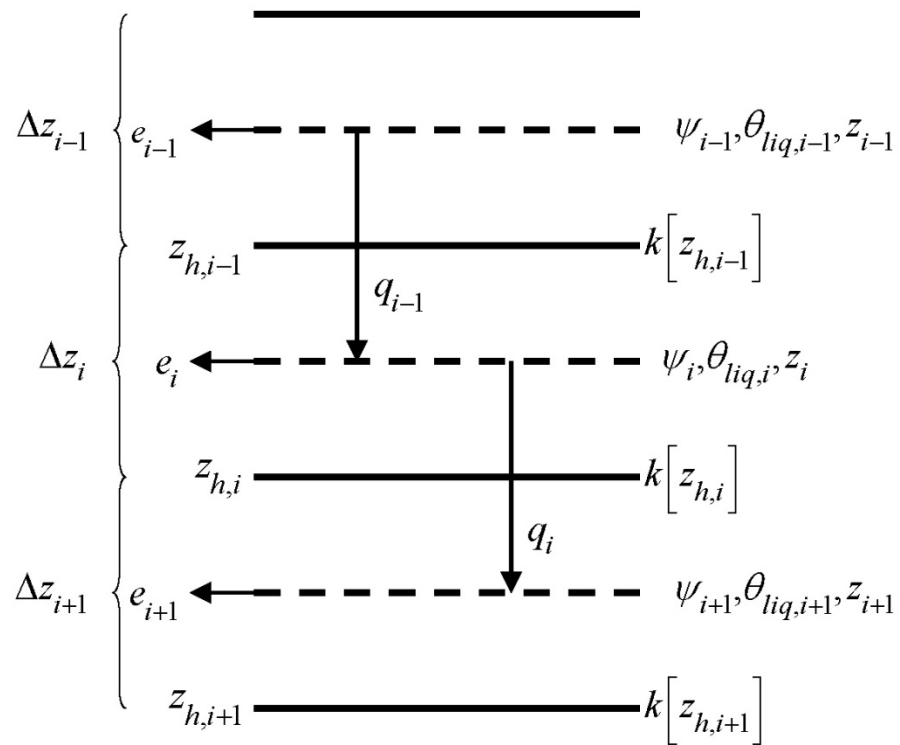
Note that because more than one plant functional type (PFT) may share a soil column, the transpiration E_v^t is a weighted sum of transpiration from all PFTs whose weighting depends on PFT area as

$$E_v^t = \sum_{j=1}^{npft} \left(E_v^t \right)_j \left(wt \right)_j \qquad (7.96)$$

where $npft$ is the number of PFTs sharing a soil column, $\left(E_v^t \right)_j$ is the transpiration from the jth PFT on the column, and $\left(wt \right)_j$ is the relative area of the jth PFT with respect to the column. The effective root fraction $r_{e,i}$ is also a column-level quantity that is a weighted sum over all PFTs. The weighting depends on the per unit area transpiration of each PFT and its relative area as

$$r_{e,i} = \frac{\sum_{j=1}^{npft} \left(r_{e,i} \right)_j \left(E_v^t \right)_j \left(wt \right)_j}{\sum_{j=1}^{npft} \left(E_v^t \right)_j \left(wt \right)_j} \qquad (7.97)$$

where $\left(r_{e,i} \right)_j$ is the effective root fraction for the jth PFT

$$\begin{aligned}
\left(r_{e,i} \right)_j &= \frac{\left(r_i \right)_j \left(w_i \right)_j}{\left(\beta_t \right)_j} & \left(\beta_t \right)_j &> 0 \\
\left(r_{e,i} \right)_j &= 0 & \left(\beta_t \right)_j &= 0
\end{aligned} \qquad (7.98)$$

and $\left(r_i \right)_j$ is the fraction of roots in layer i (section 8), $\left(w_i \right)_j$ is a soil dryness or plant wilting factor for layer i (section 8), and $\left(\beta_t \right)_j$ is a wetness factor for the total soil column for the jth PFT (section 8).

146

The soil water fluxes in equation (7.94), which are a function of $\theta_{liq,i}$ and $\theta_{liq,i+1}$ because of their dependence on hydraulic conductivity and soil matric potential, can be linearized about θ using a Taylor series expansion as

$$q_i^{n+1} = q_i^n + \frac{\partial q_i}{\partial \theta_{liq,i}} \Delta \theta_{liq,i} + \frac{\partial q_i}{\partial \theta_{liq,i+1}} \Delta \theta_{liq,i+1} \qquad (7.99)$$

$$q_{i-1}^{n+1} = q_{i-1}^n + \frac{\partial q_{i-1}}{\partial \theta_{liq,i-1}} \Delta \theta_{liq,i-1} + \frac{\partial q_{i-1}}{\partial \theta_{liq,i}} \Delta \theta_{liq,i} . \qquad (7.100)$$

Substitution of these expressions for q_i^{n+1} and q_{i-1}^{n+1} into equation (7.94) results in a general tridiagonal equation set of the form

$$r_i = a_i \Delta \theta_{liq,i-1} + b_i \Delta \theta_{liq,i} + c_i \Delta \theta_{liq,i+1} \qquad (7.101)$$

where

$$a_i = -\frac{\partial q_{i-1}}{\partial \theta_{liq,i-1}} \qquad (7.102)$$

$$b_i = \frac{\partial q_i}{\partial \theta_{liq,i}} - \frac{\partial q_{i-1}}{\partial \theta_{liq,i}} - \frac{\Delta z_i}{\Delta t} \qquad (7.103)$$

$$c_i = \frac{\partial q_i}{\partial \theta_{liq,i+1}} \qquad (7.104)$$

$$r_i = q_{i-1}^n - q_i^n + e_i . \qquad (7.105)$$

The tridiagonal equation set is solved over $i = 1, \ldots, N_{levsoi} + 1$ where the layer $i = N_{levsoi} + 1$ is a virtual layer representing the aquifer.

The finite-difference forms of the fluxes and partial derivatives in equations (7.102) -(7.105) can be obtained from equation (7.78) as

147

$$q_{i-1}^n = -k\left[z_{h,i-1}\right]\left[\frac{\left(\psi_{i-1}-\psi_i\right)+\left(\psi_{E,i}-\psi_{E,i-1}\right)}{z_i-z_{i-1}}\right] \tag{7.106}$$

$$q_i^n = -k\left[z_{h,i}\right]\left[\frac{\left(\psi_i-\psi_{i+1}\right)+\left(\psi_{E,i+1}-\psi_{E,i}\right)}{z_{i+1}-z_i}\right] \tag{7.107}$$

$$\frac{\partial q_{i-1}}{\partial \theta_{liq,i-1}} = -\left[\frac{k\left[z_{h,i-1}\right]}{z_i-z_{i-1}}\frac{\partial \psi_{i-1}}{\partial \theta_{liq,i-1}}\right] - \frac{\partial k\left[z_{h,i-1}\right]}{\partial \theta_{liq,i-1}}\left[\frac{\left(\psi_{i-1}-\psi_i\right)+\left(\psi_{E,i}-\psi_{E,i-1}\right)}{z_i-z_{i-1}}\right] \tag{7.108}$$

$$\frac{\partial q_{i-1}}{\partial \theta_{liq,i}} = \left[\frac{k\left[z_{h,i-1}\right]}{z_i-z_{i-1}}\frac{\partial \psi_i}{\partial \theta_{liq,i}}\right] - \frac{\partial k\left[z_{h,i-1}\right]}{\partial \theta_{liq,i}}\left[\frac{\left(\psi_{i-1}-\psi_i\right)+\left(\psi_{E,i}-\psi_{E,i-1}\right)}{z_i-z_{i-1}}\right] \tag{7.109}$$

$$\frac{\partial q_i}{\partial \theta_{liq,i}} = -\left[\frac{k\left[z_{h,i}\right]}{z_{i+1}-z_i}\frac{\partial \psi_i}{\partial \theta_{liq,i}}\right] - \frac{\partial k\left[z_{h,i}\right]}{\partial \theta_{liq,i}}\left[\frac{\left(\psi_i-\psi_{i+1}\right)+\left(\psi_{E,i+1}-\psi_{E,i}\right)}{z_{i+1}-z_i}\right] \tag{7.110}$$

$$\frac{\partial q_i}{\partial \theta_{liq,i+1}} = \left[\frac{k\left[z_{h,i}\right]}{z_{i+1}-z_i}\frac{\partial \psi_{i+1}}{\partial \theta_{liq,i+1}}\right] - \frac{\partial k\left[z_{h,i}\right]}{\partial \theta_{liq,i+1}}\left[\frac{\left(\psi_i-\psi_{i+1}\right)+\left(\psi_{E,i+1}-\psi_{E,i}\right)}{z_{i+1}-z_i}\right]. \tag{7.111}$$

The derivatives of the soil matric potential at the node depth are derived from equation (7.85)

$$\frac{\partial \psi_{i-1}}{\partial \theta_{liq,i-1}} = -B_{i-1}\frac{\psi_{i-1}}{\theta_{i-1}} \tag{7.112}$$

$$\frac{\partial \psi_i}{\partial \theta_{liq,i}} = -B_i\frac{\psi_i}{\theta_i} \tag{7.113}$$

$$\frac{\partial \psi_{i+1}}{\partial \theta_{liq,i+1}} = -B_{i+1}\frac{\psi_{i+1}}{\theta_{i+1}} \tag{7.114}$$

with the constraint $0.01\theta_{sat,i} \leq \theta_i \leq \theta_{sat,i}$.

The derivatives of the hydraulic conductivity at the layer interface are derived from equation (7.80)

$$\frac{\partial k\left[z_{h,i-1}\right]}{\partial \theta_{liq,i-1}} = \frac{\partial k\left[z_{h,i-1}\right]}{\partial \theta_{liq,i}} = \left(1 - \frac{f_{frz,i-1} + f_{frz,i}}{2}\right)(2B_{i-1} + 3)k_{sat}\left[z_{h,i-1}\right] \times$$
$$\left[\frac{0.5\left(\theta_{i-1} + \theta_i\right)}{0.5\left(\theta_{sat,i-1} + \theta_{sat,i}\right)}\right]^{2B_{i-1}+2}\left(\frac{0.5}{\theta_{sat,i-1}}\right) \tag{7.115}$$

$$\frac{\partial k\left[z_{h,i}\right]}{\partial \theta_{liq,i}} = \frac{\partial k\left[z_{h,i}\right]}{\partial \theta_{liq,i+1}} = \left(1 - \frac{f_{frz,i} + f_{frz,i+1}}{2}\right)(2B_i + 3)k_{sat}\left[z_{h,i}\right] \times$$
$$\left[\frac{0.5\left(\theta_i + \theta_{i+1}\right)}{0.5\left(\theta_{sat,i} + \theta_{sat,i+1}\right)}\right]^{2B_i+2}\left(\frac{0.5}{\theta_{sat,i}}\right) \tag{7.116}$$

7.4.2.1 Equilibrium soil matric potential and volumetric moisture

The equilibrium soil matric potential ψ_E can be derived from equation (7.77) as

$$\psi_E = \psi_{sat}\left(\frac{\theta_E(z)}{\theta_{sat}}\right)^{-B} \tag{7.117}$$

and the equilibrium volumetric water content $\theta_E(z)$ at depth z can also be derived as

$$\theta_E(z) = \theta_{sat}\left(\frac{\psi_{sat} + z_\nabla - z}{\psi_{sat}}\right)^{-\frac{1}{B}}. \tag{7.118}$$

Here, the soil matric potentials, the water table depth z_∇ and the soil depths have units of mm. For the finite-difference scheme, a layer-average equilibrium volumetric water content is used in equation (7.117) and can be obtained from

$$\overline{\theta_{E,i}} = \int_{z_{h,i-1}}^{z_{h,i}} \frac{\theta_E(z)}{z_{h,i} - z_{h,i-1}} dz \tag{7.119}$$

which when integrated yields

$$\overline{\theta_{E,i}} = \frac{\theta_{sat,i}\psi_{sat,i}}{\left(z_{h,i} - z_{h,i-1}\right)\left(1 - \frac{1}{B_i}\right)}\left[\left(\frac{\psi_{sat,i} - z_\nabla + z_{h,i}}{\psi_{sat,i}}\right)^{1-\frac{1}{B_i}} - \left(\frac{\psi_{sat,i} - z_\nabla + z_{h,i-1}}{\psi_{sat,i}}\right)^{1-\frac{1}{B_i}}\right].\text{(7.120)}$$

Equation (7.120) is valid when the water table z_∇ is deeper than both interface depths $z_{h,i-1}$ and $z_{h,i}$. Since the water table can be within the soil column, the equation is modified if the water table is within soil layer i ($z_{h,i-1} < z_\nabla < z_{h,i}$) as a weighted average of the saturated part and the unsaturated part

$$\overline{\theta_{E,i}} = \overline{\theta_{E,sat,i}}\left(\frac{z_{h,i} - z_\nabla}{z_{h,i} - z_{h,i-1}}\right) + \overline{\theta_{E,unsat,i}}\left(\frac{z_\nabla - z_{h,i-1}}{z_{h,i} - z_{h,i-1}}\right) \tag{7.121}$$

where $\overline{\theta_{E,sat,i}} = \theta_{sat,i}$ and the unsaturated part $\overline{\theta_{E,unsat,i}}$ is

$$\overline{\theta_{E,unsat,i}} = \frac{\theta_{sat,i}\psi_{sat,i}}{\left(z_\nabla - z_{h,i-1}\right)\left(1 - \frac{1}{B_i}\right)}\left[1 - \left(\frac{\psi_{sat,i} - z_\nabla + z_{h,i-1}}{\psi_{sat,i}}\right)^{1-\frac{1}{B_i}}\right]. \tag{7.122}$$

If $z_\nabla < z_{h,i-1}$, then $\overline{\theta_{E,i}} = \overline{\theta_{E,sat,i}} = \theta_{sat,i}$. If the water table is below the soil column ($z_\nabla > z_{h,N_{levsoi}}$), an equilibrium volumetric soil moisture is calculated for a virtual layer $i = N_{levsoi} + 1$ as

$$\overline{\theta_{E,i=N_{levsoi+1}}} = \frac{\theta_{sat,i-1}\psi_{sat,i-1}}{\left(z_\nabla - z_{h,i-1}\right)\left(1 - \frac{1}{B_{i-1}}\right)}\left[1 - \left(\frac{\psi_{sat,i-1} - z_\nabla + z_{h,i-1}}{\psi_{sat,i-1}}\right)^{1-\frac{1}{B_{i-1}}}\right] \tag{7.123}$$

The equilibrium volumetric soil moisture is constrained by

$$0 \le \overline{\theta_{E,i}} \le \theta_{sat,i} \tag{7.124}$$

The equilibrium soil matric potential is then

$$\psi_{E,i} = \psi_{sat,i} \left(\frac{\overline{\theta_{E,i}}}{\theta_{sat,i}} \right)^{-B_i} \geq -1 \times 10^8 \qquad \frac{\overline{\theta_{E,i}}}{\theta_{sat,i}} \geq 0.01 \qquad (7.125)$$

7.4.2.2 Equation set for layer $i = 1$

For the top soil layer ($i = 1$), the boundary condition is the infiltration rate (section 7.3), $q_{i-1}^{n+1} = -q_{infl}^{n+1}$, and the water balance equation is

$$\frac{\Delta z_i \Delta \theta_{liq,i}}{\Delta t} = q_{infl}^{n+1} + q_i^{n+1} - e_i \,. \qquad (7.126)$$

After grouping like terms, the coefficients of the tridiagonal set of equations for $i = 1$ are

$$a_i = 0 \qquad (7.127)$$

$$b_i = \frac{\partial q_i}{\partial \theta_{liq,i}} - \frac{\Delta z_i}{\Delta t} \qquad (7.128)$$

$$c_i = \frac{\partial q_i}{\partial \theta_{liq,i+1}} \qquad (7.129)$$

$$r_i = q_{infl}^{n+1} - q_i^n + e_i \,. \qquad (7.130)$$

7.4.2.3 Equation set for layers $i = 2, \ldots, N_{levsoi} - 1$

The coefficients of the tridiagonal set of equations for $i = 2, \ldots, N_{levsoi} - 1$ are

$$a_i = -\frac{\partial q_{i-1}}{\partial \theta_{liq,i-1}} \qquad (7.131)$$

$$b_i = \frac{\partial q_i}{\partial \theta_{liq,i}} - \frac{\partial q_{i-1}}{\partial \theta_{liq,i}} - \frac{\Delta z_i}{\Delta t} \qquad (7.132)$$

$$c_i = \frac{\partial q_i}{\partial \theta_{liq,i+1}} \qquad (7.133)$$

$$r_i = q_{i-1}^n - q_i^n + e_i.$$ (7.134)

7.4.2.4 Equation set for layers $i = N_{levsoi}, \ldots N_{levsoi} + 1$

For the lowest soil layer ($i = N_{levsoi}$), the bottom boundary condition depends on the depth of the water table. If the water table is within the soil column ($z_\nabla \leq z_{h,N_{levsoi}}$), a zero-flux bottom boundary condition is applied ($q_i^n = 0$) and the coefficients of the tridiagonal set of equations for $i = N_{levsoi}$ are

$$a_i = -\frac{\partial q_{i-1}}{\partial \theta_{liq,i-1}}$$ (7.135)

$$b_i = -\frac{\partial q_{i-1}}{\partial \theta_{liq,i}} - \frac{\Delta z_i}{\Delta t}$$ (7.136)

$$c_i = 0$$ (7.137)

$$r_i = q_{i-1}^n + e_i.$$ (7.138)

The coefficients for the aquifer layer $i = N_{levsoi} + 1$ are then

$$a_i = 0$$ (7.139)

$$b_i = -\frac{\Delta z_i}{\Delta t}$$ (7.140)

$$c_i = 0$$ (7.141)

$$r_i = 0.$$ (7.142)

If the water table is below the soil column ($z_\nabla > z_{h,N_{levsoi}}$), the coefficients for $i = N_{levsoi}$ are

$$a_i = -\frac{\partial q_{i-1}}{\partial \theta_{liq,i-1}}$$ (7.143)

152

$$b_i = \frac{\partial q_i}{\partial \theta_{liq,i}} - \frac{\partial q_{i-1}}{\partial \theta_{liq,i}} - \frac{\Delta z_i}{\Delta t} \tag{7.144}$$

$$c_i = \frac{\partial q_i}{\partial \theta_{liq,i+1}} \tag{7.145}$$

$$r_i = q_{i-1}^n - q_i^n + e_i. \tag{7.146}$$

The $i = N_{levsoi} + 1$ terms are evaluated using

$$\psi_{N_{levsoi}+1} = \psi_{sat,N_{levsoi}} \left[s_{N_{levsoi}+1} \right]^{-B_{N_{levsoi}}} \geq -1 \times 10^8 \tag{7.147}$$

$$z_{N_{levsoi}+1} = 0.5\left(z_\nabla + z_{N_{levsoi}} \right) \tag{7.148}$$

where

$$s_{N_{levsoi}+1} = 0.5 \left(\frac{\theta_{sat,N_{levsoi}} + \theta_{N_{levsoi}}}{\theta_{sat,N_{levsoi}}} \right) \qquad 0.01 \leq s_{N_{levsoi}+1} \leq 1, \tag{7.149}$$

$\psi_{E,N_{levsoi}+1}$ is evaluated from equations (7.123) and (7.125), and

$$\frac{\partial \psi_{N_{levsoi}+1}}{\partial \theta_{liq,N_{levsoi}+1}} = -B_{N_{levsoi}} \frac{\psi_{N_{levsoi}+1}}{s_{N_{levsoi}} \theta_{sat,N_{levsoi}}}. \tag{7.150}$$

The coefficients for the aquifer layer $i = N_{levsoi} + 1$ are then

$$a_i = -\frac{\partial q_{i-1}}{\partial \theta_{liq,i-1}} \tag{7.151}$$

$$b_i = -\frac{\partial q_{i-1}}{\partial \theta_{liq,i}} - \frac{\Delta z_i}{\Delta t} \tag{7.152}$$

$$c_i = 0 \tag{7.153}$$

$$r_i = q_{i-1}^n. \tag{7.154}$$

Upon solution of the tridiagonal equation set (Press et al. 1992), the liquid water contents are updated as follows

$$w_{liq,i}^{n+1} = w_{liq,i}^{n} + \Delta\theta_{liq,i}\Delta z_i \qquad i = 1,\ldots,N_{levsoi}. \qquad (7.155)$$

The volumetric water content is

$$\theta_i = \frac{w_{liq,i}}{\Delta z_i \rho_{liq}} + \frac{w_{ice,i}}{\Delta z_i \rho_{ice}}. \qquad (7.156)$$

7.5 Groundwater-Soil Water Interactions

Drainage or sub-surface runoff is based on the SIMTOP scheme (Niu et al. 2005) with a modification to account for reduced drainage in frozen soils. In the work of Niu et al. (2005), the drainage q_{drai} (kg m^{-2} s^{-1}) was formulated as

$$q_{drai} = q_{drai,\max}\exp\left(-f_{drai}z_\nabla\right). \qquad (7.157)$$

Here, the water table depth z_∇ has units of meters. To restrict drainage in frozen soils, Niu et al. (2005) added the following condition

$$q_{drai} = 0 \qquad \text{for } w_{ice,N_{levsoi}} > w_{liq,N_{levsoi}}. \qquad (7.158)$$

In preliminary testing it was found that a more gradual restriction of drainage was required so that the water table depth remained dynamic under partially frozen conditions. The following modification is made to equation (7.157)

$$q_{drai} = \left(1 - f_{imp}\right)q_{drai,\max}\exp\left(-f_{drai}z_\nabla\right) \qquad (7.159)$$

where f_{imp} is the fraction of impermeable area determined from the ice content of the soil layers interacting with the water table

$$f_{imp} = \frac{\exp\left[-\alpha\left(1 - \dfrac{\displaystyle\sum_{i=jwt}^{i=N_{levsoi}}\dfrac{w_{ice,i}}{w_{ice,i}+w_{liq,i}}\Delta z_i}{\displaystyle\sum_{i=jwt}^{i=N_{levsoi}}\Delta z_i}\right)\right] - \exp(-\alpha)}{1 - \exp(-\alpha)} \geq 0 \qquad (7.160)$$

where $\alpha = 3$ is an adjustable scale-dependent parameter, jwt is the index of the layer directly above the water table, $w_{ice,i}$ and $w_{liq,i}$ are the ice and liquid water contents of soil layer i (kg m^{-2}), and Δz_i is the layer thickness (mm). This expression is functionally the same as that used to determine the impermeable fraction (equation (7.63)). In equation (7.159), the decay factor $f_{drai} = 2.5$ m^{-1} and the maximum drainage when the water table depth is at the surface $q_{drai,max} = 5.5 \times 10^{-3}$ kg m^{-2} s^{-1} were determined for global simulations through sensitivity analysis and comparison with observed runoff.

Determination of water table depth z_{∇} is based on work by Niu et al. (2007). In this approach, a groundwater component is added in the form of an unconfined aquifer lying below the soil column (Figure 7.1). The groundwater solution is dependent on whether the water table is within or below the soil column. Two water stores are used to account for these solutions. The first, W_a, is the water stored in the unconfined aquifer (mm) and is proportional to the change in water table depth when the water table is below the lower boundary of the hydrologically-active soil column. The second, W_t, is the actual groundwater which can include water within the soil column. When the water table is below the soil column $W_t = W_a$. When the water table is within the soil column, W_a is constant because there is no water exchange between the soil column and the underlying aquifer, while W_t varies with soil moisture conditions.

In either case, W_t is first updated as

$$W_t^{n+1} = W_t^n + \left(q_{recharge} - q_{drai} \right) \Delta t \tag{7.161}$$

155

where Δt is the model time step (s), $q_{recharge}$ is the recharge to the aquifer (kg m^{-2} s^{-1}), and the drainage q_{drai} calculated from equation (7.159) is equivalent to the groundwater discharge.

For the case when the water table is below the soil column, the water stored in the unconfined aquifer W_a (mm) is updated as

$$W_a^{n+1} = W_a^n + \left(q_{recharge} - q_{drai} \right) \Delta t \tag{7.162}$$

and W_t^{n+1} is reset as $W_t^{n+1} = W_a^{n+1}$. The recharge rate is defined as positive when water enters the aquifer

$$q_{recharge} = \frac{\Delta \theta_{liq,N_{levsoi}+1} \Delta z_{N_{levsoi}+1}}{\Delta t} \tag{7.163}$$

where $\Delta \theta_{liq,N_{levsoi}+1} = \theta_{liq,N_{levsoi}+1}^{n+1} - \theta_{liq,N_{levsoi}+1}^{n}$ is the change in liquid water content for layer $i = N_{levsoi} + 1$ calculated from the solution of the soil water equations (section 7.4), and $\Delta z_{N_{levsoi}+1}$ (mm) is

$$\Delta z_{N_{levsoi}+1} = z_\nabla^n - z_{h,N_{levsoi}} . \tag{7.164}$$

The water table depth is calculated from the aquifer water storage scaled by the average specific yield $S_y = 0.2$ [the fraction of water volume that can be drained by gravity in an unconfined aquifer (Niu et al. 2007)]

$$z_\nabla = z_{h,N_{levsoi}} + 25 - \frac{W_a}{10^3 S_y} . \tag{7.165}$$

The form of equation (7.165) originates from the assumption that the initial amount of water in the aquifer is 4800 mm and the corresponding water table depth is one meter below the bottom of the soil column. The water table depth is at the bottom of the soil

column ($z_\nabla = z_{h,N_{levsoi}}$) when the aquifer water is at its prescribed maximum value (5000 mm). The bottom soil layer liquid water content is updated for excess aquifer water as

$$w_{liq,N_{levsoi}}^{n+1} = w_{liq,N_{levsoi}}^{n} + \max\left(0, W_a - 5000\right) \tag{7.166}$$

and aquifer water is reset to $W_a \leq 5000$.

For the case when the water table is within the soil column, there is no water exchange between the soil column and the underlying aquifer. However, variations of the water table depth are still calculated as

$$z_\nabla = \begin{cases} z_{h,\,jwt+1} - \left[\dfrac{W_t - 10^3 \times 25 S_y - \displaystyle\sum_{i=jwt+2}^{N_{levsoi}} \Delta z_i \left(\theta_{sat,i} - \theta_{ice,i}\right)}{10^3 \left(\theta_{sat,\,jwt+1} - \theta_{ice,\,jwt+1}\right)} \right] & jwt = 1,\ldots N_{levsoi} - 2 \\[3em] z_{h,\,jwt+1} - \left[\dfrac{W_t - 10^3 \times 25 S_y}{10^3 \left(\theta_{sat,\,jwt+1} - \theta_{ice,\,jwt+1}\right)} \right] & jwt = N_{levsoi} - 1 \end{cases} \tag{7.167}$$

where jwt is the index of the layer directly above the water table, and limits are placed on the water table depth as $0.05 \leq z_\nabla \leq 80$. In the work of Niu et al. (2007), the water table depth in this case was calculated with the specific yield determined by the volume of air pores (the pore space not filled with water) within the soil to convert W_t to a water table depth. However, this was found to result in unstable water table calculations for a significant proportion of grid cells in global simulations. More specifically, when repeatedly forcing the model with a single year of atmospheric data, the temporal evolution of water table depth was significantly different from year to year for some grid cells, with occasional rapid (within a few days) movement of the water table to the soil surface in some cases. This occurred in grid cells with soil water contents near saturation because of the small amount of available pore space. This had deleterious implications

157

for stability of surface fluxes and temperature. In equation (7.167), the calculation is based on effective porosity ($\theta_{sat,i} - \theta_{ice,i} \geq 0.01$) only. Although less defensible from a physical viewpoint, the approach stabilizes the water table calculation for these grid cells and eliminates unrealistic oscillations in surface fluxes and temperature.

In this case, the drainage q_{drai} is extracted from the soil liquid water in layers within the water table. The partitioning of drainage from these layers is proportional to the layer thickness-weighted hydraulic conductivity as

$$w_{liq,i}^{n+1} = w_{liq,i}^{n} - \frac{q_{drai}k\left[z_{h,i}\right]\Delta t \Delta z_i}{\displaystyle\sum_{i=jwt+1}^{i=N_{levsoi}} k\left[z_{h,i}\right]\Delta z_i} \qquad i = jwt+1,\ldots,N_{levsoi} \qquad (7.168)$$

where Δt is the time step (s).

After the above calculations, two numerical adjustments are implemented to keep the liquid water content of each soil layer ($w_{liq,i}$) within physical constraints of $w_{liq}^{min} \leq w_{liq,i} \leq \left(\theta_{sat,i} - \theta_{ice,i}\right)\Delta z_i$ where $w_{liq}^{min} = 0.01$ (mm). First, beginning with the bottom soil layer $i = N_{levsoi}$, any excess liquid water in each soil layer ($w_{liq,i}^{excess} = w_{liq,i} - \left(\theta_{sat,i} - \theta_{ice,i}\right)\Delta z_i \geq 0$) is successively added to the layer above. Any excess liquid water that remains after saturating the entire soil column (plus a maximum surface ponding depth $w_{liq}^{pond} = 10$ kg m^{-2}), is added to drainage q_{drai}. Second, to prevent negative $w_{liq,i}$, each layer is successively brought up to $w_{liq,i} = w_{liq}^{min}$ by taking the required amount of water from the layer below. If this results in $w_{liq,N_{levsoi}} < w_{liq}^{min}$, then the layers above are searched in succession for the required amount of water ($w_{liq}^{min} - w_{liq,N_{levsoi}}$)

and removed from those layers subject to the constraint $w_{liq,i} \geq w_{liq}^{min}$. If sufficient water

is not found, then the water is removed from W_t and q_{drai}.

The soil surface layer liquid water and ice contents are then updated for dew q_{sdew},

frost q_{frost}, or sublimation q_{subl} (section 5.4) as

$$w_{liq,1}^{n+1} = w_{liq,1}^{n} + q_{sdew}\Delta t \tag{7.169}$$

$$w_{ice,1}^{n+1} = w_{ice,1}^{n} + q_{frost}\Delta t \tag{7.170}$$

$$w_{ice,1}^{n+1} = w_{ice,1}^{n} - q_{subl}\Delta t . \tag{7.171}$$

Sublimation of ice is limited to the amount of ice available.

7.6 Runoff from glaciers, wetlands, and snow-capped surfaces

All surfaces are constrained to have a snow water equivalent $W_{sno} \leq 1000$ kg m^{-2}.

For snow-capped surfaces, the solid and liquid precipitation reaching the snow surface

and dew in solid or liquid form, is separated into solid $q_{snwcp,ice}$ and liquid $q_{snwcp,liq}$ runoff

terms

$$q_{snwcp,ice} = q_{grnd,ice} + q_{frost} \tag{7.172}$$

$$q_{snwcp,liq} = q_{grnd,liq} + q_{dew} \tag{7.173}$$

and snow pack properties are unchanged. The $q_{snwcp,ice}$ runoff is sent to the River

Transport Model (RTM) (section 11) where it is routed to the ocean as an ice stream and,

if applicable, the ice is melted there.

For snow-capped surfaces other than glaciers, wetlands, and lakes the $q_{snwcp,liq}$

runoff is assigned to the glaciers, wetlands, and lakes runoff term q_{rgwl} (e.g.

$q_{rgwl} = q_{snwcp,liq}$). For glacier and wetland surfaces the runoff term q_{rgwl} is calculated from the residual of the water balance

$$q_{rgwl} = q_{grnd,ice} + q_{grnd,liq} - E_g - E_v - \frac{\left(W_b^{n+1} - W_b^n\right)}{\Delta t} - q_{snwcp,ice} \qquad (7.174)$$

where W_b^n and W_b^{n+1} are the water balances at the beginning and ending of the time step defined as

$$W_b = W_{can} + W_{sno} + \sum_{i=1}^{N}\left(w_{ice,i} + w_{liq,i}\right). \qquad (7.175)$$

Currently, glaciers and wetlands are non-vegetated and $E_v = W_{can} = 0$. The contribution of lake runoff to q_{rgwl} is described in section 9.3. The runoff term q_{rgwl} may be negative for glaciers, wetlands, and lakes, which reduces the total amount of runoff available to the RTM.

8.   Stomatal Resistance and Photosynthesis

Leaf stomatal resistance, which is needed for the water vapor flux (section 5), is coupled to leaf photosynthesis in a manner similar to Collatz et al. (1991, 1992) (see also Sellers et al. 1992, 1996). These equations are solved for sunlit and shaded leaves using average absorbed photosynthetically active radiation for sunlit and shaded leaves [ϕ^{sun}, ϕ^{sha} W m^{-2} (section 4.1)] to give sunlit and shaded stomatal resistance (r_s^{sun}, r_s^{sha} s m^{-1}) and photosynthesis (A^{sun}, A^{sha} µmol CO$_2$ m^{-2} s^{-1}).   Canopy photosynthesis is $A^{sun}L^{sun} + A^{sha}L^{sha}$, where L^{sun} and L^{sha} are the sunlit and shaded leaf area indices (section 4.1). Canopy conductance is $\dfrac{1}{r_s^{sun}}L^{sun} + \dfrac{1}{r_s^{sha}}L^{sha}$.

The equation set and its numerical implementation are unchanged from Bonan (1996) and Oleson et al. (2004). New features are the calculation of the photosynthetic parameter $V_{c\max}$ and the scaling of photosynthesis over canopy depth for sunlit and shaded leaves.

8.1   Stomatal resistance

Leaf stomatal resistance is calculated from the Ball-Berry conductance model as described by Collatz et al. (1991) and implemented in a global climate model by Sellers et al. (1996). The model relates stomatal conductance (i.e., the inverse of resistance) to net leaf photosynthesis, scaled by the relative humidity at the leaf surface and the CO$_2$ concentration at the leaf surface. The primary difference between the CLM implementation and that used by Collatz et al. (1991) and Sellers et al. (1996) is that they used net photosynthesis (i.e., leaf photosynthesis minus leaf respiration) instead of gross

photosynthesis. As implemented here, stomatal conductance equals the minimum conductance (b) when gross photosynthesis (A) is zero. Leaf stomatal resistance is

$$\frac{1}{r_s} = m\frac{A}{c_s}\frac{e_s}{e_i}P_{atm} + b \tag{8.1}$$

where r_s is leaf stomatal resistance (s m^2 μmol^{-1}), m is a plant functional type dependent parameter (Table 8.1), A is leaf photosynthesis (μmol CO$_2$ m^{-2} s^{-1}), c_s is the CO$_2$ partial pressure at the leaf surface (Pa), e_s is the vapor pressure at the leaf surface (Pa), e_i is the saturation vapor pressure (Pa) inside the leaf at the vegetation temperature T_v, P_{atm} is the atmospheric pressure (Pa), and $b = 2000$ is the minimum stomatal conductance (μmol m^{-2} s^{-1}) when $A = 0$. Typical values are $m = 9$ for C$_3$ plants and $m = 4$ for C$_4$ plants (Collatz et al. 1991, 1992, Sellers et al. 1996). Sellers et al. (1996) used $b = 10000$ for C$_3$ plants and $b = 40000$ for C$_4$ plants. Here, b was chosen to give a maximum stomatal resistance of 20000 s m^{-1}. Leaf photosynthesis is calculated separately for sunlit (A^{sun}) and shaded (A^{sha}) leaves to give r_s^{sun} and r_s^{sha}.

Resistance is converted from units of s m^2 μmol^{-1} to s m^{-1} as: 1 s m^{-1} = $1 \times 10^{-9} R_{gas}\frac{\theta_{atm}}{P_{atm}}$ μmol^{-1} m^2 s, where R_{gas} is the universal gas constant (J K^{-1} kmol^{-1}) (Table 1.4) and θ_{atm} is the atmospheric potential temperature (K).

Table 8.1. Plant functional type (PFT) photosynthetic parameters.

PFT	m	α	CN_L	F_{LNR}	$f(N)$	SLA_0	SLA_m	ψ_o	ψ_c
NET Temperate	6	0.06	35	0.05	0.72	0.010	0.00125	-66000	-255000
NET Boreal	6	0.06	40	0.04	0.78	0.008	0.001	-66000	-255000
NDT Boreal	6	0.06	25	0.08	0.79	0.024	0.003	-66000	-255000
BET Tropical	9	0.06	30	0.06	0.83	0.012	0.0015	-66000	-255000
BET temperate	9	0.06	30	0.06	0.71	0.012	0.0015	-66000	-255000
BDT tropical	9	0.06	25	0.09	0.66	0.030	0.004	-35000	-224000
BDT temperate	9	0.06	25	0.09	0.64	0.030	0.004	-35000	-224000
BDT boreal	9	0.06	25	0.09	0.70	0.030	0.004	-35000	-224000
BES temperate	9	0.06	30	0.06	0.62	0.012	0	-83000	-428000
BDS temperate	9	0.06	25	0.09	0.60	0.030	0	-83000	-428000
BDS boreal	9	0.06	25	0.09	0.76	0.030	0	-83000	-428000
C_3 arctic grass	9	0.06	25	0.09	0.68	0.030	0	-74000	-275000
C_3 grass	9	0.06	25	0.09	0.61	0.030	0	-74000	-275000
C_4 grass	5	0.04	25	0.09	0.64	0.030	0	-74000	-275000
Crop1	9	0.06	25	0.10	0.61	0.030	0	-74000	-275000
Crop2	9	0.06	25	0.10	0.61	0.030	0	-74000	-275000

α (mol CO_2 mol^{-1} photon); CN_L (g C g^{-1} N); F_{LNR} (g N Rubisco g^{-1} N); SLA_0 (m^2 g^{-1} C);

ψ_o and ψ_c (mm).

8.2 Photosynthesis

Photosynthesis in C_3 plants is based on the model of Farquhar et al. (1980) as modified by Collatz et al. (1991). Photosynthesis in C_4 plants is based on the model of Collatz et al. (1992). Leaf photosynthesis is $A = \min(w_c, w_j, w_e)$. The RuBP carboxylase (Rubisco) limited rate of carboxylation w_c (μ mol CO_2 m^{-2} s^{-1}) is

$$
w_c = \begin{cases} \dfrac{V_{c\max}\left(c_i - \Gamma_*\right)}{c_i + K_c\left(1 + o_i/K_o\right)} & \text{for } C_3 \text{ plants} \\[2ex] V_{c\max} & \text{for } C_4 \text{ plants} \end{cases} \qquad c_i - \Gamma_* \geq 0. \tag{8.2}
$$

The maximum rate of carboxylation allowed by the capacity to regenerate RuBP (i.e., the light-limited rate) w_j (μ mol CO_2 m^{-2} s^{-1}) is

$$
w_j = \begin{cases} \dfrac{\left(c_i - \Gamma_*\right) 4.6\phi\alpha}{c_i + 2\Gamma_*} & \text{for } C_3 \text{ plants} \\[2ex] 4.6\phi\alpha & \text{for } C_4 \text{ plants} \end{cases} \qquad c_i - \Gamma_* \geq 0. \tag{8.3}
$$

The export limited rate of carboxylation for C_3 plants and the PEP carboxylase limited rate of carboxylation for C_4 plants w_e (μ mol CO_2 m^{-2} s^{-1}) is

$$
w_e = \begin{cases} 0.5V_{c\max} & \text{for } C_3 \text{ plants} \\[2ex] 4000V_{c\max} \dfrac{c_i}{P_{atm}} & \text{for } C_4 \text{ plants} \end{cases}. \tag{8.4}
$$

Collatz et al. (1992) used the term $18000V_{c\max}$ for C_4 w_e, and Sellers et al. (1996) used $20000V_{c\max}$. These values cause C_4 photosynthesis to saturate at low values of ambient CO_2. The term $4000V_{c\max}$ results in saturation at about 400 ppm.

In these equations, c_i is the internal leaf CO_2 partial pressure (Pa) and $o_i = 0.209P_{atm}$ is the O_2 partial pressure (Pa). K_c and K_o are the Michaelis-Menten constants (Pa) for CO_2 and O_2. These vary with vegetation temperature T_v (ºC) according to the Q_{10} function as in Collatz et al. (1991) and Sellers et al. (1996)

$$
K_c = K_{c25}\left(a_{kc}\right)^{\frac{T_v - 25}{10}} \tag{8.5}
$$

$$
K_o = K_{o25}\left(a_{ko}\right)^{\frac{T_v - 25}{10}} \tag{8.6}
$$

164

where $K_{c25} = 30.0$ and $K_{o25} = 30000.0$ are values (Pa) at 25ºC, and $a_{kc} = 2.1$ and $a_{ko} = 1.2$ are the relative changes in K_{c25} and K_{o25}, respectively, for a 10ºC change in temperature. The CO_2 compensation point Γ_* (Pa) is

$$\Gamma_* = \frac{1}{2}\frac{K_c}{K_o}0.21o_i.$$ (8.7)

The term 0.21 represents the ratio of maximum rates of oxygenation to carboxylation, which is virtually constant with temperature (Farquhar and von Caemmerer 1982). α is the quantum efficiency (μmol CO_2 per μmol photons) (Table 8.1), and ϕ is the absorbed photosynthetically active radiation (W m^{-2}) (section 4.1), which is converted to photosynthetic photon flux assuming 4.6 μmol photons per Joule. $V_{c\max}$ is the maximum rate of carboxylation (µmol CO_2 m^{-2} s^{-1}) and varies among plant functional types and with sunlit and shaded leaves. Photosynthesis is calculated for sunlit and shaded leaves using ϕ^{sun} and ϕ^{sha} and $V_{c\max}^{sun}$ and $V_{c\max}^{sha}$.

8.3 V_{cmax}

The maximum rate of carboxylation varies with foliage nitrogen concentration and specific leaf area and is calculated as in Thornton and Zimmermann (2007). At 25ºC,

$$V_{c\max 25} = N_a F_{LNR} F_{NR} a_{R25}$$ (8.8)

where N_a is the area-based leaf nitrogen concentration (g N m^{-2} leaf area), F_{LNR} is the fraction of leaf nitrogen in Rubisco (g N in Rubisco g^{-1} N), $F_{NR} = 7.16$ is the mass ratio of total Rubisco molecular mass to nitrogen in Rubisco (g Rubisco g^{-1} N in Rubisco), and $a_{R25} = 60$ is the specific activity of Rubisco (µmol CO_2 g^{-1} Rubisco s^{-1}). N_a is calculated from mass-based leaf N concentration and specific leaf area

$$N_a = \frac{1}{CN_L \ SLA} \tag{8.9}$$

where CN_L is the leaf carbon-to-nitrogen ratio (g C g^{-1} N) and SLA is specific leaf area (m^2 leaf area g^{-1} C). Table 8.1 lists values of F_{LNR} and CN_L for each plant functional type.

$V_{c\max 25}$ is calculated separately for sunlit and shaded leaves using specific leaf area for sunlit and shaded leaves (SLA^{sun}, SLA^{sha}) as in Thornton and Zimmermann (2007). This canopy scaling approach keeps mass-based leaf N concentration (CN_L) constant with depth in the canopy, but allows SLA to increase with greater cumulative leaf area index so that N_a and $V_{c\max 25}$ decrease with leaf area index. Specific leaf area is assumed to increase linearly with greater cumulative leaf area index (x, m^2 m^{-2})

$$SLA(x) = SLA_0 + SLA_m x \tag{8.10}$$

where SLA_0 is the value for SLA at the top of the canopy (m^2 leaf area g^{-1} C) and SLA_m is the linear slope coefficient (Table 8.1). The mean specific leaf area for sunlit leaves is

$$SLA^{sun} = \frac{\int_0^L SLA(x)e^{-Kx}dx}{L^{sun}} = \frac{-\left(cSLA_m KL + cSLA_m + cSLA_0 K - SLA_m - SLA_0 K\right)}{K^2 L^{sun}} \tag{8.11}$$

and similarly for shaded leaves

$$SLA^{sha} = \frac{\int_0^L SLA(x)\left[1 - e^{-Kx}\right]dx}{L^{sha}} = \frac{L\left(SLA_0 + \frac{SLA_m L}{2}\right) - SLA^{sun} L^{sun}}{L^{sha}} \tag{8.12}$$

where L is the exposed leaf area index (m^2 m^{-2}) (section 2.3), exp($-Kx$) is the fraction of sunlit leaves at canopy depth x (section 4.1), L^{sun} and L^{sha} are the sunlit and shaded leaf area index (section 4.1), K is the light extinction coefficient (section 4.1), and

$c = \exp(-KL)$. Because K, L^{sun}, and L^{sha} vary with solar zenith angle, SLA^{sun} and

SLA^{sha} (and hence $V_{c\max}^{sun}$ and $V_{c\max}^{sha}$) vary over the course of a day and through the year.

$V_{c\max 25}$ is calculated from equation (8.8) for sunlit and shaded leaves using SLA^{sun}

and SLA^{sha} to derive N_a in equation (8.9). Table 8.2 list derived values for $V_{c\max 25}$ at the

top of the canopy using SLA_0.

Table 8.2. Values for $V_{c\max 25}$ at the top of the canopy.

Plant Functional Type	$V_{c\max 25}$	$V_{c\max 25} \times f(N)$
NET Temperate	61	44
NET Boreal	54	42
NDT Boreal	57	45
BET Tropical	72	59
BET temperate	72	51
BDT tropical	52	34
BDT temperate	52	33
BDT boreal	52	36
BES temperate	72	44
BDS temperate	52	31
BDS boreal	52	39
C$_3$ grass arctic	52	35
C$_3$ grass	52	31
C$_4$ grass	52	33
Crop1	57	35
Crop2	57	35

$V_{c\max}$ varies with leaf temperature (T_v), soil water (β_t), and as a function of daylength (DYL)

$$V_{c\max} = \begin{cases} V_{c\max 25}\left(2.4\right)^{\frac{T_v-25}{10}} f\left(T_v\right)\beta_t f\left(DYL\right)f\left(N\right) & \text{w/o active bgc} \\ V_{c\max 25}\left(2.4\right)^{\frac{T_v-25}{10}} f\left(T_v\right)\beta_t f\left(DYL\right) & \text{with active bgc} \end{cases}. \quad (8.13)$$

The term $f\left(N\right)$ scales $V_{c\max}$ for nitrogen limitation. $V_{c\max}$ as defined by Thornton and Zimmermann (2007) represents the maximum achievable photosynthetic rate in the absence of nitrogen limitation. When the biogeochemical model is active, the photosynthetic rate calculated using equations (8.2)-(8.4) represents a potential photosynthesis that is subsequently reduced if mineralized nitrogen is not sufficient to sustain the potential growth. In the standard CLM, without biogeochemistry active, $V_{c\max}$ is multiplied by a prescribed nitrogen availability factor [$f\left(N\right)$] that varies among plant functional types (Table 8.1). This factor was derived so that the simulated photosynthetic rate is comparable to the realized photosynthetic rate when the biogeochemistry model is active.

$V_{c\max}$ varies with leaf temperature according to a Q_{10} function. Additionally, $f\left(T_v\right)$ is a function that mimics thermal breakdown of metabolic processes (Farquhar et al. 1980, Collatz et al. 1991)

$$f\left(T_v\right) = \left[1 + \exp\left(\frac{-220000 + 710\left(T_v + T_f\right)}{0.001 R_{gas}\left(T_v + T_f\right)}\right)\right]^{-1} \quad (8.14)$$

where T_f is the freezing temperature of water (K) (Table 1.4), and R_{gas} is the universal gas constant (J K^{-1} kmol^{-1}) (Table 1.4).

$f(DYL)$ is a function that scales $V_{c\max}$ for daylength and introduces seasonal variation to $V_{c\max}$

$$f(DYL) = \frac{(DYL)^2}{(DYL_{\max})^2} \tag{8.15}$$

with $0.01 \leq f(DYL) \leq 1$. Daylength (seconds) is given by

$$DYL = 2 \times 13750.9871 \cos^{-1}\left[\frac{-\sin(lat)\sin(decl)}{\cos(lat)\cos(decl)}\right] \tag{8.16}$$

where *lat* (latitude) and *decl* (declination angle) are from section 3.3. Maximum daylength ($DYL_{\max}$) is calculated similarly but using the maximum declination angle for present-day orbital geometry ($\pm 23.4667°$ [± 0.409571 radians], positive for Northern Hemisphere latitudes and negative for Southern Hemisphere).

The function β_t ranges from one when the soil is wet to near zero when the soil is dry and depends on the soil water potential of each soil layer, the root distribution of the plant functional type, and a plant-dependent response to soil water stress

$$\beta_t = \sum_i w_i r_i \tag{8.17}$$

where w_i is a plant wilting factor for layer i and r_i is the fraction of roots in layer i. The plant wilting factor w_i is

$$w_i = \begin{cases} \dfrac{\psi_c - \psi_i}{\psi_c - \psi_o}\left[\dfrac{\theta_{sat,i} - \theta_{ice,i}}{\theta_{sat,i}}\right] \leq 1 & \text{for } T_i > T_f - 2 \\ 0 & \text{for } T_i \leq T_f - 2 \end{cases} \tag{8.18}$$

where ψ_i is the soil water matric potential (mm) and ψ_c and ψ_o are the soil water potential (mm) when stomata are fully closed or fully open (respectively) (Table 8.1).

169

The term in brackets scales w_i by the ratio of the effective porosity (after accounting for the ice fraction) relative to the total porosity. $w_i = 0$ when the temperature of the soil layer (T_i) is below some threshold (-2°C) or when there is no liquid water in the soil layer ($\theta_{liq,i} \leq 0$).

Here, the soil water matric potential ψ_i is defined somewhat differently than in section 7.4.1

$$\psi_i = \psi_{sat,i} s_i^{-B_i} \geq \psi_c \tag{8.19}$$

where s_i is the soil wetness for layer i with respect to the effective porosity (after accounting for ice fraction) and $\psi_{sat,i}$ and B_i are the saturated soil matric potential (mm) and the Clapp and Hornberger (1978) parameter (section 7.4.1). The soil wetness s_i is

$$s_i = \frac{\theta_{liq,i}}{\theta_{sat,i} - \theta_{ice,i}} \geq 0.01 \tag{8.20}$$

where $\theta_{ice,i} = w_{ice,i} / \left(\rho_{ice} \Delta z_i \right) \leq \theta_{sat,i}$ and $\theta_{liq,i} = w_{liq,i} / \left(\rho_{liq} \Delta z_i \right) \leq \theta_{sat,i} - \theta_{ice,i}$. $w_{ice,i}$ and $w_{liq,i}$ are the ice and liquid water contents (kg m^{-2}) (section 7), $\theta_{sat,i}$ is the saturated volumetric water content (section 7.4.1), ρ_{ice} and ρ_{liq} are the densities of ice and liquid water (kg m^{-3}) (Table 1.4), and Δz_i is the soil layer thickness (m) (section 6.1).

The root fraction r_i in each soil layer depends on the plant functional type

$$r_i = \begin{cases} 0.5 \begin{bmatrix} \exp\left(-r_a z_{h,i-1}\right) + \exp\left(-r_b z_{h,i-1}\right) - \\ \exp\left(-r_a z_{h,i}\right) - \exp\left(-r_b z_{h,i}\right) \end{bmatrix} & \text{for } 1 \leq i < N_{levsoi} \\ 0.5 \left[\exp\left(-r_a z_{h,i-1}\right) + \exp\left(-r_b z_{h,i-1}\right) \right] & \text{for } i = N_{levsoi} \end{cases} \tag{8.21}$$

where $z_{h,i}$ (m) is the depth from the soil surface to the interface between layers i and $i+1$ ($z_{h,0} = 0$, the soil surface) (section 6.1), and r_a and r_b are plant-dependent root distribution parameters adopted from Zeng (2001) (Table 8.3).

Table 8.3. Plant functional type root distribution parameters.

Plant Functional Type	r_a	r_b
NET Temperate	7.0	2.0
NET Boreal	7.0	2.0
NDT Boreal	7.0	2.0
BET Tropical	7.0	1.0
BET temperate	7.0	1.0
BDT tropical	6.0	2.0
BDT temperate	6.0	2.0
BDT boreal	6.0	2.0
BES temperate	7.0	1.5
BDS temperate	7.0	1.5
BDS boreal	7.0	1.5
C_3 grass arctic	11.0	2.0
C_3 grass	11.0	2.0
C_4 grass	11.0	2.0
Crop1	6.0	3.0
Crop2	6.0	3.0

8.4   Numerical implementation

The CO_2 partial pressure at the leaf surface c_s (Pa) and the vapor pressure at the leaf surface e_s (Pa), needed for the stomatal resistance model in equation (8.1), and the

internal leaf CO_2 partial pressure c_i (Pa), needed for the photosynthesis model in equations (8.2)-(8.4), are calculated assuming there is negligible capacity to store CO_2 and water vapor at the leaf surface so that

$$A = \frac{c_a - c_i}{(1.37 r_b + 1.65 r_s) P_{atm}} = \frac{c_a - c_s}{1.37 r_b P_{atm}} = \frac{c_s - c_i}{1.65 r_s P_{atm}} \tag{8.22}$$

and the transpiration fluxes are related as

$$\frac{e'_a - e_i}{(r_b + r_s)} = \frac{e'_a - e_s}{r_b} = \frac{e_s - e_i}{r_s} \tag{8.23}$$

where r_b is leaf boundary layer resistance (s m^2 μmol^{-1}) (section 5.3), the terms 1.37 and 1.65 are the ratios of diffusivity of CO_2 to H_2O for the leaf boundary layer resistance and stomatal resistance, $c_a = CO_2 \left(mol\ mol^{-1}\right) P_{atm}$ is the atmospheric CO_2 partial pressure (Pa) calculated from CO_2 concentration (ppmv), e_i is the saturation vapor pressure (Pa) evaluated at the leaf temperature T_v, and the vapor pressure of air (Pa) is $e'_a = \max\left(\min\left(e_a, e_i\right), 0.25 e_i\right)$. The lower limit $0.25 e_i$ is used to prevent numerical instability in the iterative stomatal resistance calculation. For C_4 plants, this lower limit is $0.40 e_i$ because C_4 plants are not as sensitive to vapor pressure as C_3 plants. The vapor pressure of air in the plant canopy e_a (Pa) is determined from

$$e_a = \frac{P_{atm} q_s}{0.622} \tag{8.24}$$

where q_s is the specific humidity of canopy air (kg kg^{-1}) (section 5.3). Equations (8.22) and (8.23) are solved for c_s and e_s

$$c_s = c_a - 1.37 r_b P_{atm} A \tag{8.25}$$

172

$$e_s = \frac{e'_a r_s + e_i r_b}{r_b + r_s}.$$ (8.26)

Substitution of equation (8.26) into equation (8.1) yields stomatal resistance (r_s)

as a function of photosynthesis (A)

$$\left(\frac{mAP_{atm}e'_a}{c_s e_i} + b \right) r_s^2 + \left(\frac{mAP_{atm}r_b}{c_s} + br_b - 1 \right) r_s - r_b = 0.$$ (8.27)

Stomatal resistance r_s is the larger of the two roots that satisfy the quadratic equation.

This equation is iterated three times with an initial arbitrary value of $c_i = 0.7c_a$ for C$_3$

plants and $c_i = 0.4c_a$ for C$_4$ plants used to calculate A from equations (8.2)-(8.4).

Subsequent values for c_i are given by

$$c_i = c_s - 1.65r_s P_{atm}A$$ (8.28)

The equation set is solved separately for sunlit (A^{sun}, r_s^{sun}) and shaded (A^{sha}, r_s^{sha})

leaves, where average absorbed photosynthetically active radiation (ϕ^{sun}, ϕ^{sha}) and

specific leaf area (SLA^{sun}, SLA^{sha}) [and hence $V_{c\max}^{sun}$ and $V_{c\max}^{sha}$] vary between sunlit and

shaded leaves.

9.   Lake Model

The lake model is from Zeng et al. (2002), which utilized concepts from the lake models of Bonan (1996), Henderson-Sellers (1985, 1986), Hostetler and Bartlein (1990) and the coupled lake-atmosphere model of Hostetler et al. (1993, 1994). All lakes are currently "deep" lakes of 50 m depth. Temperatures are simulated for $N_{levlak} = 10$ layers with layer thicknesses Δz_i of 0.1, 1, 2, 3, 4, 5, 7, 7, 10.45, and 10.45 m, and node depths z_i located at the center of each layer (i.e., 0.05, 0.6, 2.1, 4.6, 8.1, 12.6, 18.6, 25.6, 34.325, 44.775 m). Lake surface fluxes closely follow the formulations for non-vegetated surfaces (section 5.2). The lake surface temperature T_g is solved for simultaneously with the surface fluxes. Snow on lakes is based on a bulk approach, not on the multi-layer model described in section 7.2.

9.1   Surface Fluxes and Surface Temperature

The sensible heat flux (W m^{-2}) is

$$H_g = -\rho_{atm} C_p \frac{\left(\theta_{atm} - T_g\right)}{r_{ah}} \tag{9.1}$$

where ρ_{atm} is the density of moist air (kg m^{-3}) (section 5), C_p is the specific heat capacity of air (J kg^{-1} K^{-1}) (Table 1.4), θ_{atm} is the atmospheric potential temperature (K) (section 5), T_g is the lake surface temperature (K), and r_{ah} is the aerodynamic resistance to sensible heat transfer (s m^{-1}) (section 5.1).

The water vapor flux (kg m^{-2} s^{-1}) is

$$E_g = -\frac{\rho_{atm}\left(q_{atm} - q_{sat}^{T_g}\right)}{r_{aw}} \tag{9.2}$$

where q_{atm} is the atmospheric specific humidity (kg kg^{-1}) (section 1.2.1), $q_{sat}^{T_g}$ is the saturated specific humidity (kg kg^{-1}) (section 5.5) at the lake surface temperature T_g, and r_{aw} is the aerodynamic resistance to water vapor transfer (s m^{-1}) (section 5.1).

The zonal and meridional momentum fluxes are

$$\tau_x = -\rho_{atm} \frac{u_{atm}}{r_{atm}}$$

(9.3)

$$\tau_y = -\rho_{atm} \frac{v_{atm}}{r_{atm}}$$

(9.4)

where u_{atm} and v_{atm} are the zonal and meridional atmospheric winds (m s^{-1}) (section 1.2.1), and r_{am} is the aerodynamic resistance for momentum (s m^{-1}) (section 5.1).

The heat flux into the lake surface G (W m^{-2}) (positive into the surface) is

$$G = \frac{\lambda_1}{\Delta z_1} \left(T_g - T_1 \right)$$

(9.5)

where λ_1 is the thermal conductivity (W m^{-1} K^{-1}), Δz_1 is the thickness (m), and T_1 is the temperature (K) of the top lake layer. If snow is on the frozen lake, the depth of snow z_{sno} (m) (section 9.3) is combined with the thickness of the top lake layer, Δz_1, to create a snow/soil layer of thickness $\Delta z_1 + z_{sno}$. The thermal conductivity is

$$\lambda_1 = \begin{cases} \lambda_{liq} & T_g > T_f \\ \lambda_{ice} & T_g \leq T_f \end{cases}$$

(9.6)

where λ_{liq} and λ_{ice} are the thermal conductivities of water and ice (W m^{-1} K^{-1}) (Table 1.4), and T_f is the freezing temperature of water (K) (Table 1.4).

The absorbed solar radiation $\vec{S}_g$ is

$$\vec{S}_g = \sum_{\Lambda} S_{atm} \downarrow_{\Lambda}^{\mu} \left(1 - \alpha_{g,\Lambda}^{\mu}\right) + S_{atm} \downarrow_{\Lambda} \left(1 - \alpha_{g,\Lambda}\right) \qquad (9.7)$$

where $S_{atm} \downarrow_{\Lambda}^{\mu}$ and $S_{atm} \downarrow_{\Lambda}$ are the incident direct beam and diffuse solar fluxes (W m^{-2}) and Λ denotes the visible ($< 0.7 \, \mu$m) and near-infrared ($\geq 0.7 \, \mu$m) wavebands (section 1.2.1), and $\alpha_{g,\Lambda}^{\mu}$ and $\alpha_{g,\mu}$ are the direct beam and diffuse lake albedos (section 3.2).

The net longwave radiation (positive toward the atmosphere) is

$$\vec{L}_g = L_g \uparrow - L_{atm} \downarrow \qquad (9.8)$$

where $L_g \uparrow$ is the upward longwave radiation from the surface, $L_{atm} \downarrow$ is the downward atmospheric longwave radiation (section 1.2.1). The upward longwave radiation from the surface is

$$L \uparrow = \left(1 - \varepsilon_g\right) L_{atm} \downarrow + \varepsilon_g \sigma \left(T_g^n\right)^4 + 4\varepsilon_g \sigma \left(T_g^n\right)^3 \left(T_g^{n+1} - T_g^n\right) \qquad (9.9)$$

where $\varepsilon_g = 0.97$ is the lake surface emissivity, σ is the Stefan-Boltzmann constant (W m^{-2} K^{-4}) (Table 1.4), and $T_g^{n+1} - T_g^n$ is the difference in lake surface temperature between Newton-Raphson iterations (see below).

The sensible heat H_g, the water vapor flux E_g through its dependence on the saturated specific humidity, the net longwave radiation $\vec{L}_g$, and the ground heat flux G, all depend on the lake surface temperature T_g. Newton-Raphson iteration is applied to solve for T_g and the surface fluxes as

$$\Delta T_g = \frac{\vec{S}_g - \vec{L}_g - H_g - \lambda E_g - G}{\dfrac{\partial \vec{L}_g}{\partial T_g} + \dfrac{\partial H_g}{\partial T_g} + \dfrac{\partial \lambda E_g}{\partial T_g} + \dfrac{\partial G}{\partial T_g}} \qquad (9.10)$$

where $\Delta T_g = T_g^{n+1} - T_g^n$ and the subscript "n" indicates the iteration. Therefore, the surface temperature T_g^{n+1} can be written as

$$T_g^{n+1} = \frac{\vec{S}_g - \vec{L}_g - H_g - \lambda E_g - G + T_g^n \left(\frac{\partial \vec{L}_g}{\partial T_g} + \frac{\partial H_g}{\partial T_g} + \frac{\partial \lambda E_g}{\partial T_g} + \frac{\partial G}{\partial T_g} \right)}{\frac{\partial \vec{L}_g}{\partial T_g} + \frac{\partial H_g}{\partial T_g} + \frac{\partial \lambda E_g}{\partial T_g} + \frac{\partial G}{\partial T_g}} \qquad (9.11)$$

where the partial derivatives are

$$\frac{\partial \vec{L}_g}{\partial T_g} = 4 \varepsilon_g \sigma \left(T_g^n \right)^3, \qquad (9.12)$$

$$\frac{\partial H_g}{\partial T_g} = \frac{\rho_{atm} C_p}{r_{ah}}, \qquad (9.13)$$

$$\frac{\partial \lambda E_g}{\partial T_g} = \frac{\lambda \rho_{atm}}{r_{aw}} \frac{dq_{sat}^{T_g}}{dT_g}, \qquad (9.14)$$

$$\frac{\partial G}{\partial T_g} = \frac{\lambda_1}{\Delta z_1}. \qquad (9.15)$$

The fluxes of momentum, sensible heat, and water vapor are solved for simultaneously with lake surface temperature as follows. The stability-related equations are the same as for non-vegetated surfaces (section 5.2).

1. An initial guess for the wind speed V_a including the convective velocity U_c is obtained from eq. (5.24) assuming an initial convective velocity $U_c = 0$ m s^{-1} for stable conditions ($\theta_{v,atm} - \theta_{v,s} \geq 0$ as evaluated from eq. (5.50)) and $U_c = 0.5$ for unstable conditions ($\theta_{v,atm} - \theta_{v,s} < 0$).

2. An initial guess for the Monin-Obukhov length L is obtained from the bulk Richardson number using equations (5.46) and (5.48).

177

3. The following system of equations is iterated three times:

- Thermal conductivity λ_1 (eq. (9.6))

- Friction velocity u_* (eqs. (5.32), (5.33), (5.34), (5.35))

- Potential temperature scale θ_* (eqs. (5.37), (5.38), (5.39), (5.40))

- Humidity scale q_* (eqs. (5.41), (5.42), (5.43), (5.44))

- Aerodynamic resistances r_{am}, r_{ah}, and r_{aw} (eqs. (5.55), (5.56), (5.57))

- Lake surface temperature T_g^{n+1} (eq. (9.11))

- Sensible heat flux H_g is updated for T_g^{n+1} (eq. (9.1))

- Water vapor flux E_g is updated for T_g^{n+1} as

$$
E_g = -\frac{\rho_{atm}}{r_{aw}}\left[q_{atm} - q_{sat}^{T_g} - \frac{\partial q_{sat}^{T_g}}{\partial T_g}\left(T_g^{n+1} - T_g^n \right) \right]
\tag{9.16}
$$

where the last term on the right side of equation (9.16) is the change in saturated specific humidity due to the change in T_g between iterations.

- Saturated specific humidity $q_{sat}^{T_g}$ and its derivative $\dfrac{dq_{sat}^{T_g}}{dT_g}$ are updated for T_g^{n+1}

(section 5.1).

- Virtual potential temperature scale θ_{v*} (eq. (5.17))

- Wind speed including the convective velocity, V_a (eq. (5.24))

- Monin-Obukhov length L (eq. (5.49)).

Once the final lake surface temperature has been calculated, if there is snow on the lake ($W_{sno} > 0.5$ kg m^{-2}) and $T_g > T_f$, the surface temperature is reset to freezing

temperature and the surface fluxes H_g, E_g are re-evaluated with $T_g = T_f$ using equations (9.1) and (9.16). The final ground heat flux G is calculated from the residual of the energy balance

$$G = \vec{S}_g - \left(L_g \uparrow - L_{atm} \downarrow \right) - H_g - \lambda E_g \tag{9.17}$$

where $L_g \uparrow$ is evaluated from equation (9.9). If the ground heat flux $G > 0$ (i.e., there is a flux of heat into the snow), the energy (W m^{-2}) available to melt snow (phase change energy) is

$$E_p = G \leq \frac{W_{sno} L_f}{\Delta t} \tag{9.18}$$

where L_f is the latent heat of fusion (J kg^{-1}) (Table 1.4) and Δt is the time step (s). This equation limits snowmelt to be less than or equal to the amount of snow on the lake surface. Any excess energy is used to warm the top lake layer. The rate of snowmelt is $M = E_p / L_f$ (kg m^{-2} s^{-1}).

The roughness lengths used to calculate r_{am}, r_{ah}, and r_{aw} are $z_{0m} = z_{0h} = z_{0w} = z_{0m,g}$. The momentum roughness length is $z_{0m,g} = 0.01$ for unfrozen lakes ($T_g \geq T_f$) and $z_{0m,g} = 0.04$ for frozen lakes ($T_g < T_f$) whether snow-covered or not. The displacement height $d = 0$. When converting water vapor flux to an energy flux, the term λ is defined as follows

$$\lambda = \begin{cases} \lambda_{sub} & T_{atm} \leq T_f \\ \lambda_{vap} & T_{atm} > T_f \end{cases} \tag{9.19}$$

where λ_{sub} and λ_{vap} are the latent heat of sublimation and vaporization, respectively (J kg^{-1}) (Table 1.4).

9.2 Lake Temperatures

The governing equation for lake temperature, assuming constant cross-sectional area with depth, is (Hostetler and Bartlein 1990)

$$\frac{\partial T}{\partial t} = \frac{\partial}{\partial z}\left[\left(\kappa_m + \kappa_e\right)\frac{\partial T}{\partial z}\right] + \frac{1}{c_{liq}}\frac{d\phi}{dz} \tag{9.20}$$

where T is lake temperature (K), $\kappa_m = \lambda_{liq}/c_{liq}$ and κ_e are the molecular and eddy diffusion coefficients for heat (m^2 s^{-1}), λ_{liq} is the thermal conductivity of water (W m^{-1} K^{-1}) (Table 1.4), $c_{liq} = C_{liq}\rho_{liq}$ is the volumetric heat capacity of water (J m^{-3} K^{-1}) where C_{liq} is the specific heat capacity of water (J kg^{-1} K^{-1}) (Table 1.4) and ρ_{liq} is the density of water (kg m^{-3}) (Table 1.4), ϕ is a subsurface solar radiation heat source term (W m^{-2}), and z is depth from the surface (m). Using a method similar to that for snow/soil (section 6.1), this equation is solved numerically to calculate temperatures for N_{levlak} layer lakes with boundary conditions of zero heat flux at the bottom and the net flux of energy at the surface F_0 (W m^{-2})

$$F_0 = \beta\vec{S}_g - \vec{L}_g - H_g - \lambda E_g - E_p \tag{9.21}$$

where $\beta = 0.4$ is the fraction of $\vec{S}_g$ absorbed in the surface layer and E_p is phase change energy (W m^{-2}).

Similar to snow/soil, the heat flux F_i (W m^{-2}) from layer i to $i+1$ is

$$F_i = -c_{liq}\left[\left(T_i - T_{i+1}\right)\left(\frac{\Delta z_i}{2\left(\kappa_m + \kappa_{e,i}\right)} + \frac{\Delta z_{i+1}}{2\left(\kappa_m + \kappa_{e,i+1}\right)}\right)^{-1}\right] \tag{9.22}$$

which is derived assuming the heat flux from i (depth z_i) to the interface between i and $i+1$ (depth $z_i + 0.5\Delta z_i$) equals the heat flux from the interface to $i+1$ (depth z_{i+1}), i.e.,

$$-c_{liq}\left(\kappa_m + \kappa_{e,i}\right)\left(\frac{T_i - T_m}{\frac{1}{2}\Delta z_i}\right) = -c_{liq}\left(\kappa_m + \kappa_{e,i+1}\right)\left(\frac{T_m - T_{i+1}}{\frac{1}{2}\Delta z_{i+1}}\right) \tag{9.23}$$

where T_m is the interface temperature.

The energy balance for the ith layer is

$$\frac{c_{liq}\Delta z_i}{\Delta t}\left(T_i^{n+1} - T_i^n\right) = -F_{i-1} + F_i + \left(\phi_{i-\frac{1}{2}} - \phi_{i+\frac{1}{2}}\right) \tag{9.24}$$

where the superscripts n and $n+1$ indicate values at the beginning and end of the time step, respectively, and Δt is the time step (s). This equation is solved using the Crank-Nicholson method, which combines the explicit method with fluxes evaluated at n (F_{i-1}^n, F_i^n) and the implicit method with fluxes evaluated at $n+1$ (F_{i-1}^{n+1}, F_i^{n+1})

$$\frac{c_{liq}\Delta z_i}{\Delta t}\left(T_i^{n+1} - T_i^n\right) = \alpha\left(-F_{i-1}^n + F_i^n\right) + \left(1-\alpha\right)\left(-F_{i-1}^{n+1} + F_i^{n+1}\right) + \left(\phi_{i-\frac{1}{2}} - \phi_{i+\frac{1}{2}}\right) \tag{9.25}$$

where $\alpha = 0.5$, resulting in a tridiagonal system of equations

$$r_i = a_i T_{i-1}^{n+1} + b_i T_i^{n+1} + c_i T_{i+1}^{n+1}. \tag{9.26}$$

For the top lake layer $i = 1$, $F_{i-1} = F_0$, and the equations are

$$T_i^{n+1} - T_i^n = \frac{\Delta t}{\Delta z_i}\frac{F_0}{c_{liq}} - \left[\left(\frac{T_i^n - T_{i+1}^n + T_i^{n+1} - T_{i+1}^{n+1}}{\frac{\Delta z_i}{\kappa_m + \kappa_{e,i}} + \frac{\Delta z_{i+1}}{\kappa_m + \kappa_{e,i+1}}}\right) + \frac{\phi_{i-\frac{1}{2}} - \phi_{i+\frac{1}{2}}}{c_{liq}}\right] \tag{9.27}$$

$$a_i = 0 \tag{9.28}$$

$$b_i = 1 + \frac{\Delta t}{\Delta z_i}\left(\frac{\Delta z_i}{\kappa_m + \kappa_{e,i}} + \frac{\Delta z_{i+1}}{\kappa_m + \kappa_{e,i+1}}\right)^{-1} \tag{9.29}$$

$$c_i = -\frac{\Delta t}{\Delta z_i}\left(\frac{\Delta z_i}{\kappa_m + \kappa_{e,i}} + \frac{\Delta z_{i+1}}{\kappa_m + \kappa_{e,i+1}}\right)^{-1} \tag{9.30}$$

181

$$r_i = T_i^n + \frac{\Delta t}{\Delta z_i}\left[\frac{F_0}{c_{liq}} - \left(T_i^n - T_{i+1}^n\right)\left(\frac{\Delta z_i}{\kappa_m + \kappa_{e,i}} + \frac{\Delta z_{i+1}}{\kappa_m + \kappa_{e,i+1}}\right)^{-1} + \frac{\phi_{i-\frac{1}{2}} - \phi_{i+\frac{1}{2}}}{c_{liq}}\right]. \qquad (9.31)$$

The boundary condition at the bottom of the lake column is zero heat flux, $F_i = 0$,

resulting in, for $i = N_{levlak}$,

$$T_i^{n+1} - T_i^n = \frac{\Delta t}{\Delta z_i}\left[\left(\frac{T_{i-1}^n - T_i^n + T_{i-1}^{n+1} - T_i^{n+1}}{\frac{\Delta z_{i-1}}{\kappa_m + \kappa_{e,i-1}} + \frac{\Delta z_i}{\kappa_m + \kappa_{e,i}}}\right) + \frac{\phi_{i-\frac{1}{2}} - \phi_{i+\frac{1}{2}}}{c_{liq}}\right] \qquad (9.32)$$

$$a_i = -\frac{\Delta t}{\Delta z_i}\left(\frac{\Delta z_{i-1}}{\kappa_m + \kappa_{e,i-1}} + \frac{\Delta z_i}{\kappa_m + \kappa_{e,i}}\right)^{-1} \qquad (9.33)$$

$$b_i = 1 + \frac{\Delta t}{\Delta z_i}\left(\frac{\Delta z_{i-1}}{\kappa_m + \kappa_{e,i-1}} + \frac{\Delta z_i}{\kappa_m + \kappa_{e,i}}\right)^{-1} \qquad (9.34)$$

$$c_i = 0 \qquad (9.35)$$

$$r_i = T_i^n + \frac{\Delta t}{\Delta z_i}\left[\left(T_{i-1}^n - T_i^n\right)\left(\frac{\Delta z_{i-1}}{\kappa_m + \kappa_{e,i-1}} + \frac{\Delta z_i}{\kappa_m + \kappa_{e,i}}\right)^{-1} + \frac{\phi_{i-\frac{1}{2}} - \phi_{i+\frac{1}{2}}}{c_{liq}}\right]. \qquad (9.36)$$

For the interior lake layers, $1 < i < N_{levlak}$,

$$T_i^{n+1} - T_i^n = \frac{\Delta t}{\Delta z_i}\left(T_{i-1}^n - T_i^n + T_{i-1}^{n+1} - T_i^{n+1}\right)\left(\frac{\Delta z_{i-1}}{\kappa_m + \kappa_{e,i-1}} + \frac{\Delta z_i}{\kappa_m + \kappa_{e,i}}\right)^{-1}$$

$$- \frac{\Delta t}{\Delta z_i}\left(T_i^n - T_{i+1}^n + T_i^{n+1} - T_{i+1}^{n+1}\right)\left(\frac{\Delta z_i}{\kappa_m + \kappa_{e,i}} + \frac{\Delta z_{i+1}}{\kappa_m + \kappa_{e,i+1}}\right)^{-1} \qquad (9.37)$$

$$+ \frac{\Delta t}{\Delta z_i}\left(\frac{\phi_{i-\frac{1}{2}} - \phi_{i+\frac{1}{2}}}{c_{liq}}\right)$$

$$a_i = -\frac{\Delta t}{\Delta z_i}\left(\frac{\Delta z_{i-1}}{\kappa_m + \kappa_{e,i-1}} + \frac{\Delta z_i}{\kappa_m + \kappa_{e,i}}\right)^{-1} \qquad (9.38)$$

$$b_i = 1 + \frac{\Delta t}{\Delta z_i} \left(\frac{\Delta z_{i-1}}{\kappa_m + \kappa_{e,i-1}} + \frac{\Delta z_i}{\kappa_m + \kappa_{e,i}} \right)^{-1} + \frac{\Delta t}{\Delta z_i} \left(\frac{\Delta z_i}{\kappa_m + \kappa_{e,i}} + \frac{\Delta z_{i+1}}{\kappa_m + \kappa_{e,i+1}} \right)^{-1} \qquad (9.39)$$

$$c_i = -\frac{\Delta t}{\Delta z_i} \left(\frac{\Delta z_i}{\kappa_m + \kappa_{e,i}} + \frac{\Delta z_{i+1}}{\kappa_m + \kappa_{e,i+1}} \right)^{-1} \qquad (9.40)$$

$$r_i = T_i^n + \frac{\Delta t}{\Delta z_i} \left(T_{i-1}^n - T_i^n \right) \left(\frac{\Delta z_{i-1}}{\kappa_m + \kappa_{e,i-1}} + \frac{\Delta z_i}{\kappa_m + \kappa_{e,i}} \right)^{-1}$$

$$- \frac{\Delta t}{\Delta z_i} \left(T_i^n - T_{i+1}^n \right) \left(\frac{\Delta z_i}{\kappa_m + \kappa_{e,i}} + \frac{\Delta z_{i+1}}{\kappa_m + \kappa_{e,i+1}} \right)^{-1} \qquad (9.41)$$

$$+ \frac{\Delta t}{\Delta z_i} \frac{\phi_{i-\frac{1}{2}} - \phi_{i+\frac{1}{2}}}{c_{liq}}$$

The eddy diffusion coefficient $\kappa_{e,i}$ (m^2 s^{-1}) for layers $1 \le i < N_{levlak}$ is

$$\kappa_{e,i} = \begin{cases} \dfrac{kw^* z_i}{P_0 \left(1 + 37 Ri^2 \right)} \exp\left(-k^* z_i \right) & T_g > T_f \\ 0 & T_g \le T_f \end{cases} \qquad (9.42)$$

where k is the von Karman constant (Table 1.4), $P_0 = 1$ is the neutral value of the turbulent Prandtl number, z_i is the node depth (m), the surface friction velocity (m s^{-1}) is $w^* = 0.0012 u_2$, and k^* varies with latitude ϕ as $k^* = 6.6 u_2^{-1.84} \sqrt{|\sin \phi|}$. For the bottom layer, $\kappa_{e,10} = \kappa_{e,9}$. As in Hostetler and Bartlein (1990), the 2-m wind speed u_2 (m s^{-1}) is used to evaluate w^* and k^* rather than the 10-m wind used by Henderson-Sellers (1985). The 2-m wind speed is

$$u_2 = \frac{u_*}{k} \ln \left(\frac{2}{z_{0m}} \right) \ge 1. \qquad (9.43)$$

The Richardson number is

$$Ri = \frac{-1 + \sqrt{1 + \dfrac{40 N^2 k^2 z_i^2}{w^{*2} \exp\left(-2k^* z_i\right)}}}{20}$$ (9.44)

where

$$N^2 = -\frac{g}{\rho_i} \frac{\partial \rho}{\partial z}$$ (9.45)

and g is the acceleration due to gravity (m s^{-2}) (Table 1.4), ρ_i is the density of water (kg

m^{-3}), and $\dfrac{\partial \rho}{\partial z}$ is approximated as $\dfrac{\rho_{i+1} - \rho_i}{z_{i+1} - z_i}$. The density of water is (Hostetler and

Bartlein 1990)

$$\rho_i = 1000\left(1 - 1.9549 \times 10^{-5} |T_i - 277|^{1.68}\right).$$ (9.46)

The term $\phi_{i-\frac{1}{2}}$ is the solar radiation flux into the top of the ith layer (depth

$z = z_i - \frac{1}{2}\Delta z_i$) and $\phi_{i+\frac{1}{2}}$ is the solar radiation flux out of the bottom of the ith layer (depth

$z = z_i + \frac{1}{2}\Delta z_i$). For $z > z_a$, where $z_a = 0.6$ m is the base of the surface absorption layer,

the solar radiation at depth z is (Henderson-Sellers 1986)

$$\phi = (1 - \beta)\vec{S}_g \exp\left[-\eta(z - z_a)\right]$$ (9.47)

where $\eta = 0.1$ is the light extinction coefficient for water. The net solar radiation flux

absorbed by layers $1 \le i < N_{levlak}$, $\phi_{i-\frac{1}{2}} - \phi_{i+\frac{1}{2}}$, for an unfrozen lake ($T_g > T_f$), is then

$$\phi_{i-\frac{1}{2}} - \phi_{i+\frac{1}{2}} = (1 - \beta)\vec{S}_g \left\{ \exp\left[-\eta\left(z_i - \tfrac{1}{2}\Delta z_i - z_a\right)\right] - \exp\left[-\eta\left(z_i + \tfrac{1}{2}\Delta z_i - z_a\right)\right] \right\}.$$ (9.48)

For the bottom layer $i = N_{levlak}$, $\phi_{i+\frac{1}{2}} = 0$, and

$$\phi_{i-\frac{1}{2}} - \phi_{i+\frac{1}{2}} = (1 - \beta)\vec{S}_g \left\{ \exp\left[-\eta\left(z_i - \tfrac{1}{2}\Delta z_i - z_a\right)\right] \right\}.$$ (9.49)

For frozen lakes, the solar radiation is absorbed in the surface layer only so that

$$\phi_{i-\frac{1}{2}} - \phi_{i+\frac{1}{2}} = \begin{cases} (1-\beta)\vec{S}_g & i = 1 \\ 0 & 1 < i \le N_{levlak} \end{cases}.$$
(9.50)

Convective mixing occurs using the same scheme as in Hostetler et al.'s (1993, 1994) coupled lake-atmosphere model. Unfrozen lakes overturn when $\rho_i > \rho_{i+1}$, in which case the layer thickness weighted average temperature for layers 1 to $i+1$ is applied to layers 1 to $i+1$ and the densities are updated. This scheme is applied iteratively to layers $1 \le i < 10$.

The solution for lake temperature conserves energy as

$$\sum_{i=1}^{10} \frac{c_{liq}\Delta z_i}{\Delta t}\left(T_i^{n+1} - T_i^n\right) = F_0 + \sum_{i=1}^{10}\left(\phi_{i-\frac{1}{2}} - \phi_{i+\frac{1}{2}}\right).$$
(9.51)

9.3   Lake Hydrology

The volume of water in lakes is assumed to be constant, i.e., lake levels and area do not change. The runoff term q_{rgwl} (section 7.6) accounts for the excess or deficit of water required to keep the lake volume constant as

$$q_{rgwl} = q_{rain} + q_{sno} - E_g - \frac{W_{sno}^{n+1} - W_{sno}^n}{\Delta t} - q_{snwcp,ice}$$
(9.52)

where q_{rain} and q_{sno} are atmospheric inputs of rain and snow (kg m^{-2} s^{-1}) (section 1.2.1), E_g is the water vapor flux (kg m^{-2} s^{-1}) (section 9.1), $q_{snwcp,ice}$ is the snow-capped ice runoff (section 7.6), and $W_{sno}^{n+1} - W_{sno}^n$ is the change in snow mass (kg m^{-2}) in time step Δt (s).

The snow mass is updated for melt and sublimation or frost as

$$W_{sno}^{n+1} = \begin{cases} W_{sno}^n + \left(q_{sno} - M - q_{subl} + q_{frost}\right)\Delta t \geq 0 & W_{sno} \leq 1000 \\ W_{sno}^n - \left(M + q_{subl}\right)\Delta t \geq 0 & W_{sno} > 1000 \\ 0 & T_g > T_f \end{cases} \qquad (9.53)$$

where M is snowmelt (kg m^{-2} s^{-1}) (section 9.1), q_{subl} is the sublimation from snow (kg

m^{-2} s^{-1}), and q_{frost} is frost on snow (kg m^{-2} s^{-1}). As with snow on ground, W_{sno} is capped

to not exceed 1000 kg m^{-2}. The depth of snow z_{sno} (m) is $z_{sno} = W_{sno}/\rho_{sno}$ assuming a

constant density of snow $\rho_{sno} = 250$ kg m^{-3}. The water vapor flux E_g (section 9.1) is

partitioned into q_{subl} or q_{frost} as

$$q_{subl} = \min\left(E_g, \frac{W_{sno}}{\Delta t} - M\right) \qquad E_g \geq 0 \qquad (9.54)$$

$$q_{frost} = \left|E_g\right| \qquad E_g < 0 \text{ and } T_g < T_f + 0.1. \qquad (9.55)$$

10. Dust Model

Atmospheric dust is mobilized from the land by wind in the CLM. The most important factors determining soil erodibility and dust emission include the wind friction speed, the vegetation cover, and the soil moisture. The CLM dust mobilization scheme (Mahowald et al. 2006) accounts for these factors based on the DEAD (Dust Entrainment and Deposition) model of Zender et al. (2003). Please refer to the Zender et al. (2003) article for additional information regarding the equations presented in this section.

The total vertical mass flux of dust, F_j (kg m^{-2} s^{-1}), from the ground into transport bin j is given by

$$F_j = TSf_m \alpha Q_s \sum_{i=1}^{I} M_{i,j} \tag{10.1}$$

where T is a global factor that compensates for the DEAD model's sensitivity to horizontal and temporal resolution and equals 5 x 10^{-4} in the CLM instead of 7 x 10^{-4} in Zender et al. (2003). S is the source erodibility factor set to 1 in the CLM and serves as a place holder at this time.

The grid cell fraction of exposed bare soil suitable for dust mobilization f_m is given by

$$f_m = \left(1 - f_{lake} - f_{wetl}\right)\left(1 - f_{sno}\right)\left(1 - f_v\right)\frac{w_{liq,1}}{w_{liq,1} + w_{ice,1}} \tag{10.2}$$

where f_{lake} and f_{wetl} and f_{sno} are the CLM grid cell fractions of lake and wetland (section 1.2.3) and snow cover (section 3.2), all ranging from zero to one. Not mentioned by Zender et al. (2003), $w_{liq,1}$ and $w_{ice,1}$ are the CLM top soil layer liquid water and ice

contents (mm) entered as a ratio expressing the decreasing ability of dust to mobilize

from increasingly frozen soil. The grid cell fraction of vegetation cover, f_v, is defined as

$$0 \le f_v = \frac{L+S}{(L+S)_t} \le 1 \quad \text{where } (L+S)_t = 0.3 \text{ m}^2 \text{m}^{-2} \tag{10.3}$$

where equation (10.3) applies only for dust mobilization and is not related to the plant

functional type fractions prescribed from the CLM input data or simulated by the CLM

dynamic vegetation model (section 14). L and S are the CLM leaf and stem area index

values (m^2 m^{-2}) averaged at the land unit level so as to include all the pfts and the bare

ground present in a vegetated land unit. L and S may be prescribed from the CLM

input data (section 2.3) or simulated by the CLM biogeochemistry model (section 14).

The sandblasting mass efficiency α (m^{-1}) is calculated as

$$\alpha = 100 e^{(13.4 M_{clay} - 6.0) \ln 10} \begin{cases} M_{clay} = \% clay \times 0.01 & 0 \le \% clay \le 20 \\ M_{clay} = 20 \times 0.01 & 20 < \% clay \le 100 \end{cases} \tag{10.4}$$

where M_{clay} is the mass fraction of clay particles in the soil and %clay is determined from

the surface dataset (section 1.2.3). $M_{clay} = 0$ corresponds to sand and $M_{clay} = 0.2$ to

sandy loam.

Q_s is the total horizontally saltating mass flux (kg m^{-1} s^{-1}) of "large" particles

(Table 10.1), also referred to as the vertically integrated streamwise mass flux

$$Q_s = \begin{cases} \dfrac{c_s \rho_{atm} u_{*s}^3}{g} \left(1 - \dfrac{u_{*t}}{u_{*s}}\right) \left(1 + \dfrac{u_{*t}}{u_{*s}}\right)^2 & \text{for } u_{*t} < u_{*s} \\ 0 & \text{for } u_{*t} \ge u_{*s} \end{cases} \tag{10.5}$$

where the saltation constant c_s equals 2.61 and ρ_{atm} is the atmospheric density (kg m^{-3}) (Table 1.1), g the acceleration of gravity (m s^{-2}) (Table 1.4). The threshold wind friction speed for saltation u_{*t} (m s^{-1}) is

$$u_{*t} = f_z \left[\text{Re}_{*t}^f \, \rho_{osp} g D_{osp} \left(1 + \frac{6 \times 10^{-7}}{\rho_{osp} g D_{osp}^{2.5}} \right) \right]^{\frac{1}{2}} \rho_{atm}^{-\frac{1}{2}} f_w \tag{10.6}$$

where f_z is a factor dependent on surface roughness but set to 1 as a place holder for now, ρ_{osp} and D_{osp} are the density (2650 kg m^{-3}) and diameter (75 x 10^{-6} m) of optimal saltation particles, and f_w is a factor dependent on soil moisture:

$$f_w = \begin{cases} 1 & \text{for } w \leq w_t \\ \sqrt{1 + 1.21 \left[100(w - w_t) \right]^{0.68}} & \text{for } w > w_t \end{cases} \tag{10.7}$$

where

$$w_t = a \left(0.17 M_{clay} + 0.14 M_{clay}^2 \right) \qquad 0 \leq M_{clay} = \% clay \times 0.01 \leq 1 \tag{10.8}$$

and

$$w = \frac{\theta_1 \rho_{liq}}{\rho_{d,1}} \tag{10.9}$$

where $a = M_{clay}^{-1}$ for tuning purposes, θ_1 is the volumetric soil moisture in the top soil layer (m^3 m^{-3}) (section 7.4), ρ_{liq} is the density of liquid water (kg m^{-3}) (Table 1.4), and $\rho_{d,1}$ is the bulk density of soil in the top soil layer (kg m^{-3}) defined as in section 6.3 rather than as in Zender et al. (2003). Re_{*t}^f from equation (10.6) is the threshold friction Reynolds factor

$$\text{Re}_{*t}^{f} = \begin{cases} \dfrac{0.1291^{2}}{-1 + 1.928\,\text{Re}_{*t}} & \text{for } 0.03 \leq \text{Re}_{*t} \leq 10 \\[2ex] 0.12^{2}\left(1 - 0.0858e^{-0.0617(\text{Re}_{*t}-10)}\right)^{2} & \text{for } \text{Re}_{*t} > 10 \end{cases} \tag{10.10}$$

and Re_{*t} is the threshold friction Reynolds number approximation for optimally sized particles

$$\text{Re}_{*t} = 0.38 + 1331\left(100 D_{osp}\right)^{1.56} \tag{10.11}$$

In equation (10.5), u_{*s} is defined as the wind friction speed (m s^{-1}) accounting for the Owen effect (Owen 1964)

$$u_{*s} = \begin{cases} u_{*} & \text{for } U_{10} < U_{10,t} \\[1.5ex] u_{*} + 0.003\left(U_{10} - U_{10,t}\right)^{2} & \text{for } U_{10} \geq U_{10,t} \end{cases} \tag{10.12}$$

where u_{*} is the CLM wind friction speed (m s^{-1}), also known as friction velocity (section 5.1), U_{10} is the 10-m wind speed (m s^{-1}) calculated as the wind speed at the top of the canopy in Chapter 4.3 of Bonan (1996) but here for 10 m above the ground, and $U_{10,t}$ is the threshold wind speed at 10 m (m s^{-1})

$$U_{10,t} = u_{*t}\frac{U_{10}}{u_{*}} \tag{10.13}$$

In equation (10.1) we sum $M_{i,j}$ over $I = 3$ source modes i where $M_{i,j}$ is the mass fraction of each source mode i carried in each of $J = 4$ transport bins j

$$M_{i,j} = \frac{m_{i}}{2}\left[\text{erf}\left(\frac{\ln\frac{D_{j,\text{max}}}{\tilde{D}_{v,i}}}{\sqrt{2}\ln\sigma_{g,i}}\right) - \text{erf}\left(\frac{\ln\frac{D_{j,\text{min}}}{\tilde{D}_{v,i}}}{\sqrt{2}\ln\sigma_{g,i}}\right)\right] \tag{10.14}$$

where m_{i}, $\tilde{D}_{v,i}$, and $\sigma_{g,i}$ are the mass fraction, mass median diameter, and geometric standard deviation assigned to each particle source mode i (Table 10.1), while $D_{j,\text{min}}$ and

$D_{j,\text{max}}$ are the minimum and maximum diameters (m) in each transport bin j (Table 10.2).

Table 10.1. Mass fraction m_i, mass median diameter $\tilde{D}_{v,i}$, and geometric standard

deviation $\sigma_{g,i}$, per dust source mode i

i	m_i (fraction)	$\tilde{D}_{v,i}$ (m)	$\sigma_{g,i}$
1	0.036	0.832 x 10^{-6}	2.1
2	0.957	4.820 x 10^{-6}	1.9
3	0.007	19.38 x 10^{-6}	1.6

Table 10.2. Minimum and maximum particle diameters in each dust transport bin j

j	$D_{j,\text{min}}$ (m)	$D_{j,\text{max}}$ (m)
1	0.1 x 10^{-6}	1.0 x 10^{-6}
2	1.0 x 10^{-6}	2.5 x 10^{-6}
3	2.5 x 10^{-6}	5.0 x 10^{-6}
4	5.0 x 10^{-6}	10.0 x 10^{-6}

11.   River Transport Model (RTM)

The RTM was developed to route total runoff from the land surface model to either the active ocean or marginal seas which enables the hydrologic cycle to be closed (Branstetter 2001, Branstetter and Famiglietti 1999). This is needed to model ocean convection and circulation, which is affected by freshwater input. It also provides another method of diagnosing the performance of the land model because the river flow can be directly compared to gauging station data (e.g., Dai and Trenberth 2002).

To improve global energy conservation when CLM is being run as part of the Community Climate System Model, runoff is split into two streams, a liquid water stream and an ice water stream (derived from excess snowfall in snow-capped grid cells, Section 7.6). The liquid and ice streams are routed through the RTM, passed to, and dealt with by the ocean separately.

The RTM uses a linear transport scheme at 0.5° resolution to route water from each grid cell to its downstream neighboring grid cell. The change in storage S of river water, whether it be liquid or ice, within a RTM grid cell (m^3 s^{-1}) is

$$\frac{dS}{dt} = \sum F_{in} - F_{out} + R \qquad (11.1)$$

where $\sum F_{in}$ is the sum of inflows of water from neighboring upstream grid cells (m^3 s^{-1}), F_{out} is the flux of water leaving the grid cell in the downstream direction (m^3 s^{-1}), and R is the total runoff generated by the land model (m^3 s^{-1}). Downstream water flow direction in each grid cell is determined as one of eight compass points (north, northeast, east, southeast, south, southwest, west, and northwest) based on the steepest downhill

slope as determined from a digital elevation model (Graham et al. 1999). The flux of water leaving the grid cell F_{out} is

$$F_{out} = \frac{v}{d} S$$

(11.2)

where v is the effective water flow velocity (m s^{-1}), d is the distance between centers of neighboring grid cells (m), and S is the volume of river water stored within the grid cell (m^3). The effective water flow velocity is a global constant and is chosen to be $v = 0.35$ m s^{-1} following Miller et al. (1994). The distance d between two grid cell centers depends on river direction, latitude, and longitude as

$$d = \sqrt{\Delta x^2 + \Delta y^2} \, .$$

(11.3)

The distance in the zonal direction Δx (m) is

$$\Delta x = \left(1 \times 10^3 \left| \theta_{i,j} - \theta_{i*,j*} \right| R_e \right) \left[0.5 \left(\cos \phi_{i,j} + \cos \phi_{i*,j*} \right) \right]$$

(11.4)

where $\theta_{i,j}$ and $\theta_{i*,j*}$ are the latitudes (radians) of the upstream and downstream grid cells, $\phi_{i,j}$ and $\phi_{i*,j*}$ are the longitudes (radians) of the upstream and downstream grid cells, R_e is the radius of the earth (km) (Table 1.4), and i and j are grid cell indices. The distance in the meridional direction Δy (m) is

$$\Delta y = \left(1 \times 10^3 \left| \theta_{i,j} - \theta_{i*,j*} \right| R_e \right).$$

(11.5)

The RTM is generally run at a time step greater than that of the CLM because of computational constraints. The total runoff from the land model at each time step is accumulated until the RTM is invoked. The total liquid water runoff at the land model resolution (kg m^{-2} s^{-1}) is

$$R_{liq} = q_{over} + q_{drai} + q_{rgwl}$$

(11.6)

where q_{over} is surface runoff (section 7.3), q_{drai} is sub-surface drainage (section 7.5), and q_{rgwl} is liquid runoff from glaciers, wetlands, and lakes (all in kg m^{-2} s^{-1}) (sections 7.6 and 9.3). The total ice water runoff, also at the land model resolution is

$$R_{ice} = q_{snwcp,ice} \qquad (11.7)$$

where $q_{snwcp,ice}$ is the ice runoff from snow-capped surfaces (section 7.6). The runoff at the land model resolution is interpolated to the resolution of RTM and converted to units of m^3 s^{-1} for use in equation (11.1) by multiplying by $1 \times 10^{-3} A$ where A is the area (m^2) of the RTM grid cell.

The RTM grid cells that are at river mouths, hence providing freshwater flux to the ocean, are identified by examining each RTM ocean grid cell and determining if a RTM land grid cell flows to that ocean grid cell. River mouth grid cells are also assigned if any overlapping grid cells at the land model resolution contain land. When used as part of the Community Climate System Model, the ocean freshwater liquid and ice fluxes at the RTM resolution are passed to the flux coupler which distributes the fluxes to the appropriate ocean grid cells. When used with the Community Atmosphere Model or when run offline, RTM serves only as a diagnostic tool. The river-routing scheme conserves water globally as

$$\sum_{i,j} \left(\frac{dS}{dt} \right)_{i,j} = \sum_{i,j} R_{i,j} . \qquad (11.8)$$

12. Biogenic Volatile Organic Compounds (BVOCs)

This section describes the Heald et al. (2008) BVOC emissions model that will be implemented in the public release of CLM4. The alpha release of CLM4 contains the CLM3.0 BVOC emissions model, which is documented in section 11 of Oleson et al. (2004).

Heald et al. (2008) have implemented an update of the CLM3.0 biogenic volatile organic compound (BVOC) emissions model (Levis et al. 2003; Oleson et al. 2004) in the CLM4. The CLM3 version was based on Guenther et al. (1995). The CLM4 version is, in addition, based on Guenther et al. (2006). Both versions simulate only the emissions from plants given that about 90% of isoprene and monoterpene emissions originate from plant foliage.

Terrestrial BVOC emissions from plants to the atmosphere are calculated as a flux, F_i (μ g C m^{-2} ground area h^{-1}), for emission type i, ranging from 1 to 5 in this order: isoprenes, monoterpenes, other VOCs (OVOC), other reactive VOCs (ORVOC), and carbon monoxide (CO).

$$F_i = \gamma_i \rho \sum_j \varepsilon_{i,j} \chi_j \tag{12.1}$$

where γ_i is the emission activity factor accounting for responses to meteorological and phenological conditions, ρ is the canopy loss and production factor also known as escape efficiency (set to 1), and $\varepsilon_{i,j}$ (μ g C m^{-2} ground area h^{-1}) is the emission factor at standard conditions of light, temperature, and leaf area for plant functional type (pft) j with fractional coverage $\left(wt \right)_j$.

The emission factor, $\varepsilon_{i,j}$, implicitly includes a source density factor. To calculate emissions of monoterpenes, OVOCs, ORVOCs, and CO, we use equation (12.1) in the CLM3 form [equation (1) of Levis et al. (2003) or equation (11.1) of Oleson et al. (2004)], which separates the source density factor (g dry weight foliar mass m^{-2} ground) and the emission capacity (same symbol, ε, as the emission factor but different units, μ g C g^{-1} dry foliar mass h^{-1}) (Table 12.1). Levis et al. (2003) and Oleson et al. (2004) document the CLM3 form of equation (12.1) in detail.

The remainder of this section covers the CLM4 calculation of isoprene emissions, following the new Guenther et al. (2006) treatment. Isoprene emission factors, $\varepsilon_{1,j}$ (μ g C m^{-2} ground area h^{-1}), vary spatially according to pft-dependent data introduced to the CLM4 surface dataset. These data are read in in units of μ g isoprene m^{-2} ground area h^{-1} and are converted to μ g C m^{-2} ground area h^{-1} by multiplying by 0.882 g C g^{-1} isoprene.

The isoprene activity factor, γ_1, is calculated as

$$\gamma_1 = C_{CE} L \gamma_\phi \gamma_T \gamma_{\tau_{leaf}} \gamma_\theta \tag{12.2}$$

where C_{CE} is the canopy environment constant derived to set emission activity to 1 at standard (defined later) conditions

$$\begin{aligned} C_{CE} &= 0.40 \quad \text{for} \quad f_{sun}^{10d} > 0 \\ C_{CE} &= 0.47 \quad \text{for} \quad f_{sun}^{10d} = 0 \end{aligned} \tag{12.3}$$

and f_{sun}^{10d} is the 10-day running mean sunlit fraction of leaf area in the canopy f_{sun} (section 4.1), L is the exposed leaf area index (m^2 leaf area m^{-2} ground area) (section 2.3).

γ_ϕ, γ_T, $\gamma_{\tau_{leaf}}$, and γ_θ are scaling terms for light, temperature, leaf age, and soil moisture, respectively. The scaling term for light is

$$\gamma_\phi = \gamma_\phi^{sun} + \gamma_\phi^{sha} \qquad (12.4)$$

where

$$\gamma_\phi^{sun/sha} = f_{sun/sha} ca_3 e^{ca_2\left(Q_{sun/sha}^{1d} - Q_{sun/sha}^{std}\right)} \left(Q_{sun/sha}^{10d}\right)^{0.6} \frac{\alpha_{sun/sha} Q_{sun/sha}}{\sqrt{1 + \alpha_{sun/sha}^2 Q_{sun/sha}^2}} \qquad (12.5)$$

and

$$\alpha_{sun/sha} = ca_1 - ca_2 \ln Q_{sun/sha}^{10d}, \qquad (12.6)$$

$$Q_{sun} = 4.6\left(S_{atm}\downarrow_{vis}^{\mu} + f_{sun} S_{atm}\downarrow_{vis}\right) \quad \text{and} \quad Q_{sha} = 4.6\left(f_{sha} S_{atm}\downarrow_{vis}\right), \qquad (12.7)$$

$$Q_{sun}^{1d} = 4.6\left(S_{atm}^{1d}\downarrow_{vis}^{\mu} + f_{sun}^{1d} S_{atm}^{1d}\downarrow_{vis}\right) \quad \text{and} \quad Q_{sha}^{1d} = 4.6\left(f_{sha}^{1d} S_{atm}^{1d}\downarrow_{vis}\right), \qquad (12.8)$$

$$Q_{sun}^{10d} = 4.6\left(S_{atm}^{10d}\downarrow_{vis}^{\mu} + f_{sun}^{10d} S_{atm}^{10d}\downarrow_{vis}\right) \quad \text{and} \quad Q_{sha}^{10d} = 4.6\left(f_{sha}^{10d} S_{atm}^{10d}\downarrow_{vis}\right), \qquad (12.9)$$

where $f_{sha} = 1 - f_{sun}$ is the shaded fraction of leaf area in the canopy, $Q_{sun/sha}$ are the fluxes of photosynthetically active radiation (PAR) on sunlit or shaded leaves (μ mol photons m^{-2} s^{-1}), and $S_{atm}\downarrow_{vis}^{\mu}$ and $S_{atm}\downarrow_{vis}$ are the incident visible direct-beam and diffuse solar radiation (W m^{-2}) (section 1.2.1). The factor 4.6 has units of μ mol photons J^{-1} and converts PAR to photosynthetic photon flux. $Q_{sun}^{std} = 200$ and $Q_{sha}^{std} = 50$ (μ mol photons m^{-2} s^{-1}) represent standard conditions for 1 day, while $ca_1 = 0.004, ca_2 = 0.0005,$ and $ca_3 = 0.0468$ are empirical coefficients. For arbitrary initial conditions (section 1.2.2), the 1 and 10-day running means of $f_{sun/sha}$, $S_{atm}\downarrow_{vis}^{\mu}$, and $S_{atm}\downarrow_{vis}$ may not be available, so we set $\alpha_{sun/sha} = 0.001$ and

$$ca_3 e^{ca_2\left(Q_{sun/sha}^{1d} - Q_{sun/sha}^{std}\right)} \left(Q_{sun/sha}^{10d}\right)^{0.6} = 1.21.$$

The scaling term for temperature is

$$\gamma_T = co_3 e^{co_4\left(T_v^{1d}-T^{std}\right)} e^{co_4\left(T_v^{10d}-T^{std}\right)} \frac{ct_2 e^{ct_1 x}}{ct_2 - ct_1\left(1-e^{ct_2 x}\right)} \qquad (12.10)$$

where

$$x = \frac{\frac{1}{co_1 + co_2\left(T_v^{10d}-T^{std}\right)} - \frac{1}{T_v}}{ct_3} \qquad (12.11)$$

and $co_1 = 313$, $co_2 = 0.6$, $co_3 = 2.034$, $co_4 = 0.05$, $ct_1 = 95$, $ct_2 = 230$, and $ct_3 = 0.00831$

are all empirical coefficients, while T_v^{1d} and T_v^{10d} are the 1-day and 10-day average leaf

temperatures (K) and $T^{std} = 297$ is the standard temperature (K) used here. For arbitrary

initial conditions (section 1.2.2), T_v^{1d} and T_v^{10d} may not be available, so terms in

equations (12.10) and (12.11) are set to values equivalent to setting $T_v^{1d} \approx 292.4$ and

$T_v^{10d} = 303.6$.

The scaling factor for leaf age is

$$\begin{aligned} \gamma_{\tau_{leaf}} &= 1 & \text{for } L = 0 \text{ and for evergreen tree pfts} \\ \gamma_{\tau_{leaf}} &= f_{new}A_{new} + f_{mat}A_{mat} + f_{sen}A_{sen} & \text{all other cases} \end{aligned} \qquad (12.12)$$

where $A_{new} = 0.01$, $A_{mat} = 0.01$, and $A_{sen} = 0.33$ are the relative emission factors for new,

mature, and senescing leaves, respectively, while the f terms are the corresponding

fractions of leaves in each category

$$\begin{aligned} f_{new} &= 1 - \frac{L^{n-1} - \Delta L}{L^n} & f_{mat} &= \frac{L^{n-1} - \Delta L}{L^n} & f_{sen} &= 0 & \text{when} \quad \Delta L > 0 \\ f_{new} &= 0 & f_{mat} &= 1 & f_{sen} &= 0 & \text{when} \quad \Delta L = 0 \\ f_{new} &= 0 & f_{mat} &= 1 + \frac{2\Delta L}{L^{n-1} - \Delta L} & f_{sen} &= -\frac{2\Delta L}{L^{n-1} - \Delta L} & \text{when} \quad \Delta L < 0 \end{aligned} \qquad (12.13)$$

where n is the current time step and $\Delta L = L^n - L^{n-1}$.

The scaling factor for soil moisture is

$$\gamma_\theta = \frac{1}{K} \sum_{k=1}^{K} \begin{cases} 1 & \text{for } k \text{ where } \theta_k - \theta_k^{wilt} \geq \Delta\theta \\ \dfrac{\theta_k - \theta_k^{wilt}}{\Delta\theta} & \text{for } k \text{ where } 0 < \theta_k - \theta_k^{wilt} < \Delta\theta \end{cases} \tag{12.14}$$

where k is the soil layer index, K equals the index of the deepest soil layer for which

$\sum_{k=1}^{K} \Delta z_k < z_j^{root}$, where Δz_k (m) is the soil layer thickness (section 6.1) and z_j^{root} is the

rooting depth (m) of pft j as set for the BVOC model (Table 12.1) and not associated with

the CLM root calculation discussed in section 8.3. $\Delta\theta$ is set to 0.06, θ_k (mm^3 water mm$^-$

^{3} soil) is the volumetric soil moisture (section 7), and θ_k^{wilt} is the volumetric soil moisture

at the wilting point for plants (m^3 water m^{-3} soil)

$$\theta_k^{wilt} = \left(\frac{\psi_{max}}{\psi_{sat,k}} \right)^{-\frac{1}{B_k}} \left(\theta_{sat,k} - \theta_{ice,k} \right) \tag{12.15}$$

where $\psi_{max} = -2.57 \times 10^5$ mm is the maximum soil matric potential, while $\psi_{sat,k}$

(saturated soil matric potential, mm), B_k (Clapp-Hornberger exponent), $\theta_{sat,k}$ (porosity,

mm^3 water mm^{-3} soil), and $\theta_{ice,k}$ (volumetric ice content, mm^3 water mm^{-3} soil) are

calculated for soil layer k according to equations (7.87), (7.84), (7.82), and (8.20).

Table 12.1. Plant functional type VOC emission capacities and specific leaf area.

Plant functional type	ε_1	ε_2	ε_3	ε_4	ε_5	SLA	z_j^{root}
NET Temperate	2.0	2.0	1.0	1.0	0.3	0.0125	1.8
NET Boreal	4.0	2.0	1.0	1.0	0.3	0.0125	1.8
NDT Boreal	0.0	1.6	1.0	1.0	0.3	0.0125	2.0
BET Tropical	24	0.4	1.0	1.0	0.3	0.0250	3.0
BET temperate	24	0.4	1.0	1.0	0.3	0.0250	3.0
BDT tropical	24	0.4	1.0	1.0	0.3	0.0250	2.0
BDT temperate	24	0.4	1.0	1.0	0.3	0.0250	2.0
BDT boreal	24	0.4	1.0	1.0	0.3	0.0250	2.0
BES temperate	24	0.8	1.0	1.0	0.3	0.0250	2.5
BDS temperate	24	0.8	1.0	1.0	0.3	0.0250	2.5
BDS boreal	24	0.8	1.0	1.0	0.3	0.0250	2.5
C_3 arctic grass	0.0	0.1	1.0	1.0	0.3	0.0200	1.5
C_3 grass	0.0	0.1	1.0	1.0	0.3	0.0200	1.5
C_4 grass	0.0	0.1	1.0	1.0	0.3	0.0200	1.5
Crop1	0.0	0.1	1.0	1.0	0.3	0.0200	1.5
Crop2	0.0	0.1	1.0	1.0	0.3	0.0200	1.5

ε_1 (isoprene), ε_2 (monoterpenes), ε_3 (other VOCs), ε_4 (other reactive VOCs), ε_5 (carbon monoxide) (μg C g^{-1} dry foliar mass h^{-1}), SLA (m^2 leaf area g^{-1} C), z_j^{root} (m).

13. Urban Model (CLMU)

At the global scale, and at the coarse spatial resolution of current climate models, urbanization has negligible impact on climate. However, the urban parameterization (CLMU; Oleson et al. 2008b,c) allows simulation of the urban environment within a climate model, and particularly the temperature where people live. As such, the urban model allows scientific study of how climate change affects the urban heat island and possible urban planning and design strategies to mitigate warming (e.g., white roofs). The urban model is separately described in the urban technical note (Oleson et al. 2010). Here, we provide a brief overview.

Urban areas in CLM are represented by a single urban landunit (Figure 1.1). The urban landunit is based on the "urban canyon" concept of Oke (1987) in which the canyon geometry is described by building height (H) and street width (W) (Figure 13.1). The canyon system consists of roofs, walls, and canyon floor. Walls are further divided into shaded and sunlit components. The canyon floor is divided into pervious (e.g., to represent residential lawns, parks) and impervious (e.g., to represent roads, parking lots, sidewalks) fractions. Vegetation is not explicitly modeled for the pervious fraction; instead evaporation is parameterized by a simplified bulk scheme.

Each of the five urban surfaces is treated as a column within the landunit (Figure 13.1). Radiation parameterizations account for trapping of solar and longwave radiation inside the canyon. Momentum fluxes are determined for the urban landunit using a roughness length and displacement height appropriate for the urban canyon and stability formulations from CLM. A one-dimensional heat conduction equation is solved numerically for a multiple-layer ($N_{levgrnd}$) column to determine conduction fluxes into

and out of canyon surfaces. The interior boundary conditions for roofs and walls are determined by an interior building temperature (T_{iB}) held between prescribed maximum and minimum temperatures ($T_{iB,\max}, T_{iB,\min}$), thus explicitly resolving space heating and air conditioning fluxes. Anthropogenic sources of waste heat ($Q_{H,waste}$) from air conditioning and space heating are incorporated as modifications to the canyon energy budget. Turbulent [sensible heat ($Q_{H,u}$) and latent heat ($Q_{E,u}$)] and storage ($Q_{S,u}$) heat fluxes and surface ($T_{u,s}$) and internal ($T_{u,i=1,N_{levgrnd}}$) temperatures are determined for each urban surface u. Hydrology on the roof and canyon floor is simulated and walls are hydrologically inactive. A snowpack can form on the active surfaces. A certain amount of liquid water is allowed to pond on these surfaces which supports evaporation. Water in excess of the maximum ponding depth runs off ($R_{roof}, R_{imprvrd}, R_{prvrd}$).

The heat and moisture fluxes from each surface interact with each other through a bulk air mass that represents air in the urban canopy layer for which specific humidity (q_{ac}) and temperature (T_{ac}) are prognosed (Figure 13.2). The air temperature can be compared with that from surrounding vegetated/soil (rural) surfaces in the model to ascertain heat island characteristics. As with other landunits, the CLMU is forced either with output from a host atmospheric model (e.g., the Community Atmosphere Model (CAM)) or observed forcing (e.g., reanalysis or field observations). The urban model produces sensible, latent heat, and momentum fluxes, emitted longwave, and reflected solar radiation, which are area-averaged with fluxes from non-urban "landunits" (e.g., vegetation, lakes) to supply grid cell averaged fluxes to the atmospheric model.

Present day global urban extent and urban properties were developed by Jackson et al. (2010). Urban extent, defined for four classes [tall building district (TBD), and high, medium, and low density (HD, MD, LD)], was derived from LandScan 2004, a population density dataset derived from census data, nighttime lights satellite observations, road proximity, and slope (Dobson et al. 2000). The urban extent data is aggregated from the original 1 km resolution to a 0.5° by 0.5° global grid. For the current implementation, only the sum of the TBD, HD, and MD classes are used to define urban extent as the LD class is highly rural and better modeled as a vegetated/soil surface.

For each of 33 distinct regions across the globe, thermal (e.g., heat capacity and thermal conductivity), radiative (e.g., albedo and emissivity) and morphological (e.g., height to width ratio, roof fraction, average building height, and pervious fraction of the canyon floor) properties are provided for each of the density classes. Building interior minimum and maximum temperatures are prescribed based on climate and socioeconomic considerations. Urban parameters are determined for the 0.5° by 0.5° global grid based on the dominant density class by area. This prevents potentially unrealistic parameter values that may result if the density classes are averaged. As a result, the current global representation of urban is almost exclusively medium density. Future implementations of the model could represent each of the density classes as a separate landunit. The surface dataset creation routines (see CLM4 User's Guide) aggregate the data to the desired resolution.

Figure 13.1. Schematic representation of the urban land unit.

See the text for description of notation. Incident, reflected, and net solar and longwave

radiation are calculated for each individual surface but are not shown for clarity.
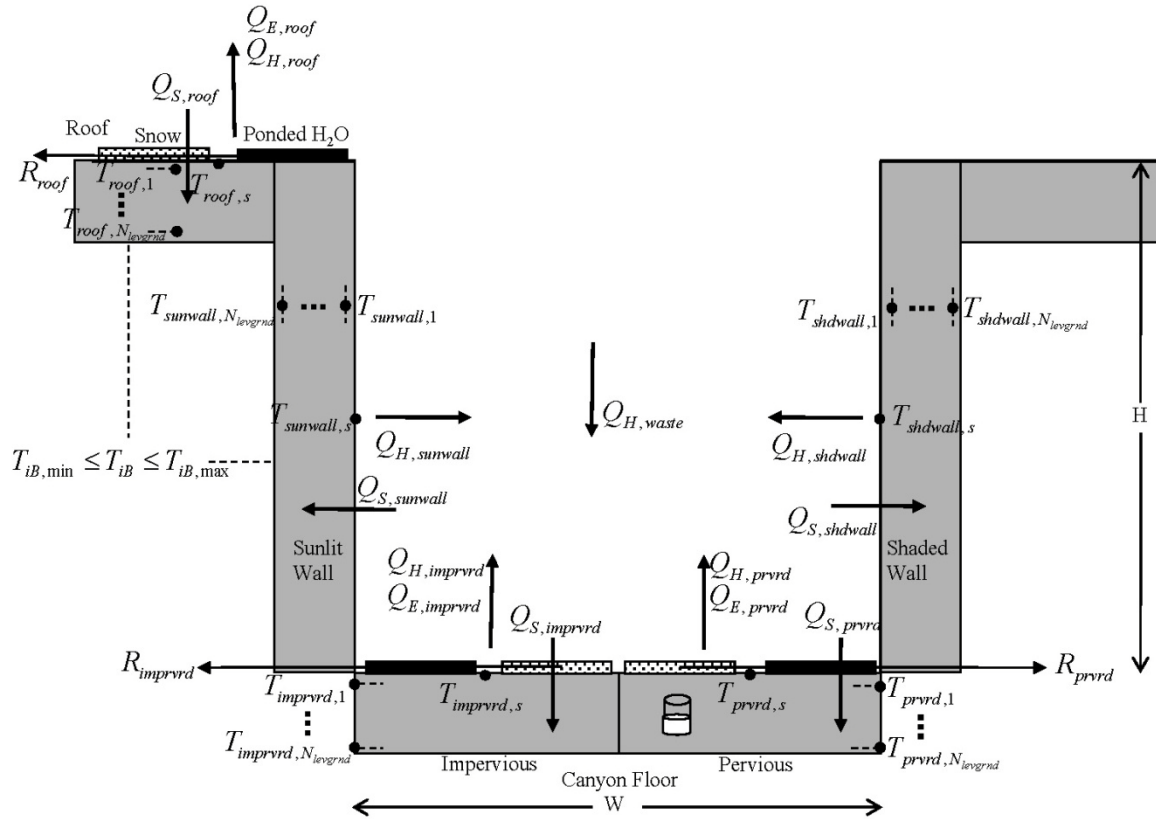
Figure 13.2. Schematic of urban and atmospheric model coupling.

The urban model is forced by the atmospheric model wind (u_{atm}), temperature (T_{atm}),

specific humidity (q_{atm}), precipitation (P_{atm}), solar ($S_{atm}\downarrow$) and longwave ($L_{atm}\downarrow$)

radiation at reference height z'_{atm} (section 1.2.1).   Fluxes from the urban landunit to the

atmosphere are turbulent sensible (H) and latent heat (λE), momentum (τ), albedo

($I\uparrow$), emitted longwave ($L\uparrow$), and absorbed shortwave ($\vec{S}$) radiation. Air temperature

(T_{ac}), specific humidity (q_{ac}), and wind speed (u_c) within the urban canopy layer are

diagnosed by the urban model. H is the average building height.
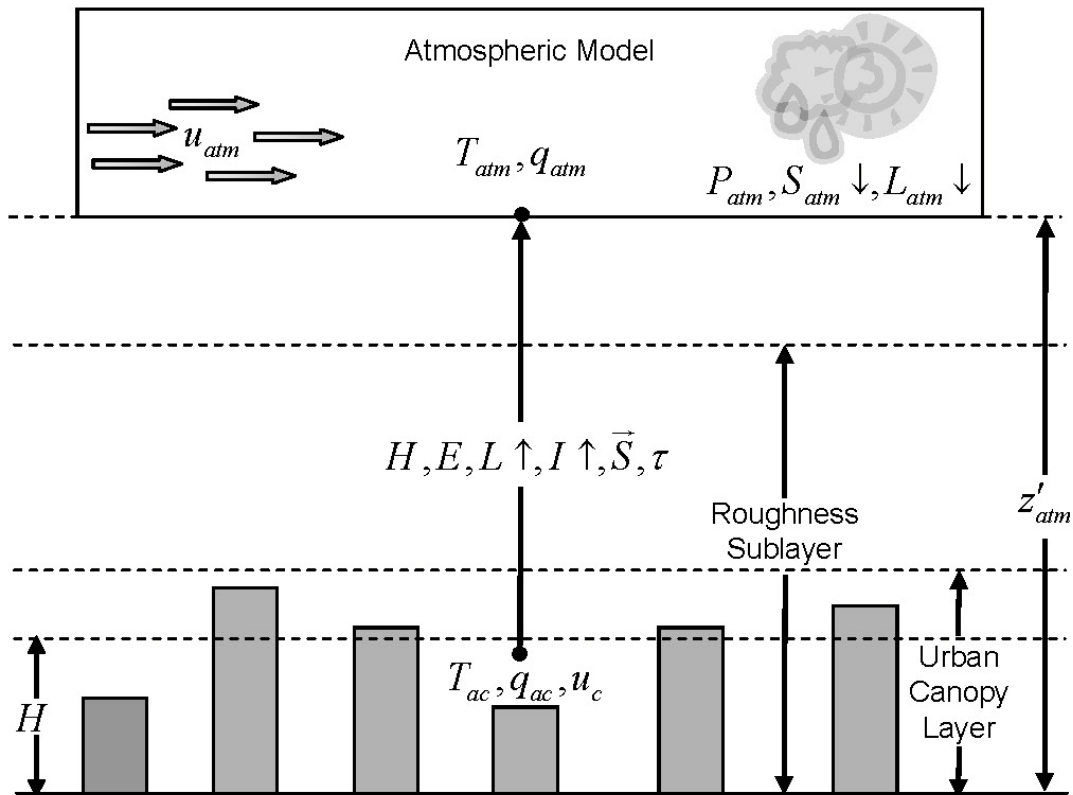
14. Carbon-Nitrogen Model (CN)

14.1 Model description

CLM4 includes a fully-prognostic treatment of the terrestrial carbon and nitrogen cycles, commonly referred to as CN, including interactions between these cycles as mediated by biological mechanisms of plants and soil heterotrophs. This integrated land biogeochemistry model was developed initially through merging the biophysical framework of the Community Land Model (CLM 3.0) (Bonan and Levis 2006, Dickinson et al. 2006, Oleson et al. 2004) with the fully prognostic carbon and nitrogen dynamics of the terrestrial biogeochemistry model Biome-BGC (version 4.1.2) (Thornton et al. 2002, Thornton and Rosenbloom 2005). The resulting model is fully prognostic with respect to all carbon and nitrogen state variables in the vegetation, litter, and soil organic matter, and retains all prognostic quantities for water and energy in the vegetation-snow-soil column from CLM. The seasonal timing of new vegetation growth and litterfall is also prognostic, responding to soil and air temperature, soil water availability, and daylength, in varying degrees depending on a specified phenology type for each PFT. The prognostic LAI, SAI, and vegetation heights are utilized by the biophysical model. General descriptions are provided below for all biogeochemical components of CN. Complete detail on all algorithms and parameterizations is provided in a separate technical note (Thornton et al. 2010). Example applications of the model to study multiple components of the global carbon-nitrogen-climate feedback are given in Thornton et al. (2007) for a modified version of CLM3 with CN driven by offline atmospheric forcing, and in Thornton et al. (2009) for results from a fully-coupled implementation using a modified version of CCSM3.

14.2 Vegetation state variables

The model includes a prognostic treatment for carbon and nitrogen state variables in multiple vegetation tissue types. Separate state variables for C and N are tracked for leaf, live stem, dead stem, live coarse root, dead coarse root, and fine root pools (Figure 14.1). Each of these pools has two corresponding storage pools representing, respectively, short-term and long-term storage of non-structural carbohydrates and labile nitrogen. There are two additional carbon pools, one for the storage of growth respiration reserves, and another used to meet excess demand for maintenance respiration during periods with low photosynthesis. One additional nitrogen pool tracks retranslocated nitrogen, mobilized from leaf tissue prior to abscission and litterfall. Altogether there are 20 state variables for vegetation carbon, and 19 for vegetation nitrogen.

Figure 14.1. Carbon and nitrogen pools.
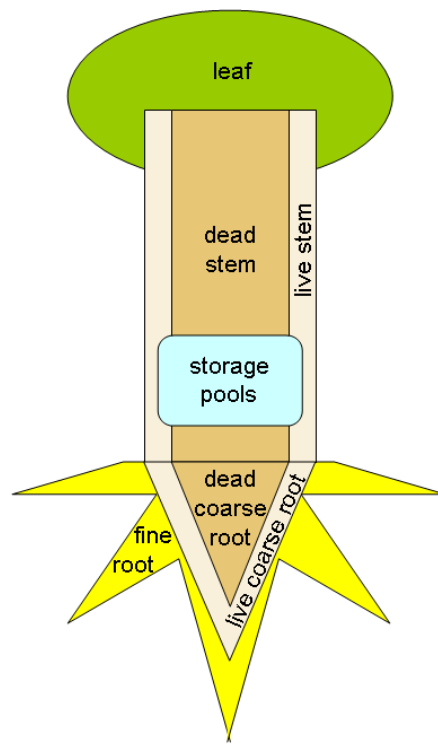
CLM vegetation state variables (pools):

C and N pools for each tissue (structural pools):
- Leaf
- Stem (live and dead)
- Coarse root (live and dead)
- Fine root

Each structural pool has two corresponding storage pools:
- Long-term storage (> 1 yr)
- Short-term storage (< 1 yr)

Additional pools:
- Growth respiration storage (C)
- Maintenance respiration reserve (C)
- Retranslocated nitrogen

Total number of pools…

Carbon: 6 + 12 + 2 = 20

Nitrogen: 6 + 12 + 1 = 19

14.3 Canopy integration and photosynthesis

Canopy integration and photosynthesis are the same as in the biophysical model (see section 4.1 and section 8.2). Canopy-level photosynthesis (or gross primary production, GPP) is derived by summing the sunlit and shaded leaf-level rates scaled by the sunlit and shaded leaf area indices, with potential reductions due to limited availability of mineral nitrogen, as described below.

14.4 Autotrophic respiration

The model treats maintenance and growth respiration processes separately (Lavigne and Ryan 1997, Sprugel et al. 1995). Maintenance respiration (*MR*) is a function of temperature and tissue N concentration (Ryan 1991) for live biomass (excludes dead stem and coarse root pools) (Thornton and Rosenbloom 2005). Rates for aboveground pools are based on the 2 meter air temperature, and rates for belowground pools (fine and coarse roots) depend on fractional rooting distribution with depth (see section 8.3) and the associated prognostic soil temperatures. Growth respiration is calculated as a factor of 0.3 times the total carbon in new growth on a given time step, based on construction costs for a range of woody and non-woody tissues (Larcher 1995).

14.5 Heterotrophic respiration

The model includes carbon and nitrogen states for three litter pools, three soil organic matter pools, and a coarse woody debris pool, structured as a converging cascade. This model structure, the specification of base rates, soil moisture and temperature controls, and the relationship between upstream and downstream nitrogen concentrations, respiration fractions, and nitrogen mineralization and immobilization are described in detail by Thornton and Rosenbloom (2005). Steps in the decomposition process which result in mineralization of nitrogen proceed at their potential (water and temperature

208

limited) rates, but steps which result in immobilization of mineral nitrogen can be limited by its availability (Hunt et al. 1988, Randlett et al. 1996, Rastetter et al. 1991). The total heterotrophic demand for mineral nitrogen is expressed as the sum of potential immobilization over all immobilizing steps in the cascade. For each time step, this heterotrophic demand is in competition with the total plant nitrogen demand from all PFTs sharing space on a single soil column. Once this competition has been resolved (see below), actual immobilization is calculated as a proportion of potential immobilization, with the same proportion applied to all immobilizing steps.

14.6 Carbon and nitrogen allocation

On each model time step and for each PFT sharing space on a soil column, the carbon available for allocation to new growth (C_{AVAIL}) is calculated as $C_{AVAIL} = GPP - MR$. If $MR \geq GPP$, e.g. at night or under conditions of low light or drought stress, then all of the current photosynthesis is directed toward satisfying MR, $C_{AVAIL} = 0$, and any remaining MR requirement is met by drawing down a special storage pool (MR_{POOL}), intended to represent a carbohydrate reserve (Sprugel et al. 1995). Otherwise ($C_{AVAIL} > 0$) the first priority for new allocation is to reduce any deficit in MR_{POOL} that may have accumulated over previous time steps, at a rate that would eliminate the current deficit in 30 days. Any remaining carbon is available for allocation to new plant growth. The allometric relationships that define new allocation of carbon to leaves as a function of ratios between new leaf growth and growth of new fine roots and wood are described in detail by Thornton and Zimmermann (2007), and are modified

here to make the ratio of allocation of new stem to new leaf growth (a_3) a dynamic function of annual net primary production (*NPP*)

$$a_3 = \frac{2.7}{1 + \exp\left[-0.004\left(NPP - 300\right)\right]} - 0.4 \qquad (14.1)$$

giving $a_3 = 2.0$ at *NPP* = 800 gC m^{-2} y^{-1}. This mechanism has the effect of increasing woody allocation in favorable growth environments (Allen et al. 2005, Vanninen and Makela 2005) and during the phase of stand growth prior to canopy closure (Axelsson and Axelsson 1986).

Total plant nitrogen demand for the time step is calculated from carbon allometry and nitrogen concentrations for each tissue type (specified by PFT). Nitrogen concentrations at the tissue level (e.g. leaf N concentration) are specified as constants (Aber et al. 2003, Garcia et al. 1988, Niinemets et al. 1998) that vary between PFTs, following the synthesis of literature values by White et al. (2000). This demand is offset by the deployment of nitrogen retranslocated from senescing leaves to a storage pool in previous time steps. Deployment from this pool occurs at a rate proportional to the pool size and current nitrogen demand as a fraction of the total annual nitrogen demand from the previous year, imposing a demand-based seasonal cycle on the rate of deployment of previously retranslocated nitrogen. Remaining plant nitrogen demand is summed over all PFTs to calculate the demand-based competition between plant uptake and microbial immobilization for a potentially limiting column-level soil mineral nitrogen resource. Unmet plant nitrogen demand is translated back to a carbon supply surplus which is eliminated through reduction of GPP (McGuire et al. 1992), representing direct downregulation of photosynthetic rate under nitrogen limitation. The indirect nitrogen

limitation effect of reduced allocation to new growth on light capture is another significant downregulation mechanism in the model, which operates on longer time scales and has a strong influence on global-scale plant-soil system states and fluxes.

As described by Thornton and Zimmermann (2007), a fraction of the carbon and nitrogen allocated on each time step is stored and displayed as new growth in the following year. The storage fraction is specified as a single value for each PFT, and the timing of display of stored carbon and nitrogen is controlled by the phenology algorithms (see below). Transfer of previously allocated carbon and nitrogen from storage to display as new growth is the mechanism by which deciduous perennial vegetation is able to initiate rapid growth early in the growing season, and here all deciduous PFTs have storage growth set to 50%. The mechanism is less critical for evergreen vegetation, and here we have set storage growth to 0% for all evergreen PFTs.

The model does not impose any fixed constraints on maximum or minimum accumulations of carbon or nitrogen in leaves or other tissues. Vegetation carbon and nitrogen pool sizes at steady state are determined by the dynamic equilibrium between new growth, litterfall, mortality, and losses due to fire. In cases where the combination of climate and plant ecophysiological parameterization does not permit net growth, the vegetation carbon and nitrogen pools are eventually turned over completely to litter. For climate and PFT combinations with very strong growth potential, the accumulation of leaf carbon leads to canopy leaf area index which limits light penetration and mean photosynthetic rate in the shaded canopy fraction, slowing growth and placing a mechanistic upper limit on new growth.

14.7 Phenology

The seasonal timing of new vegetation growth and litterfall is prognostic, responding to soil and air temperature, soil water availability, and daylength, in varying degrees depending on a specified phenology type for each PFT. Three phenology types are considered: evergreen, seasonal deciduous, and stress deciduous. The current treatment of evergreen phenology is very simple, with litterfall occurring at a constant rate through the year, depending on the specified leaf longevity, and with allocation to new growth from current photosynthesis controlling the seasonal cycle of growth and canopy development. The seasonal deciduous phenology algorithm allows a single leaf onset and litterfall period per year. It is applied to temperate and boreal deciduous trees, which typically exhibit a single annual growing season, and for which litterfall is strongly controlled by autumn daylength. Initiation of leaf onset is controlled by a critical degree-day summation, and leaf litterfall is initiated when daylength is shorter than a critical value, following the algorithm and parameterization proposed by White et al. (1997). The period for transfer of new growth from storage and the period for complete leaf litterfall are both set to 15 days.

The stress deciduous algorithm permits multiple growing seasons per year, depending on favorable soil moisture and temperature conditions, and is applied to tropical deciduous trees, and all shrub and grass types. This approach has not been previously published, but it is an extension of the grass phenology algorithm proposed by White et al. (1997). Their algorithm is generalized here to allow multiple growing seasons, for example in warm climates with several distinct dry periods, and to allow stress deciduous types to shift temporarily to an evergreen habit during extended periods (longer than one year) without a critical moisture or cold stress event. If the number of

days with temperature below freezing exceeds a critical value (set here to 15 days) during a dormant period, then initiation of new growth from storage depends on accumulated degree days and accumulated days (set here to 15) with soil water potential above a critical threshold (set here to -2.0 MPa) for the third model soil layer (~4.5 cm below the soil surface). Otherwise, in climates without prolonged soil freezing, initiation of new growth depends only on accumulated favorable soil water conditions. Initiation of leaf litterfall is triggered by accumulated soil water stress, defined as more than 15 days with soil water potential in the third layer < -2.0 MPa, or accumulated cold stress, defined as more than 15 days with soil temperature in the third layer below freezing. For both water and cold stress litterfall triggers, periods with soil water potential or soil temperature above the critical threshold decrease the accumulated quantities, such that a relatively continuous period of either cold or drought stress is required to trigger initiation of litterfall.

14.8 Vegetation structure

On each time step, the prognostic leaf carbon pool is translated to a canopy-scale projected leaf area index, based on the assumption of a vertical gradient in specific leaf area that is linear with overlying leaf area index (Thornton and Zimmermann 2007). The biophysical model requires an estimate of vegetation height (z_{top}). Height is diagnosed for woody vegetation from prognostic stem carbon (C_{stem} C_{stem}, kg C m^{-2}) and a simple allometric model that assumes stems with a fixed linear taper (t = height:radius = 200 for trees (Makela 2002), t =10 for shrubs), fixed stocking density (s = 0.1 stems m^{-2}), and fixed wood density (d = 250 kg C m^{-3}), as $z_{top} = \left(\dfrac{3C_{stem}t^2}{\pi s d} \right)^{1/3}$. Height for non-woody

vegetation types is calculated as a function of total canopy leaf area index, as given by Levis et al. (2004).

14.9 Fire and mortality

The model includes two independent mortality mechanisms; a prognostic fire algorithm that depends on fuel availability and near-surface soil moisture conditions, and whole-plant mortality intended to represent the death of individual plants due to all other causes. The fire routine is based on the model of Thonicke et al. (2001), with modifications to translate the original annual time step to the sub-daily time step of CLM. This time step translation is accomplished with minimal modification to the underlying logic of the original model, and consists mainly of re-interpreting the annual fractional area burned at each time step, as opposed to once per year, and using a running mean of the daily fire probability, with an e-folding time constant of one year, as opposed to a simple annual summation of daily fire probability. The result is that the fractional area burned for a given grid cell acquires a seasonal cycle that corresponds to the seasonal increases and decreases in daily fire probability as predicted by the original model.

The fractional area burned on each time step is applied to the column-level litter and coarse woody debris (CWD) carbon and nitrogen pools, and is applied differentially to the vegetation carbon and nitrogen pools depending on a fire resistivity specified for each PFT (Levis et al. 2004). Combustion is assumed to be complete for the affected proportion of leaf, fine root, and litter pools, while stem and coarse root wood pools and CWD are assumed to undergo incomplete combustion (fixed here at 20% of the affected fraction of the pool). Combusted fractions of carbon pools are returned to the atmosphere as part of the net carbon flux, and combusted nitrogen pools are treated as losses to the

atmosphere. The uncombusted fractions of affected vegetation wood pools are assumed to persist as new additions to the CWD pool, while the uncombusted fraction of affected CWD pool remains in place. Whole-plant mortality is estimated on each time step, and is treated simply as a percentage of total mass in each vegetation pool lost to litter and coarse woody debris pools on an annual basis. A value of 2% yr^{-1} is used here for all PFTs, although a more mechanistic treatment with dependencies on PFT, age, and size distribution of individuals (Bugmann and Solomon 2000, Busing 2005, Gomes et al. 2003, Kohyama et al. 2001) is desirable.

14.10 Nitrogen sources and sinks

The long-term balance between gains and losses of nitrogen is a dominant control on productivity and carbon storage for many ecosystems (Galloway et al. 2004, Gosz et al. 1973, Vitousek and Howarth 1991). Thornton and Rosenbloom (2005) demonstrated the importance of this control for the Biome-BGC model, and these dynamics apply as well to CN. The model includes deposition of mineral nitrogen, combining deposition of NO_y and NH_x, from the atmosphere and biological nitrogen fixation as the sources of new mineral nitrogen entering terrestrial ecosystems. Both sources are assumed to enter the soil mineral nitrogen pool directly. Atmospheric deposition is prescribed as an annual rate for each grid cell, with the option of providing a time varying field. Values are time-interpolated if necessary to produce a smoothly varying field at each grid cell. These rates were obtained from a transient 1850-2009 CAM simulation (at a resolution of 1.9x2.5x26L) with interactive chemistry (troposphere and stratosphere) driven by CCSM3 20th century sea-surface temperatures and emissions (Lamarque et al. 2010, in preparation) for short-lived gases and aerosols; observed concentrations were specified

for methane, N_2O, the ozone-depleting substances (CFCs) ,and CO_2. Biological nitrogen fixation (*BNF*, g N m-2 y^{-1}) is estimated as a function of annual net primary production (*NPP*, g C m^{-2}y^{-1}), as $BNF = 1.8\left[1-\exp\left(-0.003NPP\right)\right]$. This formulation captures the observed broad-scale dependency of *BNF* on ecosystem productivity (Cleveland et al. 1999, Luo et al. 2006). This functional form has smaller increases in *BNF* at higher *NPP*, which is intended to represent the hypothesis that N fixation is eventually limited by other nutrients, especially phosphorus (Vitousek and Howarth 1991). The model includes four pathways for nitrogen loss: denitrification, volatilization, leaching, and losses due to fire, as described by Thornton and Rosenbloom (2005).

15. Transient Landcover Change

CLM includes a treatment of mass and energy fluxes associated with prescribed temporal change in land cover. Using an annual time series of the spatial distribution of PFTs, CLM diagnoses the change in area for PFTs at each model time step and then performs mass and energy balance accounting necessary to represent the expansion and contraction of PFT area. This implementation currently only pertains to the case where all PFTs for a particular grid cell coexist on a single soil/snow column. In this case, the only biogeophysical state variable affected is canopy water (W_{can}). The biogeochemical implementation is described in Thornton et al. (2010). Other implementations are possible, such as changing the area of soil/snow columns or landunit area. These would require additional consideration of conservation of mass and energy among the soil/snow columns and landunits.

15.1 Annual Transient Land Cover Data and Time Interpolation

The changes in area over time associated with individual PFTs are prescribed through a forcing dataset, referred to here as the *dynpft* dataset. The *dynpft* dataset consists of an annual time series of global grids, where each annual time slice describes the fractional area occupied by all PFTs within each grid cell. Changes in area for each PFT within a grid cell at each model time step are inferred from a time-interpolation of the area information for the PFT from the two bracketing annual time slices in the *dynpft* dataset.

As a special case, when the time dimension of the *dynpft* dataset starts at a later year than the current model time step, the first time slice from the *dynpft* dataset is used to represent the current time step PFT fractional area distributions. Similarly, when the

time dimension of the *dynpft* dataset stops at an earlier year than the current model time step, the last time slice of the *dynpft* dataset is used. Thus, the simulation will have invariant representations of PFT distributions through time for the periods prior to and following the time duration of the *dynpft* dataset, with transient PFT distributions during the period covered by the *dynpft* dataset.

The following equations capture this logic, where $year_{cur}$ is the calendar year for the current timestep, $dynpft\_year(1)$ and $dynpft\_year(nyears)$ are the first and last calendar years in the *dynpft* dataset, respectively, $nyears$ is the number of years in the *dynpft* dataset, nt_1 and nt_2 are the two bracketing years used in the interpolation algorithm, and n is the index value for the $dynpft\_year$ array corresponding to $dynpft\_year(n) = year_{cur}$:

$$nt_1 = \begin{cases} 1 & \text{for} & year_{cur} < dynpft\_year(1) \\ n & \text{for} & dynpft\_year(1) \le year_{cur} < dynpft\_year(nyears) \\ nyears & \text{for} & year_{cur} \ge dynpft\_year(nyears) \end{cases} \quad (15.1)$$

$$nt_2 = \begin{cases} 1 & \text{for} & year_{cur} < dynpft\_year(1) \\ n+1 & \text{for} & dynpft\_year(1) \le year_{cur} < dynpft\_year(nyears) \\ nyears & \text{for} & year_{cur} \ge dynpft\_year(nyears) \end{cases} \quad (15.2)$$

Interpolation of PFT weights between annual time slices in the *dynpft* dataset uses a simple linear algorithm, based on the conversion of the current time step information into a floating-point value for the number of calendar days since January 1 of the current model year ($cday$). The interpolation weight for the current time step tw_{cday} is

$$tw_{cday} = \frac{366 - cday}{365} \quad (15.3)$$

where the numerator is 366 instead of 365 because the time manager function for CLM returns a value of $cday = 1.0$ for a time of 0Z on January 1. With weights $w_p(nt_1)$ and $w_p(nt_2)$ obtained from the *dynpft* dataset for PFT p at the bracketing annual time slices nt_1 and nt_2, the interpolated PFT weight for the current time step ($w_{p,t}$) is

$$w_{p,t} = tw_{cday}\left[w_p(nt_1) - w_p(nt_2)\right] + w_p(nt_2) \tag{15.4}$$

The form of this equation is designed to improve roundoff accuracy performance, and guarantees $w_{p,t}$ stays in the range [0,1]. Note that values for $w_p(nt_1)$, $w_p(nt_2)$, and $w_{p,t}$ are fractional weights at the column level of the subgrid hierarchy.

The change in weight for a PFT between the current and previous time steps (Δw_p) is

$$\Delta w_p = w_p^n - w_p^{n-1} \tag{15.5}$$

where n denotes the current time step. The area of a given PFT increases for $\Delta w_p > 0$ and decreases for $\Delta w_p < 0$.

15.2 Mass and Energy Conservation

Mass conservation is maintained across a PFT weight transition by summing up all the water state variables to get the total vegetated landunit water content before ($W_{tot,1}$) and after ($W_{tot,2}$) new PFT weights are calculated. For example, $W_{tot,1}$ is

$$W_{tot,1} = W_a + W_{sno} + \sum_{i=1}^{N_{levgrnd}} \left(w_{liq,i} + w_{ice,i}\right) + \sum_{j=1}^{npft}\left(W_{can,j} wt_{j,1}\right) \tag{15.6}$$

where W_a is the aquifer water, W_{sno} is the snow water, $w_{liq,i}$ and $w_{ice,i}$ are the liquid and ice soil water contents, $W_{can,j}$ is the canopy water content for PFT j, and $wt_{j,1}$ is the PFT

weight for PFT j. For the situation where only PFT weights are changing and all other landunit fractions are constant, any difference between $W_{tot,1}$ and $W_{tot,2}$ can only be due to differences in the total canopy water before and after the PFT weight change. To ensure water conservation, the typically very small difference between $W_{tot,2}$ and $W_{tot,1}$ is subtracted from the grid cell runoff

$$R_{liq} = R_{liq} + W_{tot,2} - W_{tot,1}.$$ (15.7)

Total energy is unperturbed in this case and therefore an energy conservation treatment is not required. As noted above, other implementations are possible and will be desirable in the future, such as changing the area of soil/snow columns or landunit area, for example in a situation in which crops are implemented on a separate soil column. These would require additional consideration of conservation of mass and energy among the soil/snow columns and landunits.

15.3 Annual Transient Land Cover Dataset Development

This section describes the development of the d*ynpft* dataset. Development of this dataset requires adapting for use with the CLM a harmonized dataset of land cover change for the historical period and for different representations of the scenario period.

15.3.1 UNH Transient Land Use and Land Cover Change Dataset

To coordinate the processing and consistency of land use and land cover change data between the historical period (1850-2005) and the four IPCC representative concentration pathways (RCPs) derived from integrated assessment models (IAM), the University of New Hampshire (UNH) research group (Louise Chini, George Hurtt, Steve Frolking; luh.unh.edu) produced a harmonized transient dataset for use in climate change simulations. The historical component of the transient land use and land cover change

dataset is Version 1 of the Land-Use History A product (LUHa.v1) covering the period 1850-2005. The RCP transient land use and land cover change components (2005-2100) are referred to as the Future Land-Use Harmonization A products. Version 1 (LUHa.v1_future.v1) is used for the AIM, MESSAGE, and MiniCAM IAMs; Version 1.1 (LUHa.v1_future.v1.1) is used for the IMAGE IAM. The land cover information is provided at 0.5 degree grid resolution and includes fractional grid cell coverage by crops, pasture, and primary and secondary natural vegetation.

The crop fraction of the grid cell represents the area of the grid cell used to grow any type of crop. Similarly, pasture represents the fraction of a grid cell used for grazing livestock. The remaining area in a half degree grid cell is partitioned into primary and secondary vegetation. Primary vegetation represents the fractional area of a grid cell with vegetation undisturbed by human activities. Secondary vegetation represents vegetated areas that have recovered from some human disturbance; this could include re-vegetation of pasture and crop areas as well as primary vegetation areas that have been logged.

The UNH dataset provides a transition matrix that describes the annual fraction of land that is transformed from one category to another (e.g. primary land to crop, pasture to crop, etc.; Hurtt et al. 2006). Included in these transitions is the conversion of secondary land to secondary land, representing the logging on land recovering from an earlier disturbance. These transitions provide not only information on changes in land cover; the sum of all the wood harvest for all the transitions in a given year gives an estimate of the amount of biomass harvested from the grid cell.

15.3.2 Representing Land Use and Land Cover Change in CLM

CLM represents the land surface as a hierarchy of sub-grid types: glacier; lake; wetland; urban; and vegetated land. The vegetated land is further divided into a mosaic of PFTs. To represent the UNH transient land use and land cover change dataset in CLM, the annual fractional composition of crop, pasture, primary vegetation, and secondary vegetation land units specified in the UNH dataset needs to be faithfully represented with a corresponding PFT mosaic in CLM. To achieve this, each land unit is translated into fractional PFT values based on current day and potential vegetation CLM land surface parameters for that grid cell and for that year, as shown in Figure 15.1.

The methodology for creating the transient PFT dataset is based on four steps which are applied across the time series. First, crop PFT composition is directly specified from the crop land unit fractional area. Second, pasture PFTs are assigned based on grass PFTs found in the potential vegetation and current day CLM land surface parameters scaled by the area of pasture. Third, potential vegetation PFTs are assigned to the grid cell scaled by the fractional area of the primary land unit. Last, current day non-crop and non-pasture PFTs are assigned to the grid cell scaled by the fractional area of the secondary land unit. The annual tree harvest values also are calculated from the harvest information of the UNH dataset used in conjunction with transient tree PFT values. Separate datasets representing the extent of water, wetland, ice and urban land cover are used to compile the final land cover present in each CLM grid cell. These additional non-vegetated land cover fractions are held constant throughout the time series. All datasets are resolved at the half degree grid resolution.

15.3.3 Present Day PFT Dataset

The present day dataset is based on the methodology of Lawrence and Chase (2007) and uses a variety of satellite products to develop present day PFT distributions with matching leaf area index values. The dataset initially derives fractions of bare ground and forest land cover from the Moderate Resolution Imaging Spectroradiometer (MODIS) continuous vegetation fields (Hansen et al. 2003). To further distinguish tree types, the tree fraction is divided into broadleaf/needleleaf and evergreen/deciduous types based on the Advanced Very High Resolution Radiometer (AVHRR) continuous fields tree cover (DeFries et al. 2000). The remaining grid cell area is assumed to be herbaceous grasses and shrubs, including crops. The area of crop is initially determined from Ramankutty et al. (2008) circa 2000 global crop land areas, and the remaining grass and shrub fractions are derived from the MODIS land cover (Friedl et al. 2002). Further subdivisions of grass, shrub and tree PFTs into tropical, temperate and boreal types were based on the physiology and climate rules from Nemani and Running (1996), and for C3/C4 photosynthetic pathways based on MODIS derived leaf area index values and the mapping methods of Still et al. (2003). In contrast to Lawrence and Chase (2007), the understory grasses have been removed from the dataset. Some advantages of this dataset are that it reproduces the physical properties as observed by the MODIS land surface data (e.g. grid cell albedo and leaf area index values) while maintaining the multiple PFT representation. Upon completion of the natural PFT calculations, the final crop area was adjusted to that of the UNH dataset for the 2005 base year. Non-tree PFTs in the grid cell were adjusted to accommodate any displaced area.

15.3.4 Potential PFT Distribution

Essential to any reconstruction of past vegetation distributions is the need to know the potential vegetation that would be there prior to human activities. Many researchers have worked to estimate potential vegetation types at regional and global scales from remnant vegetation and other field data or from bioclimatic models. The CLM potential PFT distribution is derived from Ramankutty et al. (2008) at 5 arc-minute resolution. However, this product is based on a biome type classification system that is not directly compatible with the CLM PFT distributions.

The CLM potential vegetation is described by Lawrence and Chase (2010). This reconstruction describes potential PFT distributions extrapolated from the current day PFT composition of remnant natural biomes as mapped by Ramankutty et al. (2008). The current day remnant natural PFT parameters were taken from the Lawrence and Chase (2007) dataset to ensure consistency between the two datasets. The current day remnant natural PFT biome compositions were spatially extrapolated to the potential vegetation biome distributions provided by Ramankutty et al. (2008) using inverse distance weighted methods. The resulting product is a CLM PFT distribution that may have existed prior to human disturbance under current day climate conditions.

15.3.5 Transient Land Cover Change Dataset

For each year from 1850 to 2005 and to 2100 for each of the four RCPs, PFT distributions are adjusted based on the UNH dataset. Initially the grid cell is checked to adjust the crop area based on the UNH crop area. If the crop area exceeds the available land area (i.e. the grid cell area minus the area assigned to glacier, wetlands, lake and urban areas) then all the available area is allocated to crops and no other PFTs are added. After the crop area is assigned, any remaining area is considered available for pasture.

As the pasture data from the UNH dataset represents grazing, pasture areas are assigned in the present day based on the availability of grasses (C3, C4 and boreal C3 PFTs) and shrubs relative to the bare soil fraction. If the grazing area exceeds the total vegetated area from both the potential and current day PFT data, then the grazed area is limited to the larger of the potential or current day vegetated area. This is done to prevent representing sparsely vegetated grazing areas as 100% vegetated pastures. Once the grazing area is less than or equal to the total vegetated area, then grazing areas are assigned to the C3 and C4 grass areas based on their potential vegetation and current day fractions. In areas where the grazing area cannot be met through the current day or potential vegetation grass fraction alone, the current day tree PFTs are converted to grass PFTs, with the remaining shrub PFTs included as being grazed.

Once crop and pasture areas are assigned to a grid cell, the remaining area is assigned to primary and secondary natural vegetation. Primary vegetation is assumed to be undisturbed and reflects the potential vegetation PFT distributions. In the secondary region, the PFT distributions are based on the current day non-crop and non-pasture PFTs in the grid cell. This process ensures that the PFT distributions are kept consistent with the original current day and potential vegetation CLM parameters, while remaining faithful to the UNH assigned areas.

15.3.6 Forest Harvest Dataset

In addition to land cover change, CLM includes the effects of wood harvest, represented as removal of biomass from any trees present in a grid cell (used only with the biogeochemical model). However, not all harvest types in the UNH dataset originate directly from tree harvest (e.g. the non-forested types), and thus there is a discrepancy in

the way wood is harvested in CLM and how it is represented in the UNH dataset. Comparison of average global carbon densities in the UNH dataset showed that secondary mature tree and secondary young tree harvest have carbon densities equal to about 60% of the carbon density values associated with mature primary forest harvest areas; non-forested primary and secondary lands have typical carbon densities equal to about 5% of those in the primary forested lands. To represent these decreased carbon densities in CLM, which does not distinguish among these land types, the actual tree area harvested is determined as

$$\text{Harvest area} = vh1 + 0.05 \, vh2 + 0.6 \, sh1 + 0.6 \, sh2 + 0.05 \, sh3 \qquad (15.8)$$

where $vh1$ represents the fractional area that has wood harvested from primary (undisturbed) forest, $vh2$ represents the fractional area that has wood harvested from primary non-forested land, $sh1$ represents the fractional harvest area from mature secondary forest, $sh2$ represents the fractional harvest area from young secondary forest, and $sh3$ represents the fractional harvest area from secondary non-forested land.

Equation (15.8) is the preferred representation of harvest to account for different harvest types. The default representation in CLM uses unscaled fractions so that

$$\text{Harvest area} = vh1 + vh2 + sh1 + sh2 + sh3. \qquad (15.9)$$

Figure 15.1. Schematic of translation of annual UNH land units to CLM4 plant
functional types.
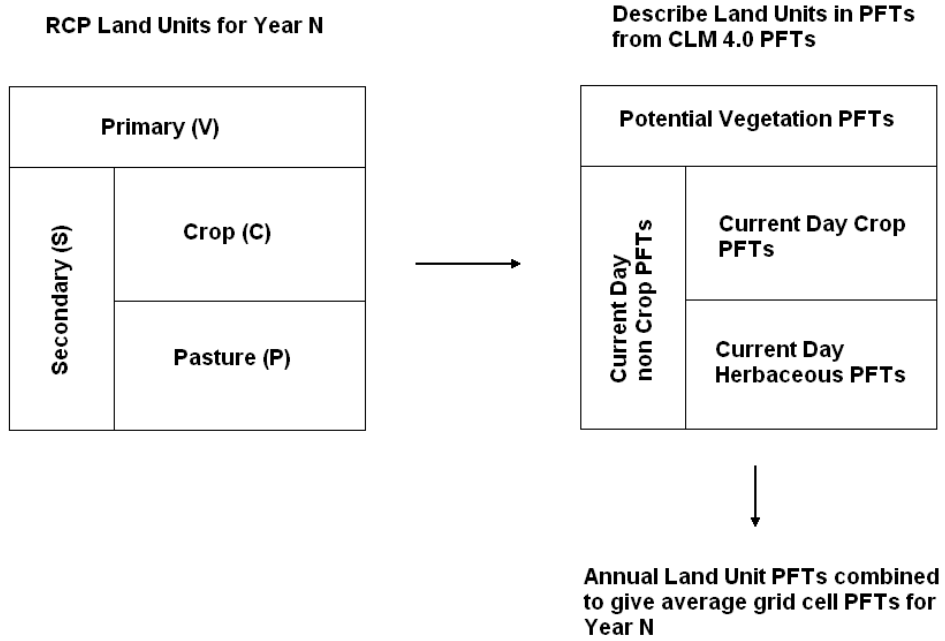
16. Dynamic Global Vegetation Model

Prior versions of CLM permitted the model to be run as a dynamic global vegetation model (CLM-dgvm) (Levis et al. 2004). However, these prior versions of the dgvm are not compatible with the new carbon and nitrogen biogeochemistry model (CN, see section 14) since both the CLM-dgvm and CN included their own carbon calculations, and the dgvm did not include a nitrogen cycle. Note that the standard CN model performs carbon and nitrogen calculations but does not allow for dynamic biogeography.

In CLM4 the user may choose to run the CN model as a dgvm (CNDV). Note that CN must be active to run the dgvm in CLM4. In this section, a general description of the dgvm processes and how they integrate with CN are provided. Further details are available in the CN Technical Note (Thornton et al., 2010) and the CLM3.0 DGVM Technical Note (Levis et al, 2004). The focus here is on the differences relative to the corresponding processes in the CLM-dgvm.

As with the CLM-dgvm, CNDV can only simulate biogeographical changes of natural vegetation. In CNDV, the vegetated landunit is separated into naturally vegetated and human managed landunits to permit a coexistence of natural and human managed vegetation. This only works if the human managed landunits is fixed. CLM's transient land cover and land use change capability (see section 15), which permits transitions between natural and human managed plant functional types (PFTs), is incompatible with the CNDV option at this time.

To implement CNDV, CLM-dgvm code was introduced to the hourly CN framework only to the extent necessary to simulate annual biogeography updates. This

includes the annual processes of light competition, establishment, and survival (see sections 2.7 and 2.10, Levis et al. (2004)) as they pertain to the calculations of PFT cover (FPC) and population (P) but not processes related to carbon pools, leaf area index (LAI), or canopy height. In CNDV we added complexity to the gap mortality calculation with annual heat stress and growth efficiency considerations from the corresponding CLM-dgvm algorithm (section 2.8, Levis et al. (2004)). All other ecosystem processes (allocation, phenology, fire, etc.) are handled by CN modules. Unlike in the CLM-dgvm, in CNDV, annual biogeography updates are interpolated to hourly intervals.

16.1 Establishment and survival

The PFT distribution in the vegetated landunit is typically prescribed in CLM (see section 1.1.2) except for the case when CNDV is active. In CNDV the model begins with no PFT information per grid cell and evaluates whether or not a PFT may establish or survive according to the PFT's bioclimatic limits (Table 16.1). Shrub PFTs are treated as trees at establishment.

CNDV omits the CLM-dgvm's annual introduction of saplings when a PFT can establish. The CLM-dgvm merged sapling carbon pools with a PFT's existing carbon. The resultant leaf carbon (annual maximum value) would update the FPC, i.e. the foliar projective cover or fraction of the vegetated landunit occupied by the PFT (section 2.10, Levis et al. (2004)). Instead, CNDV updates the FPC using the PFT's annual maximum leaf carbon without an addition from saplings. For newly established PFTs, CNDV assigns seed leaf carbon equal to 1 g C m^{-2} of landunit area and seed FPC equal to 0.05 for grasses and 0.000844 for trees (values determined from CLM-dgvm simulations). The

addition of establishing individuals to *P*, a PFT's population, is handled as in the CLM-dgvm.

FPC changes annually as in the CLM-dgvm but now is interpolated to an hourly increment using the algorithms designed to conserve energy and mass in the CLM's dynamic land use option.

16.2 Light competition

In CNDV's order of annual processes, light competition is invoked before establishment and survival. However, light competition does not affect a simulation starting from bare ground until the vegetation fills the landunit (a few years at least).

Light competition starts with a calculation updating *FPC*. For reference, this update was included at the end of allocation in the CLM-dgvm (section 2.6, Levis et al. (2004)).

Due to their height advantage, trees will cover up to 95% of the landunit when their productivity permits, as in the CLM-dgvm, regardless of grass and shrub productivity. Grasses get second priority, as in the CLM-dgvm, even with shrubs included now. Shrubs, then, have access to the remaining space and follow the tree algorithm for self thinning (section 2.7, Levis et al. (2004)). As a result, trees typically dominate in the most productive regions, grasses in less productive regions, and shrubs in the least productive non-desert regions (Zeng et al. 2008).

16.3 CN processes modified for the CNDV coupling

Gap mortality and mortality from fire: Constant annual mortality rate of 0.02 is changed for trees and shrubs to an annual rate calculated as in the CLM-dgvm accounting for background and stress mortality (section 2.8, Levis et al. (2004)). The CN module converts the annual rate to hourly.

The CLM-dgvm used the concepts of average plant individual and PFT population, *P*. CNDV retains these concepts in the light competition, establishment, and survival calculations. In CNDV we account for the individuals removed hourly from *P* in response to CN's fire and gap mortality, while the carbon pools per individual and FPC remain constant. Ultimately, *P* updates should only affect the annual processes of light competition, establishment, and survival, so the *P* update may be moved to the end of the year in a future version of CNDV.

Vegetation Structure Update: CN stocking is a constant, while in CNDV stocking changes as P and FPC change. This affects the top-of-canopy height calculation. CN specific leaf area and stem diameter calculations are kept, while the height calculation is replaced with the CLM-dgvm's (section 2.6, Levis et al. (2004)). CN stem area index (SAI) is kept.

Allocation: CN calculates a PFT's fraction of currently allocated carbon relative to the total allocation instead of obtaining a constant value from CLM's PFT-physiology file. In CNDV, we returned to the constant values in the old PFT-physiology file to get a reasonable simulation of PFTs. For CNDV to use the calculated fraction, we will need to change the algorithm for PFTs in early stages of growth.

Table 16.1. Plant functional type (PFT) biogeography rules with respect to climate. Adapted from Table 1 of Levis et al. (2004) to include shrub PFTs. $T_{c,\min}$, coldest minimum monthly air temperature for survival of previously established PFTs; $T_{c,\max}$, warmest minimum monthly air temperature for establishment of new PFTs; $GDD_{\min}$, minimum annual growing degree-days above 5°C for establishment of new PFTs. Levis et al. (2004) include an explanation of these variables and their use.

PFT and PFT number corresponding to the list of PFTs in Table 2.1		Survival	Establishment	
		$T_{c,\min}$ (°C)	$T_{c,\max}$ (°C)	$GDD_{\min}$
Tropical broadleaf evergreen tree (BET)	(4)	15.5	No limit	0
Tropical broadleaf deciduous tree (BDT)	(6)	15.5	No limit	0
Temperate needleleaf evergreen tree (NET)	(1)	-2.0	22.0	900
Temperate broadleaf evergreen tree (BET)	(5)	3.0	18.8	1200
Temperate broadleaf deciduous tree (BDT)	(7)	-17.0	15.5	1200
Boreal needleleaf evergreen tree (NET)	(2)	-32.5	-2.0	600
Boreal deciduous tree	(8)	No limit	-2.0	350
Temperate broadleaf deciduous shrub (BDS)	(10)	-17.0	No limit	1200
Boreal broadleaf deciduous shrub (BDS)	(11)	No limit	-2.0	350
C_4	(14)	15.5	No limit	0
C_3	(13)	-17.0	15.5	0
C_3 arctic	(12)	No limit	-17.0	0

17. Offline Mode

In offline mode (uncoupled to an atmospheric model), the atmospheric forcing required by CLM (Table 1.1) is supplied by observed datasets. The standard forcing provided with the model is a 57-year (1948-2004) dataset that is described in Qian et al. (2006) though alternative observed forcing datasets could also be used. The forcing data is ingested into a data atmosphere model in three "streams"; precipitation (P) (mm s^{-1}), solar radiation (S_{atm}) (W m^{-2}), and four other fields [atmospheric pressure P_{atm} (Pa), atmospheric specific humidity q_{atm} (kg kg^{-1}), atmospheric temperature T_{atm} (K), and atmospheric wind W_{atm} (m s^{-1})]. These are separate streams because they are handled differently according to the type of field and the temporal resolution at which they are provided. In the Qian et al. (2006) dataset, the precipitation stream is provided at six hour intervals and the data atmosphere model prescribes the same precipitation rate for each model time step within the six hour period. The four fields that are grouped together in another stream (pressure, humidity, temperature, and wind) are provided at three hour intervals and the data atmosphere model linearly interpolates these fields to the time step of the model.

The total solar radiation is provided at six hour intervals. The data is fit to the model time step using a diurnal function that depends on the cosine of the solar zenith angle μ to provide a smoother diurnal cycle of solar radiation and to ensure that all of the solar radiation supplied by the six-hourly forcing data is actually used. The solar radiation at model time step t_M is

$$S_{atm}(t_M) = \frac{\frac{\Delta t_{FD}}{\Delta t_M} S_{atm}(t_{FD}) \mu(t_M)}{\sum_{i=1}^{\frac{\Delta t_{FD}}{\Delta t_M}} \mu(t_{M_i})} \qquad \text{for } \mu(t_M) > 0.001$$

$$S_{atm}(t_M) = 0 \qquad \text{for } \mu(t_M) \le 0.001$$

(17.1)

where Δt_{FD} is the time step of the forcing data (6 hours $\times$ 3600 seconds hour^{-1} = 21600 seconds), Δt_M is the model time step (seconds), $S_{atm}(t_{FD})$ is the six-hourly solar radiation from the forcing data (W m^{-2}), and $\mu(t_M)$ is the cosine of the solar zenith angle at model time step t_M (section 3.3). The term in the denominator of equation (17.1) is the sum of the cosine of the solar zenith angle for each model time step falling within the six hour period. For numerical purposes, $\mu(t_{M_i}) \ge 0.001$.

The total incident solar radiation S_{atm} at the model time step t_M is then split into near-infrared and visible radiation and partitioned into direct and diffuse according to factors derived from one year's worth of hourly CAM output from CAM version cam3_5_55 as

$$S_{atm} \downarrow_{vis}^{\mu} = R_{vis}(\alpha S_{atm})$$

(17.2)

$$S_{atm} \downarrow_{nir}^{\mu} = R_{nir}[(1-\alpha) S_{atm}]$$

(17.3)

$$S_{atm} \downarrow_{vis} = (1 - R_{vis})(\alpha S_{atm})$$

(17.4)

$$S_{atm} \downarrow_{nir} = (1 - R_{nir})[(1-\alpha) S_{atm}].$$

(17.5)

where α, the ratio of visible to total incident solar radiation, is assumed to be

$$\alpha = \frac{S_{atm} \downarrow_{vis}^{\mu} + S_{atm} \downarrow_{vis}}{S_{atm}} = 0.5 .$$

(17.6)

The ratio of direct to total incident radiation in the visible R_{vis} is

$$R_{vis} = a_0 + a_1 \times \alpha S_{atm} + a_2 \times (\alpha S_{atm})^2 + a_3 \times (\alpha S_{atm})^3 \quad 0.01 \le R_{vis} \le 0.99 \tag{17.7}$$

and in the near-infrared R_{nir} is

$$R_{nir} = b_0 + b_1 \times (1-\alpha) S_{atm} + b_2 \times \left[(1-\alpha) S_{atm}\right]^2 + b_3 \times \left[(1-\alpha) S_{atm}\right]^3 \quad 0.01 \le R_{nir} \le 0.99 \tag{17.8}$$

where $\quad a_0 = 0.17639, a_1 = 0.00380, a_2 = -9.0039 \times 10^{-6}, a_3 = 8.1351 \times 10^{-9} \quad$ and

$b_0 = 0.29548, b_1 = 0.00504, b_2 = -1.4957 \times 10^{-5}, b_3 = 1.4881 \times 10^{-8}$ are coefficients from

polynomial fits to the CAM data.

The additional atmospheric forcing variables required by Table 1.1 are derived as

follows. The atmospheric reference height z'_{atm} (m) is set to 30 m. The directional wind

components are derived as $u_{atm} = v_{atm} = W_{atm}/\sqrt{2}$. The potential temperature $\overline{\theta}_{atm}$ (K) is

set to the atmospheric temperature T_{atm}. The atmospheric longwave radiation $L_{atm}\downarrow$ (W

m^{-2}) is derived from the atmospheric vapor pressure e_{atm} and temperature T_{atm} (Idso

1981) as

$$L_{atm}\downarrow = 0.70 + 5.95 \times 10^{-5} \times 0.01 e_{atm} \exp\left(\frac{1500}{T_{atm}}\right) \sigma T_{atm}^4 \tag{17.9}$$

where

$$e_{atm} = \frac{P_{atm} q_{atm}}{0.622 + 0.378 q_{atm}} \tag{17.10}$$

and σ is the Stefan-Boltzmann constant (W m^{-2} K^{-4}) (Table 1.4). The fraction of

precipitation P (mm s^{-1}) falling as rain and/or snow is

$$q_{rain} = P(f_P), \tag{17.11}$$

$$q_{snow} = P(1 - f_P) \qquad (17.12)$$

where

$$f_P = 0 < 0.5(T_{atm} - T_f) < 1. \qquad (17.13)$$

The aerosol deposition rates D_{sp} (14 rates as described in Table 1.1) are provided by a time-varying, globally-gridded deposition file defined in the namelist (see the CLM User's Guide).

If the user wishes to provide atmospheric forcing data from another source, the data format outlined above will need to be followed with the following exceptions. The data atmosphere model will accept a user-supplied relative humidity RH (%) and derive specific humidity q_{atm} (kg kg^{-1}) from

$$q_{atm} = \frac{0.622e_{atm}}{P_{atm} - 0.378e_{atm}} \qquad (17.14)$$

where the atmospheric vapor pressure e_{atm} (Pa) is derived from the water ($T_{atm} > T_f$) or ice ($T_{atm} \le T_f$) saturation vapor pressure $e_{sat}^{T_{atm}}$ as $e_{atm} = \frac{RH}{100} e_{sat}^{T_{atm}}$ where T_f is the freezing temperature of water (K) (Table 1.4), and P_{atm} is the pressure at height z_{atm} (Pa). The data atmosphere model will also accept a user-supplied dew point temperature T_{dew} (K) and derive specific humidity q_{atm} from

$$q_{atm} = \frac{0.622e_{sat}^{T_{dew}}}{P_{atm} - 0.378e_{sat}^{T_{dew}}}. \qquad (17.15)$$

Here, e_{sat}^T, the saturation vapor pressure as a function of temperature, is derived from Lowe's (1977) polynomials (section 5.5). If not provided by the user, the atmospheric

pressure P_{atm} (Pa) is set equal to the standard atmospheric pressure $P_{std} = 101325$ Pa, and surface pressure P_{srf} (Pa) is set equal to P_{atm}.

The user may provide the total direct and diffuse solar radiation, $S_{atm}\downarrow^{\mu}$ and $S_{atm}\downarrow$. These will be time-interpolated using the procedure described above and then each term equally apportioned into the visible and near-infrared wavebands (e.g., $S_{atm}\downarrow^{\mu}_{vis} = 0.5 S_{atm}\downarrow^{\mu}$, $S_{atm}\downarrow^{\mu}_{nir} = 0.5 S_{atm}\downarrow^{\mu}$).

18. References

Aber, J.D., Goodale, C.L., Ollinger, S.V., Smith, M.-L., Magill, A.H., Martin, M.E., Hallett, R.A., and Stoddard, J.L. 2003. Is nitrogen deposition altering the nitrogen status of northeastern forests? BioScience 53:375-389.

Allen, C.B., Will, R.E., and Jacobson, M.A. 2005. Production efficiency and radiation use efficiency of four tree species receiving irrigation and fertilization. Forest Science 51:556-569.

Anderson, E.A. 1976. A point energy and mass balance model of a snow cover. NOAA Technical Report NWS 19, Office of Hydrology, National Weather Service, Silver Spring, MD.

André, J.-C., Goutorbe, J.-P., and Perrier, A. 1986. HAPEX-MOBILHY: A hydrologic atmosphere experiment for the study of water budget and evaporation flux at the climatic scale. Bull. Amer. Meteor. Soc. 67:138-144.

Arya, S.P. 2001. Introduction to Meteorology. Academic Press, San Diego, CA.

Asner, G.P., Wessman, C.A., Schimel, D.S., and Archer, S. 1998. Variability in leaf and litter optical properties: implications for BRDF model inversions using AVHRR, MODIS, and MISR. Remote Sens. Environ. 63:243-257.

Axelsson, E., and Axelsson, B. 1986. Changes in carbon allocation patterns in spruce and pine trees following irrigation and fertilization. Tree Phys. 2:189-204.

Baldocchi, D., et al. 2001. FLUXNET: A new tool to study the temporal and spatial variability of ecosystem-scale carbon dioxide, water vapor, and energy flux densities. Bull. Amer. Meteor. Soc. 82:2415-2433.

Berger, A.L. 1978a. Long-term variations of daily insolation and quaternary climatic changes. J. Atmos. Sci. 35:2362-2367.

Berger, A.L. 1978b. A simple algorithm to compute long-term variations of daily or monthly insolation. Contribution de l'Institut d'Astronomie et de Géophysique, Université Catholique de Louvain, Louvain-la-Neuve, No. 18.

Berger, A., Loutre, M.-F., and Tricot, C. 1993. Insolation and Earth's orbital periods. J. Geophys. Res. 98:10341-10362.

Berkowitz, B., and Balberg, I. 1992. Percolation approach to the problem of hydraulic conductivity in porous media. Transport in Porous Media 9:275–286.

Beven, K.J., and Kirkby, M.J. 1979. A physically based variable contributing area model of basin hydrology. Hydrol. Sci. Bull. 24:43-69.

Bohren, C. F., and Huffman, D. R. 1983. Absorption and scattering of light by small particles. John Wiley & Sons, New York, NY.

Bonan, G.B. 1996. A land surface model (LSM version 1.0) for ecological, hydrological, and atmospheric studies: Technical description and user's guide. NCAR Technical Note NCAR/TN-417+STR, National Center for Atmospheric Research, Boulder, CO, 150 pp.

Bonan, G.B. 1998. The land surface climatology of the NCAR Land Surface Model coupled to the NCAR Community Climate Model. J. Climate 11:1307-1326.

Bonan, G.B. 2002. Ecological Climatology: Concepts and Applications. Cambridge University Press.

Bonan, G.B., Oleson, K.W., Vertenstein, M., Levis, S., Zeng, X., Dai, Y., Dickinson, R.E., and Yang, Z.-L. 2002a. The land surface climatology of the Community Land Model coupled to the NCAR Community Climate Model. J. Climate 15: 3123-3149.

Bonan, G.B., Levis, S., Kergoat, L., and Oleson, K.W. 2002b. Landscapes as patches of plant functional types: An integrating concept for climate and ecosystem models. Global Biogeochem. Cycles 16: 5.1-5.23.

Bonan, G.B., and Levis, S. 2006. Evaluating aspects of the Community Land and Atmosphere Models (CLM3 and CAM3) using a dynamic global vegetation model. J. Climate 19:2290-2301.

Branstetter, M.L., and Famiglietti, J.S. 1999. Testing the sensitivity of GCM-simulated runoff to climate model resolution using a parallel river transport algorithm. Preprints, 14th Conference on Hydrology, Dallas, TX, Amer. Meteor. Soc., 391-392.

Branstetter, M.L. 2001. Development of a parallel river transport algorithm and applications to climate studies. Ph.D. dissertation, University of Texas at Austin.

Brun, E. 1989. Investigation of wet-snow metamorphism in respect of liquid water content. Ann. Glaciol. 13:22-26.

Bugmann, H., and Solomon, A.M. 2000. Explaining forest composition and biomass across multiple biogeographical regions. Ecol. Appl. 10:95-114.

Busing, R.T. 2005. Tree mortality, canopy turnover, and woody detritus in old cove forests of the southern Appalachians. Ecology 86:73-84.

Campbell, G.S., and Norman, J.M. 1998. An Introduction to Environmental Biophysics (2nd edition). Springer-Verlag, New York.

Clapp, R.B., and Hornberger, G.M. 1978. Empirical equations for some soil hydraulic properties. Water Resour. Res. 14:601-604.

Clauser, C., and Huenges, E. 1995. Thermal conductivity of rocks and minerals. pp. 105-126. In: T. J. Ahrens (editor) Rock Physics and Phase Relations: A Handbook of Physical Constants. Washington, D.C.

Cleveland, C.C., Townsend, A.R., Schimel, D.S., Fisher, H., Howarth, R.W., Hedin, L.O., Perakis, S.S., Latty, E.F., Von Fischer, J.C., Elseroad, A., and Wasson, M.F. 1999. Global patterns of terrestrial biological nitrogen (N2) fixation in natural ecosystems. Global Biogeochem. Cycles 13:623-645.

Cogley, J.G. 1991. GGHYDRO – Global Hydrographic Data Release 2.0. Trent Climate Note 91-1, Dept. Geography, Trent University, Peterborough, Ontario.

Collatz, G.J., Ball, J.T., Grivet, C., and Berry, J.A. 1991. Physiological and environmental regulation of stomatal conductance, photosynthesis, and transpiration: A model that includes a laminar boundary layer. Agric. For. Meteor. 54:107-136.

Collatz, G.J., Ribas-Carbo, M., and Berry, J.A. 1992. Coupled photosynthesis-stomatal conductance model for leaves of C_4 plants. Aust. J. Plant Physiol. 19:519-538.

Conway, H., Gades, A., and Raymond, C.F. 1996. Albedo of dirty snow during conditions of melt. Water Resour. Res. 32:1713-1718.

Cosby, B.J., Hornberger, G.M., Clapp, R.B., and Ginn, T.R. 1984. A statistical exploration of the relationships of soil moisture characteristics to the physical properties of soils. Water Resour. Res. 20:682-690.

Dai, Y., and Zeng, Q. 1997. A land surface model (IAP94) for climate studies. Part I: formulation and validation in off-line experiments. Adv. Atmos. Sci. 14:433-460.

Dai, Y., et al. 2001. Common Land Model: Technical documentation and user's guide [Available online at http://climate.eas.gatech.edu/dai/clmdoc.pdf].

Dai, Y., Zeng, X., Dickinson, R.E., Baker, I., Bonan, G.B., Bosilovich, M.G., Denning, A.S., Dirmeyer, P.A., Houser, P.R., Niu, G., Oleson, K.W., Schlosser, C.A., and Yang, Z.-L. 2003. The Common Land Model. Bull. Amer. Meteor. Soc. 84:1013-1023.

Dai, Y., Dickinson, R.E., and Wang, Y.-P. 2004. A two-big-leaf model for canopy temperature, photosynthesis, and stomatal conductance. J. Climate 17:2281-2299.

Dai, A., and Trenberth, K.E. 2002. Estimates of freshwater discharge from continents: Latitudinal and seasonal variations. J. Hydrometeor. 3:660-687.

DeFries, R.S., Hansen, M.C., Townshend, J.R.G., Janetos, A.C., and Loveland, T.R. 2000. A new global 1-km dataset of percentage tree cover derived from remote sensing. Global Change Biol. 6:247-254.

de Vries, D.A. 1963. Thermal Properties of Soils. In: W.R. van Wijk (editor) Physics of the Plant Environment. North-Holland, Amsterdam.

Dickinson, R.E. 1983. Land surface processes and climate-surface albedos and energy balance. Adv. Geophys. 25:305-353.

Dickinson, R.E., Henderson-Sellers, A., and Kennedy, P.J. 1993. Biosphere-Atmosphere Transfer Scheme (BATS) version 1e as coupled to the NCAR Community Climate Model. NCAR Technical Note NCAR/TN-387+STR. National Center for Atmospheric Research, Boulder, CO.

Dickinson, R.E., Oleson, K.W., Bonan, G., Hoffman, F., Thornton, P., Vertenstein, M., Yang, Z.-L., and Zeng, X. 2006. The Community Land Model and its climate statistics as a component of the Community Climate System Model. J. Climate 19:2302-2324.

Dirmeyer, P.A., Dolman, A.J., and Sato, N. 1999. The pilot phase of the Global Soil Wetness Project. Bull. Amer. Meteor. Soc. 80:851-878.

Dobson, J.E., Bright, E.A., Coleman, P.R., Durfee, R.C., and Worley, B.A. 2000. LandScan: A global population database for estimating populations at risk. Photogramm. Eng. Rem. Sens. 66:849-857.

Dorman, J.L., and Sellers, P.J. 1989. A global climatology of albedo, roughness length and stomatal resistance for atmospheric general circulation models as represented by the simple biosphere model (SiB). J. Appl. Meteor. 28:833-855.

Dougherty, R.L., Bradford, J.A., Coyne, P.I., and Sims, P.L. 1994. Applying an empirical model of stomatal conductance to three C4 grasses. Agric. For. Meteor. 67:269-290.

Entekhabi, D., and Eagleson, P.S. 1989. Land surface hydrology parameterization for atmospheric general circulation models including subgrid scale spatial variability. J. Climate 2:816-831.

Farouki, O.T. 1981. The thermal properties of soils in cold regions. Cold Regions Sci. and Tech. 5:67-75.

Farquhar, G.D., von Caemmerer, S., and Berry, J.A. 1980. A biochemical model of photosynthetic CO_2 assimilation in leaves of C_3 species. Planta 149:78-90.

Farquhar, G.D., and von Caemmerer, S. 1982. Modeling of photosynthetic response to environmental conditions. pp. 549-587. In: O.L. Lange, P.S. Nobel, C.B. Osmond,

and H. Zeigler (editors) Encyclopedia of Plant Physiology. Vol. 12B. Physiological Plant Ecology. II. Water Relations and Carbon Assimilation. Springer-Verlag, New York.

Flanner, M.G., and Zender. C.S. 2005. Snowpack radiative heating: Influence on Tibetan Plateau climate. Geophys. Res. Lett. 32:L06501. DOI:10.1029/2004GL022076.

Flanner, M.G., and Zender, C.S. 2006. Linking snowpack microphysics and albedo evolution. J. Geophys. Res. 111:D12208. DOI:10.1029/2005JD006834.

Flanner, M.G., Zender, C.S., Randerson, J.T., and Rasch, P.J. 2007. Present day climate forcing and response from black carbon in snow. J. Geophys. Res. 112:D11202. DOI:10.1029/2006JD008003.

Flatau, P.J., Walko, R.L., and Cotton, W.R. 1992. Polynomial fits to saturation vapor pressure. J. Appl. Meteor. 31:1507-1513.

Friedl, M.A., McIver, D.K., Hodges, J.C.F., Zhang, X.Y., Muchoney, D., Strahler, A.H., Woodcock, C.E., Gopal, S., Schneider, A., Cooper, A., Baccini, A., Gao, F., and Schaaf, C. 2002. Global land cover mapping from MODIS: algorithms and early results. Remote Sens. Environ. 83:287-302.

Galloway, J.N., et al. 2004. Nitrogen cycles: past, present, and future. Biogeochem. 70:153-226.

Garcia, R.L., Kanemasu, E.T., Blad, B.L., Bauer, A., Hatfield, J.L., Major, D.A., Reginato, R.J., and Hubbard, K.G. 1988. Interception and use efficiency of light in winter wheat under different nitrogen regimes. Agric. For. Meteor. 44:175-186.

Gash, J.H.C., Nobre, C.A., Roberts, J.M., and Victoria, R.L. 1996. An overview of ABRACOS. pp. 1-14. In: J.H.C. Gash, C.A. Nobre, J.M. Roberts, and R.L. Victoria

(editors) Amazonian Deforestation and Climate. John Wiley and Sons, Chichester, England.

Global Soil Data Task 2000. Global soil data products CD-ROM (IGBP-DIS). International Geosphere-Biosphere Programme-Data and Information Available Services [Available online at http://www.daac.ornl.gov].

Gomes, E.P.C., Mantovani, W., and Kageyama, P.Y. 2003. Mortality and recruitment of trees in a secondary montane rain forest in southeastern Brazil. Brazilian Journal of Biology 63:47-60.

Gosz, J.R., Likens, G.E., and Bormann, F.H. 1973. Nutrient release from decomposing leaf and branch litter in the Hubbard Brook Forest, New Hampshire. Ecological Monographs 43:173-191.

Graham, S.T., Famiglietti, J.S., and Maidment, D.R. 1999. Five-minute, 1/2°, and 1° data sets of continental watersheds and river networks for use in regional and global hydrologic and climate system modeling studies. Water Resour. Res. 35:583-587.

Grenfell, T.C., and Warren, S.G. 1999. Representation of a nonspherical ice particle by a collection of independent spheres for scattering and absorption of radiation. J. Geophys. Res. 104(D24):37697-37709.

Guenther, A., Hewitt, C.N., Erickson, D., Fall, R., Geron, C., Graedel, T., Harley, P., Klinger, L., Lerdau, M., McKay, W.A., Pierce, T., Scholes, B., Steinbrecher, R., Tallamraju, R., Taylor, J., and Zimmerman, P. 1995. A global model of natural volatile organic compound emissions. J. Geophys. Res. 100:8873-8892.

Guenther, A., Karl, T., Harley, P., Wiedinmyer, C., Palmer. P.I., and Geron, C. 2006. Estimates of global terrestrial isoprene emissions using MEGAN (Model of Emissions of Gases and Aerosols from Nature). Atmos. Chem. Phys. 6:3181–3210.

Hack, J.J., Caron, J.M., Yeager, S.G., Oleson, K.W., Holland, M.M., Truesdale, J.E., and Rasch, P.J. 2006. Simulation of the global hydrological cycle in the CCSM Community Atmosphere Model version 3 (CAM3): mean features. J. Climate 19:2199-2221.

Hansen, M., DeFries, R.S., Townshend, J.R.G., Carroll, M., Dimiceli, C., and Sohlberg, R.A. 2003. Global percent tree cover at a spatial resolution of 500 meters: first results of the MODIS vegetation continuous fields algorithm. Earth Interactions 7(10):1-15.

Heald, C.L., Henze, D.K., Horowitz, L.W., Feddema, J., Lamarque, J.-F., Guenther, A., Hess, P.G., Vitt, F., Seinfeld, J.H., Goldstein, A.H., and Fung, I. 2008. Predicted change in global secondary organic aerosol concentrations in response to future climate, emissions, and land use change. J. Geophys. Res. 113:D05211. DOI:10.1029/2007JD009092.

Henderson-Sellers, B. 1985. New formulation of eddy diffusion thermocline models. Appl. Math. Modelling 9:441-446.

Henderson-Sellers, B. 1986. Calculating the surface energy balance for lake and reservoir modeling: A review. Rev. Geophys. 24:625-649.

Henderson-Sellers, A., Yang, Z.-L., and Dickinson, R.E. 1993. The project for intercomparison of land-surface parameterization schemes. Bull. Amer. Meteor. Soc. 74: 1335-1349.

Hostetler, S.W., and Bartlein, P.J. 1990. Simulation of lake evaporation with application to modeling lake level variations of Harney-Malheur Lake, Oregon. Water Resour. Res. 26:2603-2612.

Hostetler, S.W., Bates, G.T., and Giorgi, F. 1993. Interactive coupling of a lake thermal model with a regional climate model. J. Geophys. Res. 98:5045-5057.

Hostetler, S.W., Giorgi, F., Bates, G.T., and Bartlein, P.J. 1994. Lake-atmosphere feedbacks associated with paleolakes Bonneville and Lahontan. Science 263:665-668.

Hunt, H.W., Ingham, E.R., Coleman, D.C., Elliott, E.T., and Reid, C.P.P. 1988. Nitrogen limitation of production and decomposition in prairie, mountain meadow, and pine forest. Ecology 69:1009-1016.

Hurtt, G.C., Frolking, S., Fearon, M.G., Moore, B., Shevliakova, E., Malyshev, S., Pacala, S.W., and Houghton, R.A. 2006. The underpinnings of land-use history: three centuries of global gridded land-use transitions, wood-harvest activity, and resulting secondary lands. Global Change Biol. 12:1208-1229.

Idso, S.B. 1981. A set of equations for full spectrum and 8- to 14-μm and 10.5- to 12.5-μm thermal radiation from cloudless skies. Water Resour. Res. 17:295-304.

Jackson, T.L., Feddema, J.J., Oleson, K.W., Bonan, G.B., and Bauer, J.T. 2010. Parameterization of urban characteristics for global climate modeling. Annals of the Association of American Geographers, in press.

Jordan, R. 1991. A One-dimensional Temperature Model for a Snow Cover: Technical Documentation for SNTHERM.89. U.S. Army Cold Regions Research and Engineering Laboratory, Special Report 91-16.

Kohyama, T., Suzuki, E., Partomihardjo, T., and Yamada, T. 2001. Dynamic steady state of patch-mosaic tree size structure of a mixed diptocarp forest regulated by local crowding. Ecological Research 16:85-98.

Lamarque, J.F., et al. 2010, in preparation.

Larcher, W. 1995. Physiological Plant Ecology, Springer-Verlag, Berlin Heidelberg.

Lavigne, M.B., and Ryan, M.G. 1997. Growth and maintenance respiration rates of aspen, black spruce, and jack pine stems at northern and southern BOREAS sites. Tree Phys. 17:543-551.

Lawrence, D.M., Thornton, P.E., Oleson, K.W., and Bonan, G.B. 2007. The partitioning of evapotranspiration into transpiration, soil evaporation, and canopy evaporation in a GCM: Impacts on land-atmosphere interaction. J. Hydrometeor. 8:862-880.

Lawrence, D.M., and Slater, A.G. 2008. Incorporating organic soil into a global climate model. Clim. Dyn. 30. DOI:10.1007/s00382-007-0278-1.

Lawrence, D.M., Slater, A.G., Romanovsky, V.E., and Nicolsky, D.J. 2008. The sensitivity of a model projection of near-surface permafrost degradation to soil column depth and inclusion of soil organic matter. J. Geophys. Res. 113:F02011. DOI:10.1029/2007JF000883.

Lawrence, P.J., and Chase, T.N. 2007. Representing a MODIS consistent land surface in the Community Land Model (CLM 3.0). J. Geophys. Res. 112:G01023. DOI:10.1029/2006JG000168.

Lawrence, P.J., and Chase, T.N. 2010. Investigating the climate impacts of global land cover change in the Community Land Model. Int. J. Climatol., in press.

Letts, M.G., Roulet, N.T., Comer, N.T., Skarupa, M.R., and Verseghy, D.L. 2000. Parametrization of peatland hydraulic properties for the Canadian Land Surface Scheme. Atmos.-Ocean 38:141-160.

Levis, S., Wiedinmyer, C., Bonan, G.B., and Guenther, A. 2003. Simulating biogenic volatile organic compound emissions in the Community Climate System Model. J. Geophys. Res. 108:4659. DOI:10.1029/2002JD003203.

Levis, S., Bonan, G.B., Vertenstein, M., and Oleson, K.W. 2004. The community land model's dynamic global vegetation model (CLM-DGVM): technical description and user's guide. NCAR Technical Note NCAR/TN-459+STR. National Center for Atmospheric Research, Boulder, CO, 50 pp.

Loveland, T.R., Reed, B.C., Brown, J.F., Ohlen, D.O., Zhu, Z., Yang, L., and Merchant, J.W. 2000. Development of a global land cover characteristics database and IGBP DISCover from 1 km AVHRR data. Int. J. Remote Sens. 21:1303-1330.

Lowe, P.R. 1977. An approximating polynomial for the computation of saturation vapor pressure. J. Appl. Meteor. 16:100-103.

Luo, Y., Hui, D., and Zhang, D. 2006. Elevated CO2 stimulates net accumulations of carbon and nitrogen in land ecosystems: a meta-analysis. Ecology 87:53-63.

Mahowald, N.M., Muhs, D.R., Levis, S., Rasch, P.J., Yoshioka, M., Zender, C.S., and Luo, C. 2006. Change in atmospheric mineral aerosols in response to climate: last glacial period, pre-industrial, modern and doubled CO_2 climates. J. Geophys. Res. 111:D10202. DOI:10.1029/2005JD006653.

Makela, A. 2002. Derivation of stem taper from the pipe model theory in a carbon balance framework. Tree Phys. 22:891-905.

McGuire, A.D., Melillo, J.M., Joyce, L.A., Kicklighter, D.W., Grace, A.L., Moore III, B., and Vorosmarty, C.J. 1992. Interactions between carbon and nitrogen dynamics in estimating net primary productivity for potential vegetation in North America. Global Biogeochem. Cycles 6:101-124.

Miller, J.R., Russell, G.L., and Caliri, G. 1994. Continental-scale river flow in climate models. J. Climate 7:914-928.

Myneni, R.B., et al. 2002. Global products of vegetation leaf area and fraction absorbed PAR from year one of MODIS data. Remote Sens. Environ. 83:214-231.

Nemani, R.R., and Running, S.W. 1996. Implementation of a hierarchical global vegetation classification in ecosystem function models. J. Veg. Sci. 7:337-346.

Niinemets, U., Kull, O., and Tenhunen, J.D. 1998. An analysis of light effects on foliar morphology, physiology, and light interception in temperate deciduous woody species of contrasting shade tolerance. Tree Phys. 18:681-696.

Niu, G.-Y., Yang, Z.-L., Dickinson, R.E., and Gulden, L.E. 2005. A simple TOPMODEL-based runoff parameterization (SIMTOP) for use in global climate models. J. Geophys. Res. 110:D21106. DOI: 10.1029/2005JD006111.

Niu, G.-Y., and Yang, Z.-L. 2006. Effects of frozen soil on snowmelt runoff and soil water storage at a continental scale. J. Hydrometeor. 7:937-952.

Niu, G.-Y., Yang, Z.-L., Dickinson, R.E., Gulden, L.E., and Su, H. 2007. Development of a simple groundwater model for use in climate models and evaluation with Gravity Recovery and Climate Experiment data. J. Geophys. Res. 112:D07103. DOI:10.1029/2006JD007522.

Niu, G.-Y., and Yang, Z.-L. 2007. An observation-based formulation of snow cover fraction and its evaluation over large North American river basins. J. Geophys. Res. 112:D21101. DOI:10.1029/2007JD008674.

Oke, T. 1987. Boundary Layer Climates (2nd edition). Routledge, London and New York.

Oleson, K.W., and Bonan, G.B. 2000. The effects of remotely-sensed plant functional type and leaf area index on simulations of boreal forest surface fluxes by the NCAR land surface model. J. Hydrometeor. 1:431-446.

Oleson, K.W., Dai, Y., Bonan, G., Bosilovich, M., Dickinson, R., Dirmeyer, P., Hoffman, F., Houser, P., Levis, S., Niu, G.-Y., Thornton, P., Vertenstein, M., Yang, Z.-L., and Zeng. X. 2004. Technical description of the Community Land Model (CLM). NCAR Technical Note NCAR/TN-461+STR. National Center for Atmospheric Research, Boulder, CO, 173 pp.

Oleson, K.W., Niu, G.-Y., Yang, Z.-L., Lawrence, D.M., Thornton, P.E., Lawrence, P.J., Stöckli, R., Dickinson, R.E., Bonan, G.B., Levis, S., Dai, A., and Qian, T. 2008a. Improvements to the Community Land Model and their impact on the hydrological cycle. J. Geophys. Res. 113:G01021. DOI:10.1029/2007JG000563.

Oleson, K.W., Bonan, G.B., Feddema, J., Vertenstein, M., and Grimmond, C.S.B. 2008b. An urban parameterization for a global climate model. 1. Formulation and evaluation for two cities. J. Appl. Meteor. Clim. 47:1038-1060.

Oleson, K.W., Bonan, G.B., Feddema, J., and Vertenstein, M. 2008c. An urban parameterization for a global climate model. 2. Sensitivity to input parameters and the simulated urban heat island in offline simulations. J. Appl. Meteor. Clim. 47:1061-1076.

Oleson, K.W., Bonan, G.B., Feddema, J., Jackson, T., Vertenstein, M., and Kluzek, E. 2010. Technical description of an urban parameterization for the Community Land Model (CLMU). NCAR Technical Note NCAR/TN-480+STR, National Center for Atmospheric Research, Boulder, CO, 169 pp.

Owen, P.R. 1964. Saltation of uniform grains in air. J. Fluid Mech. 20:225-242.

Panofsky, H.A., and Dutton, J.A. 1984. Atmospheric Turbulence: Models and Methods for Engineering Applications. John Wiley and Sons, New York.

Philip, J.R. 1957. Evaporation, and moisture and heat fields in the soil. J. Meteor. 14:354-366.

Press, W.H., Teukolsky, S.A., Vetterling, W.T., and Flannery, B.P. 1992. Numerical Recipes in FORTRAN: The Art of Scientific Computing. Cambridge University Press, New York.

Qian, T., Dai, A., Trenberth, K.E., and Oleson, K.W. 2006. Simulation of global land surface conditions from 1948 to 2004: Part I: Forcing data and evaluations. J. Hydrometeor. 7:953-975.

Ramankutty, N., Evan, A., Monfreda, C., and Foley, J.A. 2008. Farming the Planet. Part 1: The Geographic Distribution of Global Agricultural Lands in the Year 2000. Global Biogeochem. Cycles. 22:GB1003. DOI:10.1029/2007GB002952.

Randlett, D.L., Zak, D.R., Pregitzer, K.S., and Curtis, P.S. 1996. Elevated atmospheric carbon dioxide and leaf litter chemistry: Influences on microbial respiration and net nitrogen mineralization. Soil Sci. Soc. Am. J. 60:1571-1577.

Rastetter, E.B., Ryan, M.G., Shaver, G.R., Melillo, J.M., Nadelhoffer, K.J., Hobbie, J.E., and Aber, J.D. 1991. A general biogeochemical model describing the responses of the C and N cycles in terrestrial ecosystems to changes in CO2, climate and N deposition. Tree Phys. 9:101-126.

Ryan, M. G. 1991. A simple method for estimating gross carbon budgets for vegetation in forest ecosystems. Tree Phys. 9:255-266.

Sakaguchi, K., and Zeng, X. 2009. Effects of soil wetness, plant litter, and under-canopy atmospheric stability on ground evaporation in the Community Land Model (CLM3.5). J. Geophys. Res. 114:D01107. DOI:10.1029/2008JD010834.

Schaaf, C.B., Gao, F., Strahler, A.H., Lucht, W., Li, X., Tsang, T., Strugnell, N.C., Zhang, X., Jin, Y., and Muller, J.-P. 2002. First operational BRDF, albedo nadir reflectance products from MODIS. Remote Sens. Environ. 83:135-148.

Sellers, P.J. 1985. Canopy reflectance, photosynthesis and transpiration. Int. J. Remote Sens. 6:1335-1372.

Sellers, P.J., Mintz, Y., Sud, Y.C., and Dalcher, A. 1986. A simple biosphere model (SiB) for use within general circulation models. J. Atmos. Sci. 43:505-531.

Sellers, P.J., Hall, F.G., Asrar, G., Strebel, D.E., and Murphy, R.E. 1988. The First ISLSCP Field Experiment (FIFE). Bull. Amer. Meteor. Soc. 69:22-27.

Sellers, P.J., Berry, J.A., Collatz, G.J., Field, C.B., and Hall, F.G. 1992. Canopy reflectance, photosynthesis, and transpiration. III. A reanalysis using improved leaf models and a new canopy integration scheme. Remote Sens. Environ. 42:187-216.

Sellers, P.J., et al. 1995. The Boreal Ecosystem-Atmosphere Study (BOREAS): An overview and early results from the 1994 field year. Bull. Amer. Meteor. Soc. 76:1549-1577.

Sellers, P.J., Randall, D.A., Collatz, G.J., Berry, J.A., Field, C.B., Dazlich, D.A., Zhang, C., Collelo, G.D., and Bounoua, L. 1996. A revised land surface parameterization (SiB2) for atmospheric GCMs. Part I: Model formulation. J. Climate 9:676-705.

Sprugel, D.G., Ryan, M.G., Brooks, J.R., Vogt, K.A., and Martin, T.A. 1995. Respiration from the organ level to stand level. pp. 255-299. In: W. K. Smith and T. M. Hinkley (editors) Resource Physiology of Conifers. Academic Press, San Diego,CA.

Stauffer, D., and Aharony, A. 1994. Introduction to Percolation Theory. Taylor and Francis, London.

Still, C.J., Berry, J.A., Collatz, G.J., and DeFries, R.S. 2003. Global distribution of C3 and C4 vegetation: carbon cycle implications. Global Biogeochem. Cycles 17:1006. DOI: 10.1029/2001GB001807.

Stöckli, R., Lawrence, D.M., Niu, G.-Y., Oleson, K.W., Thornton, P.E., Yang, Z.-L., Bonan, G.B., Denning, A.S., and Running, S.W. 2008. Use of FLUXNET in the Community Land Model development. J. Geophys. Res. 113:G01025. DOI:10.1029/2007JG000562.

Strahler, A.H., Muchoney, D., Borak, J., Friedl, M., Gopal, S., Lambin, E., and Moody. A. 1999. MODIS Land Cover Product: Algorithm Theoretical Basis Document (Version 5.0). Boston University, Boston.

Stull, R.B. 1988. An Introduction to Boundary Layer Meteorology. Kluwer Academic Publishers, Dordrecht.

Thonicke, K., Venevsky, S., Sitch, S., and Cramer, W. 2001. The role of fire disturbance for global vegetation dynamics: coupling fire into a Dynamic Global Vegetation Model. Global Ecology and Biogeography 10:661-667.

Thornton, P.E., Law, B.E., Gholz, H.L., Clark, K.L., Falge, E., Ellsworth, D.S., Goldstein, A.H., Monson, R.K., Hollinger, D., Falk, M., Chen, J., and Sparks, J.P. 2002. Modeling and measuring the effects of disturbance history and climate on

carbon and water budgets in evergreen needleleaf forests. Agric. For. Meteor. 113:185-222.

Thornton, P.E., and Rosenbloom, N.A. 2005. Ecosystem model spin-up: estimating steady state conditions in a coupled terrestrial carbon and nitrogen cycle model. Ecological Modelling 189:25-48.

Thornton, P.E., and Zimmermann, N.E. 2007. An improved canopy integration scheme for a land surface model with prognostic canopy structure. J. Climate 20:3902-3923.

Thornton, P.E., Lamarque, J.-F., Rosenbloom, N.A., and Mahowald, N.M. 2007. Influence of carbon-nitrogen cycle coupling on land model response to CO_2 fertilization and climate variability. Global Biogeochem. Cycles 21:GB4018.

Thornton, P.E., Doney, S.C., Lindsay, K., Moore, J.K., Mahowald, N., Randerson, J.T., Fung, I., Lamarque, J.F., Feddema, J.J., and Lee, Y.H. 2009. Carbon-nitrogen interactions regulate climate-carbon cycle feedbacks: results from an atmosphere-ocean general circulation model. Biogeosci. 6:2099-2120.

Thornton, P.E., et al. 2010. Technical description of the Community Land Model Carbon-Nitrogen model (CLM-CN), in preparation.

Toon, O.B., McKay, C.P., Ackerman, T.P., and Santhanam, K. 1989. Rapid calculation of radiative heating rates and photodissociation rates in inhomogeneous multiple scattering atmospheres. J. Geophys. Res. 94(D13):16,287-16,301.

Unland, H.E., Houser, P.R., Shuttleworth, W.J., and Yang, Z.-L. 1996. Surface flux measurement and modeling at a semi-arid Sonoran Desert site. Agric. For. Meteor. 82:119-153.

Vanninen, P., and Makela, A. 2005. Carbon budget for Scots pine trees: effects of size, competition and site fertility on growth allocation and production. Tree Phys. 25:17-30.

Vitousek, P.M., and Howarth, R.W. 1991. Nitrogen limitation on land and in the sea: How can it occur? Biogeochem. 13:87-115.

Wang, A., and Zeng, X. 2009. Improving the treatment of vertical snow burial fraction over short vegetation in the NCAR CLM3. Adv. Atmos. Sci. 26:877-886. DOI:10.1007/s00376-009-8098-3.

White, M.A., Thornton, P.E., and Running, S.W. 1997. A continental phenology model for monitoring vegetation responses to interannual climatic variability. Global Biogeochem. Cycles 11:217-234.

White, M.A., Thornton, P.E., Running, S.W., and Nemani, R.R. 2000. Parameterization and sensitivity analysis of the Biome-BGC terrestrial ecosystem model: net primary production controls. Earth Interactions 4:1-85.

Wiscombe, W.J., and Warren, S.G. 1980. A model for the spectral albedo of snow. I. Pure snow. J. Atmos. Sci. 37:2712-2733.

Yang, Z.-L. 1998. Technical note of a 10-layer soil moisture and temperature model. Unpublished manuscript.

Zender, C.S., Bian, H., and Newman, D. 2003. Mineral dust entrainment and deposition (DEAD) model: Description and 1990s dust climatology. J. Geophys. Res. 108(D14): 4416. DOI:10.1029/2002JD002775.

Zeng, X., and Dickinson, R.E. 1998. Effect of surface sublayer on surface skin temperature and fluxes. J.Climate 11:537-550.

Zeng, X., Zhao, M., and Dickinson, R.E. 1998. Intercomparison of bulk aerodynamic algorithms for the computation of sea surface fluxes using the TOGA COARE and TAO data. J. Climate 11:2628-2644.

Zeng, X. 2001. Global vegetation root distribution for land modeling. J. Hydrometeor. 2:525-530.

Zeng, X., Shaikh, M., Dai, Y., Dickinson, R.E., and Myneni, R. 2002. Coupling of the Common Land Model to the NCAR Community Climate Model. J. Climate 15:1832-1854.

Zeng, X., Dickinson, R.E., Barlage, M., Dai, Y., Wang, G., and Oleson, K. 2005. Treatment of under-canopy turbulence in land models. J. Climate 18:5086-5094.

Zeng, X., and Wang, A. 2007. Consistent parameterization of roughness length and displacement height for sparse and dense canopies in land models. J. Hydrometeor. 8:730-737.

Zeng, X., and Decker, M. 2009. Improving the numerical solution of soil moisture-based Richards equation for land models with a deep or shallow water table. J. Hydrometeor. 10:308-319.

Zeng, X., Zeng, X., and Barlage, M. 2008. Growing temperate shrubs over arid and semiarid regions in the Community Land Model - Dynamic Global Vegetation Model. Global Biogeochem. Cycles 22:GB3003. DOI:10.1029/2007GB003014.

Zilitinkevich, S.S. 1970. Dynamics of the Atmospheric Boundary Layer. Leningrad Gidrometeor.